



CENTRO BRASILEIRO DE PESQUISAS FÍSICAS
DOCTORATE PROGRAM

Juan Baptista de Souza Leite

Amplitude analysis of the $D_s^+ \rightarrow \pi^- \pi^+ \pi^+$ decay

Rio de Janeiro/RJ

2023

“AMPLITUDE ANALYSIS OF THE $D_s^+ \rightarrow \pi^- \pi^+ \pi^+$ DECAY”

JUAN BAPTISTA DE SOUZA LEITE

Tese de Doutorado em Física apresentada no
Centro Brasileiro de Pesquisas Físicas do
Ministério da Ciência Tecnologia e Inovação.
Fazendo parte da banca examinadora os seguintes
professores:



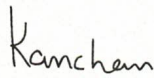
Alberto Correa dos Reis - Orientador/CBPF



Ivone Freire da Mota e Albuquerque - USP



Patrícia Camargo Magalhães - UNICAMP



Kanchan Pradeepkumar Khmenshandani – USP



Michael David Sokoloff – UNIVERSITY OF CINCINNATI

Rio de Janeiro, 27 de setembro de 2023.

Abstract

In this thesis, the amplitude analysis of the $D_s^+ \rightarrow \pi^- \pi^+ \pi^+$ decay was performed to determine the $\pi^- \pi^+$ S -wave amplitude and the resonant structure of the P- and D-waves. The analysis is based on proton-proton collision data recorded by the LHCb experiment in 2012 at a centre-of-mass energy of 8 TeV and corresponding to an integrated luminosity of 1.5 fb^{-1} . The analysis includes the first observation of the following decay channels in the $D_s^+ \rightarrow \pi^- \pi^+ \pi^+$ decay: $D_s^+ \rightarrow \omega(782)\pi^+$, $D_s^+ \rightarrow \rho(1700)^0\pi^+$ and $D_s^+ \rightarrow f_2'(1525)\pi^+$. The resonant structures of the $D_s^+ \rightarrow \pi^- \pi^+ \pi^+$ and $D^+ \rightarrow \pi^- \pi^+ \pi^+$ decays are also compared, providing information about the mechanisms for the hadron formation in these decays. Furthermore, technical contributions made to the LHCb experiment during the PhD studies, specifically in the preparation for the LHC Run 3, are described.

Keywords: CHARM. LHCb. RESONANCES.

Agradecimentos

O presente trabalho foi realizado com apoio da Coordenação de Aperfeiçoamento de Pessoal de Nível Superior (CAPES) e Conselho Nacional de Desenvolvimento Científico e Tecnológico (CNPq).

Essa tese é dedicada à minha mãe Jacqueline Baptista de Souza Leite que infelizmente não viveu o suficiente para presenciar esse momento, e à minha segunda mãe, minha avó materna Heloisa Gonçalves Batista. Muito obrigado pelos valorosos sacrifícios e assistências que tornaram possível esse momento. Obrigado vó, por ter substituído minha mãe com tamanha excelência e gentileza.

Agradeço primeiramente a meu orientador Alberto Reis, meu ‘pai’ e sensei acadêmico. Comecei a ser orientado pelo Alberto ainda na iniciação científica pela indicação do grande José Helayel, a quem também agradeço. Durante quase 7 anos tentei absorver o que pude do seu vasto conhecimento e me inspirar na sua confiança, liderança, senso crítico e entusiasmo. Obrigado por ter acreditado no meu potencial e por sempre me apontar na direção do êxito. Serei eternamente grato. Foi um privilégio ser teu aluno.

Agradeço também as Charmosas do grupo de Charm physics do LHCb-Rio, Sandra Amato, Carla Gobel e Érica Policarpo. Obrigado por todas as discussões e sugestões sobre as análises, os bons conselhos e encaminhamentos na vida profissional. Agradeço à Érica, por me socorrer sempre que precisava debugar os códigos da análise e me ensinar truques de VIM. Agradeço à Carla, minha quase orientadora, por todas as dicas de análise e cartas de recomendações, e agradeço à Sandra por todas as dicas e por ser uma espécie de Git das nossas reuniões. Eu não poderia ter escolhido um grupo melhor, foi um privilégio.

Agradeço os colaboradores do grupo de B-physics do LHCb-Rio, Diego, Patrícia, Juan, Fernando, Irina, Helder et al. Em especial agradeço: Ignácio e Jussara pelas dúvidas respondidas e pelas dicas. Ao André Massafferri pela oportunidade do doutorado sanduíche e por ser um dos poucos flamenguistas do quinto andar do CBPF. E ao Alvaro que infelizmente nos deixou prematuramente.

Agradeço também meus colegas do grupo do charm, aka. charmosinhos, Beatriz, Victória, Leonardo, Caio, Gustavo, Romão, Ivanildo, Alexandre e Carolina. Algumas menções especiais: Fernanda Abrantes, minha ex-parceira de análise, juntos produzimos resultados super legais, obrigado pela amizade e pela colaboração nos trabalhos. Felipe Luan, obrigado pela amizade, pela colaboração nos trabalhos, pelos debates sobre política, e por fingir rir das dezenas de memes que te encaminho por semana. Lucas Falcão (aka Stark), esse eu aturo faz quase 10 anos, obrigado pela amizade, pelos comentários completamente fora da realidade sobre política e economia, e pelas reações síncricas dos

memes que te encaminhinho.

Agradeço meus professores da UERJ e do CBPF. Em especial: O Professor Wagner Carvalho de Paula (UERJ), meu primeiro orientador em física de altas energias ainda na graduação, com quem aprendi muito. O Professor Sebastião Alves (CBPF) pelo ótimo curso de Métodos Teóricos, só faltando uma dobradinha com o Alberto para trazer um pouco do lado experimental ao curso.

Agradeço aos meus colegas do LAPE-UFRJ, Lucas Meyer e o Professor Murilo Santana.

Agradeço aos meus ex-colegas de graduação Victor, Pedro, Rui, Luiz Felipe, Matheus, Marcele e Késia. E minha ex-colega do CBPF, Sheila.

Agradeço a todos os familiares, em especial: A minha avó materna Ieunice Sant'Anna, A minha tia-avó Terezinha Machado. Meu tio Edson Araújo, a quem atribuo meu gosto musical. E minha tia Lucimar Leite, pelo apoio, conversas e debates sobre a política gonçalense.

Agradeço o corpo de funcionários do CBPF, em especial as secretárias Sônia, Thaíssa, Bete e Laríssa. Obrigado por sempre estarem prontas a ajudar.

I special thank Rosen Matev, for his extremely kind and professional supervision during my two stays at CERN. I thank Vava, for supporting me and for his inspiring leadership. I thank the LHCb ladies: Carla Benito, for her inspiring leadership. Marianna Fontanna and Elizabeth Niel, for their contributions to the review of the $D_s^+ \rightarrow \pi^- \pi^+ \pi^+$ analysis and for being very kind. Florian Reiss and Thomas Boettcher, for their help with GooFit. The LHCb secretaries, Nathalie, Kevin and Cindy, for the always excellent assistance. I special thank Michael D. Sokoloff, for his inspiring leadership, trajectory, support, histories of his travel to Rio in the 1980s, and the kind recommendations of Roma tourist places and what to avoid for my personal security there.

Contents

1	INTRODUCTION	1
2	THEORETICAL BACKGROUND AND ANALYSIS TOOLS	4
2.1	The theoretical background	4
2.1.1	The Standard Model	4
2.1.2	Flavour Physics	6
2.1.3	Dalitz plot	7
2.1.4	Dalitz plot formalism	9
2.2	The analysis tools	16
2.2.1	sPlot	17
2.2.2	Multivariate Analysis	18
2.2.3	Rewighting	20
2.2.4	GooFit	21
2.3	Definition of variables	21
3	THE LHCb EXPERIMENT	23
3.1	The LHC	23
3.2	LHCb detector	25
3.2.1	The tracking system	26
3.2.2	The particle identification system	30
3.2.3	The trigger system	35
4	LHCb DETECTOR UPGRADE	41
4.0.1	The tracking system	43
4.0.2	The particle identification system	45
4.0.3	The Trigger system	46
5	AMPLITUDE ANALYSIS OF THE $D_s^+ \rightarrow \pi^- \pi^+ \pi^+$ DECAY	48
5.1	Statistical treatment of data and simulation samples	48
5.2	Invariant mass fit and analysis sample	60
5.3	Result	68
6	INTRODUCTION TO THE DALITZ PLOT ANALYSIS OF THE $D^+ \rightarrow \pi^- \pi^+ \pi^+$ DECAY RESULTS	75
6.1	Selection	75
6.2	Dalitz plot fit	77
6.3	Summary of the results	79

7	INTEPRETATION OF THE RESULTS	81
7.1	The $\pi^+\pi^-$ <i>S</i>-wave	81
7.2	The $\pi^+\pi^-$ <i>P</i>-wave	87
7.3	The $\pi^+\pi^-$ <i>D</i>-wave	92
7.4	Summary and conclusions	92
8	THECHNICAL CONTRIBUTIONS FOR LHCb UPGRADE	96
8.1	HLT1 GPU trigger lines	96
8.2	The ECAL π^0 Calibration	98
9	CONCLUSIONS	102
A	MVA	104
B	SYSTEMATICS	108
C	ALTERNATIVE MODELS	120
C.1	PWA-2 - Fit without $\rho(770)^0$	120
C.2	PWA-3 - Fit without $\omega(782)$	122
C.3	PWA-4 - Excluding $f_2'(1525)$	124
C.4	PWA-5 - Fit without $\rho(1700)^0$	126
C.5	PWA-6 - Fit with $\rho - \omega$ mixing amplitude	128
C.6	PWA-7 - Vetoing regions with low efficiency	131
C.7	PWA-8 - Fit including Bose-Einstein correlation	133
D	BRIEF DISCURSION ABOUT THE SCALARS	136
	REFERENCES	140

List of Figures

Figure 1	– Tree diagrams leading to of the $D^+ \rightarrow \pi^- \pi^+ \pi^+$ and $D_s^+ \rightarrow \pi^- \pi^+ \pi^+$ decays. The scalar mesons are formed by rescattering of the pseudo-scalar mesons a' and b'	3
Figure 2	– The periodic table of elementary particles.	5
Figure 3	– Dalitz plot for a three-body final state. In this example, the state is $\pi^+ \bar{K}^0 p$ at 3 GeV. Four-momentum conservation restricts events to the shaded region. Source [1]	9
Figure 4	– The $\pi^+ \pi^-$ mass resolution. In the $\omega(782)$ region, the resolution is 2.3 MeV.	14
Figure 5	– An example of a Decision Tree. Source [2].	19
Figure 6	– The gradient descent optimization. Source [3].	19
Figure 7	– A typical topology of a D-meson decay. Here, it is illustrated for the $D^+ \rightarrow \pi^- \pi^+ \pi^+$ decay.	21
Figure 8	– The LHC is the last ring (dark blue line) in a complex chain of particle accelerators. The smaller machines are used in a chain to help boost the particles to their final energies and provide beams to a whole set of smaller experiments, which also aim to uncover the mysteries of the universe. Source: CERN	24
Figure 9	– The angular distribution of $b\bar{b}$ production as a function of the angle to the beam axis (left) and as a function of the pseudorapidity (right) at $\sqrt{s} = 14$ TeV centre-of-mass energy. The distributions shown in these plots were created using PYTHIA8 [4] and CTEQ6 NLO pdf. The red square in the right figure shows the LHCb pseudorapidity acceptance. Source [5].	25
Figure 10	– The side view of the LHCb detector (Run 1). The right-handed coordinate system adopted has the z-axis along the beam, and the y-axis along the vertical. Source [6]	26
Figure 11	– The front face of the VELO modules in both the closed and open positions. In blue, the r -sensors and in red, the ϕ – sensors. Source [6].	27
Figure 12	– The LHCb dipole magnet. This is a warm magnet which allows the momenta of charged particles to be determined. Source [7]	28
Figure 13	– The front face of the VELO modules in both the closed and open positions. In blue, the r -sensors and in red, the ϕ – sensors. Source [6].	28
Figure 14	– Layout of the TT, with the LHC beam pipe passing through an opening in the centre of the detection layers. Source [8].	29

Figure 15 – (Left) Front view of a T-station with the modules of the Outer Tracker and the boxes of the Inner Tracker. (Right) Layout of an x-detection layer in the second IT station. Sources [9, 6].	30
Figure 16 – Reconstructed Cherenkov angle for <i>isolated</i> tracks, as a function of track momentum in the C ₄ F ₁₀ radiator. The Cherenkov bands for muons, pions, kaons and protons are visible. Source [10].	32
Figure 17 – Lateral segmentation of the SPD/PS and ECAL (left) and the HCAL (right). One quarter of the detector front face is shown. In the left figure, the cell dimensions are given for the ECAL. Source [6].	33
Figure 18 – Side view of the muon system. Source [6].	34
Figure 19 – Overview of the Level-0 trigger. Source [6].	36
Figure 20 – A schematic illustration of the various track types: long, upstream, downstream, VELO and T tracks. For reference, the main B-field component (B_y) is plotted above as a function of the z coordinate. Source [6].	38
Figure 21 – The LHCb trigger schemes for Run 1 (left) and Run 2 (right)	40
Figure 22 – Layout of the upgraded LHCb detector. Source [11].	42
Figure 23 – Left: relative trigger yields as a function of instantaneous luminosity, normalised to $2 \times 10^{32} \text{cm}^{-2} \text{s}^{-1}$. Right: rate of decays reconstructed in the LHCb acceptance as a function of the cut in p_T of the decaying particle, for decay time $\tau > 0.2 \text{ps}$. Source [11].	42
Figure 24 – Left: schematic top view of the z-x plane at y=0 (left) with an illustration of the z-extent of the luminous region and the nominal LHCb pseudorapidity acceptance, $2 < \eta < 5$. Right: sketch showing the nominal layout of the ASICs around the z-axis in the closed VELO configuration. Half the ASICs are placed on the upstream module face (grey) and half on the downstream face (blue). The modules on Side C are highlighted in purple on both sketches. Source [11].	43
Figure 25 – Drawing of the four UT silicon planes with indicative dimensions. Different colours designate different types of sensors: Type-A (green), Type-B (yellow), Type-C and Type-D (pink), as described in the text. Source [11].	44
Figure 26 – Front and side views of the 3D model of the SciFi Tracker detector. Source [11].	45
Figure 27 – (Left) Side view of the LHCb Muon Detector. (Right) Station layout with the four regions R1-R4 indicated. Source [12].	46
Figure 28 – Dataflow in the upgraded LHCb detector. Source [13].	47
Figure 29 – Invariant mass distribution of selected $D_s^+ \rightarrow \pi^- \pi^+ \pi^+$ candidates after PID.	53

Figure 30 – Kinematics and track multiplicity distributions for $D_s^+ \rightarrow \pi^- \pi^+ \pi^+$ after all corrections	55
Figure 31 – (a) The variation of the purity (blue, dashed curve) and significance ($S/\sqrt{S+B}$) (red, dotted line) according to the cut applied on the <code>valBDTG_mean</code> variable. (b) The Yield MC (red, dotted line) is the number of events that pass the BDTG cut, and will be used to build the efficiency. The dashed blue curve is a copy of (a).	57
Figure 32 – Invariant mass distribution of $D_s^+ \rightarrow \pi^- \pi^+ \pi^+$ candidates before (left) and after (right) the BDTG requirement is applied.	58
Figure 33 – Momentum asymmetry plots for $D_s^+ \rightarrow \pi^- \pi^+ \pi^+$ candidates after the BDTG requirement.	58
Figure 34 – Invariant masses of $\pi^- \pi^+ \pi^+$ candidates computed with different mass hypotheses.	59
Figure 35 – Difference between the slopes in XZ(left) and YZ(right) planes, before(up) and after(down) the BDT requirement, for all combinations of two tracks.	60
Figure 36 – Invariant mass distribution of the $D_s^+ \rightarrow \pi^- \pi^+ \pi^+$ candidates after final selection, with the fit result superimposed.	62
Figure 37 – Symmetrized Dalitz plot of the full sample after all selection criteria, within the $\pi^- \pi^+ \pi^+$ mass interval of [1952.,1988.] MeV.	64
Figure 38 – A zoom of the region where the $f_0(980)$ interferes with one (or two) scalar resonance(s). The mass histogram is the $m^2(\pi^+ \pi^-)$ projection of events for the square in orange. Source: Courtesy of Prof. Alberto Reis.	64
Figure 39 – The $m^2(\pi^- \pi^+)$ projection of candidates from the regions marked by the orange rectangles. Source: Courtesy of Prof. Alberto Reis.	65
Figure 40 – The Dalitz plot in 3D.	66
Figure 41 – The efficiency map before (left) and after (right) the smoothing process	67
Figure 42 – Background for the left (a) and for the right (b) region of the signal	68
Figure 43 – The background map before (left) and after (right) the smoothing process	68
Figure 44 – Fit results from model PWA-1: the projections of the lowest (top-right) and the highest (top-left) of the two $\pi^+ \pi^-$ invariant masses squared. In the bottom the $s_{\pi^+ \pi^+}$ projection.	71
Figure 45 – Fit results from model PWA-1: distribution of the normalised residuals across the Dalitz plot (left) and as 1D projection (right).	71
Figure 46 – (Left) Magnitude and (right) phase of the S-wave amplitude as a function of $m(\pi^+ \pi^-)$. The uncertainties are statistical.	72
Figure 47 – The comparison of $\pi^- \pi^+$ S-wave of the $D_s^+ \rightarrow \pi^- \pi^+ \pi^+$ with previous results from BaBar and BESIII.	73

Figure 48 – (Left) Invariant-mass distribution of $D^+ \rightarrow \pi^- \pi^+ \pi^+$ candidates after final selection, with the fit result superimposed (blue solid line). The dashed red line and the solid gray line correspond to the signal and background components of the fit, respectively. (Right) Dalitz plot distribution of the final $D^+ \rightarrow \pi^- \pi^+ \pi^+$ sample. The lines in the interval $[0.235, 0.250]$ GeV ² correspond to the veto applied to remove $D^+ \rightarrow K_s^0 \pi^+$ decays.	76
Figure 49 – Models for (left) background distribution and (right) signal efficiency across the Dalitz plot, where the z -axis scale is arbitrary.	77
Figure 50 – Fitted (left) magnitude and (right) phase of the $\pi^- \pi^+$ S-wave amplitude with statistical uncertainties as the blue bars and the total uncertainties (combined statistical, experimental and model systematics) as the green bands.	78
Figure 51 – Dalitz plot projections of (top left) $s_{\pi^- \pi^+}$, (top right) s_{23} , (middle left) s_{low} , and (middle right) s_{high} projections, where the (red) points are data and the (blue) line is the fit model result, with the fit normalised residuals displayed in the bottom plot.	79
Figure 52 – (Left) Dalitz plot of the $D_s^+ \rightarrow \pi^- \pi^+ \pi^+$ and (right) $D^+ \rightarrow \pi^- \pi^+ \pi^+$ decays [14]. The colour scale indicates the density of candidates.	81
Figure 53 – (Left) Magnitude and (right) phase of the $\pi^- \pi^+$ S-wave amplitude for the $D^+ \rightarrow \pi^- \pi^+ \pi^+$ (black line) and $D_s^+ \rightarrow \pi^- \pi^+ \pi^+$ decays (blue dot).	82
Figure 54 – The $\pi^+ \pi^-$ spectrum from $\bar{B}_s^0 \rightarrow J/\psi \pi^+ \pi^-$ decay [15], on the left, and from $\bar{B}^0 \rightarrow J/\psi \pi^+ \pi^-$ decay [16], on the right.	82
Figure 55 – The $D_s^+ \rightarrow \pi^- \pi^+ \pi^+$ Argand plot of the $\pi^+ \pi^-$ S-wave amplitude. The values of $m(\pi^+ \pi^-)$ at the edge of each interval are indicated next to the corresponding experimental point. The amplitude starts at the point circled in red and undergoes two counterclockwise circles.	83
Figure 56 – The scalar mesons are formed by rescattering of the pseudo-scalar mesons a' and b' , formed by the $d\bar{d}$ pair from the D^+ decay and a $q\bar{q}$ pair from the vacuum.	84
Figure 57 – Examples of three-body FSI connecting different channels with the vacuum quantum numbers. These amplitudes involve loops and are suppressed w.r.t tree-level diagrams.	85
Figure 58 – (Left) Comparison of the $\pi^+ \pi^-$ S-wave phase from $D_s^+ \rightarrow \pi^- \pi^+ \pi^+$ decays and the phase from $\pi^+ \pi^- \rightarrow \pi^+ \pi^-$ scattering. Data on $\pi^+ \pi^- \rightarrow \pi^+ \pi^-$ scattering above 0.6 GeV are from a re-analysis [17] of original data from [18], and below 0.4 GeV are from K_{e4} decays [19]. (Right) The S-wave phase from the $D_s^+ \rightarrow \pi^- \pi^+ \pi^+$ decay is shifted by 210°.	87

Figure 59 – The $m(\pi^+\pi^-)$ spectrum near the $\rho(770)^0$. The spectrum is divided into two regions, after (left) and before (right) the $f_0(980)$ band in the crossed channel.	87
Figure 60 – The $m(\pi^+\pi^-)$ spectrum near the $\rho(770)^0$	89
Figure 61 – The $m(\pi^+\pi^-)$ spectrum near the $\rho(770)^0$ for background sidebands. The spectrum is divided into two regions, before (left) and after (right) the $f_0(980)$ band in the crossed channel for the left (top) and the right (bottom) sidebands.	89
Figure 62 – The mechanisms for the $\omega(782) \rightarrow \pi^+\pi^-$ decay: the $\omega - \rho$ mixing, on the left, and the “direct” decay.	90
Figure 63 – The annihilation diagram of $D_s^+ \rightarrow \pi^-\pi^+\pi^+$ decay, showing how the $\rho(770)^0$ could be formed.	91
Figure 64 – A mechanism for $\omega(782)$ production in $D_s^+ \rightarrow \pi^-\pi^+\pi^+$ decays, proposed by the Cheng and Chiang [20].	91
Figure 65 – (Left) The invariant mass $B_s^0 \rightarrow \gamma\gamma$ (simulation). (Right) The invariant mass of $\pi^0 \rightarrow \gamma\gamma$ (real data).	97
Figure 66 – The π^0 calibration flow.	99
Figure 67 – Minimum bias π^0 candidates.	100
Figure 68 – The histograms of the fitted mean values of the π^0 mass for each ECAL cell and each ECAL zone, (top) before and (bottom) after the calibration. The ALL histograms are the result of merging the three zones.	101
Figure 69 – Set of input variables used for the MVA training.	104
Figure 70 – The linear correlation matrix for signal and background from fold 1 and fold 2 used to train the classifier.	105
Figure 71 – Overfitting test	106
Figure 72 – Comparison of the BDTG variable for Data sPloted and for MC reweighted. Compatibility shows that MC reweighted models this variable well.	106
Figure 73 – The BDTG variables predicted with the two classifiers trained: (a) the predicted variables for data and their mean; (b) the predicted variables for MC and their mean. The mean variable of these samples is used in the rest of analysis.	107
Figure 74 – Fit results from model PWA-2: the projections of the lowest (top left) and the highest (top right) of the two $\pi^+\pi^-$ invariant masses squared; the $\pi^+\pi^+$ projection (mid left) and the helicity angle (mid right, with two entries per event); distribution of the normalised residuals across the Dalitz plot (bottom left) and as 1D projection (bottom right). The data is represented by the red dots whilst the fit result is the histogram in black.	121
Figure 75 – Fitted S -wave for model PWA-2.	121

Figure 76 – Fit results from model PWA-3: the projections of the lowest (top left) and the highest (top right) of the two $\pi^+\pi^-$ invariant masses squared; the $\pi^+\pi^+$ projection (mid left) and the helicity angle (mid right, with two entries per event); distribution of the normalised residuals across the Dalitz plot (bottom left) and as 1D projection (bottom right). The data is represented by the red dots whilst the fit result is the histogram in black.	123
Figure 77 – Fitted S -wave for model PWA-3.	123
Figure 78 – Fit results from model PWA-4: the projections of the lowest (top left) and the highest (top right) of the two $\pi^+\pi^-$ invariant masses squared; the $\pi^+\pi^+$ projection (mid left) and the helicity angle (mid right, with two entries per event); distribution of the normalised residuals across the Dalitz plot (bottom left) and as 1D projection (bottom right). The data is represented by the red dots whilst the fit result is the histogram in black.	125
Figure 79 – Fitted S -wave for model PWA-4.	125
Figure 80 – Fit results from model PWA-5: the projections of the lowest (top left) and the highest (top right) of the two $\pi^+\pi^-$ invariant masses squared; the $\pi^+\pi^+$ projection (mid left) and the helicity angle (mid right, with two entries per event); distribution of the normalised residuals across the Dalitz plot (bottom left) and as 1D projection (bottom right). The data is represented by the red dots whilst the fit result is the histogram in black.	127
Figure 81 – Fitted S -wave for model PWA-5.	127
Figure 82 – Fit results from model PWA-6: the projections of the lowest (top left) and the highest (top right) of the two $\pi^+\pi^-$ invariant masses squared; the $\pi^+\pi^+$ projection (mid left) and the helicity angle (mid right, with two entries per event); distribution of the normalised residuals across the Dalitz plot (bottom left) and as 1D projection (bottom right). The data is represented by the red dots whilst the fit result is the histogram in black.	130
Figure 83 – Fitted S -wave for model PWA-6.	130
Figure 84 – Fit results from model PWA-7: the projections of the lowest (top left) and the highest (top right) of the two $\pi^+\pi^-$ invariant masses squared; the $\pi^+\pi^+$ projection (mid left) and the helicity angle (mid right, with two entries per event); distribution of the normalised residuals across the Dalitz plot (bottom left) and as 1D projection (bottom right). The data is represented by the red dots whilst the fit result is the histogram in black.	132
Figure 85 – Fitted S -wave for model PWA-7.	132

Figure 86 – Fit results from model PWA-8: the projections of the lowest (top left) and the highest (top right) of the two $\pi^+\pi^-$ invariant masses squared; the $\pi^+\pi^+$ projection (mid left) and the helicity angle (mid right, with two entries per event); distribution of the normalised residuals across the Dalitz plot (bottom left) and as 1D projection (bottom right). The data is represented by the red dots whilst the fit result is the histogram in black.	135
Figure 87 – Fitted S -wave for model PWA-8.	135

List of Tables

Table 1	– Spin-dependent Blatt-Weisskopf barrier factors. The normalization ensures that the barrier factors are equal to one at the resonance mass. . . .	11
Table 2	– List of resonance parameters including their spin, lineshape used and parameters of mass and width, according to PDG [21].	14
Table 3	– Generation criteria for large MC samples.	49
Table 4	– HLT1 trigger line requirements	51
Table 5	– Selection criteria used in the dedicated HLT2 Dhhh trigger line	51
Table 6	– Stripping line for $D_{(s)}^+$ decays to three hadrons.	52
Table 7	– Fiducial requirements on the p and η of the decay products, as defined in the PIDCalib package.	52
Table 8	– TMVA hyperparameters and AUC metric values.	57
Table 9	– Mass fit results for the $D_s^+ \rightarrow \pi^- \pi^+ \pi^+$ sample	63
Table 10	– Final results of the $D_s^+ \rightarrow \pi^- \pi^+ \pi^+$ Dalitz plot fit. The uncertainties are statistical, experimental systematic and associated with the decay amplitude model, respectively.	69
Table 11	– Interference fractions (%) between amplitude components for model PWA-1.	70
Table 12	– Magnitude and phase of the S-wave amplitude as a function of $\pi^- \pi^+$ invariant mass. The uncertainties are statistical, experimental and model, respectively. The $\pi^+ \pi^-$ invariant mass is expressed in GeV.	74
Table 13	– Dalitz fit results for magnitudes, phases and fit fractions (%) of the spin-1 and spin-2 components, and the S-wave fit fraction. The uncertainties quoted are, in order, statistical, experimental systematics, and model systematics.	78
Table 14	– Dalitz fit results for the interference fit fractions (%) (statistical uncertainties only).	78
Table 15	– Fit fractions (%) from the $D_s^+ \rightarrow \pi^- \pi^+ \pi^+$ and $D^+ \rightarrow \pi^- \pi^+ \pi^+$ decays. Uncertainties are statistical.	81
Table 16	– The resonant structure of the $D_s^+ \rightarrow \pi^- \pi^+ \pi^+$ decay. The fit fractions are in %. The first uncertainty is statistical, the second experimental, and the third is the uncertainty due to the fit model.	93
Table 17	– The resonant structure of the $D_s^+ \rightarrow \pi^- \pi^+ \pi^+$ decay from this analysis compared to previous determinations from BaBar [22] and BESIII [23]. The fit fractions are given in %. The statistical and systematic uncertainties are added in quadrature.	93
Table 18	– The trigger requirements of $B_{(s)}^0 \rightarrow \gamma\gamma$ and $\pi^0 \rightarrow \gamma\gamma$ respectively.	97

Table 19 – Summary of the sanity check for the uncertainties on the fit parameters. The column “stat“ has the statistical errors from MINUIT. The column “ σ “ has the standard deviation for the parameter distribution.	111
Table 20 – Systematic uncertainties related to the background parameterisation. The column “total“ contains the sum in quadrature of the values in the previous columns. Phases are in degrees.	112
Table 21 – Systematic uncertainties related to the efficiency correction. The column “total“ contains the sum in quadrature of the values in the previous columns. Phases are in degree	112
Table 22 – Systematic uncertainties related to the model parameters. The column “model“ has the sum in quadrature of the individual items.	113
Table 23 – Systematic uncertainties related to the fit bias.	113
Table 24 – Systematic uncertainties related to the mass resolution.	113
Table 25 – Summary of the systematic uncertainties. The column “total exp.“ has the sum in quadrature of the first four columns.	114
Table 26 – Systematic uncertainties on the fit fractions, in %	114
Table 27 – Systematic uncertainty on the S -wave due the background parameterization. Phases are in degrees.	115
Table 28 – Systematic uncertainty on the S -wave due the efficiency correction. Phases are in degrees.	116
Table 29 – Systematic uncertainty on the S -wave due the fit model. Phases are in degrees.	117
Table 30 – Systematic uncertainty on the S -wave due the fit bias. Phases are in degrees.	118
Table 31 – Systematic uncertainty on the S -wave due the mass resolution. Phases are in degrees.	119
Table 32 – Fit results for model PWA-2. Phases in degrees and fit fractions (FF) in %	120
Table 33 – Interference fractions (%) between amplitude components for model PWA-2.	120
Table 34 – Results from the Dalitz plot fit with model PWA-3.	122
Table 35 – Interference fractions between amplitude components for model PWA-3.	122
Table 36 – Results from the Dalitz plot fit with model PWA-4.	124
Table 37 – Interference fractions between amplitude components for model PWA-4.	124
Table 38 – Results from the Dalitz plot fit with model PWA-5.	126
Table 39 – Interference fit fractions between components of model PWA-5.	126
Table 40 – Fit results for model PWA-6. Phases in degrees and fit fractions (FF) in %	129
Table 41 – Interference fractions (%) between amplitude components for model PWA-6.	129

Table 42 – Fitted parameters of the $\rho - \omega$ mixing amplitude.	129
Table 43 – Fit results for model PWA-7. Phases in degrees and fit fractions (FF) in %.	131
Table 44 – Interference fractions (%) between amplitude components for model PWA-7.	131
Table 45 – Fit results for model PWA-8. Phases in degrees and fit fractions (FF) in %.	134
Table 46 – Interference fractions (%) between amplitude components for model PWA-8.	134

1 Introduction

Multi-body non-leptonic decays of D mesons have been used for light-meson spectroscopy for more than 20 years. These decays have unique features that make them suitable for studies of hadron-hadron interactions. The most important one is that in a single reaction, the $\pi\pi$, $K\pi$ or $K\bar{K}$ scattering amplitudes can be accessed continuously from threshold up to ~ 1.5 - 1.8 GeV.

Non-leptonic D-meson decays proceed in two stages that cannot be easily factorized: the weak decay of the charm quark and the formation of the hadrons, governed by QCD in the non-perturbative regime. One has to deal with the fundamental problem of matching quark and hadron degrees of freedom, which makes the theoretical description of non-leptonic decays of D mesons very challenging. At present, there are no tools for describing decay amplitudes that cover first principles.

Once formed, the hadrons rescatter through strong interaction in all possible ways before reaching the detector. The final state interactions (FSI) could be seen as a further complication, but these processes grant access to the meson-meson scattering amplitudes. The dynamics of the final state are often assumed to be mainly driven by two-body interactions, but even under this assumption, the scattering amplitudes cannot be directly accessed. The overall decay amplitude, in which the scattering amplitudes are embedded, includes other effects, such as those of coupled channels and different two-body isospin, as well as the effect of three-body interactions. Phenomenological analyses are necessary to obtain the scattering amplitudes from the measured two-body amplitudes.

The $D_s^+ \rightarrow \pi^- \pi^+ \pi^+$ decay provides the appropriate environment for the measurement of the $\pi^+ \pi^-$ amplitude in S-wave for two reasons. According to previous analyses of this decay, [24, 25, 22, 23], the S-wave accounts for approximately 80% of the decay rate. The $D_s^+ \rightarrow \pi^- \pi^+ \pi^+$ decay is Cabibbo allowed ($c \rightarrow s\bar{d}$) (transition between quarks of the same generation is more likely). The final state, however, has no strangeness, despite the $s\bar{s}$ pair available after the c-quark decay. The $D_s^+ \rightarrow \pi^- \pi^+ \pi^+$ decay is, therefore, an interesting process for studies of resonances that couple both to $\pi\pi$ and $K\bar{K}$ such as the controversial $f_0(980)$ meson, often interpreted as a non- $q\bar{q}$ state.

Determining the scattering amplitudes also requires accounting for phases arising at the hadron formation stage, which is directly related to the quark content of the initial state. In the $D_s^+ \rightarrow \pi^- \pi^+ \pi^+$ decay, the external W-emission amplitude, illustrated in Fig. 1, is expected to be the dominant mechanism. The resonances would emerge mainly from an $s\bar{s}$ source. The companion $D^+ \rightarrow \pi^- \pi^+ \pi^+$ decay is Cabibbo suppressed ($c \rightarrow d\bar{u}$) (transition between quarks of the different generation is less likely) and expected to proceed

via a similar diagram, but the resonant structure is instead generated by a $d\bar{d}$ source. In this respect, a detailed comparison between the resonant structures of $D_s^+ \rightarrow \pi^- \pi^+ \pi^+$ and $D^+ \rightarrow \pi^- \pi^+ \pi^+$ decays (or, for instance, $D^+ \rightarrow K^- K^+ K^+$ and $D_s^+ \rightarrow K^- K^+ K^+$) would help to understand the mechanisms of hadron formation. In particular, the measurement of the S-waves using different decay modes is of crucial importance for the development of phenomenological models.

In this thesis, the amplitude analysis of the $D_s^+ \rightarrow \pi^- \pi^+ \pi^+$ [26] was performed to determine the $\pi^- \pi^+$ S-wave amplitude and the resonant structure of the P- and D-waves. The analysis is based on 2012 LHCb collected data, corresponding to an integrated luminosity of 1.5 fb^{-1} . A quasi-model-independent approach (QMPI) is used to describe the S-wave. In this approach, S-wave is described by a generic complex function by splitting the invariant mass spectrum $s(\pi^- \pi^+)$ into equally populated intervals. At each interval edge, it is assigned a complex amplitude that depends on two real parameters: $a_i(s)$ and $\delta_i(s)$. To evaluate S-wave amplitude at any point in the spectrum, a linear interpolation is performed. This S-wave description follows the previous analysis from BESIII [23]. On the other hand, P- and D-waves are described using the Isobar model, which is why this approach is quasi-model-independent. The goal of this analysis is to provide a precise description of the resonant structure of the $D_s^+ \rightarrow \pi^- \pi^+ \pi^+$ decay channel. The resonant structures of the $D_s^+ \rightarrow \pi^- \pi^+ \pi^+$ and $D^+ \rightarrow \pi^- \pi^+ \pi^+$ decays are compared, providing information about the mechanism for the hadron production in each decay channel. Finally, the $D_s^+ \rightarrow \pi^- \pi^+ \pi^+$ is also an important control channel for searching CP-violation in the $D^+ \rightarrow \pi^- \pi^+ \pi^+$ channel [27].

The thesis is structured as follows: In Chapter 2, an overview of the related theoretical aspects is introduced. Chapter 3 introduces the LHCb experiment - the LHCb detector design and the trigger system of Run 1. Chapter 4 introduces the main changes in the LHCb detector after the Upgrade I. Chapter 5 introduces the $D_s^+ \rightarrow \pi^- \pi^+ \pi^+$ analysis. Chapter 6 introduces the results of $D^+ \rightarrow \pi^- \pi^+ \pi^+$ analysis. Chapter 7 provides the interpretation of the results of Chapter 6 and 7. Chapter 8 details the contributions to the LHCb Upgrade. And Chapter 9 has the conclusions.

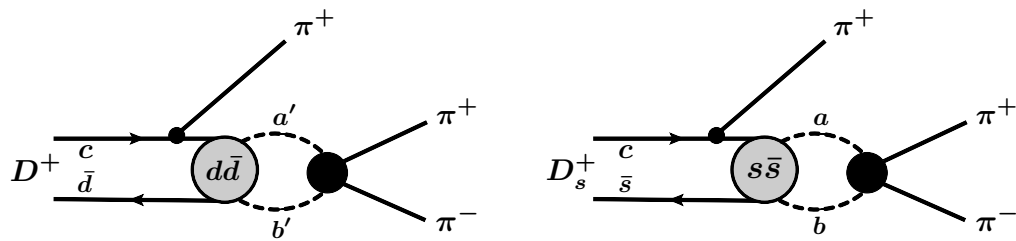


Figure 1 – Tree diagrams leading to of the $D^+ \rightarrow \pi^- \pi^+ \pi^+$ and $D_s^+ \rightarrow \pi^- \pi^+ \pi^+$ decays. The scalar mesons are formed by rescattering of the pseudo-scalar mesons a' and b' .

2 Theoretical background and analysis tools

An overview of the theoretical background and analysis tools analysis is provided in this chapter. The theoretical section has an introduction to the Standard Model, Flavour Physics, Dalitz plot and Dalitz plot formalism. The analysis tools section introduces the various techniques such as SPlot, MVA, Reweighting, and GooFit that are employed during the $D_s^+ \rightarrow \pi^- \pi^+ \pi^+$ analysis. An additional section with some important variable definitions is also included.

2.1 The theoretical background

2.1.1 The Standard Model

The Standard Model (SM) of particle physics is the quantum field theory (QFT) which describes three of the four fundamental forces of nature: weak, electromagnetic, and strong. The SM has been successful in describing many aspects of the quantum world and has been considered one of the most successful theories ever built. However, it has some limitations. The gravitational force is not included in the SM, as fitting gravity into this framework has proved to be challenging. It also does not explain the matter-antimatter asymmetry at the level observed in the universe, the hierarchy of mass of the leptons, and the universe's evolution, possibly due to Dark Matter and Energy. Due to these known limitations, physics searches for New Physics mechanisms as an extension of the theory.

The SM is based on the gauge group $SU(3)_C \times SU(2)_L \times U(1)_Y$. The gauge symmetry $SU(3)_C$ is the symmetry of the Quantum Chromo Dynamics (QCD), the theory of strong interactions that hold quarks together, and has a quantum number called color, which can assume three values: red, green and blue. The $SU(2)_L$ is the gauge group of the weak interactions that play a greater role in particle decays. The weak force has a quantum number called weak isospin, which can assume the two values $\pm \frac{1}{2}$. The $U(1)_Y$ force is felt by all particles with nonzero hypercharge (Y) quantum numbers, which can assume any real number. Whereas the $SU(3)_C$ has an exact symmetry under local gauge transformations, the $SU(2)_L \times U(1)_Y$ is spontaneously broken down to $U(1)_{em}$, the symmetry group of Quantum Electrodynamics (QED). The requirement of the local gauge invariance for each adjoint representation of these groups predicts the existence of massless gauge bosons. Eight gluons (g) for $SU(3)_C$, three W_μ^a for $SU(2)_L$ and one B_μ for $U(1)_Y$. The W_μ^a and B_μ bosons mix into W^\pm , Z^0 and the massless gauge boson γ when the $SU(2)_L \times U(1)_Y$ symmetry is spontaneously broken into $U(1)_{em}$ by the Higgs mechanism, with γ belonging to the unbroken $U(1)_{em}$. In addition to the vector bosons, there is the scalar Higgs boson. This boson is produced by an excitation of the Higgs field, which is

responsible for giving mass to the massive particles. Refer to [28] for more details.

The standard model consists of fermions and bosons. Fermions are grouped according to their quantum numbers and exist in three copies (generations). Fermions are spin-1/2 particles and are distinguished between quarks and leptons. There are five fermionic representations in the SM. The left-handed quarks (Q_L) are $SU(2)_L$ doublets and $SU(3)_c$ triples. The three quark doubles consist of the flavours $(u, d), (c, s), (t, b)$. The left-handed leptons (L_L) are also $SU(2)_L$ but singlets of $SU(3)_c$, and thus colour neutral. The lepton doublets consists of $(\nu_e, e^-), (\nu_\mu, \mu^-)$ and (ν_τ, τ^-) . There are also the $SU(2)_R$ quark right-handed singlets ($U_R = (u_R, c_R, t_R), D_R = (d_R, s_R, b_R)$) and lepton right-handed singlets ($E_R = (e_R, \mu_R, \tau_R)$). The right-handed particles are essential to the mechanism that gives fermions their mass, but they cannot *feel* the weak force [28]. The left-handed quarks are the only particles to interact through all known forces of nature. Figure 2 illustrates the periodic table of elementary particles. The first-generation particles are the building blocks of all observed matter.

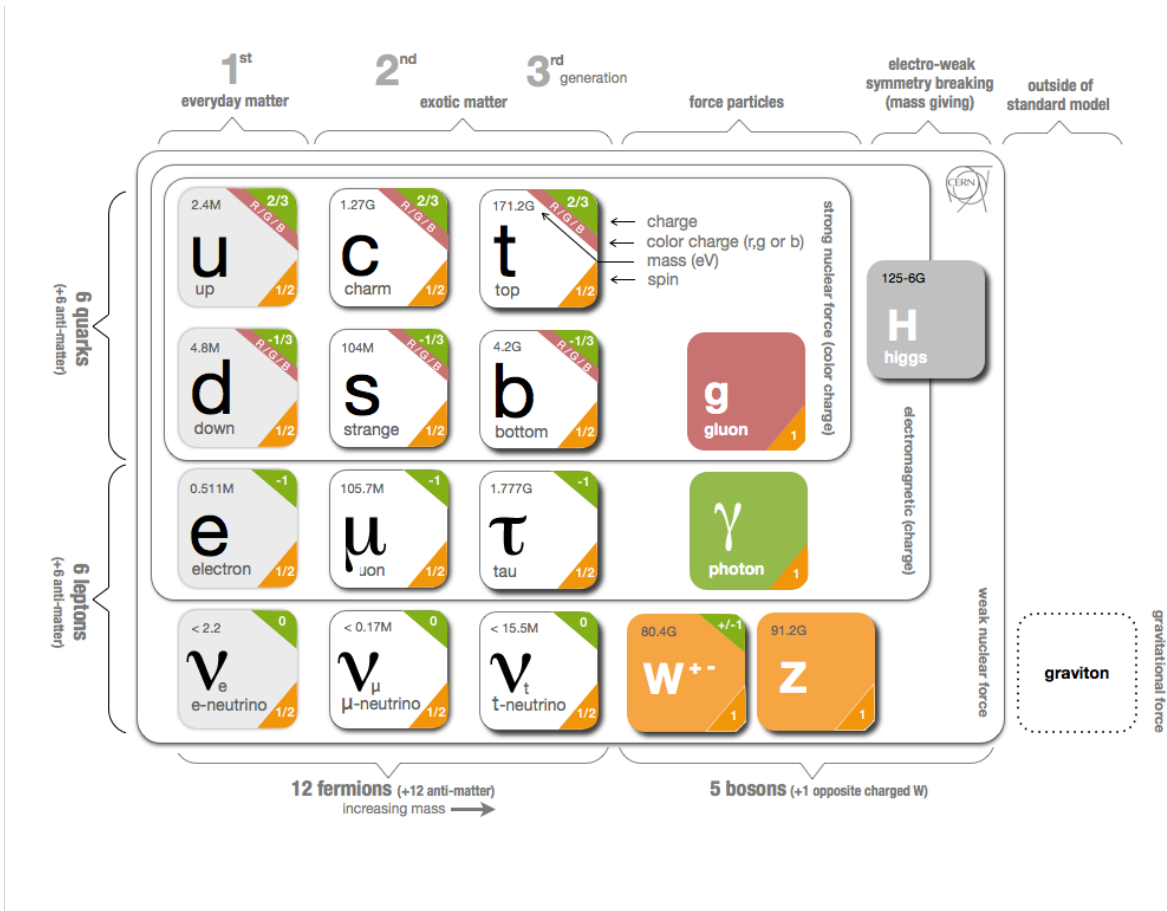


Figure 2 – The periodic table of elementary particles.

2.1.2 Flavour Physics

Flavour physics relates to the existence of different families of quarks and how they couple to each other. The Yukawa sector of the SM Lagrangian contains the couplings of the Higgs to the fermions and is crucial for the flavour structure of quarks. Equation 2.1 introduces the Yukawa Lagrangian. The fermion fields are three-component vectors that include all three generations (represented by the index $i = 1, 2, 3$). The 3×3 Yukawa matrices are given by $Y^{d,u,e}$. ϕ and $\bar{\phi}$ are the Higgs field and its charge conjugate, respectively.

$$\mathcal{L}_Y^{SM} = Y_{ij}^d \bar{Q}_{Li} \phi D_{Rj} + Y_{ij}^u \bar{Q}_{Li} \bar{\phi} U_{Rj} + Y_{ij}^e \bar{L}_{Li} \phi E_{Rj} + h.c. \quad (2.1)$$

The Yukawa matrices can be separately diagonalized by making the appropriate bi-unitary field redefinitions

$$(V_L^d)^\dagger Y^D V_R^d = \hat{Y}^D, \quad (V_L^u)^\dagger Y^U V_R^u = \hat{Y}^U \quad \text{and} \quad (V_L^e)^\dagger Y^E V_R^e = \hat{Y}^E, \quad (2.2)$$

where V_L^u, V_R^u, V_R^d and V_L^d , are 3x3 unitary matrix with the superscripts denoting quarks in their mass eigenstate basis. If one wants to diagonalize both simultaneously, it is necessary these four matrices. However, we have only the first three matrices. The matrices V_L^u, V_R^u and V_R^d are given by the fields' transformations that make the interaction Lagrangian invariant under U(3) below.

$$Q_L \rightarrow V_L^u Q_L, \quad U_R \rightarrow V_R^u U_R \quad \text{and} \quad D_R \rightarrow V_R^d D_R \quad (2.3)$$

The matrix V_L^d is missing, thus it's not possible to perform the simultaneous diagonalization. Applying these rotations we get

$$\mathcal{L}_Y^{SM} = -\phi \bar{Q}_L (V_L^u)^\dagger V_L^d \hat{Y}^D D_R - \phi \bar{Q}_L \hat{Y}^u U_R - \phi \bar{L}_L \hat{Y}^E E_R + h.c. \quad (2.4)$$

with the first term being nondiagonal. An additional rotation of the down quarks is required to get the mass eigenstate basis¹.

$$D_L \rightarrow D'_L = (V_L^u)^\dagger V_L^d D_L \quad (2.5)$$

This rotation modifies the interaction Lagrangian, which written in terms of D_L involves the matrix $(V_L^u)^\dagger V_L^d$, that is the CKM matrix, and gives rise to the interaction term

$$\frac{g}{\sqrt{2}} \bar{U}_{Li} \gamma_\mu W^{\mu+} D_{Li} \quad (2.6)$$

¹ U_L and D_L form the $SU(2)_L$ doublets Q_i (with $i = 1, 2, 3$)

It describes that the flavour-changing of quarks occurs due to a misalignment of the flavour and mass eigenstates and that the process occurs via a charged current (CC) weak processes mediated by the W^\pm boson. On the other hand, in the leptonic sector, this misalignment doesn't appear. The CC couples the charged leptons and their respective neutrinos, so no generation-changing occurs. For both leptons and quarks, there are no flavour-changing neutral currents (NC) at the tree level in the SM as a consequence of the unitarity of the CKM matrix. The NC is mediated by the Z^0 boson.

The V_{CKM} is the Cabibbo-Kobayashi-Maskara matrix [29]. It describes the mixing between the three different families of quarks. The elements of CKM describe the strength of flavour transitions and are written in terms of the quark flavour for convenience. It depends on three mixing angles and one irreducible phase. There are different parametrizations of the CKM matrix. The Particle Data Group [21] choice is

$$V_{CKM} = \begin{pmatrix} c_{12}c_{13} & s_{12}c_{13} & s_{13}e^{-i\delta_{13}} \\ -s_{12}c_{23} - c_{12}s_{23}s_{13}e^{i\delta_{13}} & c_{12}c_{23} - s_{12}s_{23}s_{13}e^{i\delta_{13}} & s_{23}c_{13} \\ s_{12}s_{23} - c_{12}c_{23}s_{13}e^{i\delta_{13}} & -c_{12}s_{23} - s_{12}c_{23}s_{13}e^{i\delta_{13}} & c_{23}c_{13} \end{pmatrix}$$

where $c_{ij} = \cos \theta_{ij}$ and $s_{ij} = \sin \theta_{ij}$. $\theta_{12} = 13.04^\circ$ is the Cabibbo angle, and δ_{13} is the CP-violating phase. Processes can be classified by the power of $\lambda = \sin \theta_{12}$. Transitions for which the amplitude depends linearly on $\sin \theta_{12}$ are called Cabibbo-suppressed. When the amplitude depends on $\sin^2 \theta_{12}$, the transitions are called doubly Cabibbo-suppressed. If that depends only on $\sin \theta_{13}$, then the process is Cabibbo-favored.

2.1.3 Dalitz plot

A common approach to studying processes in particle physics is to prepare the initial state in an asymptotic time $t \rightarrow -\infty$ and measure the final state in the limit $t \rightarrow +\infty$. The initial and final physical states are so far apart that they can be considered free particle states, as described by the free particle theory. The interaction occurs between these limits and is described using perturbative approaches.

The transition between the initial state $|i\rangle$ and the final state $|f\rangle$ is given by the unitary transition matrix S . The elements of the S -matrix are given by

$$S_{fi} = \langle i|S|f\rangle = \langle i|f\rangle - 2\pi i \langle i|\mathcal{M}|f\rangle$$

The first term describes the scenario when nothing happens, with no interaction. The second term represents when interaction happens, being the \mathcal{M} matrix that rules the dynamics of such interaction. Although the S -matrix provides the amplitude for a given process, it is not a measured quantity in Particle Physics experiments. However, it is used to compute the probabilities of outgoing states and is closely related to cross-sections and decay rates [30]. The S -matrix also can be used to identify bound states, resonances or virtual states, which appear as poles in the S -matrix in the complex-energy plane.

The decay rate (Γ) is given by the number of decays per unit of time divided by the number of initial state particles present [31]. For the particular case of the three-body decays, the differential decay rate is given by the expression

$$d\Gamma = \frac{2\pi}{2M} |\mathcal{M}|^2 \delta^4(P - \sum_{i=1}^3 p_i) \prod_{i=1}^3 \frac{d^4 p_i}{2\pi^3} \delta(p_i^2 - m_i^2). \quad (2.7)$$

The delta function ensures momentum and energy conservation.

The constraints imposed for N=3 final state of spin-0 particles reveal that only 2 of the 12 variables (3 four-momenta vectors) are independent variables². A particular choice inspired in the work of Richard Dalitz on the $\theta \rightarrow \tau$ puzzle [32], are the Lorentz invariant masses $m_{ij}^2 = (p_i^\mu + p_j^\mu)^2$, where the index ij can assume the values 12, 13, 23. These masses are related by the equation

$$m_{12}^2 + m_{13}^2 + m_{23}^2 = M^2 + m_1^2 + m_2^2 + m_3^2 \quad (2.8)$$

which constrains the system to two independent values of m_{ij}^2 . The phase space generated by plotting two of these invariant masses is called the Dalitz plot (DP); see figure 3. The momentum and energy conservation in eq. 2.7 restricts the points into a closed region of the phase space. The kinematic boundaries of the Dalitz plot are constrained by the points where $\cos^2 \theta_{ij} = 1$, with θ_{ij} being the angle between \vec{p}_i and \vec{p}_k in the rest frame ij . The invariant mass kinematical limits are

$$m_{12}^2 \in [(m_1 + m_2)^2, (M - m_3)^2], \quad (2.9)$$

$$m_{13}^2 \in [(m_1 + m_3)^2, (M - m_2)^2], \quad (2.10)$$

$$m_{23}^2 \in [(m_2 + m_3)^2, (M - m_1)^2] \quad (2.11)$$

where M is the mass of the decay particle.

The eq. 2.7 can be written in terms of two invariant masses above. The differential decay rate becomes proportional to the square of the matrix element. If the matrix element is constant, the Dalitz plot will be uniformly populated by the events. However, if any structure is observed, it reflects the decay dynamics. The latter is always the case for three-body decays of charm mesons, in which the Dalitz plot is typically nonuniform, dominated by resonances. Therefore, the Dalitz plot analysis permits us to observe the dynamics of particle decay.

$$\frac{d\Gamma}{ds_{ij} ds_{ik}} = \frac{1}{32(2\pi M)^3} |\mathcal{M}|^2. \quad (2.12)$$

² It starts with 12 Lorentz four-vector d.o.f. Energy and momentum conservation reduce to 5. The spin-0 particles are restricted to the same plane where orientation is arbitrary, thus reducing to 2 d.o.f.

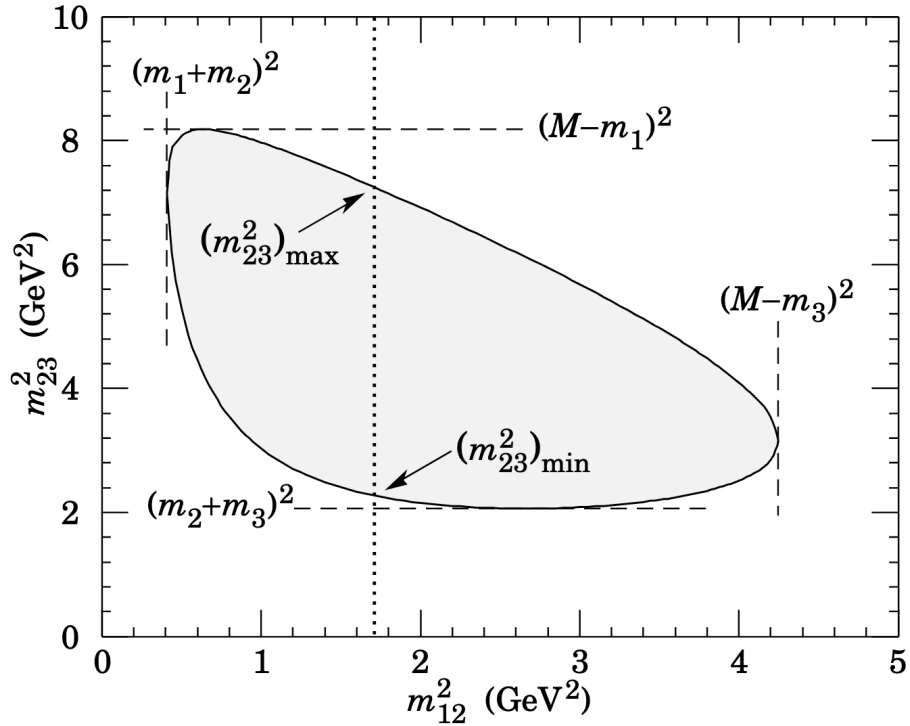


Figure 3 – Dalitz plot for a three-body final state. In this example, the state is $\pi^+ \bar{K}^0 p$ at 3 GeV. Four-momentum conservation restricts events to the shaded region. Source [1]

2.1.4 Dalitz plot formalism

This section describes the formalism for modeling the distribution of events across the $D_s^+ \rightarrow \pi^- \pi^+ \pi^+$ Dalitz plot and its implementation. The modeling of the P - and D -waves is performed using the Isobar Model approach. The S -wave component is parametrized with the QMIPWA method.

The decay amplitude

The decay amplitude is described as a coherent sum of individual resonant amplitudes, labeled according to the spin of the resonance.

$$\mathcal{A}(s_{12}) = (\mathcal{A}_S(s_{12}, s_{13}) + \sum_i a_i e^{i\delta_i} \mathcal{A}_i(s_{12}, s_{13})) + (s_{12} \leftrightarrow s_{13}), \quad (2.13)$$

where the sum runs over resonances of the P - and D -waves.

The magnitudes a_i and the relative phases δ_i of the individual spin-1 and -2 resonances are free parameters. The reference channel is the $f_2(1270)\pi^+$ mode, for which the magnitude and phase are set to 1.0 and 0.0, respectively. This choice was motivated by the fact that the $f_2(1270)$ has a large contribution in the $D_s^+ \rightarrow \pi^- \pi^+ \pi^+$ decay channel according to the previous determinations and because it populates different regions of the Dalitz plot interfering with all resonances. The magnitude and phases are therefore

relative to this state. Since the two indistinguishable bosons are in the final state, the same resonance can be formed either in the $\pi_1^- \pi_3^+$ or in the $\pi_1^- \pi_2^+$ system. Thus, the total amplitude needs to be symmetrised.

An unbinned maximum-likelihood fit to the Dalitz plot obtains the optimum values of the parameters. The likelihood function is written as a combination of the signal and background PDFs given by

$$\mathcal{L} = \prod_j f_S \times \mathcal{P}_{\text{sig}}(s_{12}^j, s_{13}^j) + (1 - f_S) \times \mathcal{P}_{\text{bkg}}(s_{12}^j, s_{13}^j), \quad (2.14)$$

where f_S is the signal fraction (purity of our final data sample) and j runs over the candidates in the sample. The background PDF, $\mathcal{P}_{\text{bkg}}(s_{12}, s_{13})$ is the normalised and smoothed background histogram. The set of optimum parameters is determined by minimizing the quantity $FCN = -2 \log \mathcal{L}$.

The normalised signal PDF, $\mathcal{P}_{\text{sig}}(s_{12}, s_{13})$, is given by

$$\mathcal{P}_{\text{sig}}(s_{12}, s_{13}) = \frac{|\mathcal{A}(s_{12}, s_{13})|^2 \epsilon(s_{12}, s_{13})}{\iint_{\text{DP}} |\mathcal{A}(s_{12}, s_{13})|^2 \epsilon(s_{12}, s_{13}) ds_{12} ds_{13}}, \quad (2.15)$$

where $\epsilon(s_{12}, s_{13})$ is the efficiency map included as a smoothed histogram, and the denominator corresponds to the normalisation factor.

The results are expressed in terms of the complex coefficient $a_j e^{i\delta_j}$ multiplying each resonant amplitude and the corresponding fit fractions. The fit fraction is a convention-independent measure (unlike the complex coefficients, which depend on the choice of phase convention and normalisation). Therefore, they can be used to calculate branching fractions³ and compare between fit models using different conventions.

The fit fractions are computed for each channel by integrating the squared modulus of the corresponding amplitude over the phase space and dividing by the integral of the total amplitude squared:

$$FF_i = \frac{\iint_{\text{DP}} |a_i e^{i\delta_i} \mathcal{A}_i(s_{12}, s_{13})|^2 ds_{12} ds_{13}}{\iint_{\text{DP}} |\sum_j a_j e^{i\delta_j} \mathcal{A}_j(s_{12}, s_{13})|^2 ds_{12} ds_{13}}. \quad (2.16)$$

The sum of these fit fractions often differs from unity due to interference between the individual amplitudes. One can also define interference fit fractions that quantify the degree of interference between two particular components in the amplitude,

$$FF_{ij} = \frac{\iint_{\text{DP}} 2 \operatorname{Re} [a_i e^{i\delta_i} (a_j e^{i\delta_j})^* \mathcal{A}_i(s_{12}, s_{13}) \mathcal{A}_j^*(s_{12}, s_{13})] ds_{12} ds_{13}}{\iint_{\text{DP}} |\sum_i a_i e^{i\delta_i} \mathcal{A}_i(s_{12}, s_{13})|^2 ds_{12} ds_{13}}. \quad (2.17)$$

By construction, the sum of (diagonal) fit fractions and interference fit fractions is 100%.

³ A branching fraction is not well defined for intermediate states due to the interference between the various resonant amplitudes.

Parameterisation of P- and D-wave resonances

The amplitude for a process of the type $D \rightarrow RP_3$; $R \rightarrow P_1P_2$, where R is an intermediate resonant state and P_i are pseudo-scalar mesons, is usually written as a product of form factors, a function accounting for the angular distribution of the decay products, and a dynamical function describing the resonance lineshape,

$$\mathcal{A}_i(s_{12}, s_{13}) = F_D^L F_R^L \mathcal{M}(\theta_{13}) T_R(s_{12}). \quad (2.18)$$

In the above equation, F_D^L and F_R^L are the barrier factors for the production of RP_3 and P_1P_2 , respectively. The form factors are parameterized by the Blatt-Weisskopf [33] penetration factors. Since the D_s^+ is a spin-0 particle, the spin of the resonance, J , is equal to the orbital angular momentum L in the decay $D_s^+ \rightarrow R\pi^+$, and also to the orbital angular momentum l in the subsequent decay $R \rightarrow \pi^-\pi^+$. The term $\mathcal{M}(\theta_{13})$ accounts for the conservation of angular momentum, where θ_{13} is the helicity angle, defined as the angle between particles 1 and 3 measured in the rest frame of $\pi_1^-\pi_2^+$. If the resonance is in the $\pi_1^-\pi_3^+$ system, the angular part of the decay amplitude is a function of θ_{12} , defined in a similar way as θ_{13} . The dynamical function $T_R(s_{12})$ is usually parameterised either by a relativistic Breit-Wigner or a Gounaris-Sakurai (GS) function, the latter being used to model $\rho(770)^0$ [34].

Blatt-Weisskopf barrier factor

The factors F_D^L and F_R^L are parameterised by Blatt-Weisskopf functions and account for the finite extension of the particles involved in the reaction. They ensure the correct behavior of the amplitude both at the threshold and the high end of the phase space. They depend on the orbital angular momentum L and on the module of the decay momentum.

These factors are defined in terms of $z = |\vec{p}|r$. The momentum $|\vec{p}|$ is calculated in the rest frame of the decaying particle, and the parameter r is often interpreted as its effective radius. The value of the parameter r is fixed at $r = r_D = 5.0 \text{ GeV}^{-1}$ for the transition $D_s \rightarrow RP_3$, and $r = r_R = 1.5 \text{ GeV}^{-1}$ for the transition $R \rightarrow P_1P_2$. Table 1 summarises the formulae for the form factors.

Table 1 – Spin-dependent Blatt-Weisskopf barrier factors. The normalization ensures that the barrier factors are equal to one at the resonance mass.

Resonance spin	Form factor
1	$(1 + z_0^2)^{1/2} \times (1 + z^2)^{-1/2}$
2	$(z_0^4 + 3z_0^2 + 9)^{1/2} \times (z^4 + 3z^2 + 9)^{-1/2}$

Angular distribution

The Lorentz-invariant functions \mathcal{M}_J describe the angular distribution of the decay particles, accounting for the conservation of the angular momentum. They are obtained using the covariant tensor formalism. In the decay $D \rightarrow Rc$, $R \rightarrow ab$, the explicit form are

$$\mathcal{M}_1 = s_{bc} - s_{ab} + \left(\frac{1}{s_{ab}} (m_D^2 - m_c^2)(m_a^2 - m_b^2) \right), \quad (2.19)$$

for spin-1 resonances, and

$$\mathcal{M}_2 = \mathcal{M}_1^2 - \frac{1}{3} \left(s_{ab} - 2m_D^2 - m_c^2 + \frac{1}{s_{ab}} (m_D^2 - m_b^2)^2 \right) \times \left(s_{ab} - 2m_a^2 - 2m_c^2 + \frac{1}{s_{ab}} (m_a^2 - m_b^2)^2 \right), \quad (2.20)$$

for spin-2 resonances.

Dynamical functions

In the isobar model, the lineshape that describes the resonances is usually the relativistic Breit-Wigner (RBW) or its extensions. One of these extensions is the Gounaris-Sakurai (GS), which is used to describe $\rho(770)^0$ from data at the elastic region up to 1 GeV². This state is broad and requires the addition of a dispersive term to the usual RBW so that the amplitude remains unitary far from the pole. Gounaris and Sakurai first noticed this in 1968 [34], while they were studying the cross-section for $e^+e^- \rightarrow \pi^+\pi^-$, in the framework of the vector dominance model ($e^+e^- \rightarrow \rho(770)^0 \rightarrow \pi^+\pi^-$). Therefore, for the $\rho(770)^0$ state, the GS lineshape is used. The GS was also tested as a description for $\rho(1450)^0$ and $\rho(1700)^0$ but no improvement was observed when compared to the usual RBW parameterization. Additionally, ref. [35] shows that this parameterization is limited to the $\rho(770)^0$ state, that's why it was not used for describing the $\rho(1450)^0$ and $\rho(1700)^0$.

Relativistic Breit-Wigner

The resonances $\omega(782)^0$, $f_2(1270)$, $\rho(1450)^0$, $f'_2(1525)$ and $\rho(1700)^0$ are described by the relativistic Breit-Wigner

$$T_R(m) = \frac{1}{m_0^2 - m^2 - im_0\Gamma(m)}, \quad (2.21)$$

where m is the $\pi^-\pi^+$ invariant mass, m_0 and $\Gamma(m)$ are the nominal resonance mass and mass-dependent width, respectively. In the general case of the decay of a spin- j resonance, $j \rightarrow 0+0$, the orbital angular momentum L of the decay products equals the resonance spin. The mass-dependent width is expressed as

$$\Gamma(m) = \Gamma_0 \left(\frac{p}{p_0} \right)^{2L+1} \frac{m_0}{m} \frac{F_R^2(z)}{F_R^2(z_0)}. \quad (2.22)$$

The symbol Γ_0 denotes the width at the nominal mass of the resonance, p is the decay momentum, p_0 is the decay momentum at $m = m_0$, and z_0 in the resonance form factor $F_R(z_0)$ listed in table 1 is calculated when $p = p_0$. The values m_0 and Γ_0 for all resonances are fixed in the fit.

Gounaris-Sakurai (GS)

This parameterisation is commonly used to describe the pion electromagnetic form factor. It is the most used parameterisation of the $\rho(770)^0$ lineshape. The Gounaris-Sakurai function is a modification of the RBW lineshape,

$$T_{GS}(m) = \frac{1 + \Gamma_0 d / m_0}{(m_0^2 - m^2) + f(m) - i m_0 \Gamma(m)}, \quad (2.23)$$

where

$$f(m) = \Gamma_0 \frac{m_0^2}{p_0^3} \left[p^2 (h(m) - h(m_0)) + (m_0^2 - m^2) p_0^2 \frac{dh}{dm} \Big|_{m_0} \right]. \quad (2.24)$$

The function $h(m)$ is given by

$$h(m) = \frac{2}{\pi} \frac{p}{m} \ln \left(\frac{m + 2p}{2m_\pi} \right), \quad (2.25)$$

with

$$\frac{dh}{dm} \Big|_{m_0} = h(m_0) \left[(8p_0^2)^{-1} - (2m_0^2)^{-1} \right] + (2\pi m_0^2)^{-1}. \quad (2.26)$$

The parameter $d = f(0)/(\Gamma_0 m_0)$ is given by

$$d = \frac{3}{\pi} \frac{m_\pi^2}{p_0^2} \ln \left(\frac{m_0 + 2p_0}{2m_\pi} \right) + \frac{m_0}{2\pi p_0} - \frac{m_\pi^2 m_0}{\pi p_0^3}. \quad (2.27)$$

Voigtian

The Voigtian lineshape [36] is the convolution of the Breit-Wigner and a Gaussian. The Gaussian lineshape includes the effect of mass resolution on the $\omega(782)$ region.

$$V(m) = \int_{-\infty}^{+\infty} G(m'; \sigma) BW(m' - m; m_0, \Gamma_0) dm' \quad (2.28)$$

with,

$$G(m; \sigma) = e^{-\frac{m^2}{2\sigma^2}} \quad (2.29)$$

$$BW(m; m_0, \Gamma_0) = \frac{1}{(m - m_0)^2 + \frac{\Gamma_0^2}{4}} \quad (2.30)$$

The defined integral is evaluated as:

$$V(m) = \frac{Re[\omega(z)]}{\sigma\sqrt{2}} \quad (2.31)$$

where $Re[\omega(z)]$ is the real part of the Faddeeva function with z given by the expression below.

$$z(m) = \frac{(m - m_0) + i\frac{\Gamma_0}{2}}{\sigma\sqrt{2}} \quad (2.32)$$

A list of the P - and D -wave resonances considered in this analysis and their respective lineshapes are shown in Table 2. The masses and widths of the resonances are fixed in the fits at their PDG average values.

Table 2 – List of resonance parameters including their spin, lineshape used and parameters of mass and width, according to PDG [21].

Resonance	Spin	Lineshape	m_0 (MeV)	Γ_0 (MeV)
$\rho(770)^0$	1	GS	775.26 ± 0.23	149.1 ± 0.8
$\omega(782)$	1	Voigtian	782.65 ± 0.13	8.49 ± 0.13
$\rho(1450)^0$	1	RBW	1465 ± 25	400 ± 60
$\rho(1700)^0$	1	RBW	1720 ± 20	250 ± 100
$f_2(1270)$	2	RBW	1275.5 ± 0.8	186.7 ± 2.2
$f_2'(1525)$	2	RBW	1525 ± 5	73_{-5}^{+6}

The mass resolution may affect the line shape of the narrow $\omega(782)$ resonance and must be considered. The mass resolution is studied using LHCb simulation by comparing the reconstructed $m(\pi^+\pi^-)_{\text{rec}}$ and generated $m(\pi^+\pi^-)_{\text{true}}$ candidates' values of $m(\pi^+\pi^-)$. The result of this study is presented in Fig. 4. On the left panel, the resolution is plotted against $m(\pi^+\pi^-)$, whereas in the right panel we have the distribution of $m(\pi^+\pi^-)_{\text{rec}} - m(\pi^+\pi^-)_{\text{true}}$ in the region around the $\omega(782)$ mass. The distribution is fitted to a Gaussian with $\sigma = 2.3$ MeV. The convolution of the $\omega(782)$ RBW with the resolution function gives the mass resolution.

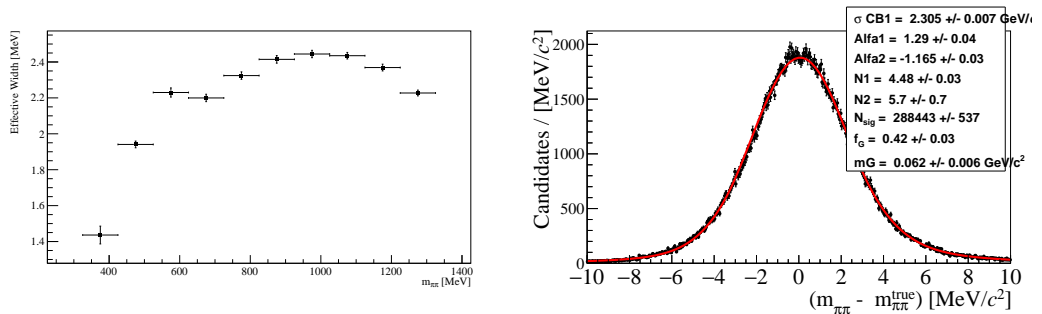


Figure 4 – The $\pi^+\pi^-$ mass resolution. In the $\omega(782)$ region, the resolution is 2.3 MeV.

Parameterisation of the S -wave

The $\pi^-\pi^+$ S -wave is determined by a model-independent amplitude, a generic complex amplitude. The decay amplitude combines the S -wave with a model-dependent parameterisation of the other waves and the decay amplitude as a whole, that's why quasi-model-independent. In essence, the fit is performed in the framework of the Isobar Model but using a binned amplitude for the S -wave instead of a sum of RBWs.

The measured $\pi^+\pi^-$ S -wave amplitude may include slowly varying phases that could arise from the weak vertex or FSI involving all three final state particles. Given the large number of free parameters, such phases might be accommodated in the S -wave. These effects should be estimated before using the S -wave measured in the $D^+ \rightarrow \pi^-\pi^+\pi^+$ decay to obtain the $\delta_{J=0}^{I=0}$ phase shift of the $\pi^+\pi^-$ scattering amplitude.

QMIPWA

The $m^2(\pi^-\pi^+)$ spectrum is divided into 50 intervals with the same population. This approach ensures that narrower intervals are taken where the amplitude varies rapidly (around the $f_0(980)$ peak, for instance). The magnitude a^k and the phase ϕ^k of the S -wave at the edges of each interval are determined by the fit, and a linear spline is used to obtain the S -wave amplitude at any point of the spectrum. Cubic spline was also tested. However, we got better results with linear spline.

The S -wave amplitude is

$$\sum_k \mathcal{A}_S^k(s_{\pi^+\pi^-}) = \sum_k a_k e^{i\phi_k}. \quad (2.33)$$

The existence of two identical pions in the final state requires the S -wave amplitude to be symmetrised. At any given point in the phase space with coordinates (s_{12}, s_{13}) corresponding to intervals k and l , the amplitude is given by

$$\mathcal{A}_S^{k,l}(s_{12}, s_{13}) = \mathcal{A}_S^k(s_{12}) + \mathcal{A}_S^l(s_{13}). \quad (2.34)$$

The complex coefficients of the P -wave and the 100 real coefficients defining the S -wave are fit parameters. The D -wave has two states, the $f_2(1270)$, defined as the reference mode, and the $f_2'(1525)$. High computational power is required for fitting over thousand events, with 110 free parameters, and in which the normalisation integral in eq. 2.15 must be evaluated at each iteration. This difficulty is handled using the GooFit framework for maximum-likelihood fits based on GPUs [37].

The results of the BaBar analysis [22] are used to provide the starting values for the magnitudes and phases of the S -wave. Once the minimum is reached, the fit is repeated 500 times with different starting values of the parameters. Given many free

parameters, other minima are found, but in all cases, they differ from the best solution by more than 1000 units of FCN. With this approach, we ensure that the fit reaches the absolute minimum.

The procedure for the starting point is as follows:

1. Magnitude and phase of BaBar analysis are plotted and interpolated by a linear spline.
2. The interpolation function is used to calculate the a^k and ϕ^k at the edges of each interval, serving as a starting value. The interpolation was performed because BaBar used 29 points for describing the S-wave, while our analysis used 50.

This algorithm depends only on the number of intervals the $s_{\pi^-\pi^+}$ spectrum is divided into, providing a suitable way to study the systematic effects of interval division.

The statistical uncertainties on the fit fractions are estimated with pseudo-experiments. A set of 100 samples is generated according to the model fitted to data, including background and efficiency. Each sample is fitted with the same procedure used to fit the data, and for each amplitude, a distribution of the corresponding fit fraction is formed. The standard deviation of the distributions is taken as the corresponding uncertainties on the fit fractions. The same pseudo-experiments are used to check if the uncertainties of all the parameters obtained from MINUIT are well estimated and if there are any biases in determining the parameters.

Goodness-of-fit

The Dalitz plot is divided into $n_b = 856$ bins with the same population to assess the goodness of fit. We compute the test statistic χ^2 defined as:

$$\chi^2 = \sum_{i=1}^{n_b} \chi_i^2 = \sum_{i=1}^{n_b} \frac{(N_i^{fit} - N_i^{obs})^2}{N_i^{obs}}, \quad (2.35)$$

where N_i^{obs} and N_i^{fit} are the observed number of candidates and the population estimated by the fit in bin i , respectively. The quantity $\chi^2/\text{n.d.o.f.}$ estimates the fit quality. The number of degrees of freedom, n.d.o.f., is in the range $[n_b - n_p - 1, n_b - 1]$, where n_p is the number of fit parameters (the exact value of n.d.o.f. has to be determined from toys [38]). In addition, the distribution of the normalised residuals $(N_i^{fit} - N_i^{obs})/\sqrt{N_i^{obs}}$ is also used.

2.2 The analysis tools

In this section, the main concepts of the tools used to perform the $D_s^+ \rightarrow \pi^-\pi^+\pi^+$ analysis are introduced. The section introduces sPlot, Reweighting, Multivariate Analysis (MVA), and GooFit.

2.2.1 sPlot

The sPlot is a technique to explore a data sample when the latter consists of several types of events merged into a single sample [39]. The events are represented by a set of variables which can be split into two components: the discriminant variables and the control variables. The first component consists of variables in which the distribution of all event types is well known (i.e, we have a P.D.F. or samples describing the signal and background), e.g. the invariant mass. The second component consists of variables in which the event types' distributions are unknown, e.g. signal and background components of D_s^+ transverse momentum.

The sPlot allows the separation of the different event types from the control variables using the knowledge of the discriminant variables if they are not correlated. The technique produces a set of weights called *sWeights* according to the number of event types; i.e. two types of events produce two sets of weights. The sWeights are used on control variables to access the distribution of the desired type.

This technique is widely used in High-Energy Physics to separate signal and background events from control samples. A simple example can be seen in ref [40]. For the $D_s^+ \rightarrow \pi^- \pi^+ \pi^+$ analysis, the knowledge about the distributions of signal and background that compose the invariant mass $m(\pi^- \pi^+ \pi^+)$ is used to calculate the sWeights. The signal sWeight is used to access the signal distribution of variables such as impact parameter and transverse momentum of the D_s^+ -meson.

The sPlot procedure is performed following the steps:

1. A unbinned extended maximum log-likelihood fit is performed to the discriminant variable to determine the signal and background yields and to optimise the PDFs free parameters. The log-likelihood is expressed as:

$$\mathcal{L} = \ln\{N_s f_s(m, \vec{\sigma}_s) + N_b f_b(m, \vec{\sigma}_b)\} - (N_s + N_b). \quad (2.36)$$

Where N_s , N_b , f_s and f_b are the yields and PDFs for signal and background, respectively. m is the invariant mass variable, $\vec{\sigma}_s$ and $\vec{\sigma}_b$ are the PDFs parameters of the signal and background, respectively.

2. The sWeights are calculated according to the expression

$$\mathcal{P}_n = \frac{\sum_{j=1}^{N_s=2} V_{nj} f_j(m)}{\sum_{k=1}^{N_s=2} N_k f_k(m)}. \quad (2.37)$$

Where N_k and f_k are each species' yield and PDFs, respectively. V_{nj} is the inverse of the covariant matrix given by the second derivative of $-\mathcal{L}$.

3. Histograms are filled by weighting the events with the sWeights \mathcal{P}_n . The sum of the entries is equal to the yields N_i provided by the fit.

This procedure is implemented on ROOFIT library [41].

2.2.2 Multivariate Analysis

The Multivariate Analysis (MVA) performed in this thesis consists of supervised machine learning techniques to discriminate signal and background events in the data sample, where each event is described by many variables. The discrimination is performed by a classifier algorithm, that receives as input signal and background proxy variables. The classifier is "trained" to find the separation boundaries between signal and background events, and then used to predict the probabilities of each event be signal or background. These probabilities are combined into a single variable, the classifier variable. A positive selection in the classifier variable reduces a certain number of background events in the data sample, while a negative selection removes a number of signal events.

The Toolkit for Multivariate Analysis (TMVA) [2] is a library that hosts various multivariate classification algorithms. The classifier used in $D_s^+ \rightarrow \pi^- \pi^+ \pi^+$ analysis was BDTG (Boosted Decision Tree Gradient) [42], which is briefly described.

A decision tree is a binary tree structure classifier, that repeatedly makes left/right (yes/no) decisions on one variable at a time which segments your data into similar groups. It's called a decision tree because it starts with a single box (or root), which then branches into several solutions, just like the tree in fig. 5. The start of the tree is the Root node, which splits by making an initial assumption. After the initial split are the decision nodes; they are referred to as decision nodes because a split in the data has been made that caused the tree to branch in two separate directions. The leaf nodes will often lead to the answer or the predicted value.

The gradient boosting builds the model in a step-wise fashion and generalizes the model by allowing optimization of an arbitrary differentiable called the *loss*. Gradient boosting combines an ensemble of weak learners (decision tree) into a single strong learner. The Decision trees in the ensemble are added one at a time. A gradient descent procedure is used to minimize the loss when adding trees. The idea of gradient boosting is that you can combine a group of relatively weak prediction models to build a stronger prediction model, see figure 6. The final model is then used to predict the classifier variable.

An important care during the classifier training is to prevent model *overfitting*. Overfitting, roughly speaking, is when the model fits the training data well but doesn't work well with new data. Model overfitting can be avoided by pruning the Decision Trees, which involves removing decision branches that rely on features with low importance. By doing so, we simplify the tree, which enhances its predictive capabilities.

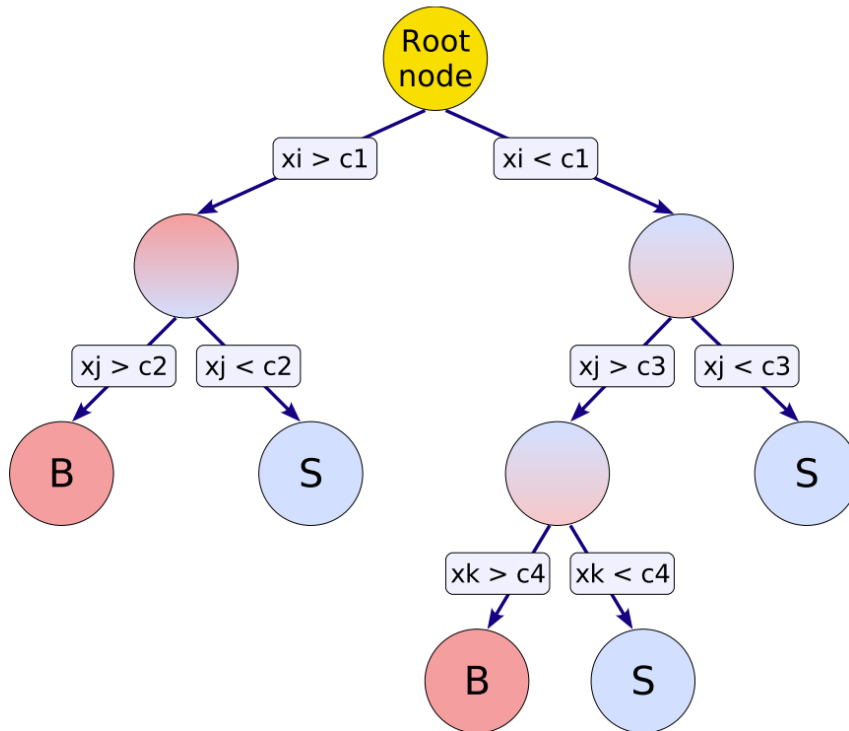


Figure 5 – An example of a Decision Tree. Source [2].

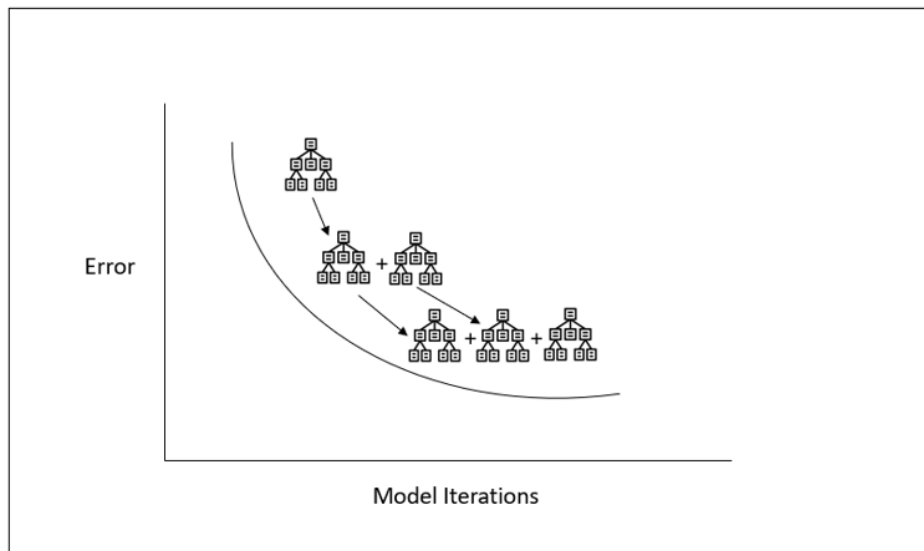


Figure 6 – The gradient descent optimization. Source [3].

It is also desirable that the classifier variable has no bias. To avoid any potential biases in our classifier variable, we utilize a technique called cross-validation during the training and prediction of probabilities (called application in TMVA language). Essentially, this technique involves dividing the training data into N -folds and using each fold as input to train N models. Then, we leverage the trained model of each fold to predict

the probabilities of the other folds that were not used during the training process. This approach helps to ensure a fair and unbiased prediction of probabilities.

During the $D_s^+ \rightarrow \pi^- \pi^+ \pi^+$ analysis, two folds were utilized to train two models that would predict two classifier variables for the role sample. To eliminate bias, the mean of these classifier variables was calculated and used as our classifier variable.

2.2.3 Reweighting

The weighting of simulated events in High-Energy Physics is a common practice to correct inconsistencies in the signal variables' distributions. This is typically done using real data sPlotted distributions as a signal proxy. The binned weighting is the most straightforward approach. It consists of taking the ratio of two variables' histograms, one from simulation (f_{MC}) and the other from data (f_{RD}), and using it to calculate weights. however, This simple approach has some limitations.

- A few variables can be weighted, usually one or two.
- Applying the weights to one variable may cause inconsistencies in the others.
- The data sample size necessary to precisely determine the ratio grows exponentially with the number of variables.
- It may provide inaccurate predictions when the density ratio is high. Bin regions with low statistics.

. The Gradient Boosting Reweighter (GB-Reweighter or Reweighting) was developed to address this problem [43]. The GB-Reweighter consists of using an ensemble of shallow decision trees (weak learners) to split the space of variables smartly. The regions are associated with the leaves of the tree. To find the regions that are suitable for reweighting, the symmetrized χ^2 is optimized in a step-wise fashion. The simulation is reweighted in each step. Each tree in the sequence covers the discrepancies that were not resolved in the previous iterations.

$$\chi^2 = \sum_{leaf} \frac{(N_{leaf,MC} - N_{leaf,RD})^2}{N_{leaf,MC} + N_{leaf,RD}}$$

where $N_{leaf,MC}$ and $N_{leaf,RD}$ are the number of events of MC and RD. The final trained model can be used to predict event-by-event weights that correct the inconsistencies.

To test the result of the reweighting, a classifier is trained to discriminate the simulation and the signal proxy. The receiver operating characteristic (ROC) curve is plotted, and its integral is calculated (AUC). The closer the curve is to the diagonal or the AUC to 0.5, the better the agreement. The Reweighting was also performed using the cross-validation approach in the $D_s^+ \rightarrow \pi^- \pi^+ \pi^+$ analysis. An enjoyable example can be found in ref. [44].

2.2.4 GooFit

The GooFit is a massively parallel framework, written using Thrust for CUDA and OpenMP, for doing maximum-likelihood fits with a familiar syntax.

Its user-friendly structure and a large ensemble of PDFs for 1D fits; and 3-Body and 4-Body amplitude analysis, allow spending less time coding and more time performing the analysis itself. GooFit can be used in C++ or Python 3. The GPU backend speeds up the fits by normalising the PDFs using very high parallelization.

High-performance fitting frameworks are mandatory to analyse the large datasets provided by the CERN experiments. Details about the performance of GooFit can be found in [37].

2.3 Definition of variables

In this section, some of the relevant variables that are used in the $D_s^+ \rightarrow \pi^- \pi^+ \pi^+$ analysis are defined. Figure 7, shows a typical decay of a D-meson in a three-body pseudoscalar final state. The D-meson is produced by the pp interaction in the Primary Vertex (PV) and decays in the Secondary Vertex (SV) after going through a Flight Distance (FD) given by VELO. The D-meson decay is described by a set of topological and kinematic variables provided by the tracking system. In addition, there are the particle identification and trigger variables. The former is provided by RICH and calorimeters. The latter by the trigger system. The main variables used in the $D_s^+ \rightarrow \pi^- \pi^+ \pi^+$ analysis are defined as follows. D means D_s^+ in the list below.

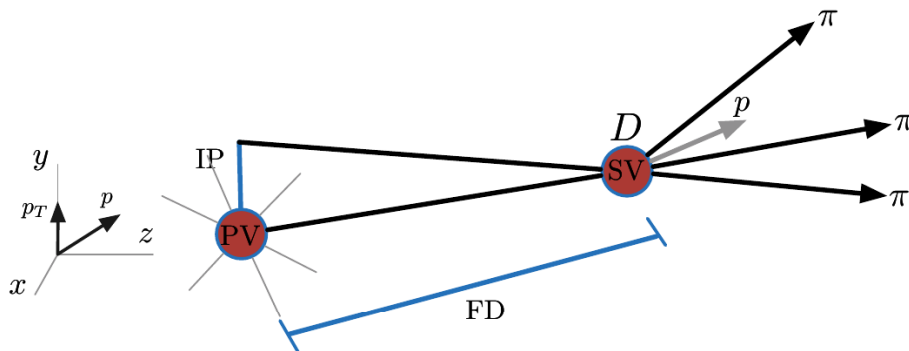


Figure 7 – A typical topology of a D-meson decay. Here, it is illustrated for the $D^+ \rightarrow \pi^- \pi^+ \pi^+$ decay.

D MASS (D_MM) The invariant mass of the three pions, $D_MM = \sqrt{(p_1^\mu + p_2^\mu + p_3^\mu)^2}$

D transverse momentum (D_PT) The absolute value of the transverse component of the D-meson momentum relative to the beam axis. $D_PT = |D_P| \sin\theta$.

- D Flight distance χ^2 (FD_{χ^2})** It is defined as the ratio between the FD squared and the fir uncertainty of PV and SV.
- D Impact parameter (D_IP)** Defined as the minimum distance between the constructed trajectory and the PV.
- D Impact parameter χ^2 ($D_IP_{\chi^2}^2$)** Defined as the χ^2 fit difference with and without the D_s^+ reconstructed track, which is defined as the difference in the vertex-fit χ^2 the PV reconstructed with and without the D^0 candidate trajectory.
- D Cosine of the direction angle (D_DIRA)** Defined as the angle between the PV-SV vector and the D_s^+ tri-momentum vector.
- D Secondary Vertex χ^2 (D_Vertex_ χ^2)** It is the χ^2 of the secondary vertex fit. Vertex χ^2 requires that decay product traces form a good vertex.
- p_i Impact parameter χ^2 ($i = 1, 2, 3$) ($p_{i,IP\chi^2}$)** The same as that for D_s^+ , but now for the decay products.
- p_i transverse momentum ($p_{i,PT}$)** The same as that for D_s^+ , but now for the decay products.
- PT_SUM** Sum of the decay product transverse momentum $p_{i,PT}$.
- DOCA $_{ij}$** Distance of closest approach between the tracks i and j .
- logIP** Defined as the logarithm of the ratio between the product of the daughter's $p_{i,IP\chi^2}$ and the $D_IP_{\chi^2}^2$
- Pointing** It is a weighted comparison of the transverse momenta of the decay particle and its decay products.
- $$Pointing = \frac{psin\theta}{psin\theta + \sum_i p_{i,T}} \quad (2.38)$$
- Particle identification (p_i PID)** Using the RICH information for each track, the likelihood to be one of the possible particles: pion, kaon, protons, electrons and muons. The p_i PID is the likelihood separation. In the $D_s^+ \rightarrow \pi^- \pi^+ \pi^+$, we use the p_i PIDK, which is the $\ln\mathcal{L}(K) - \ln\mathcal{L}(\pi)$ for the i particle.
- Particle identification NN (p_i ProbNN)** The ProbNN is a machine-learning classification based variable. It is the response of an Artificial Neural Network called PIDANN. This algorithm is tuned on simulated signal and background samples.
- Track χ^2 /ndof χ^2** per degree of freedom of the track reconstruction fit. It is the χ^2 of the track reconstruction divided by the number of degrees of freedom.

3 The LHCb experiment

The LHCb (Large Hadron Collider beauty) is a dedicated experiment for studying heavy flavour physics at the LHC (Large Hadron Collider). Its main objective is to search for indirect evidence of new physics in CP violation and rare decays of beauty and charm mesons. The level of CP violation predicted in the Standard Model (SM) weak interactions cannot explain the observed asymmetry between matter-antimatter in the universe. The effect of such new sources might be seen in heavy flavour physics. Decay modes of B and D mesons provide a good framework for testing new physics models and increasing the precision of important CP violation parameters, like the Cabibbo–Kobayashi–Maskawa (CKM) matrix elements. A detailed LHCb detector description can be found in [6]. In the following sections, the LHC (Large Hadron Collider) and the LHCb detector used in Run 1 and 2 will be introduced.

3.1 The LHC

The Large Hadron Collider (LHC) is the world’s largest and most powerful particle accelerator. The LHC consists of a 27-kilometre ring of superconducting magnets with a number of accelerating structures to boost the energy of the particles along the way.

The accelerator consists of two high-energy particle beams containing groups of protons travelling at nearly the speed of light. These beams can attain a maximum energy of 7 TeV each, resulting in collisions with a center-of-mass energy of 14 TeV. The two beams travel in opposite directions through separate beam pipes maintained at an ultra-high vacuum. The beams are directed around the accelerator ring by powerful magnetic fields produced by superconducting electromagnets. These electromagnets are made of coils of special electric cables that work in a superconducting state. They must be chilled to a temperature colder than outer space, which is -271.3°C . To achieve this temperature, much of the accelerator is connected to a liquid helium distribution system that cools the magnets and other supply services.

The Large Hadron Collider (LHC) uses thousands of magnets of various sizes and types to guide the beams around the accelerator. The accelerator has 1232 dipole magnets that are 15 meters long and bend the beams, and 392 quadrupole magnets that are 5-7 meters long and focus the beams. Before the collision, the particles are squeezed together with another type of magnet to increase the chances of collisions. All the controls for the accelerator, its services, and technical infrastructure are located at the CERN Control Centre. The beams inside the LHC collide at four locations around the accelerator ring, corresponding to the positions of four particle detectors: ATLAS, CMS, ALICE, and

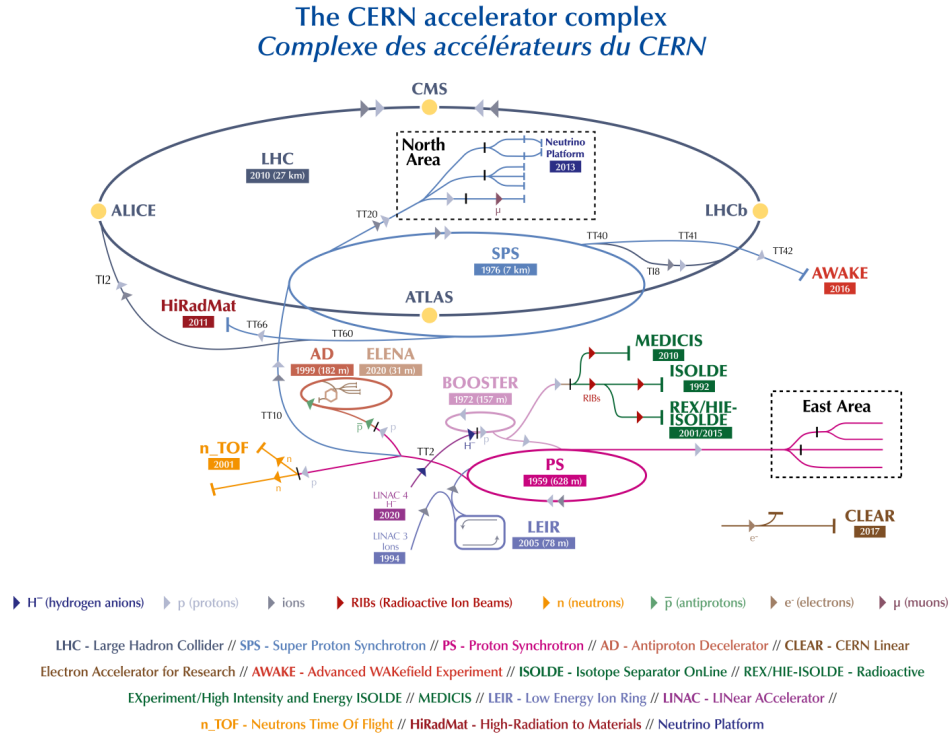


Figure 8 – The LHC is the last ring (dark blue line) in a complex chain of particle accelerators. The smaller machines are used in a chain to help boost the particles to their final energies and provide beams to a whole set of smaller experiments, which also aim to uncover the mysteries of the universe. Source: CERN

LHCb. ATLAS and CMS are general particle detectors built to collect data on the highest luminosity and center-of-mass energy. LHCb and ALICE are specialized detectors, with the former dedicated to heavy flavour physics and the latter designed to study heavy ion collisions.

The primary objective of the Large Hadron Collider (LHC) is to explore physics beyond the Standard Model. To achieve this, rare processes that could reveal new physics must be studied. Therefore, the LHC strives to maximize the center-of-mass energy and the collision rate. The collision rate is measured in terms of luminosity, which is defined by a specific expression

$$\mathcal{L} = \frac{N^2 f}{4\pi\sigma_{eff}} \quad (3.1)$$

where N is the number of protons in each bunch, f is the bunch crossing rate, and σ_{eff} is the effective RMS radius of the beams. The LHC was designed to achieve a peak luminosity of $10^{34} \text{cm}^{-2}\text{s}^{-1}$. A detailed description of LHC can be found in [45]. Figure 8 illustrates the CERN accelerator complex.

3.2 LHCb detector

The LHCb is a single-arm forward spectrometer. The detector geometry is justified because, at high energies, $b\bar{b}$ pairs are primarily produced in angles close to the beam line. It can be verified by the simulated pseudorapidity distribution of $b\bar{b}$ pairs produced in LHC collisions at 14 TeV centre-of-mass energy shown in figure 9. Therefore, the LHCb detector pseudorapidity acceptance is defined in the range $2 < \eta < 5$. This feature has the benefit of simplifying the reconstruction of tracks left by charged particles. Instead of tracking curving tracks through a magnetic field, as in other LHC experiments, tracks in LHCb can be roughly described as combinations of two straight track segments, one upstream of the magnet and the other downstream. The LHCb was designed to operate at a maximum instantaneous luminosity of $\mathcal{L} = 2 \times 10^{32} \text{cm}^{-2}\text{s}^{-1}$, much lower than CMS and ATLAS. This luminosity allows us to keep the average number of visible primary pp interactions in each bunch crossing (pile-up) close to unity since the detector performance decreases at high pile-up.

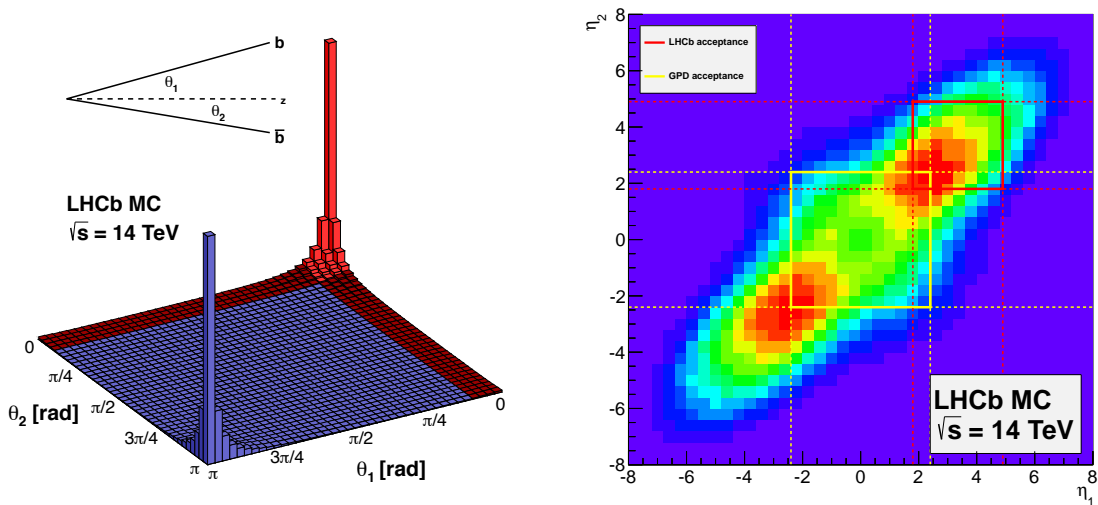


Figure 9 – The angular distribution of $b\bar{b}$ production as a function of the angle to the beam axis (left) and as a function of the pseudorapidity (right) at $\sqrt{s} = 14$ TeV centre-of-mass energy. The distributions shown in these plots were created using PYTHIA8 [4] and CTEQ6 NLO pdf. The red square in the right figure shows the LHCb pseudorapidity acceptance. Source [5].

Another feature is that heavy flavour hadrons decay via weak interaction. Hence, ground state b- and c- hadrons tend to have long lifetimes. Heavy flavour hadrons produced at the LHC will be highly boosted in the laboratory frame and travel several millimetres before decaying. This means that the primary signature of a heavy flavour decay is a set of charged tracks meeting at a vertex displaced from a proton-proton collision point. To identify these decays in the LHC environment, the LHCb detector must have excellent tracking near the beamline as close to the interaction point as possible. Finally, heavy

flavour hadrons decay into various final state particles. These particles must be correctly identified to reconstruct the parent particle accurately. This means the LHCb detector must be able to identify all species of long-lived charged hadrons and leptons correctly.

Figure 10 shows a side view of the LHCb detector. The tracking system is responsible for reconstructing the path of the charged particles and their momenta together with the magnet. It includes the Vertex Locator (VELO) and four planar tracking stations, the Tracking Turicensis (TT) and T1-T3, located upstream and downstream of the magnet. Particle identification is performed by the ring imaging Cherenkov detectors (RICH1 and RICH2) and five muon stations (M1-M5). The electromagnetic (ECAL) and hadronic (HCAL) calorimeters measure the energy of the particles.

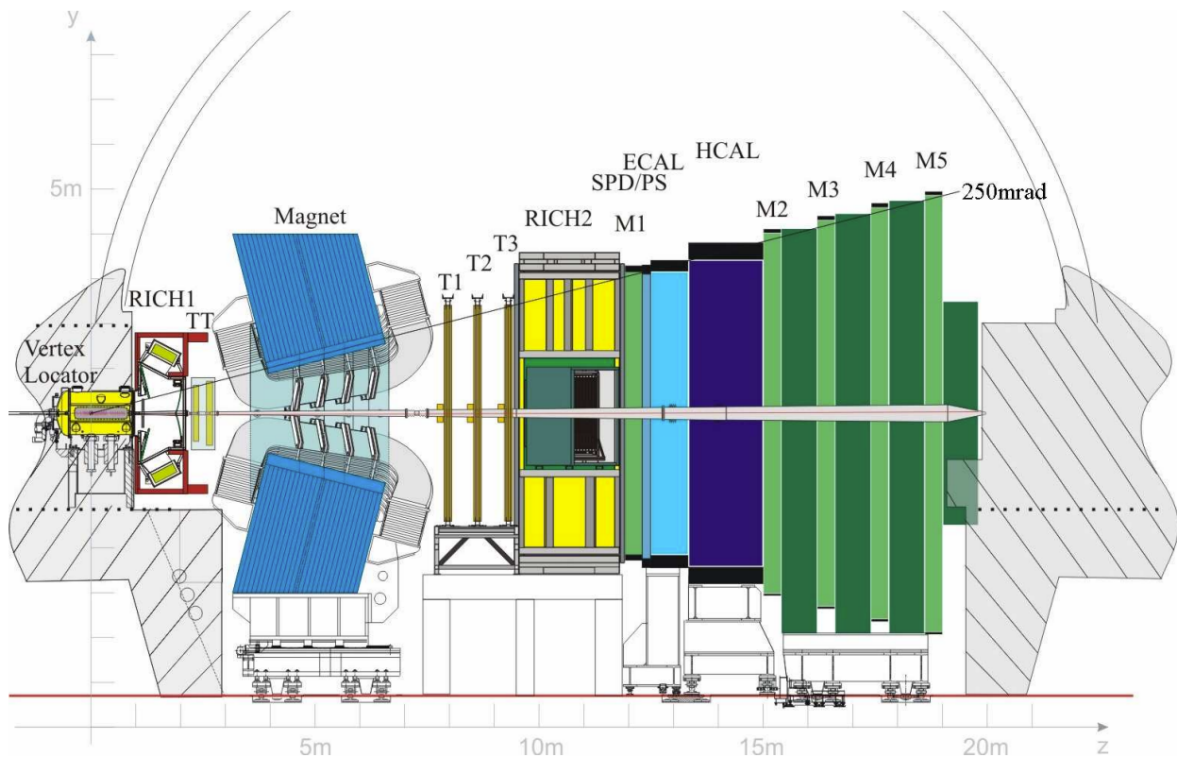


Figure 10 – The side view of the LHCb detector (Run 1). The right-handed coordinate system adopted has the z-axis along the beam, and the y-axis along the vertical. Source [6]

3.2.1 The tracking system

The tracking system of LHCb consists of the Vertex Locator, placed close to the interaction point; the Tracking Turicensis, placed upwards of the dipole magnet; the dipole magnet, used to measure the moment of the charged particles; and the Inner and Outer trackers (T1-T3), placed downwards of the dipole magnet. The LHCb tracking system was designed to provide an impressive momentum resolution, 0.5% at low momentum to 1.0% at 200 GeV/c.

The Vertex Locator

The distinction of the long-lived b - and c -hadron decays from the particles produced in the underlying pp interaction is one of the main tasks necessary to study heavy-flavour hadron decays at the LHCb. To perform this task, the Vertex Locator (VELO) precisely determines the position of the pp interaction, the primary vertex (PV), as well as the position of the displaced b - and c -hadron vertex, the secondary vertex (SV). Along with an excellent momentum resolution, VELO also provides the decay time of the particles, which is a requirement to access and study all possible final states. Another critical measurement VELO provides is the impact parameter (IP), the distance of the closest approach to the PV. Long-lived particles tend to have tracks with large impact parameter; a minimum cut on the IP is used to exclude background from short-lived particles.

The VELO consists of 42 silicon modules arranged along the beam direction. The modules are arranged to make the particles within the pseudorapidity acceptance $1.6 < \eta < 4.9$ and originated from $|z| < 10.6$ cm, which will traverse the sensitive regions of at least three modules. The modules are composed of semicircular sensors designed to measure the radial coordinate (the r -sensors) and the azimuthal angle ϕ (the ϕ -sensors), see Figure 11. The VELO sensors are placed at a radial distance from the beam, which is smaller than the aperture required by the LHC during injection and must, therefore, be retractable. During stable beams, the VELO is “closed”, and the minimum distance between the beamline and the VELO’s sensitive region is 8 mm. This is smaller than the transverse size of the LHC beams during beam injection, so the VELO can be “opened” to increase this distance to about 3 cm to avoid damage. For a more detailed discussion, see [46].

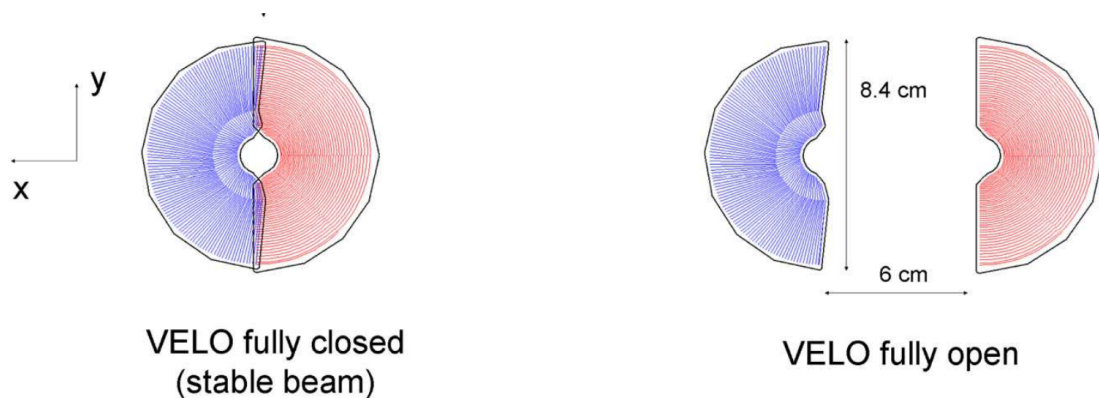


Figure 11 – The front face of the VELO modules in both the closed and open positions. In blue, the r -sensors and in red, the ϕ -sensors. Source [6].

The dipole magnet

The LHCb dipole magnet [47] is a super-conducting warm magnet designed to have a 4 Tm integrated magnetic field. The design of the magnet was constrained by the

requirement that the field level inside the RICH envelope must be less than 2 mT and be the highest possible between VELO and the TT. The dipole format that reminds of a two saddle in a window-frame yoke was thought to match the required detector acceptance; see Figure 12.

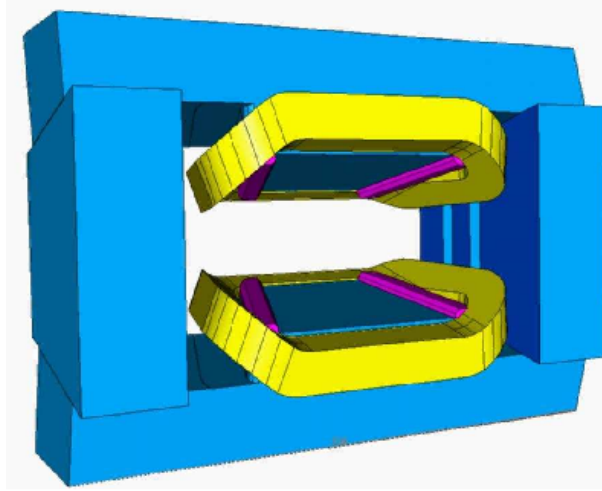


Figure 12 – The LHCb dipole magnet. This is a warm magnet which allows the momenta of charged particles to be determined. Source [7]

The dipole magnet is used to measure the momentum of charged particles. To achieve the required momentum resolution for charged particles, the integrated magnetic field must be measured with a precision of 10^{-4} Tm. An array of Hall probes is used to map the magnetic field in the volume of interest. The mapping of both magnets is compared to the magnetic field calculation obtained with TOSCA. The precision measurement of the field in the tracking volume is about 4×10^{-4} as shown in Figure 13 left. Figure 13 right shows the B_y component along the z -axis. The result shows an excellent overall agreement with the calculation.

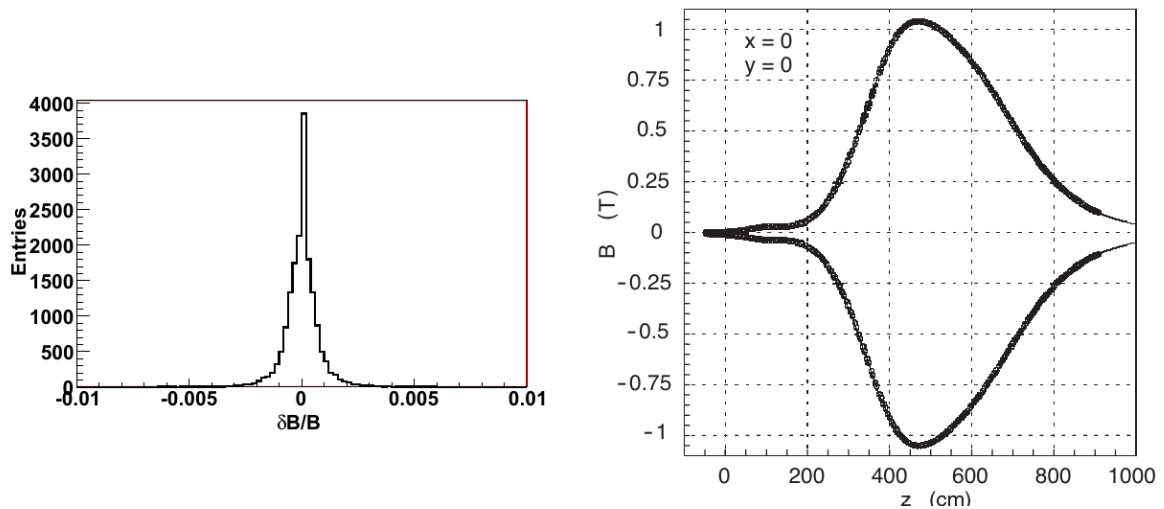


Figure 13 – The front face of the VELO modules in both the closed and open positions. In blue, the r -sensors and in red, the ϕ -sensors. Source [6].

The deflection efficiency of positive and negative charged particles depends on the left-right symmetry of the dipole magnetic field. A slight asymmetry may include systematic effects that must be understood. To reduce these effects, the polarity of the dipole is periodically reversed during the data taking. When the data samples of the two configurations, downwards (MagDown) and upwards (MagUp) to the magnetic field, are combined, these effects are mostly cancelled.

The Tracker Turicensis

The Tracker Turicensis [48] is a silicon strip detector upstream of the LHCb dipole magnet and covers the full acceptance of the experiment. The TT is a 150 cm wide and 130 cm high planar tracking station with four detection layers. The first and last layers are vertically placed, while the second and third layers are rotated by a stereo-angle of -5° (TTaU) and $+5^\circ$ (TTaV), respectively. This arrangement was designed to maximize the precision in the bending plane of the magnet. The stereo angle increases the sensibility of the tracks in the y position, which reduces the number of fake tracks. It is also replicated for the Inner Tracker (IT) and the Outer Tracker (OT). The layers of TT are divided into two halves; each half consists of 7 silicon sensors arranged vertically, each containing 512 vertical strips with a strip pitch of $183 \mu\text{m}$. The sensors are $500 \mu\text{m}$ thick.

The TT is also known as the Trigger Tracker since it provides the LHCb software trigger the initial momentum and charge determination of the tracks for the tracking stations downstream the dipole magnetic.

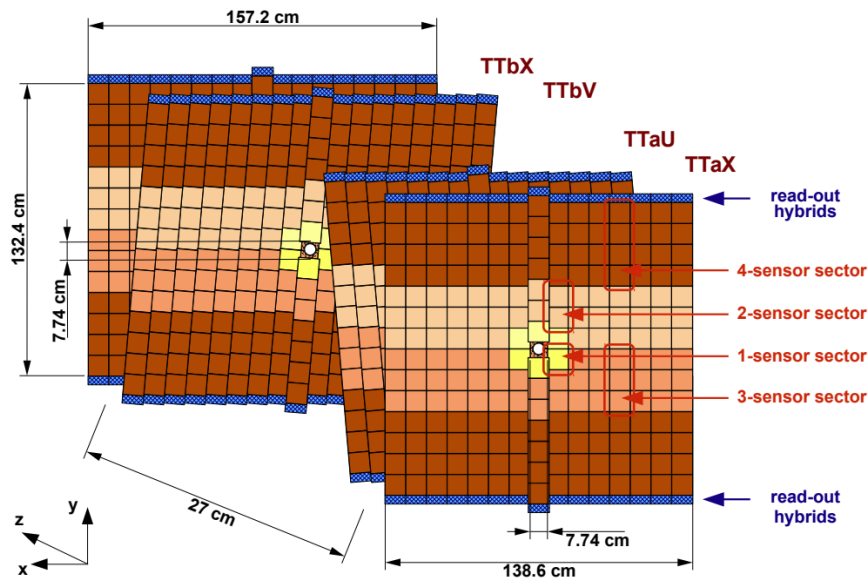


Figure 14 – Layout of the TT, with the LHC beam pipe passing through an opening in the centre of the detection layers. Source [8].

The Inner and Outer Trackers

The Inner [49] and Outer [50] trackers are located in the downward region of the LHCb dipole. They are used with the VELO, TT and the dipole magnet to provide the momenta of the charged particles precisely.

The IT silicon detector covers a 125.6 cm wide and 41.4 cm high cross-shaped region in the centre of the three tracking stations (T1-T3); see the left figure 15. The IT acceptance covers $4.5 < \eta < 4.9$ in the y direction and $3.4 < \eta < 5$ in the x direction. Each IT station comprises four individual detector boxes arranged around the beam pipe; see figure 15 right. The horizontal boxes comprise 28 modules with sensors of two different thicknesses, each carrying 384 vertical strips with a pitch of $198 \mu\text{m}$. The horizontal strip sensors are $410 \mu\text{m}$ thick. The vertical boxes are composed of 14 modules identical to the horizontal ones except for the strip sensor thickness of $320 \mu\text{m}$. The different thickness is justified to ensure sufficiently high signal-to-noise ratios for each module type.

The OT is a drift-time detector and consists of an array of gas straw-tube modules. Each module consists of two monolayers of 128 straw tubes. The straw tubes have a diameter of 4.9 mm. The detector modules and TT and IT are arranged, covering the LHCb acceptance. The gas mixture of Argon (70%) and CO_2 (30%) was chosen to guarantee a fast drift time (50 ns) and good drift-coordinate resolution ($\sim 240 \mu\text{m}$).

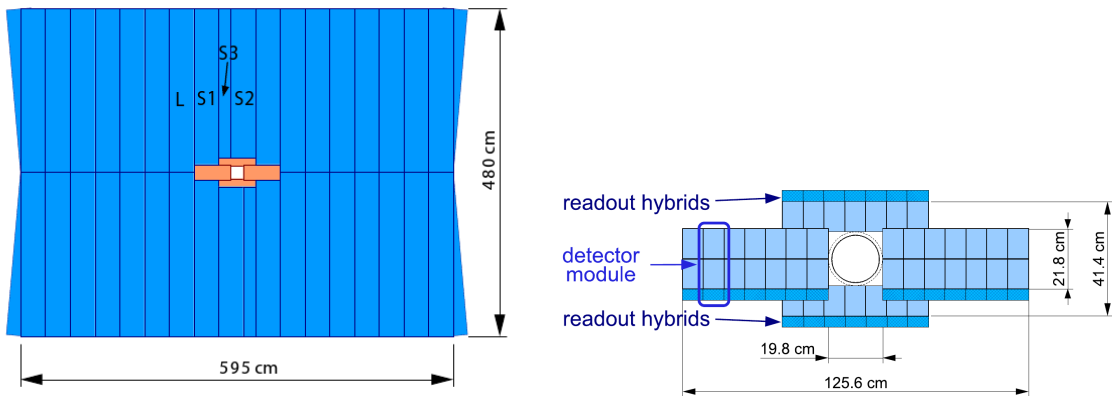


Figure 15 – (Left) Front view of a T-station with the modules of the Outer Tracker and the boxes of the Inner Tracker. (Right) Layout of an x-detection layer in the second IT station. Sources [9, 6].

3.2.2 The particle identification system

Particle Identification (PID) is crucial in studying weak decay of B and D mesons. A precise PID is essential to reconstruct the decay products of the heavy flavour decays. The LHCb PID system consists of two ring imaging Cherenkov detectors, RICH1 and RICH2; two calorimeters, the electromagnetic (ECAL) and the hadronic (HCAL); and the muon system.

The Ring Imaging Cherenkov detectors

The ring imaging Cherenkov detector is designed to use the Cherenkov effect [51] to distinguish particles. When a charged particle passes through a dielectric medium at a speed greater than the phase velocity of light in that medium, it emits electromagnetic radiation. The emitted radiation forms a cone with an opening angle θ_c concerning the particle's trajectory. θ_c angle is given by the expression

$$\theta_c = \arccos\left(\frac{1}{\eta\beta}\right) \quad (3.2)$$

where n is the index of refraction of the medium and $\beta = v_p/c$, is the ratio between the charged particle speed and the speed of light.

To distinguish two particles of the same momentum, e.g. pions and kaons, the difference of the opening angles $\Delta\theta_{k\pi}$ is calculated. the $\Delta\theta_{k\pi}$ is given by the expression below.

$$\Delta\theta_{K\pi} = \frac{1}{\sqrt{1 - \frac{1}{\eta^2}}} \left(\frac{1}{\gamma_K^2} - \frac{1}{\gamma_\pi^2} \right) \quad (3.3)$$

γ_K and γ_π are the relativistic factors for the Kaon and pion mass hypotheses, respectively. Figure 16 shows the reconstructed Cherenkov angles of different particles.

To cover all momentum spectrum, the RICH system consists of two detectors: RICH1 at the upstream region of the LHCb detector and RICH2 at the downstream region. RICH1 covers the low momentum charged particles range between 1-60 GeV/c using aerogel and C_4F_{10} radiators, while the RICH2 covers the high momentum from 15 GeV/c to 100 GeV/c. In both RICH detectors, Hybrid Photon Detectors (HPDs) are used to collect the Cherenkov photons in the wavelength range 200–600 nm. The photons are focused using a combination of spherical and flat mirrors to reflect the image out of the spectrometer acceptance.

The calorimeters

The calorimeter system of LHCb [52] consists of the Scintillator Pad Detector (SPD), the Preshower (PS), the Electromagnetic Calorimeter (ECAL), and the Hadronic Calorimeter (HCAL). This system provides particle identification of electrons, photons and hadrons, as well as their energy and position. The L0 hardware trigger uses the system to make a fast selection based on high transverse momentum candidates to reduce the background and the bunch crossing rate from 40 MHz to 1 MHz. The ultimate performance is archived during the offline selection.

All calorimeters are based on the principle when a particle interacts with the absorber material; energy is released and converted into photons in the scintillating

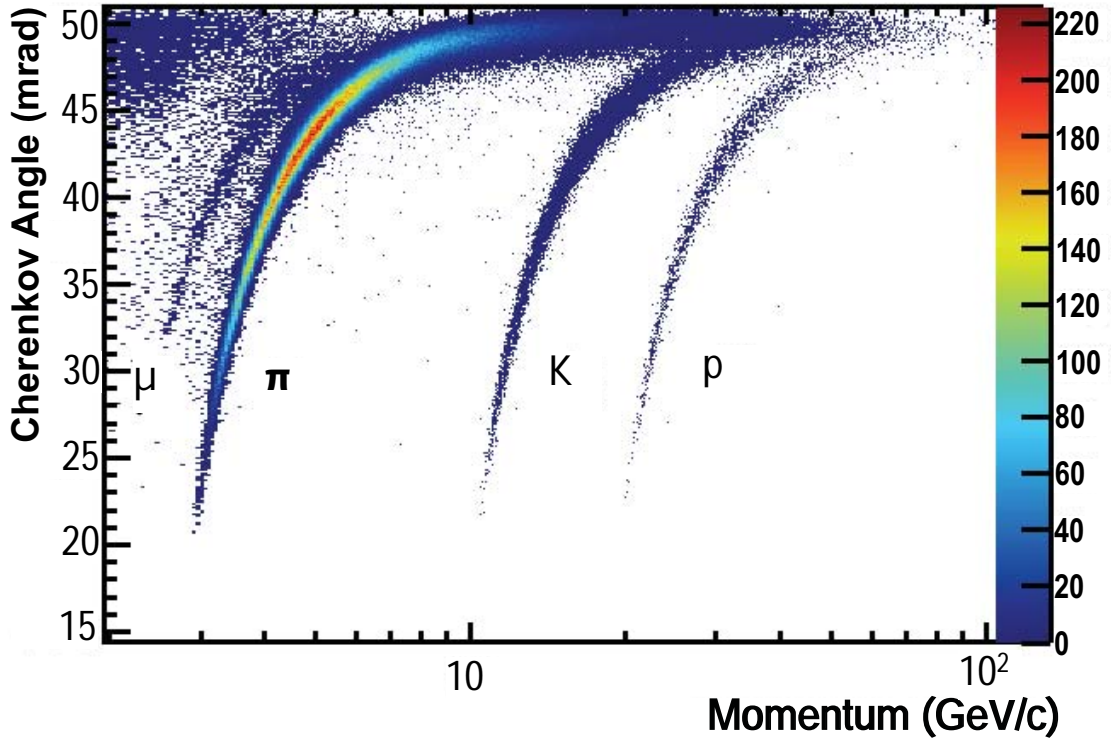


Figure 16 – Reconstructed Cherenkov angle for *isolated* tracks, as a function of track momentum in the C_4F_{10} radiator. The Cherenkov bands for muons, pions, kaons and protons are visible. Source [10].

material. The scintillation light is transmitted to a Photo-Multiplier Tube (PMT) by wavelength-shifting (WLS) fibres, and the number of detected photons is proportional to the energy of the original particle.

The ECAL is a sampling calorimeter made up of alternating layers of lead and layers of scintillators. It is used to measure the energy of photons and has an energy resolution of $\sigma_E/E = 10\%/\sqrt{E} \otimes 1\%$ (E in GeV). The SPD/PS system works as a longitudinal segment of ECAL and consists of two planes of scintillator pads, separated by a 2.5 radiation lengths lead wall. The SPD identifies charged particles and allows electrons to be distinguished from photons and the Preshower identifies electromagnetic particles. The ECAL and the SPD/PS system are essential to reconstruct B- and D-decays to channels containing a prompt photon or a π^0 and an electron.

The HCAL is a sampling calorimeter made up of iron and scintillating tiles. The difference between HCAL sampling and ECAL is that the scintillating tiles are oriented in parallel to the beam axis in the y - z plane. The HCAL measures the energy of the hadrons with an energy resolution $\sigma_E/E = 70\%/\sqrt{E} \otimes 10\%$ (E in GeV). The L0 trigger uses it to select hadron candidates with high transverse energy, which requires a modest energy resolution.

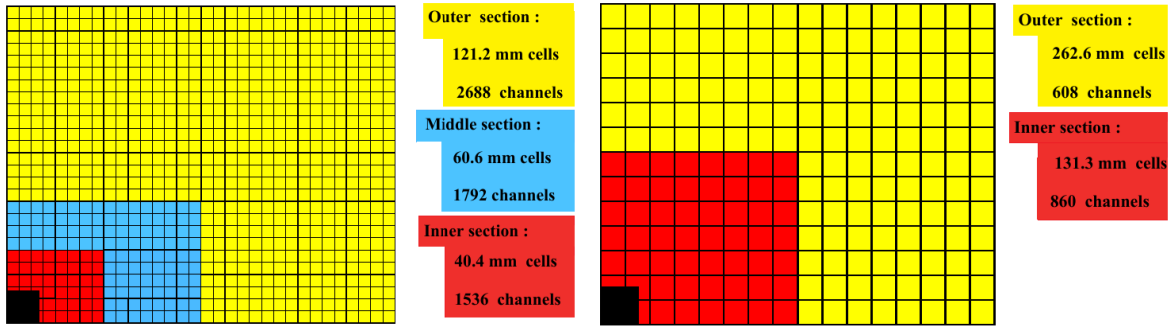


Figure 17 – Lateral segmentation of the SPD/PS and ECAL (left) and the HCAL (right). One quarter of the detector front face is shown. In the left figure, the cell dimensions are given for the ECAL. Source [6].

The detectors adopt a variable lateral segmentation since the hit density varies by two orders of magnitude over the calorimeter surface; see figure 17. The cells are scaled to provide a one-to-one-to-one projective correspondence between cells in each detector.

The Muon System

The Muon system [53] is one of the essential detectors for the LHCb experiment CPV studies program. It provides a fast selection of high transverse momentum muon trigger and particle identification for the high-level trigger (HLT) and offline analysis. Muons are present on many CP-sensitive B-decay channels like the $B_d \rightarrow J/\Psi(\mu^- \mu^+) K_s^0$ and $B_d \rightarrow J/\Psi(\mu^- \mu^+) \phi$. They are used for flavour-tagging in semi-leptonic b -decays. It is also present in rare decays, as the flavour-changing neutral current decay $B_s^0 \rightarrow \mu^+ \mu^-$, which is used to search physics beyond the standard model.

The Muon System identifies charged particles as muons based on their penetration depth. The system is made of five Stations (M1-M5) of rectangular shape, covering the LHCb acceptance of ± 300 mrad (horizontally) and ± 200 mrad (vertically). The M1 station is placed in front of the Preshower at 12m from the interaction point. The M2-M5 follow the Hadron Calorimeter (HCAL) and are separated by iron filters. The calorimeters and the iron filters provide a shield with a total absorber-thickness of 20 nuclear interaction lengths and attenuate the detection of hadrons, electrons and photons. The muon candidate to be triggered needs to hit the 5 stations, this requires a muon minimum momentum of about 6 GeV/c due to the shielding.

The stations' technology is based on Multi-wire proportional chambers (MWPC) and triple-GEM (Gas Electron Multiplier) detectors. The former consists of an array of wires spaced in 2mm at high voltage (anode), which run through a chamber with conductive walls held at ground potential (cathode). The chamber is filled with the gas mixture $Ar/CO_2/CF_4$ (40:55:5). The charged particle that passes through the chamber ionizes the surrounding gas atoms. The resulting ions and electrons are accelerated by

the electric field across the chamber, causing a localised cascade of ionization. This is collected on the nearest wire and results in a charge proportional to the ionisation effect of the detected particle. By computing pulses from all the wires, the particle trajectory can be found. The GEM detectors use the electric field produced in small holes in a thin polymer sheet instead of using wires. The cascade occurs inside these holes that eject electrons out of the sheet. The triple-GEM detector uses three foils of GEM sandwiched between the anode and cathode for multiply the electrons to be collected.

Each station consists of four regions (R1-R4) with increased distance from the beam axis. The granularity of these regions varies according to the particle density in order to keep the occupancy constant over the detector. MWPCs are used in almost all regions of the stations, except for the inner region of station M1 which uses the triple-GEM detectors due to the intense particle flux and radiation level.

The momentum resolution is defined by the x and y dimensions of the logical pads of the stations, which provide information about the track coordinates. The x dimensions of M1-M3 are designed to provide a good p_T resolution ($\sim 20\%$), while the y dimensions of all stations are determined by the required rejection of background triggers which do not point to the interaction region. Figure 18 illustrates the system.

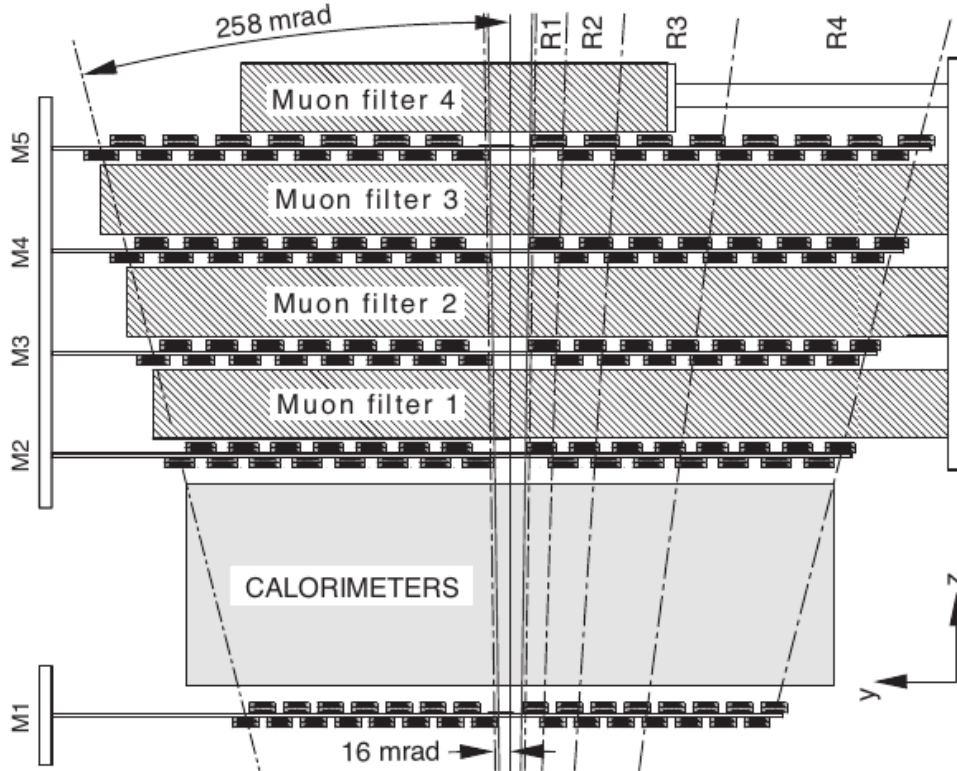


Figure 18 – Side view of the muon system. Source [6].

3.2.3 The trigger system

The LHC provides a nominal bunch crossing rate of 40 MHz with a bunch spacing of 25 ns and when running with 2808 bunches per beam, which means 600 million inelastic events per second. In Run 1, between 2010 and 2013, the LHC operated with protons at beam energies of 3.5 and 4 TeV with a bunch spacing of 50 ns (2011 and 2012) and achieved a maximum number of bunches of 1380 [54], which corresponds to a bunch crossing rate of ~ 15.5 MHz. In Run 2, between 2015 and 2018, the beam energies increased to 6.5 TeV with a nominal bunch spacing of 25 ns and with a maximum number of bunches of 2556 [55], which corresponds to a bunch crossing rate of ~ 29 MHz closer to the nominal rate.

These large rates are way above the data processing and storing capability of LHCb. The trigger system is necessary for reducing the rate by selecting potentially interesting events. The trigger system [56] is divided into two steps. The hardware trigger (L0) and the high-level trigger (HLT).

The L0 trigger

The L0 is a hardware trigger that uses the information from the calorimeters and from the muon system. The trigger is fully synchronous with the 40 MHz bunch crossing rate of LHC and was designed to reduce the rate to 1 MHz, the maximum rate imposed by front-end electronics. This includes 6 algorithms, or "lines": L0Hadron, L0Photon, L0Electron, L0Muon, L0MuonHighPt and L0Dimuon. These lines select events by transverse energy (E_T)¹ requirements.

The L0Hadron, L0Photon and L0Electron select clusters from calorimeters with minimum E_T requirement. The L0Hadron selects clusters at HCAL with minimum $E_T^{hadron} > 3.5$ GeV, while L0Photon and L0Electron select clusters from ECAL+SPD/PS with minimum E_T requirement $E_T^{e,\gamma,\pi^0} > 2.5$ GeV.

The L0Muon, L0MuonHighPt and L0Dimuon select events based on hits in the Muon system. These lines select muon candidates with $p_T^\mu > 1.2$ GeV or $p_T^{\mu_1} + p_T^{\mu_2} > 1.0$ GeV (L0Dimuon), μ_1 and μ_2 are the highest p_T muon in the event. The L0MuonHighPt is similar to L0Muon with just a higher requirement on the muon p_T .

The total number of SPD cells with a hit is determined to provide a measure of the charged track multiplicity in the crossing. The events with high multiplicity are excluded to speed up event reconstruction performance. This Global Event Cut (GEC) was used by each Run 1 L0-trigger line. In Run 2, some of the lines lose the GEC requirements, as L0DiMuon, and others abolish this requirement, as the L0MuonHighPt.

The L0 selects an event if at least one cluster in the calorimeters or a muon

¹ $E_T = \sum_i E_i \sin\theta_i$. E_i is the energy of each cell in the cluster, and θ_i is the angle between the z-axis and a line connecting the cell and the LHCb origin

candidate passes through the requirement: L0Hadron or L0Photon or L0Electron or L0Muon or L0Dimuon. This requirement is also used to tune the L0 bandwidth division. In Run 2, the bandwidth division was tuned via an automated procedure that optimized signal efficiencies using various interesting decay channels.

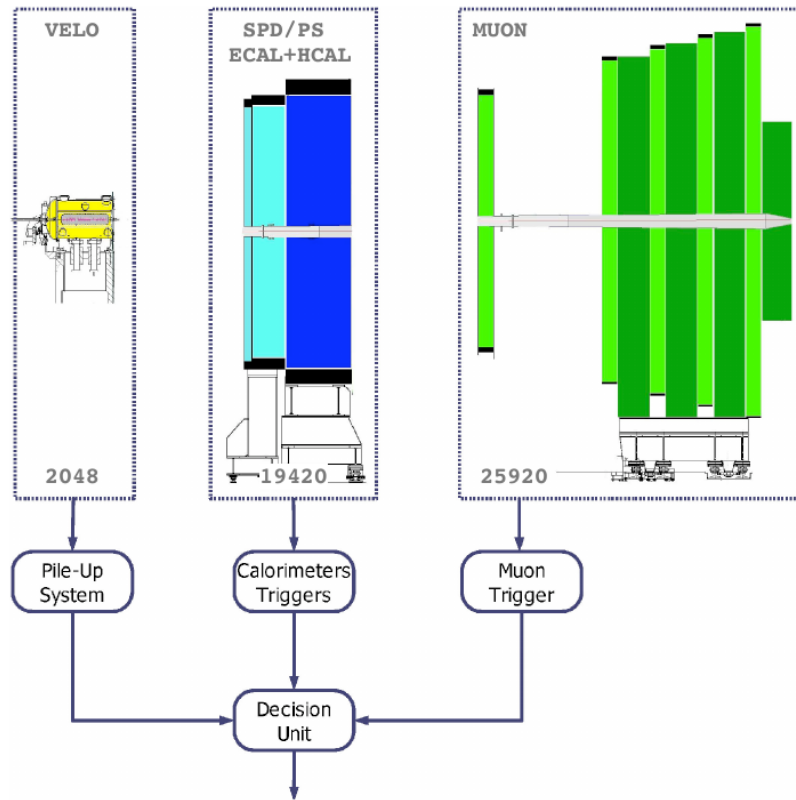


Figure 19 – Overview of the Level-0 trigger. Source [6].

The LHCb tracks

Tracks are reconstructed using the information VELO and the T-stations hits to form the particle trajectory from the VELO to the calorimeters. The reconstruction starts by searching seed tracks on the VELO and the T stations. The seed tracks are fitted with a Kalman fitter[57] to find their trajectories. The quality of the reconstruction is monitored by the χ^2 provided by the fitting algorithm. The χ^2 can be used to reject fake tracks. The successfully reconstructed tracks must have at least 70% of their associated hits originating from a single Monte Carlo particle and a small χ^2 .

The LHCb tracks are classified according to their trajectories inside the detector. Figure 20 shows the various track types.

- **Long tracks** cross the full tracking detectors from VELO to the T-stations. They have the best momentum resolution and are the most important for b-hadron decay reconstruction.
- **Upstream tracks** cross only the VELO and T-stations. These are generally lower momentum tracks that are bent out of the detector acceptance by the magnetic field. Although their momentum resolution is rather poor, they are used to understand backgrounds in the RICH particle identification algorithm, b-hadron decay reconstruction and flavour tagging.
- **Downstream tracks** cross only the TT and T stations. These are often the products of long-lived hadron decays, such as K_s^0 and Λ decays.
- **VELO tracks** are tracks measured in the VELO. They are useful for the primary vertex reconstruction.
- **T tracks** cross only the T stations. They are typically produced in secondary interactions and are useful for global pattern recognition in RICH2.

The High-Level Trigger

The high-level trigger (HLT) is a C++ software which runs on every CPU of the Event Filter Farm (EFF), which consists of up to 2000 computing nodes. The HLT accesses all L0-triggered event data² and executes the offline selection algorithms. The goal is to reduce the rate up to 5 kHz. The HLT is subdivided into two stages, HLT1 and HLT2.

HLT1 performs the partial reconstruction of the tracks using a part of the output L0 trigger data. The reconstruction is performed by confirming the L0 trigger decision by adding information from the VELO and T-stations, and by applying cuts on the p_T and

² Referred as Level-0 objects henceforward

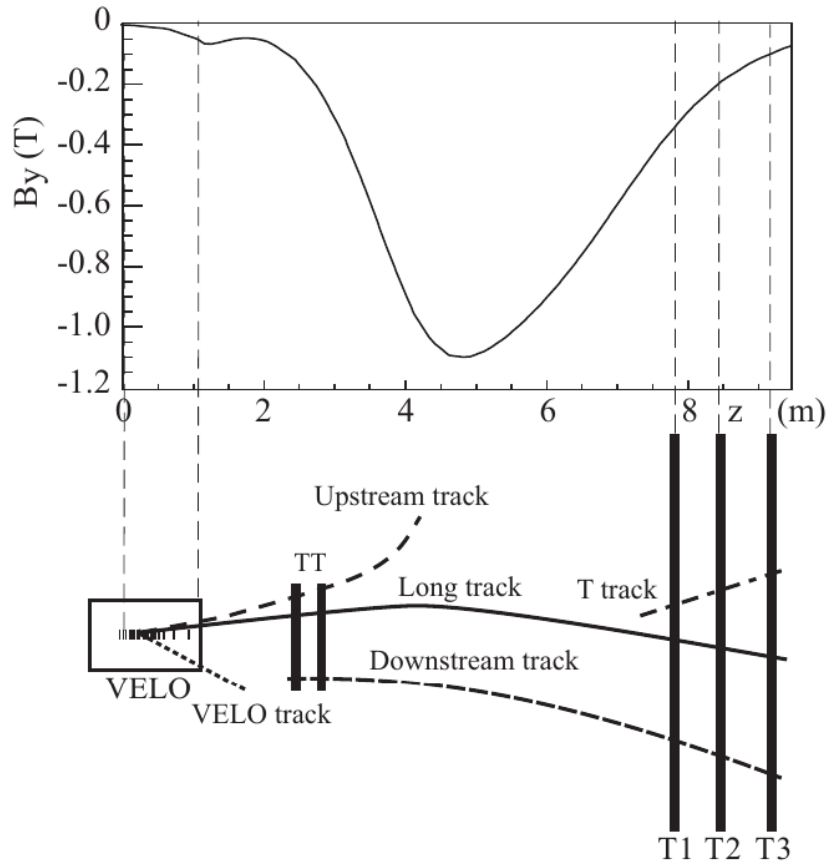


Figure 20 – A schematic illustration of the various track types: long, upstream, downstream, VELO and T tracks. For reference, the main B-field component (B_y) is plotted above as a function of the z coordinate. Source [6].

the impact parameter (IP) concerning the primary vertex. The confirmation is performed by several HLT1 algorithms called alleys. For some alleys, an inclusive selection of particles apart from the Level-0 candidate is performed to better discriminate between B-decay products and backgrounds. Examples of inclusive selections are $B^+ \rightarrow J/\Psi(\rightarrow \mu^- \mu^+) K^+$ and $B^0 \rightarrow D^0 \pi$. The HLT output tracks trajectories are determined by the Kalman Fitter, and a cut on χ^2 is applied to reject ghost tracks. At the end of HLT1, the rate is reduced from 1 MHz to tens of kHz.

HLT2 performs the full reconstruction of all tracks. It starts selecting a set of tracks with loose selection on their momentum $p_T > 300$ MeV and IP. These tracks are used to form composite particles, like $D^0 \rightarrow hh, h = \pi, K$ and $J/\Psi \rightarrow \mu^- \mu^+$. Two types of final selection are applied: the inclusive and the exclusive. Inclusive selection collects decays of resonances that are likely to have been produced through B decays, like the D^* used for particle identification calibration and J/Ψ from $B_s \rightarrow J/\Psi \phi$ decay. The exclusive selection collects specific B and D decay channels using full reconstruction, mass and vertex information. Examples of exclusive decay channels are the $D^0 \rightarrow K^- \pi^+$ and the $B^0 \rightarrow \pi^- \pi^+$. After HLT2, the rate is reduced to 5 kHz.

During Run 1, the HLT was designed to operate only during the time when the LHC was delivering stable beams, which occurred approximately 30% of the time. During the periods without stable beams, the HLT remained idle. The calibration information could not be computed to feed HLT2 during the same data-taking (known as a run), since the trigger could not wait for the computation. To address this issue, towards the end of Run 1, roughly 25% of the L0-passed events began to be buffered to local disks to be processed by HLT later. As a result, there was a 25% improvement in the HLT process rate.

In Run 2, this idea was further developed. The collaboration improved the performance of HLT reconstruction after an effort to improve the HLT software, called Moore. Additional computational resources were allocated to the experiment, and a 10 PB buffer was inserted between HLT1 and HLT2. The data processed by L0 passed to be stored into a storage disk in the online system. Fractions of HLT1 data passed to be separated for alignment and calibration of subdetectors, allowing to feed HLT2 with the latest calibration and alignment information computed in *quasi* real-time. These changes made the online reconstruction quality as good as offline, allowing the HLT2 output candidates to be analysed in real time without any further offline reconstruction. To take advantage of this upgrade, the HLT2 lines were split into two separate streams: FULL and TURBO. The difference between the two is the number of objects (tracks or detector responses) that are saved for each event. The TURBO stream only saves objects forming part of the decay used to evaluate the trigger line selection, while the FULL stream saves all event objects. The FULL stream data usually passes by further selection. Figure 21 shows the triggers of Run 1 and Run 2. The reference [58] details the Run 2 trigger. There weren't relevant changes in the detector's layout between Run 1 and Run 2.

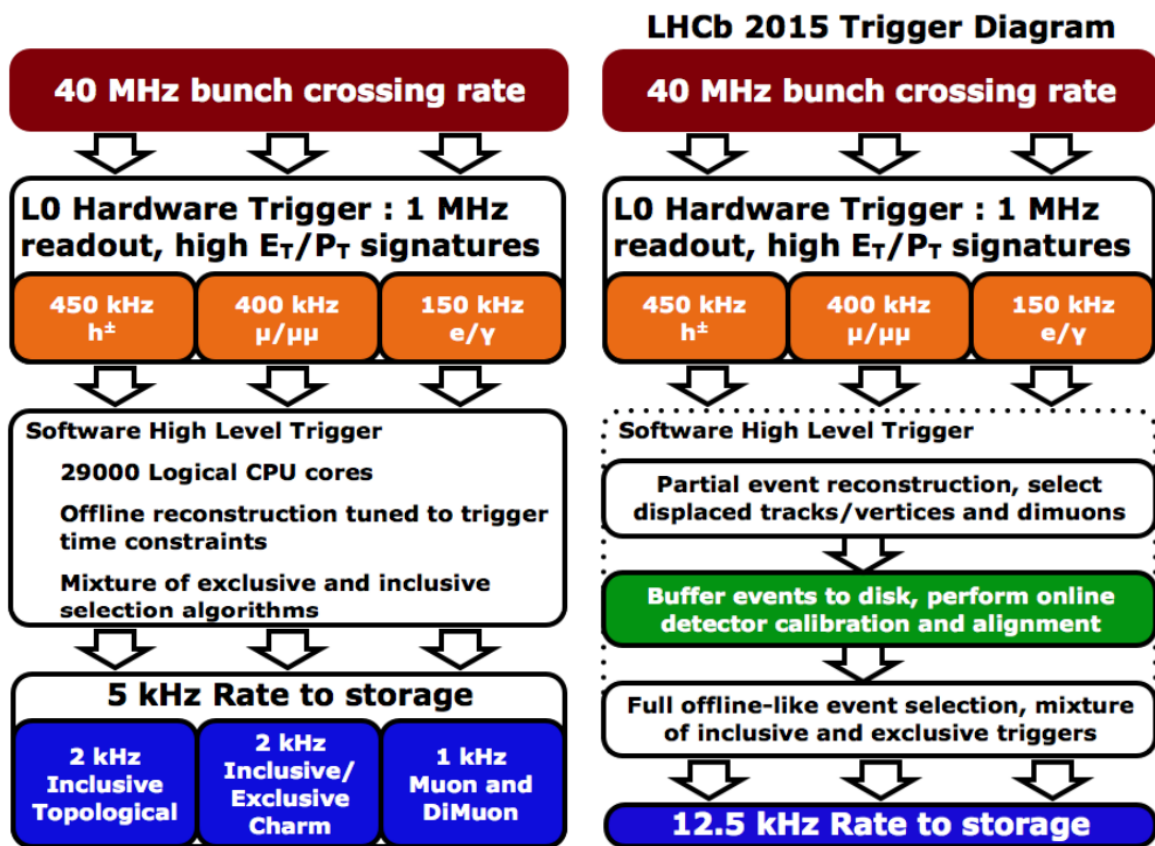


Figure 21 – The LHCb trigger schemes for Run 1 (left) and Run 2 (right)

4 LHCb detector upgrade

The LHCb detector performed excellently during Run 1 (2010-2012) and Run 2 (2015-2018), exceeding the expectations in some results. During these two runs, the detector mainly operated at an integrated luminosity of $\sim 4 \times 10^{32} \text{cm}^{-2} \text{s}^{-1}$, while it was designed to operate at an integrated luminosity of $2 \times 10^{32} \text{cm}^{-2} \text{s}^{-1}$, hence indicating the possibility of the detector to operate at higher luminosity and pile-up. It also demonstrated excellent capabilities in many other domains ranging from electroweak physics to heavy ion and fixed target physics, while it was primarily designed to search for new sources of CP-violation in heavy-flavour hadron decays. This indicates the possibility of becoming a more general propose detector.

A proposal for a major upgrade to operate LHCb at substantially larger instantaneous luminosity than Run 1-2 was formalised in a Letter of Intent [59] and detailed in a Framework TDR [60]. The physics motivations for this upgrade have been discussed in ref. [61], assuming an expected total luminosity of $\sim 50 \text{fb}^{-1}$ integrated by the end of LHC Run 4. The LHCb detector is currently operating with an instantaneous luminosity of $2 \times 10^{33} \text{cm}^{-2} \text{s}^{-1}$, collecting events at the LHC crossing rate of 30 MHz, and increasing the pile-up up to 6 pp collisions per bunch crossing.

Figure 22 shows the layout of the new LHCb detector. The upgraded detector received a new tracking system and an updated particle identification system. The new tracking system incorporates a new silicon-pixel vertex locator, a new silicon-strip tracker upstream (UT) of the dipole magnet that replaced the Tracker Turicensis, and a scintillating-fibre tracker downstream of the dipole magnet that replaced the T-stations. The Cherenkov detectors' photon detection system was upgraded using multianode photomultiplier tubes. Additionally, the calorimeters and muon detector electronics underwent a redesign and update.

In order to keep up with the high rate of events generated by the LHC at 40 MHz, a new trigger system has been implemented. This system is made up of an innovative all-software trigger that runs on GPUs and a specialized computing farm. Additionally, a completely revamped online system has also been installed. The previous L0 trigger was replaced with the new system because its simple criteria and output rate could not handle the increased luminosity and would cause the event yield to saturate, as demonstrated in figure 23.

The LHCb detector design changes are highlighted in this section. For a detailed description of the upgrade, please refer to [11].

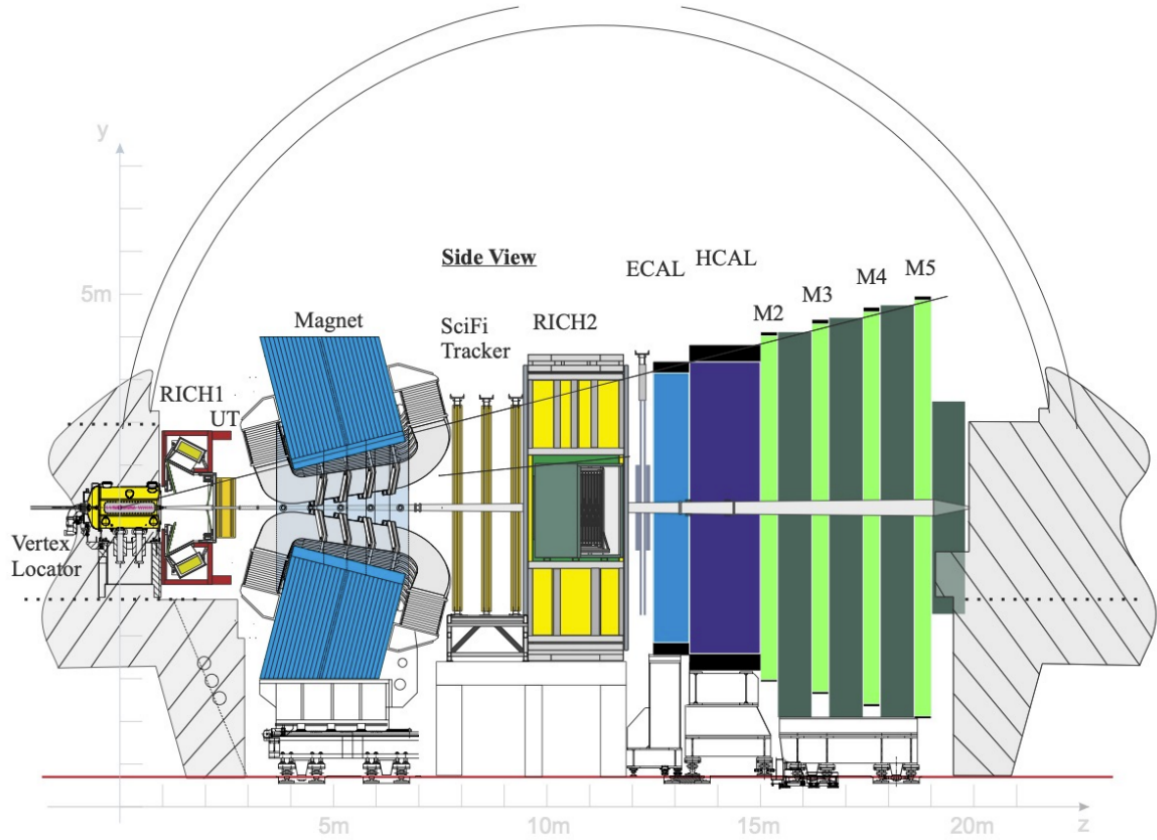
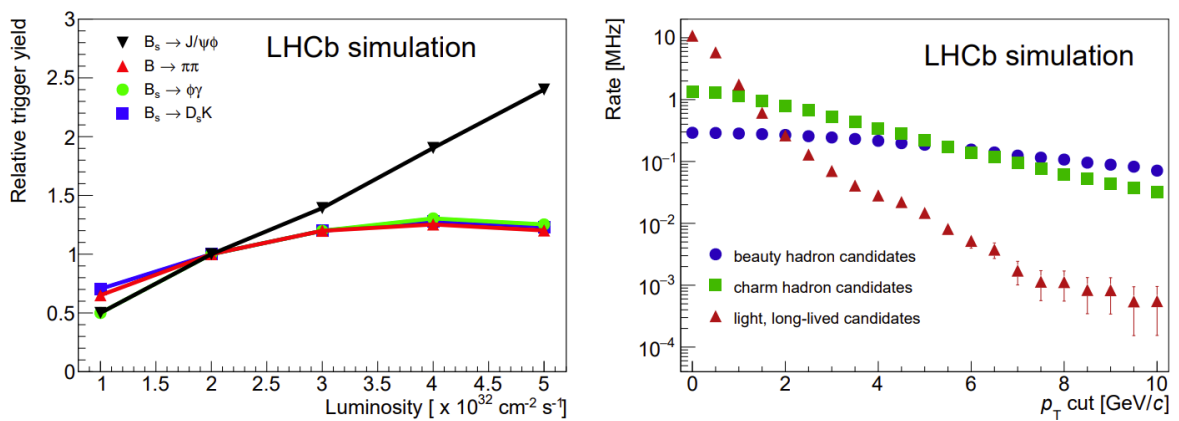


Figure 22 – Layout of the upgraded LHCb detector. Source [11].

Figure 23 – Left: relative trigger yields as a function of instantaneous luminosity, normalised to $2 \times 10^{32} \text{ cm}^{-2} \text{ s}^{-1}$. Right: rate of decays reconstructed in the LHCb acceptance as a function of the cut in p_T of the decaying particle, for decay time $\tau > 0.2 \text{ ps}$. Source [11].

4.0.1 The tracking system

The new Vertex Locator

The Vertex Locator has been redesigned to be compatible with the LHC's rate of 40 MHz [62]. The new VELO modules are made up of pixelated hybrid silicon detectors known as VELO pixel chips (VeloPix) [63]. The VeloPix tile is made up of a pixelated, planar silicon sensor and three pixelated ASIC chips. The tiles have an active matrix of 256×256 , with each sensor measuring $55\mu\text{m} \times 55\mu\text{m}$, giving a sensitive area of 1.98 cm^2 . The modules are composed of four identical tiles arranged perpendicular to the beam line. These modules cover the LHCb acceptance and ensure that most tracks from the interaction region traverse at least four pixel sensors in all ϕ directions. The arrangement is shown in Figure 24.

The upgraded VELO design was optimized to achieve performance at least equal to that predecessor, in terms of both σ_{IP} [64] and track-finding efficiency, despite the increased instantaneous luminosity.

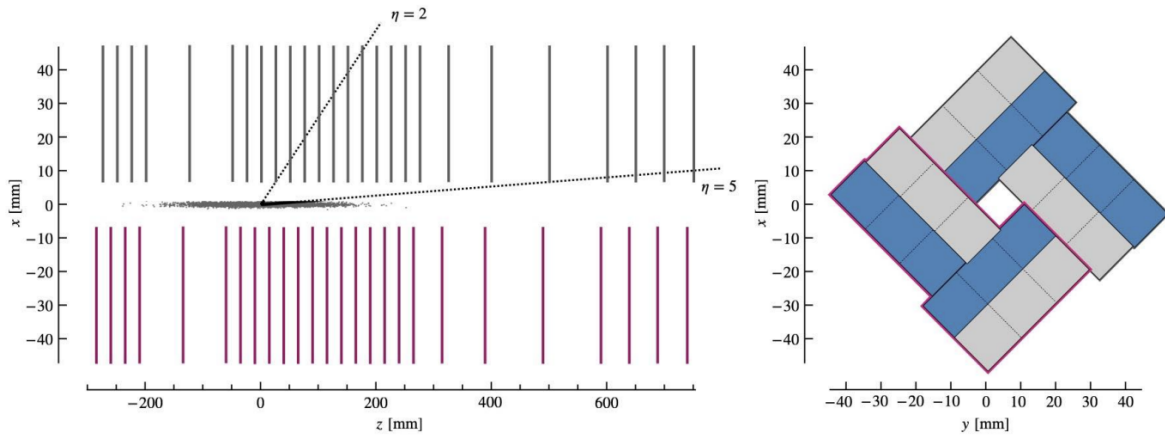


Figure 24 – Left: schematic top view of the z-x plane at $y=0$ (left) with an illustration of the z-extent of the luminous region and the nominal LHCb pseudorapidity acceptance, $2 < \eta < 5$. Right: sketch showing the nominal layout of the ASICs around the z-axis in the closed VELO configuration. Half the ASICs are placed on the upstream module face (grey) and half on the downstream face (blue). The modules on Side C are highlighted in purple on both sketches. Source [11].

The Upstream Tracker

The Upstream Tracker (UT) [65] replaced the Tracker Turicensis in the upstream region of the dipole. As the predecessor, the UT is used for charged-particle tracking, first momentum determination, and, in companion with VELO, is used by the first level trigger (HLT1).

The UT geometry and arrangement of its four planes of silicon detectors are similar to its predecessor, see figure 25. The layers are divided into three regions, each with a

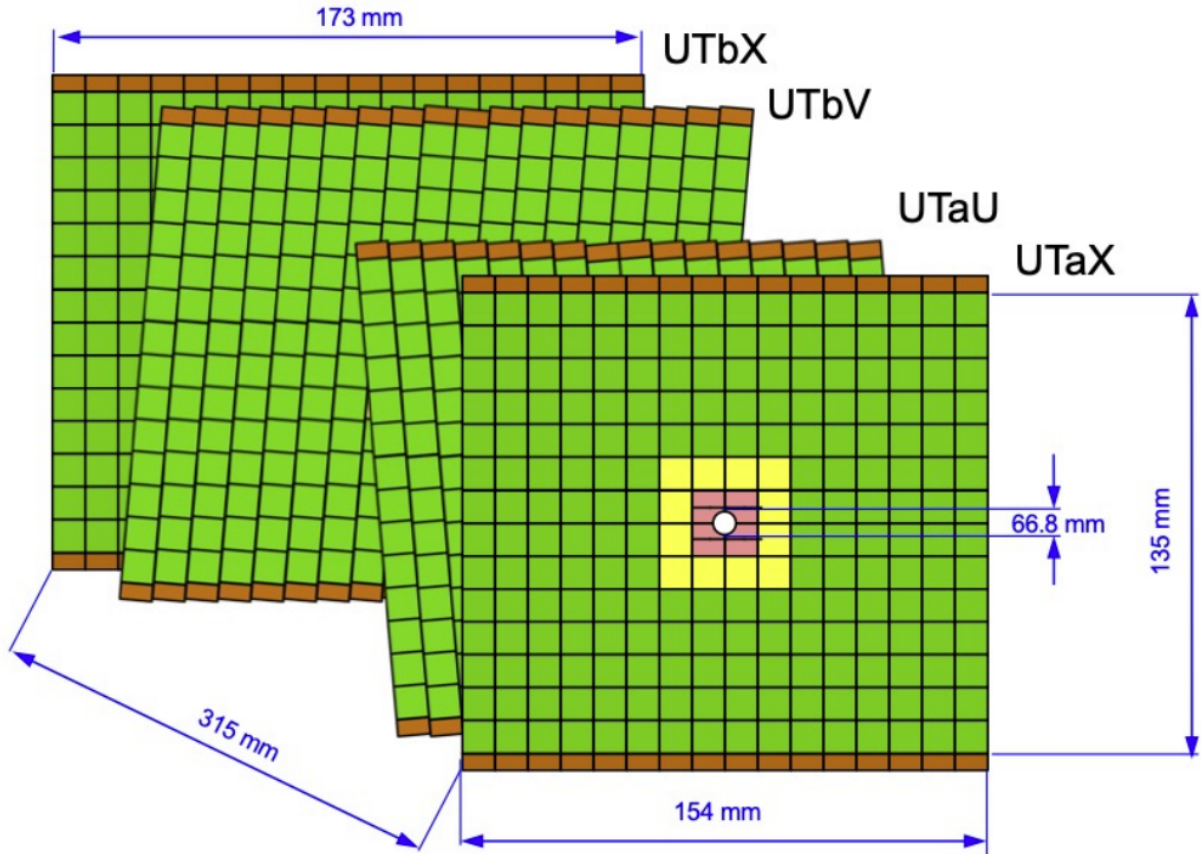


Figure 25 – Drawing of the four UT silicon planes with indicative dimensions. Different colours designate different types of sensors: Type-A (green), Type-B (yellow), Type-C and Type-D (pink), as described in the text. Source [11].

different type of sensor: Type-A, Type-B, Type-C and Type-D. Most of the detector's outer region is covered by Type-A sensors, which consist of 512 strips with a pitch of $187.5 \mu\text{m}$. All other sensor designs have 1024 with a twice smaller pitch of $93.5 \mu\text{m}$. The Type-B sensors are located in the inner region at approximately 10 cm from the beam pipe. The innermost area is covered by Type-C and Type-D sensors, which have shorter lengths than the other types. The different thickness is justified to ensure sufficiently high signal-to-noise ratios.

The Scintillating fibre tracker

The Scintillating fibre tracker (SciFi) [65] is the new tracking detector located downstream of the dipole magnet and replaced the T-stations (T1-T3). It was designed to provide a momentum resolution and track efficiency for b - and c -hadrons of the same quality (or better) as the ones obtained in Run 1 and Run 2.

The SciFi acceptance ranges from 20 mm from the edge of the beam pipe to distances of ± 3186 mm and ± 2425 mm in the horizontal and vertical directions. The detector consists of 12 detection planes arranged in 3 stations (T1, T2, T3) with four

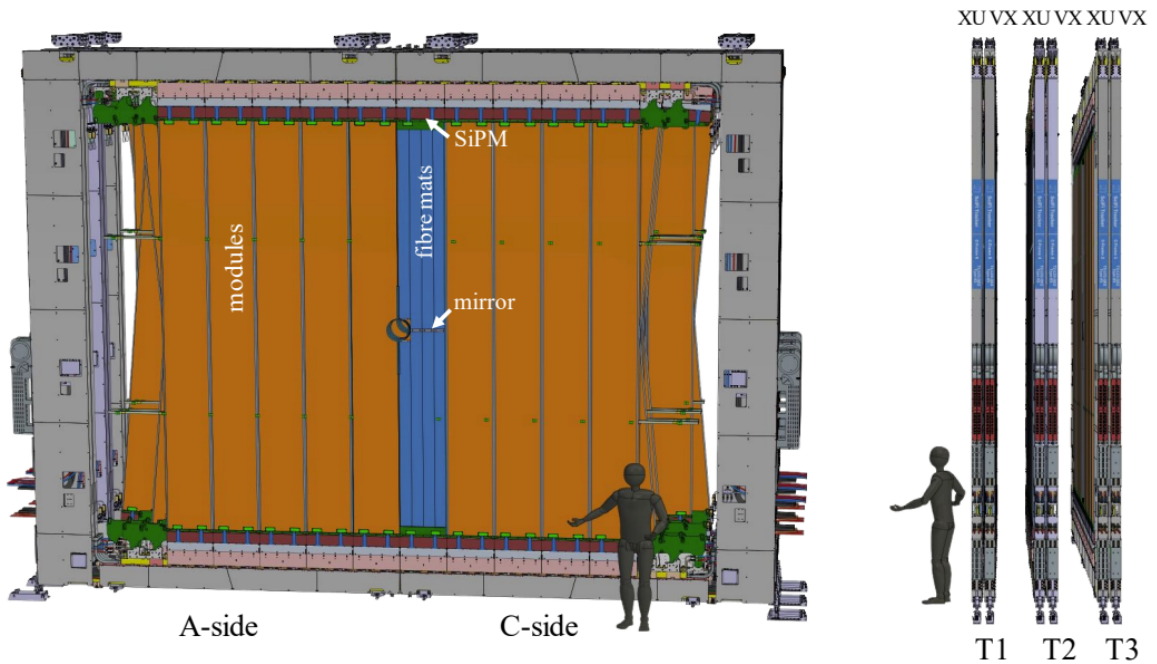


Figure 26 – Front and side views of the 3D model of the SciFi Tracker detector. Source [11].

layers arranged in an $x-u-v-x$ configuration, the same as T-stations. The layers technology is based on $250\ \mu\text{m}$ scintillating fibres. The x -layers have their fibres oriented vertically and are used to determine the charged particle deflection due to the magnet. It is essential to measure the momentum. The $u-v$ -layers have their fibres vertically oriented but rotated by $\pm 5^\circ$ and determine the vertical position of the track. When a charged particle traverses the scintillating fibres, it produces an optical signal detected by Silicon Photomultipliers (SiPM) placed on top of each SciFi module, see figure 26.

4.0.2 The particle identification system

The overall layout and concept of the RICH system and calorimeters remain mostly unchanged concerning Run 1-2 LHCb and are skipped in this section, details can be found in Refs. [12].

The Muon System

The Muon system upgrade was designed to ensure reliable muon identification while minimizing the misidentification of other particles, even at the new LHCb nominal luminosity. The detector layout of Run 1 and Run 2, introduced in Chapter 3, already meets (even exceeds) the specification imposed by the TDR. The existing front-end readout electronics also operate at a 40 MHz rate since it was designed to provide information to the removed L0 trigger.

The main changes in the Muon system are in the off-detector readout electronics

and shielding. The old off-detector readout electronics provide full hit information (position and time) at a limited rate of 1 MHz. It was necessary to redesign it to be compatible with the 40 MHz rate and the new GBT-based communication protocol. The new LHCb conditions are expected to increase the particle flux in the innermost regions of station M2. Station M1 was removed, and additional shielding was installed in front of station M2 around the beam pipe.

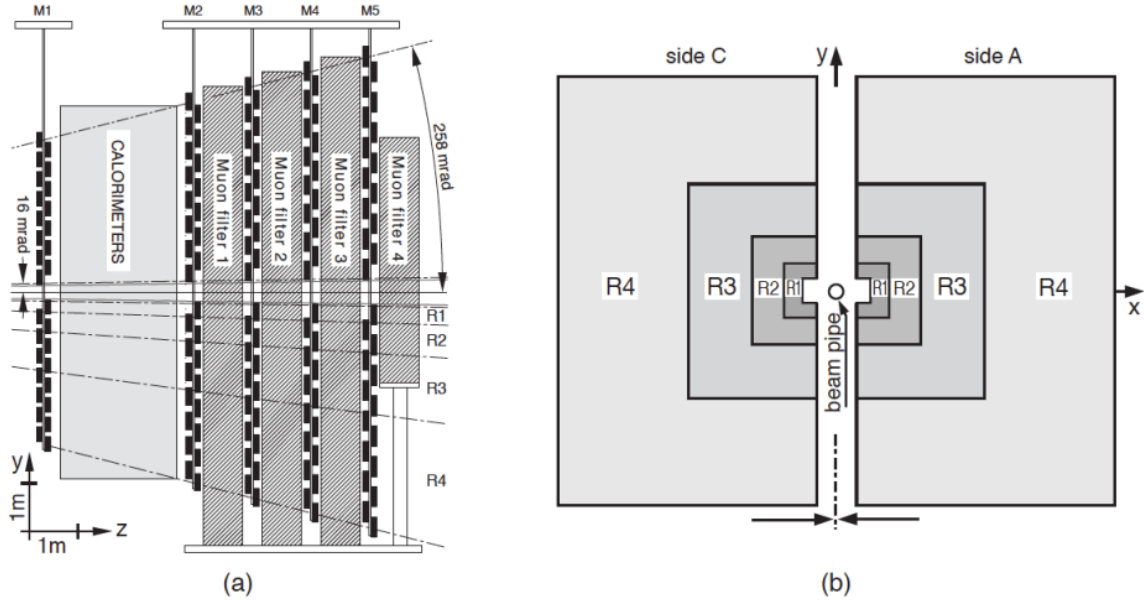


Figure 27 – (Left) Side view of the LHCb Muon Detector. (Right) Station layout with the four regions R1-R4 indicated. Source [12].

4.0.3 The Trigger system

The new trigger system was designed to run in the new conditions of the LHCb experiment. This means that all detectors readout and the HLT1 have to be able to work at 30 MHz, the operation rate. Due to this requirement, the L0 trigger was removed since its output rate is limited to 1 MHz. The new readout system is composed of the event builder, the Timing and Fast Control (TFC) distribution, the Experiment Control System (ECS) and Event Filter Farm (EFF). This system can handle a collision rate of 30 MHz.

The new trigger system is all about online reconstruction, calibration and selection. The bunch crossing fragments received by the data acquisition (DAQ) system feed the HLT1 that performs the partial reconstruction of the events in real-time. The events are grouped into packets and stored on the disk by the online system. About 6% of the events are separated for calibration, 26% for the FULL stream, and 68% for the TURBO stream. It makes the TURBO stream the natural choice for almost all Run 3 analyses. The HLT2 runs over the collected data on demand to perform the final reconstruction and selection. Figure 28 illustrates the Run 3 dataflow.

The HLT1 of Run 3 was completely redesigned. As the HLT1 tasks are inherently parallelizable, the LHCb developed a brand-new software trigger based on GPUs called Allen [66, 67]. The Allen software was written in CUDA, an NVidia language, and modern C++. It was designed to be used within the LHCb framework or standalone, which allows local development. The decision to use GPUs was based on cost and performance. About 500 GPUs are required to process the full HLT1 sequence at the desired rate. These GPUs were installed on EFF servers.

The HLT2 Run 3 philosophy is kind of the same. A good improvement was archived making the code better, which required a significant effort from the developers. It also changed the old event model to a new vectorized one, which contributed to the speed-up of the selection and paralelization.

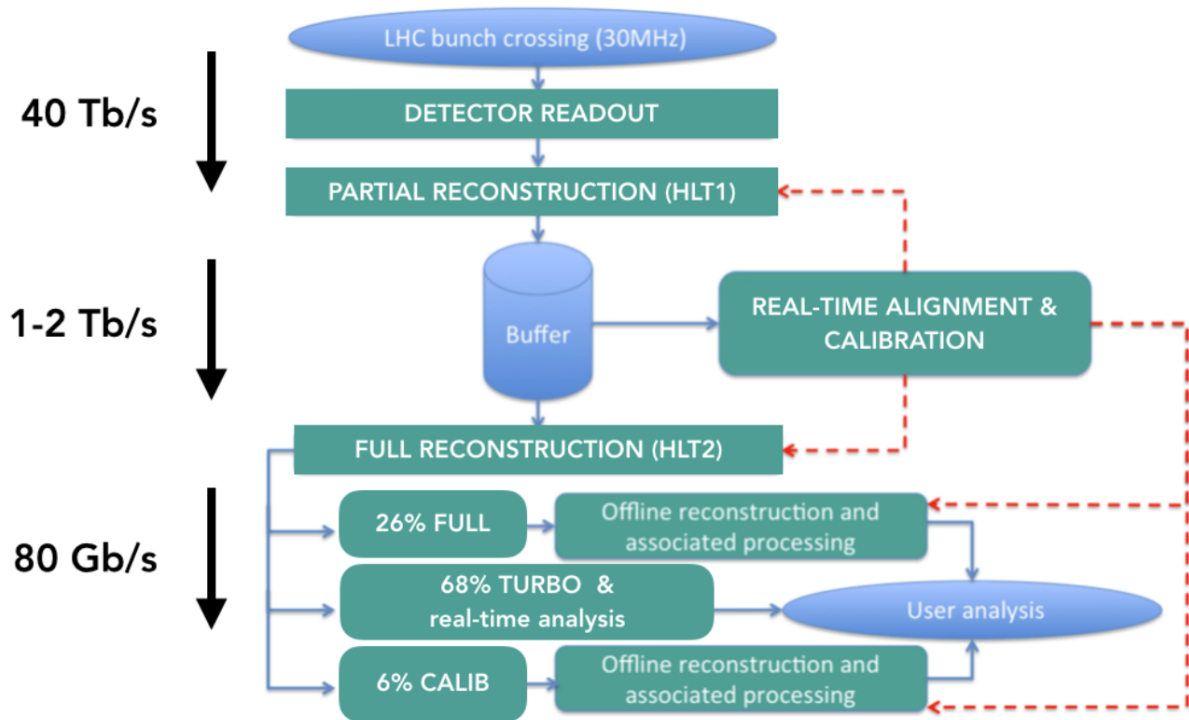


Figure 28 – Dataflow in the upgraded LHCb detector. Source [13].

5 Amplitude analysis of the $D_s^+ \rightarrow \pi^- \pi^+ \pi^+$ decay

In this work, the Dalitz plot analysis of the $D_s^+ \rightarrow \pi^- \pi^+ \pi^+$ decay is performed¹, based on 1.5 fb^{-1} of pp collision data at 8 TeV centre-of-mass energy, collected by the LHCb experiment in 2012. The primary purposes are to determine the resonant structure and to obtain the $\pi^+ \pi^-$ amplitude in S-wave through a quasi-model-independent partial wave analysis (QMIPWA), in which the S-wave is parameterised as a generic complex function to be determined by a fit to the data.

5.1 Statistical treatment of data and simulation samples

In this section, you will find a detailed explanation of the statistical treatment of the data and simulation samples. It starts with an introduction to the data and simulation samples, followed by a brief overview of the particle identification efficiency. The selection process is then described in detail in a sequential manner.

Data and simulation samples

An initial data sample with ~ 50 million $D_s^+ \rightarrow \pi^- \pi^+ \pi^+$ events was selected for the analysis. The selected candidates passed for further selections to increase the ratio of Signal/Background (S/B).

Full simulation (or LHCb simulation) produced through Monte Carlo (MC) techniques of the $D_s^+ \rightarrow \pi^- \pi^+ \pi^+$ decay is used in this analysis mainly to guide the selection criteria and to determine the efficiency variation across the Dalitz plot. A simulation sample with 5 million candidates was generated with constant matrix element, i.e. phase space decay, following the criteria summarized in Table 3 and passing through the same steps of the data selection, except for the particle identification (PID) requirements. To avoid contamination from b -hadron decays and ensure that the efficiencies computed from the simulation samples are well defined, the samples are filtered to retain only events that contain a promptly produced signal decay $D_s^+ \rightarrow \pi^- \pi^+ \pi^+$. This is requested by selecting events in the background category 0 or 50 [68]. The background categories give information about how a candidate was (mis)constructed. Category 0 selects events identified as signals with all intermediate states correctly reconstructed. Category 50 selects events that all final-state particles used to form the D_s^+ candidate are correctly

¹ Charge conjugation is implicit throughout this paper, unless otherwise stated.

identified, but their masses don't exceed the D_s^+ mass. The latter is used to simulate a Low-mass background.

Table 3 – Generation criteria for large MC samples.

Variable	Value
D candidate p_T	$> 2100 \text{ MeV}/c$
D candidate p	$> 14000 \text{ MeV}/c$
each daughter p	$> 2000 \text{ MeV}/c$
each daughter p_T	$> 250 \text{ MeV}/c$

Particle identification efficiency

The particle identification efficiency (PID eff.) is determined from data calibration samples. Decays that can be reconstructed without particle identification, such as the $D^{*+} \rightarrow D^0(\rightarrow K^- \pi^+) \pi^+$ chain, are used to determine the efficiency as a function of momentum and pseudorapidity for each decay product. The PID eff. is computed using the PIDCalib tool [69]. The latter divides the calibration sample into bins of the particle momentum and pseudorapidity and the track multiplicity of the event. The default PIDCalib binning produces the efficiency tables corresponding to the PID requirement determined during the selection studies. The efficiency of individual tracks in the simulation sample is determined on an event-by-event basis, regardless of the L0 trigger category (the underlying assumption is that the PID efficiency is not correlated with the trigger). The PID efficiency of the candidate is then obtained by multiplying the efficiencies of the decay products.

Data selection

In Dalitz plot analyses, it is convenient to work with high-purity samples, minimizing the impact of uncertainties in the background modelling, particularly when there are peaking structures or when the background is different across of invariant mass distribution.

The data selection process is split into two steps: pre-selection and selection. The former reconstructs and selects $D_s^+ \rightarrow \pi^- \pi^+ \pi^+$ candidates from the proton-proton interactions by applying trigger conditions - only candidates that pass all trigger criteria go to the next step. The latter is performed locally and imposes additional criteria to the former selected data to increase the purity, i.e. the ratio of signal yield over the total yield (S+B), without causing significant variations in the detection efficiency across the phase space - It is verified using the simulation. At this step, corrections are applied to the simulation to describe the efficiency accurately.

Pre-selection

The pre-selection includes requirements on all trigger levels: L0, HLT1 and HLT2. In addition to the trigger requirements, a last pre-selection called Stripping is applied, accounting for the signal efficiency, timing and retention. The requirements of the Stripping line are shown in Table 6.

L0: All first-level trigger (L0 or HLT) events can be split into two categories: TIS (Trigger Independent of Signal) and TOS (Trigger On Signal). The former is induced by one or more pions from the D_s^+ decay products or other activity in the event, and the latter selects the events if the particle belonging to the signal candidate is present. We found that the TOS trigger causes significant distortions in the efficiency map. The only TOS candidates represent approximately one-third of the total sample. The gain in statistics by including TOS candidates would come with increased systematic uncertainties. Hence, the analysis is restricted to TIS candidates. To avoid variations in the L0 thresholds, we analysed data collected after the July technical stop (runNumber>119956), for which the trigger settings were stable. Despite these restrictions, the $D_s^+ \rightarrow \pi^- \pi^+ \pi^+$ sample still contains several million candidates.

HLT1: It checks if at least one of the D_s^+ decay products was selected by the L0 trigger lines and includes the selection requirements summarized in Table 4.

HLT2: The output candidates of HLT1 are fully reconstructed by a dedicated HLT2 line that selects $D^\pm \rightarrow h^\mp h^\pm h^\pm$ ($h = \pi, K$) candidates. The requirements for the latter are summarized in Table 5 and demand candidates be selected by one of the existing HLT1 lines.

The data files with the candidates selected in pre-selection are saved locally. In the following section, I detail the local selection.

Table 4 – HLT1 trigger line requirements

Cuts	Value
Track IP χ^2	> 16
Track p_T	$> 1.6 \text{ GeV}/c$
Track p	$> 3 \text{ GeV}/c$
Track χ^2/ndf	< 2
Track IP	$> 0.1 \text{ mm}$
Number of VELO hits/Track	> 9
Number of missed VELO hits/Track	< 3
Number of OT + IT hits/Track	> 16
Number of VELO hits	< 6000
Number of IT hits	> 3000
Number of OT hits	< 15000
LO_Decision_Physics	

Table 5 – Selection criteria used in the dedicated HLT2 Dhhh trigger line

	Cuts	Value
Global Event Cut	N. Long Tracks	< 180
	Track χ^2/ndf	< 3
final state	p_T (MeV/c)	> 300
particles	p (MeV/c)	> 3000
	IP χ^2	> 6
hhh	Σp_T (MeV/c)	> 2800
combination	min DOCA (mm)	< 0.08
	FD χ^2	> 175
D_s^\pm	Vertex χ^2/ndf	< 15
	IP χ^2	< 12
	Mass (MeV/c ²)	1800-2040
	TOS in any Hlt1Track Line	

Selection

In this section, the different sources of background are introduced along with the application of the PID, the simulation correction, and the multivariate analysis (MVA). The section concludes with the verification of the selected data sample.

Particle identification and background

The PID system has limited discrimination power for particles with momentum above 100 GeV. Fiducial cuts, summarized in Table 7, are included in the momenta and pseudorapidity of the decay products to match the limits of the PIDCalib efficiency tables.

Mild PID requirements are made to select the $D_s^+ \rightarrow \pi^- \pi^+ \pi^+$ candidates in the

Table 6 – Stripping line for $D_{(s)}^+$ decays to three hadrons.

Variable	Selection requirement
Final state particles	
p_T	$> 250 \text{ MeV}/c$
p	$> 2000 \text{ MeV}/c$
$\sum p_T$	$> 2800 \text{ MeV}/c$
DOCA max	$< 0.5 \text{ mm}$
track IP χ^2	> 6
IP χ^2 on 2 daughters	> 10
$\Delta \log \mathcal{L}_{K\pi}$	< 5 for all tracks
Combination cuts	
$D (p_T)$	$> 1000 \text{ MeV}/c$
D Vertex χ^2	< 30
DIRA	> 0.98
D IP χ^2	< 12
D FD χ^2	> 125
Mass	$1800 \text{ MeV}/c^2 < m_D < 2040 \text{ MeV}/c^2$
Global Event Cut	
Number of tracks	< 500

Table 7 – Fiducial requirements on the p and η of the decay products, as defined in the PIDCalib package.

Variable	Cuts
Track η	$1.5 < \text{and} < 5.0$
Track p	$3 < \text{and} < 100 \text{ GeV}/c$

stripping. More stringent requirements are necessary to control the background from other charm hadron decays with a $K - \pi$, $p - \pi$, and $\mu - \pi$ misidentification (misID). We usually call this type of background cross-feed. The contamination due to a $K - \pi$ or $p - \pi$ misID is controlled with the requirement $\text{PIDK} < -2$ applied to all decay products. The cross-feed includes the decays $D^0 \rightarrow K^- \pi^+$ (either prompt D^0 plus a random pion or D^0 from D^{*+}), $\Lambda_c^+ \rightarrow p \pi^+ \pi^-$ and $D_s^+ \rightarrow K^- \pi^+ \pi^+$.

There is an important irreducible background from the $D_s^+ \rightarrow \eta' \pi^+$, $\eta' \rightarrow \pi^+ \pi^- \gamma$ decay which cannot be eliminated via PID requirements since it forms a genuine three-pion vertex. This background appears only to the left of the D_s^+ signal due to the unreconstructed photon. It is the one that will be reduced using the MVA technique.

The decay chain $D^{*+} \rightarrow D^0 (\rightarrow \pi^+ \pi^-) \pi^+$ also forms a genuine three-pion final state, peaking at the right place: the D^{*+} mass. It is eliminated by demanding $m(\pi^+ \pi^-) < 1.84 \text{ GeV}$, with 100% efficiency for the D_s^+ signal.

Semi-leptonic decays with muons in the final state, such as $D_s^+ \rightarrow \pi^+ \pi^- \mu^+ \nu_\mu$, are controlled by requiring a muon veto for the two identical pions

After including the stringent PID requirement, the invariant-mass distribution of selected candidates is shown in Fig. 29.

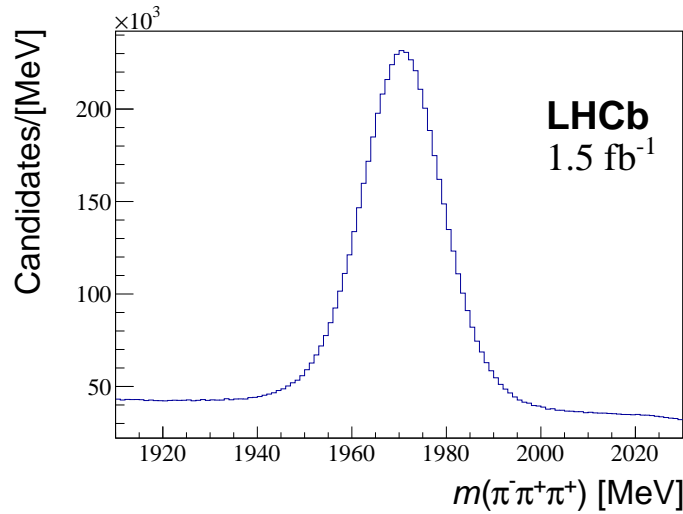


Figure 29 – Invariant mass distribution of selected $D_s^+ \rightarrow \pi^- \pi^+ \pi^+$ candidates after PID.

The data sample is ready to proceed to the MVA, but the simulation sample needs further steps. The following section outlines the necessary simulation corrections for MVA and to calculate efficiency.

Simulation corrections

The simulation samples are necessary for mainly two purposes: to guide the selection criteria - as a proxy for the signal at the MVA - and to determine the efficiency variation across the Dalitz plot. For both uses, the kinematics of the selected simulated decays must match that of the data. The simulated sample should also replicate the resonant structure of the signal and the track multiplicity in the event.

The corrections to the simulation are detailed in the following order:

Track multiplicity The track multiplicity is challenging to model theoretically. Consequently, the simulated distribution of this variable is expected to disagree with the one in the data sample. A correction is created by computing event-by-event weights ($w_{nTracks}$) and then included in the simulation sample.

The $w_{nTracks}$ weights are calculated using the track multiplicity binned distribution of the selected data weighted by the sWeights for signal, introduced in the sPlot section in Chapter 2, and the same variable distribution from simulation. The ratio of data and simulation distributions is computed to assign a correction weight to each simulation event.

Resonant structure The simulation sample generated for the analysis has constant decay amplitude, which means no dynamics are considered in the simulation process.

To include the dynamics, an event-by-event weight (w_{res}) is calculated and included in the simulation sample.

The w_{res} weights are calculated using the Dalitz plot binned distribution of the selected data (after PID) weighted by the sWeights for signal and the binned distribution of the simulation Dalitz plot corrected by the PID efficiency and by new track multiplicity weight ($w_{PID} \times w_{nTracks}$). The ratio of data and simulation Dalitz plot is computed, and it is used to assign to each event a correction weight.

Kinematics The kinematics of the simulated decays must match that of the data to be a reliable proxy for the signal at the MVA step and correctly describe the efficiency over the Dalitz plot. It is also archived by producing an event-to-event weighting.

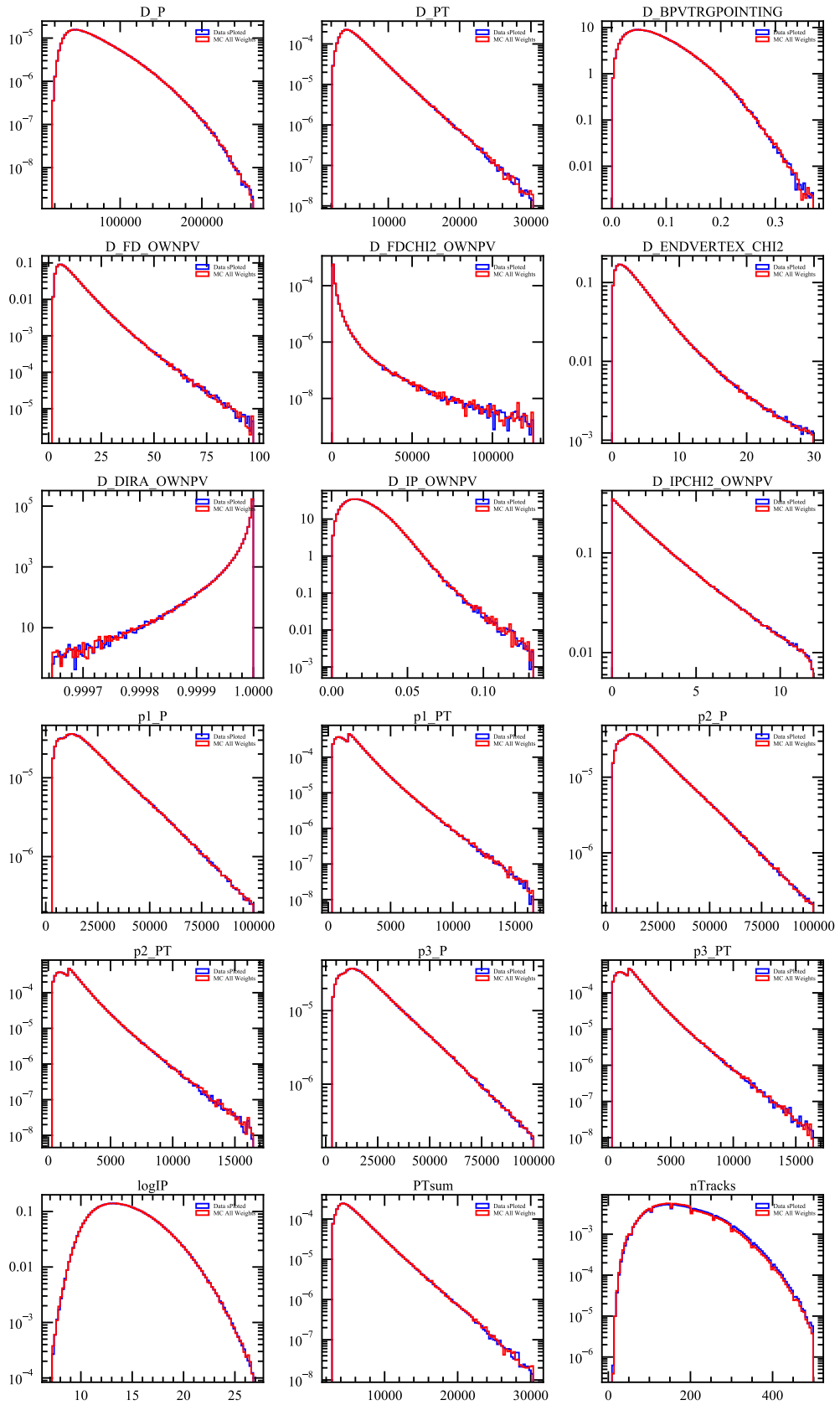
To obtain the weights necessary to match the data and simulation kinematic distributions, the GB-Reweighter introduced in Chapter 2 was used. The input for the algorithm are:

Original distributions the simulation weighted by PID efficiency, track multiplicity correction and the dynamical weight.

Target distributions selected data weighted by sWeights for signal

The weights that match the simulation (original) and signal from data (target) distributions are predicted by the algorithm after training and included in the simulation sample. Fig. 30 shows the kinematics and tracks multiplicity distributions after all corrections.

The correction weights above are necessary for the next step, the MVA. Due to our limited size simulation sample, after re-reweighting, the effective statistics of the simulation sample will be less than the data, which would increase the systematic uncertainties. The latter is estimated in the systematics uncertainties analysis.

Figure 30 – Kinematics and track multiplicity distributions for $D_s^+ \rightarrow \pi^- \pi^+ \pi^+$ after all corrections

MVA selection

The MVA, introduced in Chapter 2, aims at reducing the combinatorial background. Dalitz plot fits of high-purity samples are subject to minor uncertainties related to the background parameterization. This is particularly important in cases where the background composition is not uniform across the mass spectrum.

In this analysis, the target purity is 95% within $2\sigma_{eff}$ mass window, which is determined by fitting the invariant mass $m(\pi^- \pi^+ \pi^+)$ after run MVA. As we will see, a slight increase in purity implies a significant loss in efficiency.

To feed the BDTG algorithm for the training, the simulated sample with all corrections was used as a proxy for the signal. The signal events were selected in the range of invariant mass spectrum [1952, 1988] MeV. Events from sidebands were used as a proxy for the background. The sideband regions are between the ranges [1920, 1940] MeV and [2000, 2020] MeV.

The variables used in the training process were chosen based on their discriminant power. Variables related to the D-meson reconstruction are preferred to avoid distortions across the Dalitz plot. The variables and a comparison between their distributions for signal and background are shown in figure 69 in the appendix A.

The algorithm was trained to learn how to distinguish the two categories of events: signal and background. The training was performed using a cross-validation approach. In this approach, the signal and background proxy data are split into $N = 2$ samples (Fold_1 and Fold_2) and given as input for two independent BDTG classifiers. Each classifier is trained and then used to predict the probabilities of the events belonging to the signal and background categories. The probabilities are combined into a new variable, the valBDTG. The valBDTG variables, valBDTG_1 and valBDTG_2, are merged by taking their event-by-event mean. A positive cut at valBDTG_mean (e.g. valBDT > 0.2) rejects a certain amount of the combinatorial background, and the new yields are determined by performing invariant mass fits. The two different valBDTG variables for simulation and data, and their means are shown in figure 73 in the appendix A.

The BDTG hyperparameters used during the training step and the integral of ROC-curve (AUC - Area Under the Curve), which is a metric used to evaluate the performance of the model (the closest to unity the best), are illustrated in Table 8.

Over-fitting was verified by the Kolmogorov-Smirnov test (KS-test). The KS-test compares the classifier distribution predicted by the BDTG model when using the training or independent test samples. The distributions must be compatible. An additional test compares the classifier distribution of the corrected simulation and Data sPloted, revealing only the signal component, to see if the simulation models this variable well. The distributions must also be identical. The plots are in the Appendix A.

Table 8 – TMVA hyperparameters and AUC metric values.

Condition	BDTG
NTrees	850
MinNodeSize	2.5%
MaxDepth	3
BoostType	Grad
Shrinkage	0.1
UseBaggedBoost	true
BaggedSampleFraction	0.5
SeparationType	GiniIndex
nCuts	20
VarTransform	none
AUC for Fold1(2)	0.803(0.803)

To determine the optimal cut value for our classifier variable, we evaluated the yields through invariant mass fits for different valBDT_mean values. The variation of the purity and significance as a function of valBDT_mean is shown in Fig. 31. As mentioned before, the desired purity for this analysis is 95%. We found that it is achieved by the cut valBDTG_mean > 0.65. The mass spectrum before and after the classifier cut is shown in Figure 32.

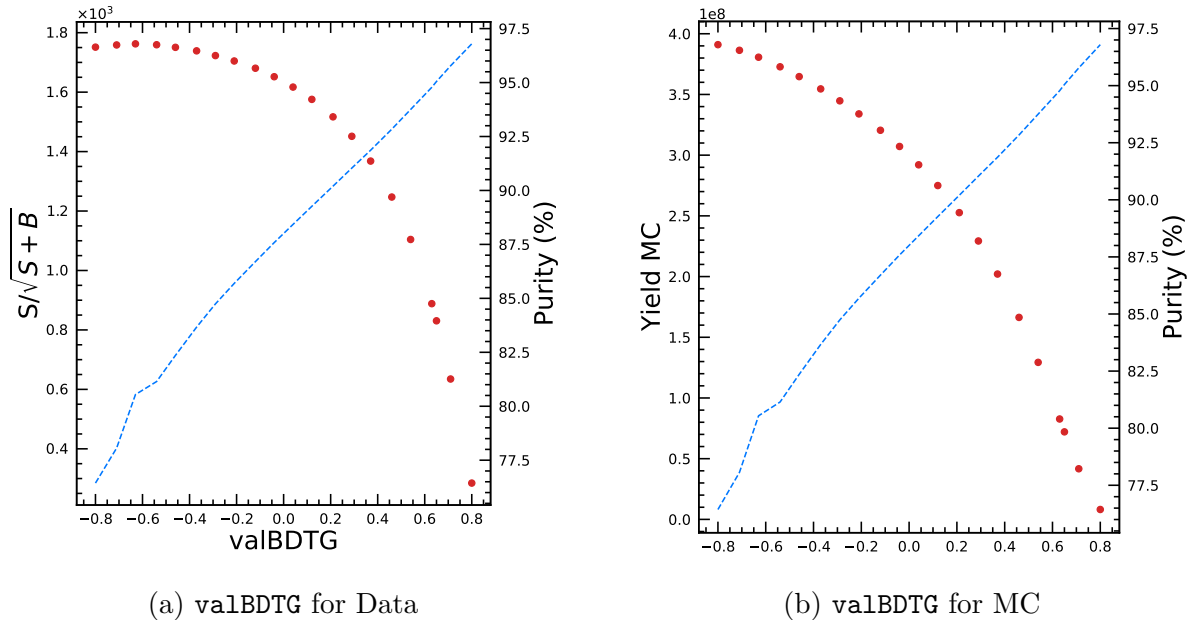


Figure 31 – (a) The variation of the purity (blue, dashed curve) and significance ($S/\sqrt{S+B}$) (red, dotted line) according to the cut applied on the valBDTG_mean variable. (b) The Yield MC (red, dotted line) is the number of events that pass the BDTG cut, and will be used to build the efficiency. The dashed blue curve is a copy of (a).

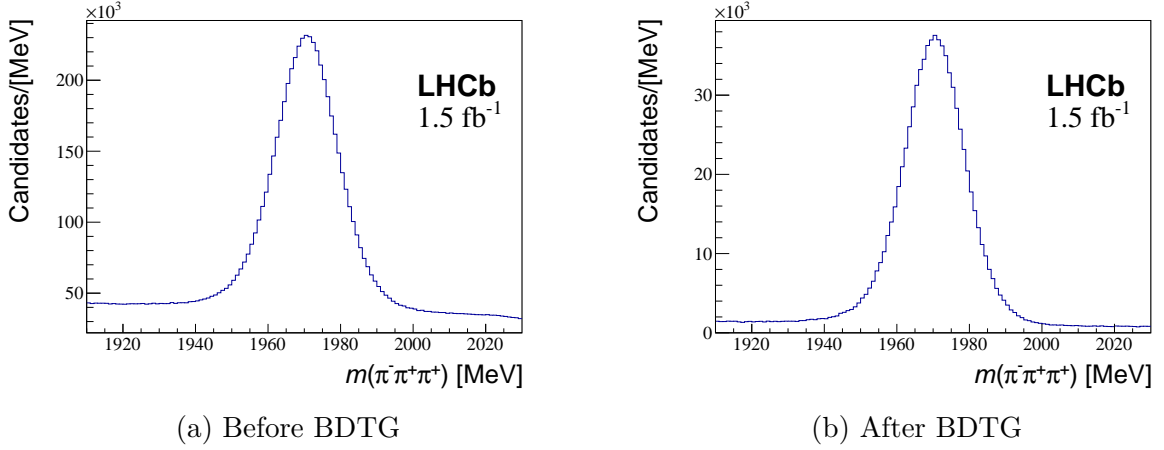


Figure 32 – Invariant mass distribution of $D_s^+ \rightarrow \pi^- \pi^+ \pi^+$ candidates before (left) and after (right) the BDTG requirement is applied.

After applying the MVA selection, the momentum asymmetries were plotted to check whether any specific background contribution may still be present. The momentum asymmetry for each final state particle k , with companion particles i and j is defined as:

$$p_{k,\text{asym}} = \frac{|p_i| + |p_j| - |p_k|}{|p_i| + |p_j| + |p_k|}. \quad (5.1)$$

By plotting the D -candidate mass versus the momentum asymmetry, any specific background will appear as a visible region/band. Fig. 33 shows the momentum asymmetries for the three particles after the BDTG cut.

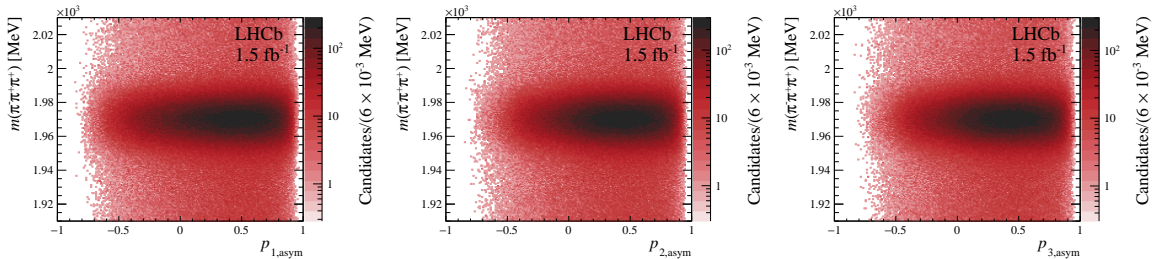


Figure 33 – Momentum asymmetry plots for $D_s^+ \rightarrow \pi^- \pi^+ \pi^+$ candidates after the BDTG requirement.

As an additional check, the invariant masses of the selected candidates were recomputed with different mass hypotheses. In particular, charm background that could enter the $\pi^- \pi^+ \pi^+$ sample through a $K^- \pi$ or $p - \pi$ misID. The most important contamination comes from the $D^0 \rightarrow K^- \pi^+$ decay that forms a three-prong vertex with an unrelated pion. A prominent peak can be seen before the MVA selection and PID requirements, as shown in Fig. 34. The $D^0 \rightarrow K^- \pi^+$ signal is used as a proxy for the $K^- \pi$ misID. Decays of heavier states, such as $\Lambda_c \rightarrow \pi^- \pi^+ p$, or $\Lambda_c \rightarrow K^- \pi^+ p$ could also be present in the $\pi^- \pi^+ \pi^+$ sample. The former is a Cabibbo-suppressed decay, but involves only one particle misID, whereas the latter is Cabibbo favoured, but involves a double misD. The mass plots in

Fig. 34 demonstrate that the MVA and PID requirements control the contamination of other charm decays.

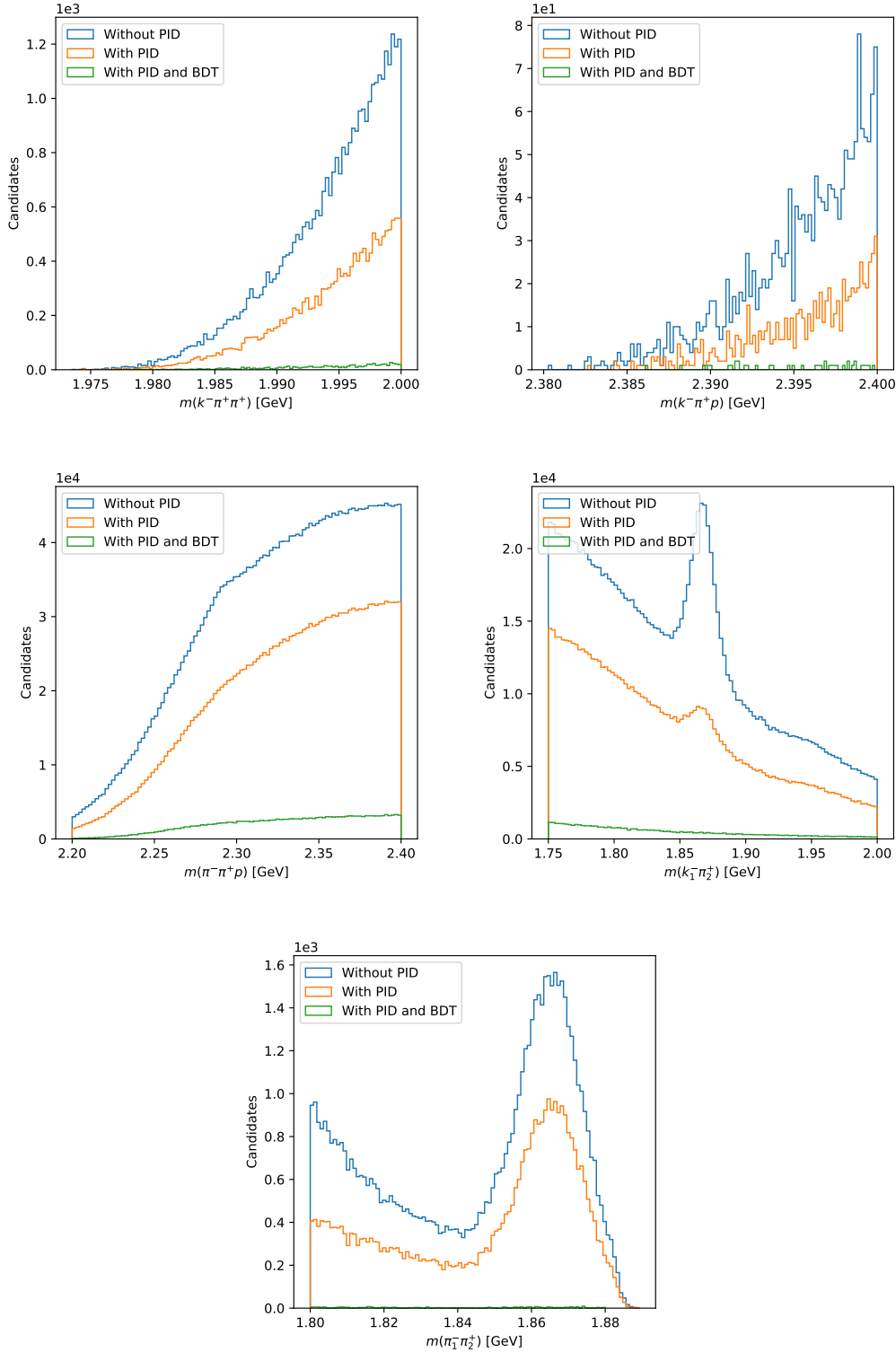


Figure 34 – Invariant masses of $\pi^- \pi^+ \pi^+$ candidates computed with different mass hypotheses.

Finally, the presence of clone tracks was investigated. Two tracks are considered clones of each other if they share at least 70% of the hits in the VELO and at least 70%

of the hits in the T-stations seeding region. The same approach as in the $D^+ \rightarrow K^- K^+ K^+$ analysis [70] was used, that is, to use the track slopes in the XZ and YZ planes and compute the difference for each pair of tracks:

$$\text{diffTX}_{ij} = \left| \frac{p_{x_i}}{p_{z_i}} - \frac{p_{x_j}}{p_{z_j}} \right|. \quad (5.2)$$

Clone tracks have very similar slopes in xz and xy planes. The distribution of the slope difference should be peaked at shallow values. The resulting distributions are shown in Fig. 35. The conclusion was that the BDT requirement controls the small fraction of clone tracks in the pre-selected sample: clones are of no concern.

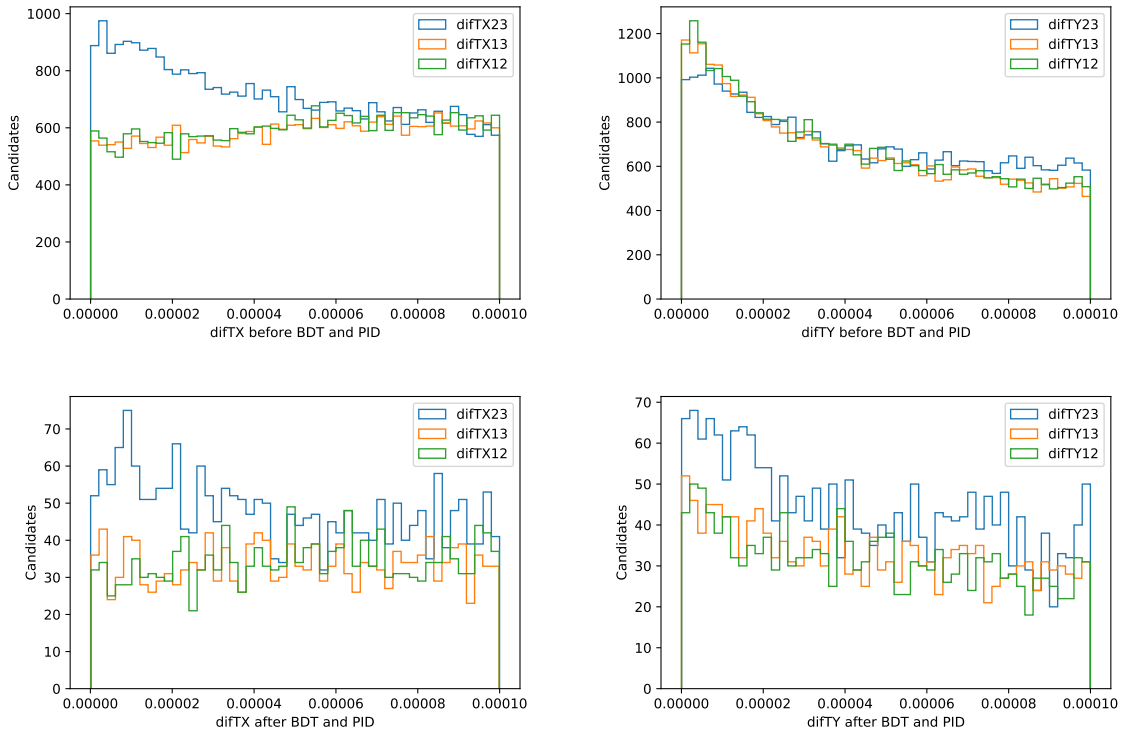


Figure 35 – Difference between the slopes in XZ(left) and YZ(right) planes, before(up) and after(down) the BDT requirement, for all combinations of two tracks.

In the following section, the results of the invariant mass fit in the selected sample are presented, along with an initial examination of the candidates used in the rest of the analysis. Additionally, the efficiency and background maps are introduced, which are the final components required for the Dalitz plot model.

5.2 Invariant mass fit and analysis sample

The $\pi^- \pi^+ \pi^+$ invariant mass spectrum was fitted to determine the signal and background yields. The fit was also used to define the signal region for the Dalitz plot fit. The mass fit was performed using *Roofit* [41].

The signal probability density function (PDF) is composed of one Crystal Ball [71] (Gaussian core with a power law tail), accounting for the left exponential tail of the signal shape, plus one Gaussian. The Crystal Ball (CB) function is parameterised by its mean μ , width σ , power of the tail n , and α that indicates a distortion from a Gaussian function. The definition of the Crystal-Ball function is as follows:

$$CB(m|\alpha, n, \mu, \sigma) = N \begin{cases} \exp\left(-\frac{(m-\mu)^2}{2\sigma^2}\right) & \text{for } \frac{(m-\mu)}{\sigma} > -\alpha \\ A \left(B - \frac{(m-\mu)}{\sigma}\right)^{-n} & \text{for } \frac{(m-\mu)}{\sigma} \leq -\alpha, \end{cases} \quad (5.3)$$

where $m \equiv (\pi^- \pi^+ \pi^+)$ and

$$\begin{aligned} A &= \left(\frac{n}{|\alpha|}\right)^n \exp\left(-\frac{|\alpha|^2}{2}\right), \\ B &= \frac{n}{|\alpha|} - |\alpha|, \\ C &= \frac{n}{|\alpha|} \frac{1}{n-1} \exp\left(-\frac{|\alpha|^2}{2}\right), \\ D &= \sqrt{\frac{\pi}{2}} \left(1 + \operatorname{erf}\left(\frac{|\alpha|}{\sqrt{2}}\right)\right), \\ N &= \frac{1}{\sigma(C+D)}. \end{aligned} \quad (5.4)$$

The expressions relate the mean(width) of the CB and the Gaussian:

$$\mu_G = \mu_{CB} + \mu_{offset} \quad (5.5)$$

$$\sigma_G = \sigma_{CB} * \sigma_{Ratio} \quad (5.6)$$

The total signal PDF expression is:

$$\mathcal{P}_s(m) = f_{CB} CB(m) + (1 - f_{CB}) G(m). \quad (5.7)$$

where f_{CB} is the relative fraction of the CB function. In the signal PDF, α , n , μ , σ , μ_{offset} , σ_{Ratio} and the fraction f_{CB} are free parameters.

The PDF for the background is an exponential function given by

$$\mathcal{P}_{bkg}(m) = \exp[\lambda m] \quad (5.8)$$

where λ is a free parameter. Two additional parameters \mathcal{N}_s and \mathcal{N}_{bkg} are included for the yields, then the total PDF is given by²:

$$\mathcal{P} = \mathcal{N}_s \mathcal{P}_{sig} + \mathcal{N}_{bkg} \mathcal{P}_{bkg}, \quad (5.9)$$

The plot for the data mass fit is shown in Fig. 36 and Table 9 summarises the fit result.

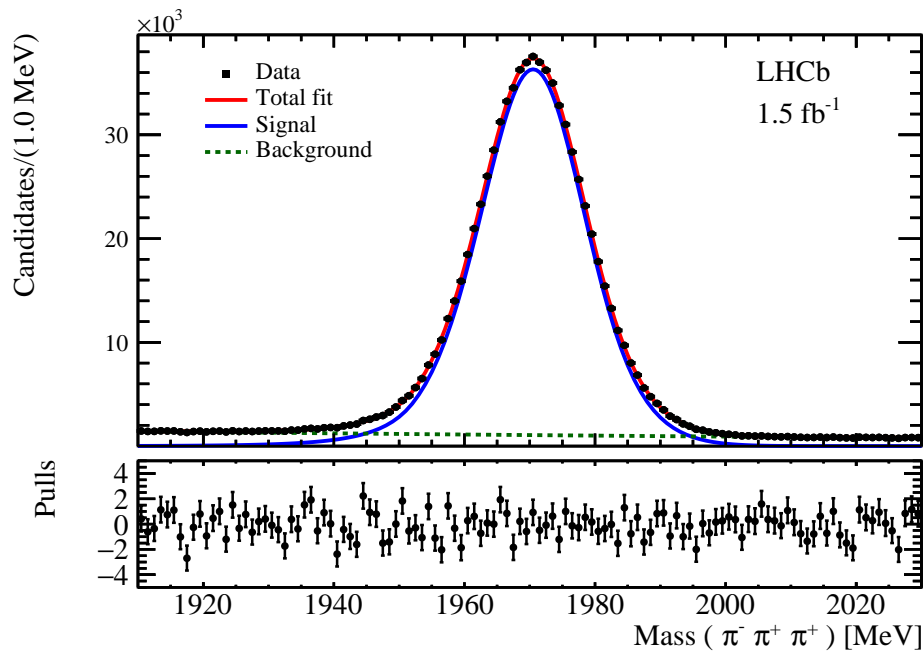


Figure 36 – Invariant mass distribution of the $D_s^+ \rightarrow \pi^- \pi^+ \pi^+$ candidates after final selection, with the fit result superimposed.

² \mathcal{P}_{sig} and \mathcal{P}_{bkg} are normalised to unity within the mass range of the fit

Table 9 – Mass fit results for the $D_s^+ \rightarrow \pi^- \pi^+ \pi^+$ sample

Parameter	Value
α	1.681 ± 0.025
n	11 ± 1
μ (MeV/ c^2)	1969.78 ± 0.07
σ (MeV/ c^2)	10.39 ± 0.14
μ_{offset} (MeV/ c^2)	0.98 ± 0.08
σ_{Ratio} (MeV/ c^2)	0.6666 ± 0.0038
f_{CB}	0.52 ± 0.03
\mathcal{N}_s	771130 ± 1058
\mathcal{N}_{bkg}	129288 ± 691

The Dalitz Plot analysis was performed with candidates in the range $\mu \pm 2\sigma_{eff}$, where the “effective width” σ_{eff} is defined as

$$\sigma_{eff} = \sqrt{f_{CB}\sigma_{CB}^2 + (1 - f_{CB})\sigma_G^2} = 8.9 \text{ MeV}/c^2. \quad (5.10)$$

The signal region corresponds to the interval [1952.4, 1988.0] MeV, where the integrated yields are 725959 ± 995 for signal and 37816 ± 202 for background candidates, with 95% purity. In the same invariant mass interval, there are 329225 MC events, after the entire selection is applied (including the same MVA cut applied on data).

Dalitz plot of selected data

The Dalitz plot of the events within the signal region is defined in terms of the two invariants $s_{12} \equiv m^2(\pi^- \pi^+ \pi^+)$ and $s_{13} \equiv m^2(\pi^- \pi^+ \pi^+)$. The momenta of the decay products are constrained so that the value of the invariant mass of the $\pi^- \pi^+ \pi^+$ combination is always equal to the known D_s^+ mass. The mass constraint is applied using `DecayTreeFitter` algorithm [72].

The mass constraint implies a single, well-defined Dalitz plot boundary. The resulting Dalitz plot of the selected candidates within the signal region is shown in Fig. 37.

The Dalitz plot exhibits a complex resonant structure. There is a clear signature of the $f_0(980)$, the most prominent structure. There is also an indication of at least one more scalar resonance at $m_{\pi^+\pi^-}^2 \sim 2.2 \text{ GeV}^2$, which interferes with the $f_0(980)$. This structure can be attributed to the $f_0(1370)/f_0(1500)$. An enlarged view of this region of the Dalitz plot is shown in Fig. 38. It is interesting to notice that the pattern observed at the crossing of this state with the $f_0(980)$ band resembles that of two interfering scalar resonances with the relative phase of π .

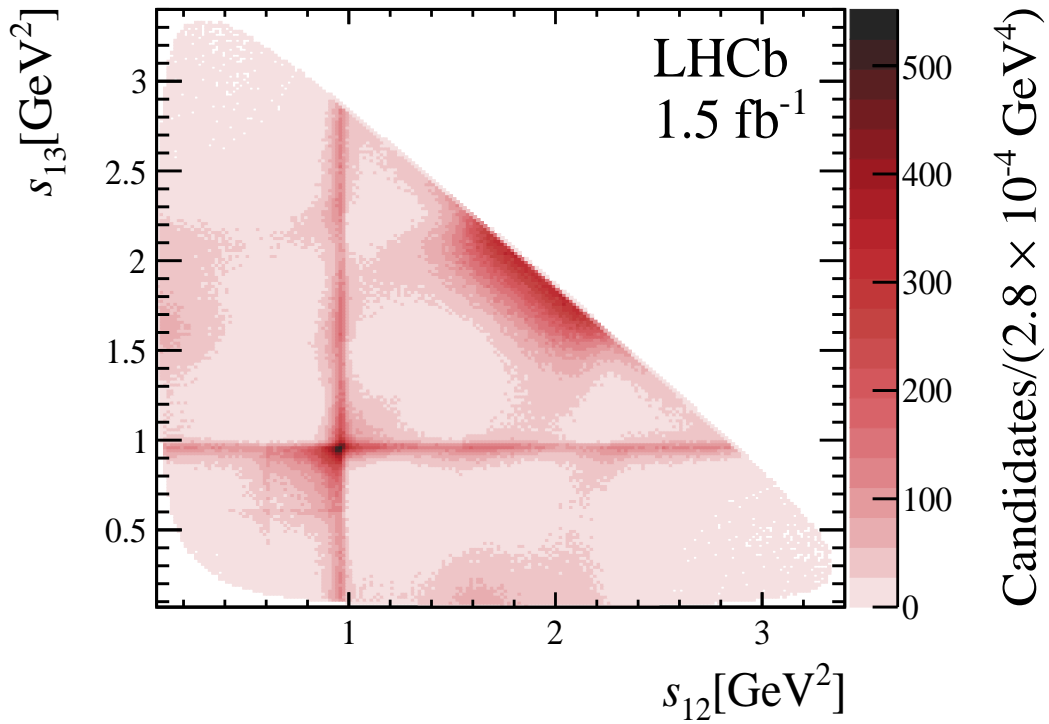


Figure 37 – Symmetrized Dalitz plot of the full sample after all selection criteria, within the $\pi^- \pi^+ \pi^+$ mass interval of [1952.,1988.] MeV.

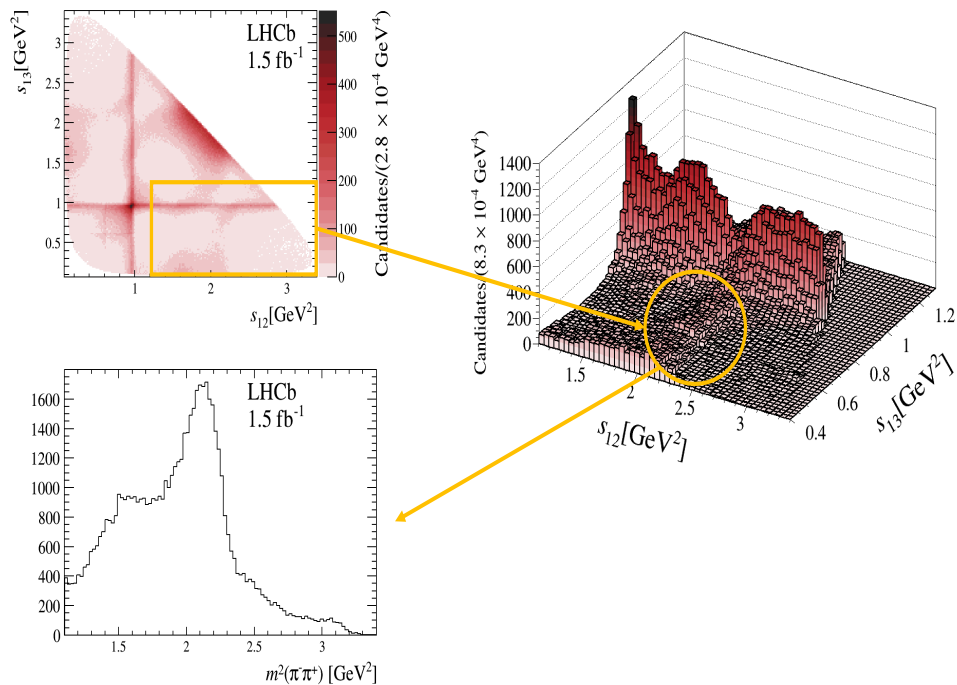


Figure 38 – A zoom of the region where the $f_0(980)$ interferes with one (or two) scalar resonance(s). The mass histogram is the $m^2(\pi^+ \pi^-)$ projection of events for the square in orange. Source: Courtesy of Prof. Alberto Reis.

A concentration of candidates is observed near the $m(\pi^+ \pi^+)$ threshold (at the up

diagonal). The structure is an indication of the presence of several states, namely $\rho(1450)^0$, $\rho(1700)^0$, $f_2(1270)$ that decay to $\pi^- \pi^+$ channel.

A narrow band corresponding to the $\omega(782)$ is observed. This is the first observation of this channel in the $D_s^+ \rightarrow \pi^- \pi^+ \pi^+$ decay. The $\omega(782)$ signal is more evident in the region below the $f_0(980)$ band and above 2.5 GeV^2 in $m^2(\pi^+ \pi^-)$, as shown in Fig. 39. The small component of the $\rho(770)^0$ overlaps with the $\omega(782)$, an effect that is more evident at the lower corner of the Dalitz plot.

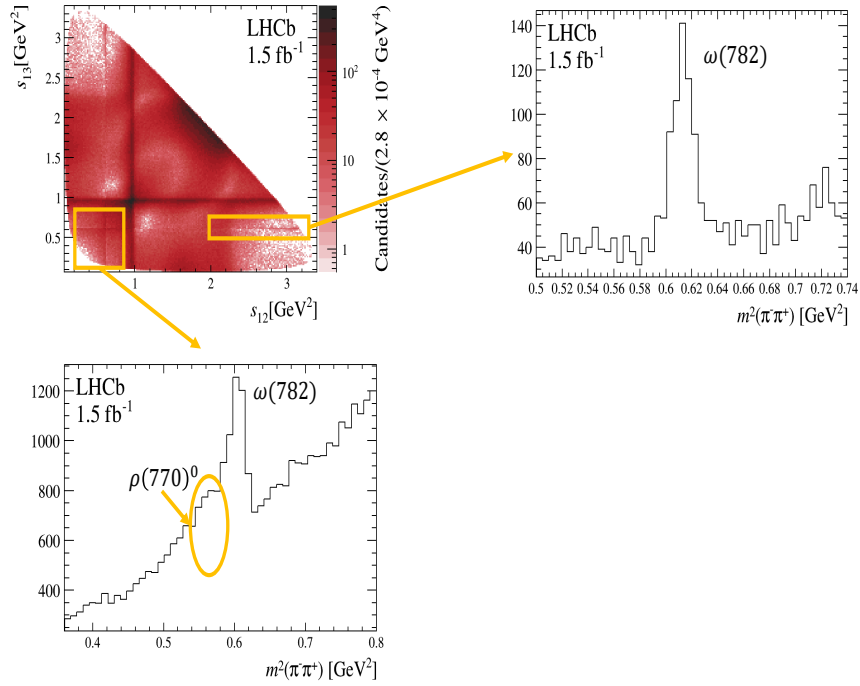


Figure 39 – The $m^2(\pi^- \pi^+)$ projection of candidates from the regions marked by the orange rectangles. Source: Courtesy of Prof. Alberto Reis.

The decay $\omega(782) \rightarrow \pi^- \pi^+$ violates isospin, but could happen through the $\rho - \omega$ mixing. This effect is clearly seen in the $D^+ \rightarrow \pi^- \pi^+ \pi^+$ decay, where the $\rho(770)^0$ is the dominant resonance in the P -wave [14]. However, another remarkable feature in the D_s^+ decay is the lack of a significant $\rho(770)^0$ contribution.

Finally, we also note that there is almost no signal near the edges of the Dalitz plot ($m_{\pi^+ \pi^-}^2 > 2.5$ and $m_{\pi^+ \pi^-}^2 < 0.5 \text{ GeV}^2$), as well as in the regions close to the crossing of the $f_0(980)$ bands. This is better seen in Fig. 40, where the Dalitz plot is shown in 3D.

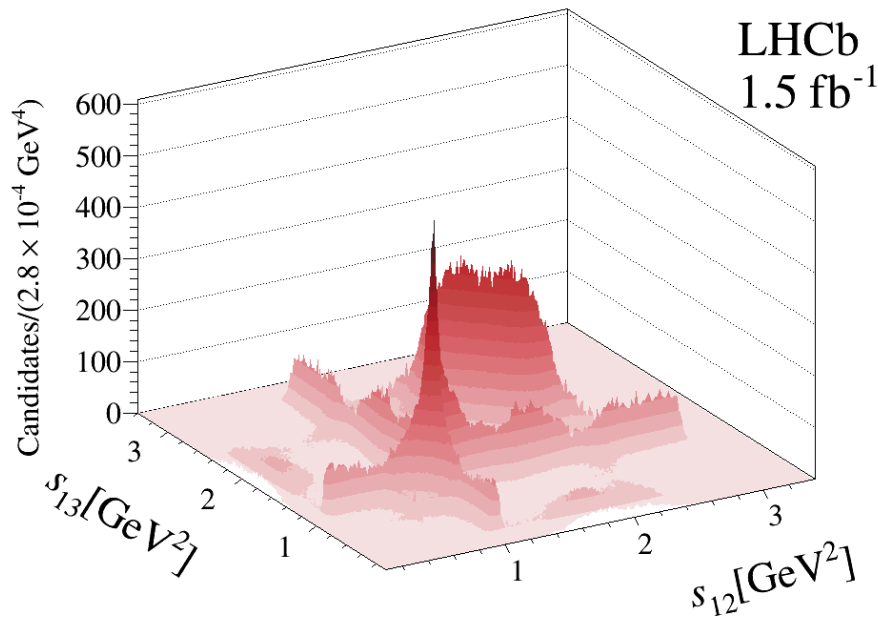


Figure 40 – The Dalitz plot in 3D.

Efficiency

To perform the Dalitz plot fit, we need to consider the variation of the detection efficiency across the phase space. A map of the efficiency is computed as a function of the Dalitz plot coordinates.

The simulated $D_s^+ \rightarrow \pi^- \pi^+ \pi^+$ decays are generated with a constant matrix element, resulting in a uniform Dalitz plot distribution. Since the phase space density in the Dalitz plot is constant, the efficiency map is determined by the distribution of the simulated events weighted by the correction weights (except by the resonance structure) passed through the same stages as the data. The final efficiency map is produced with the following steps:

1. A $s_{\pi_1^- \pi_2^+} \times s_{\pi_1^- \pi_3^+}$ histogram (15x15 bins) is filled with MC events passing all selection criteria except the PID. In this histogram, each candidate is weighted by the correction weights (except by the resonance structure!);
2. Bins at the Dalitz plot boundary are not entirely contained in the phase space, which results in a lower population. To account for this effect, the histogram of step 1 is divided by a normalization histogram made from a large toyMC sample (100M events) generated with a constant matrix element. This ensures that the efficiency is correctly computed in the bins at the Dalitz plot boundary;
3. A 2D cubic spline is then used to produce a smoothed, high-resolution (300x300 bins) histogram. This procedure avoids sudden changes in the efficiency between

neighbour bins due to statistical fluctuations. The smoothed histogram is the final efficiency map used for the Dalitz plot fit.

The efficiency at a given position in the Dalitz plot is simply the height of the corresponding bin in the efficiency map. The overall scale of the efficiency is irrelevant for the Dalitz plot fit since it amounts to an overall constant in the logarithm of the likelihood function. The final efficiency map is shown in Fig. 41 before and after the smoothing process.

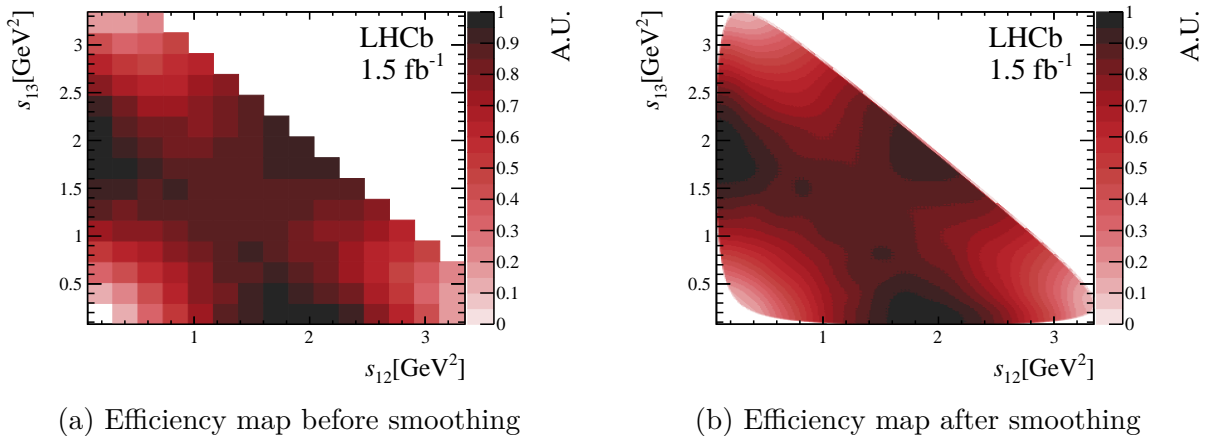
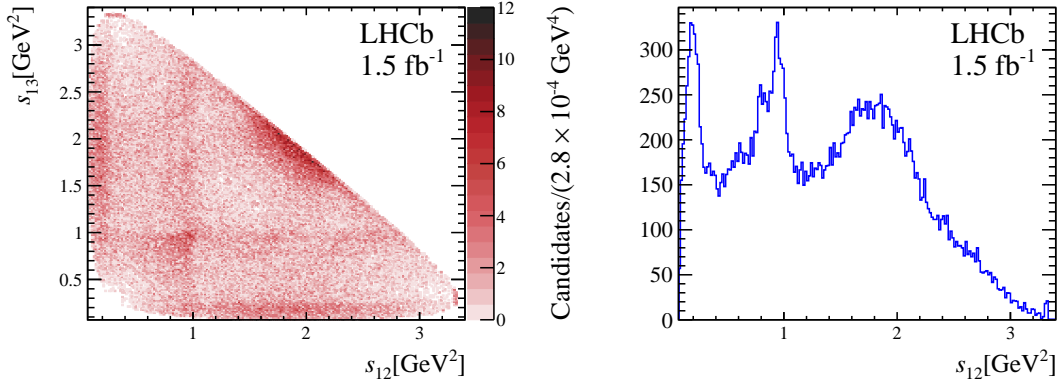


Figure 41 – The efficiency map before (left) and after (right) the smoothing process

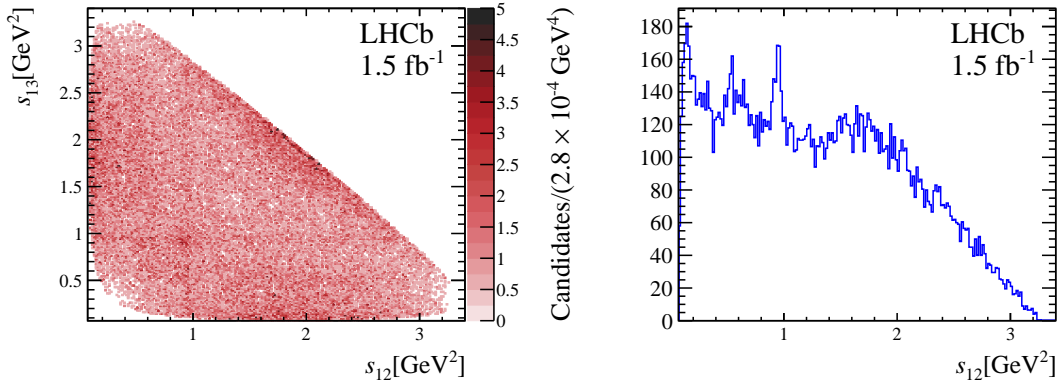
Background

The background model was determined by inspecting the sidebands of the $D_s^+ \rightarrow \pi^- \pi^+ \pi^+$ signal, [1920,1940] MeV and [2000,2020] MeV. In Figure 42, the Dalitz plots and projections onto $\pi^+ \pi^-$ axis of candidates from the two sidebands are shown separately. One observes that there are more structures in the left sideband. The background within the signal region is assumed to be a mixture of these two. A systematic uncertainty is assigned to the choice of the background by considering fit results where the model is determined by each sideband separately.

The background model for the Dalitz plot fit is a smoothed histogram (300x300 bins), following the same procedure as for the efficiency map and with the same initial binning. The histogram was produced by adding 50% of the candidates from the left sideband and the other 50% from the right. The same smoothing algorithm used for the efficiency map is also used to make the final smoothed background histogram, shown in Fig. 43. The impact of the background parameterisation will be addressed as a systematic uncertainty.

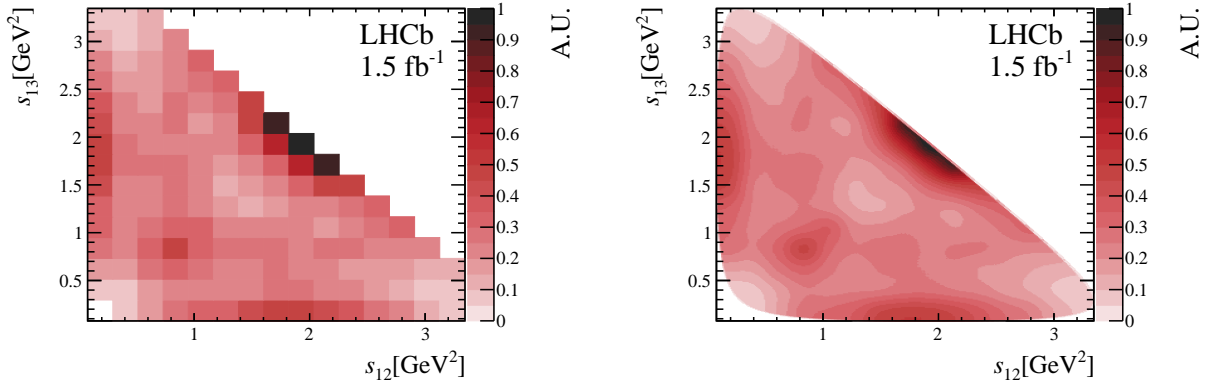


(a) Background from the left sideband - [1920,1940] MeV



(b) Background from the right sideband - [2000,2020] MeV

Figure 42 – Background for the left (a) and for the right (b) region of the signal



(a) Background map before smoothing

(b) Background map after smoothing

Figure 43 – The background map before (left) and after (right) the smoothing process

5.3 Result

The main result is obtained with a model consisting, in addition to the S -wave, of the following set of resonances: $\rho(770)^0$, $\omega(782)^0$, $\rho(1450)^0$, $\rho(1700)^0$, $f_2(1270)$ and $f_2'(1525)$. This model is referred as PWA-1.

The PWA-1 result is compared to the data plotting the distribution of normalised residuals over the folded Dalitz plot (which has 500 events per bin), as well as the projections onto s_{high} , s_{low} and $s_{\pi^+\pi^+}$ axes, where s_{high} and s_{low} are the highest and lowest of the two $\pi^+\pi^-$ invariant masses squared. Alternative models are tried to further check this model. See appendix C.

The PWA-1 results are summarised in Table 10 and Figs. 44 and 45. The interference fit fractions are collected in Table 11. The values of the S -wave magnitude and phase at each edge of $\pi^-\pi^+$ mass squared intervals are presented in Table 12 and can be visualised in figure 46. The estimation of systematic uncertainties is detailed in appendix B. The model PWA-1 provides a good description of the data, with χ^2/ndof in the range of [1.45 - 1.57].

Table 10 – Final results of the $D_s^+ \rightarrow \pi^-\pi^+\pi^+$ Dalitz plot fit. The uncertainties are statistical, experimental systematic and associated with the decay amplitude model, respectively.

Resonance	Magnitude			Phase [°]	
$\rho(770)^0$	$0.1201 \pm$	$0.0030 \pm$	$0.0050 \pm$	0.0062	$79.4 \pm 1.8 \pm 7.8 \pm 4.4$
$\omega(782)$	$0.04001 \pm$	$0.00090 \pm$	$0.0018 \pm$	0.00086	$-109.9 \pm 1.7 \pm 0.94 \pm 1.4$
$\rho(1450)^0$	$1.277 \pm$	$0.026 \pm$	$0.023 \pm$	0.48	$-115.2 \pm 2.6 \pm 2.8 \pm 10$
$\rho(1700)^0$	$0.873 \pm$	$0.061 \pm$	$0.054 \pm$	0.62	$-60.9 \pm 6.1 \pm 6.7 \pm 12$
$f_2(1270)$	1 (fixed)			0 (fixed)	
$f'_2(1525)$	$0.1098 \pm$	$0.0069 \pm$	$0.019 \pm$	0.015	$178.1 \pm 4.2 \pm 12 \pm 7$
	Fit Fraction (FF) [%]				
S-wave	$84.97 \pm$	$0.14 \pm$	$0.30 \pm$	0.63	
$\rho(770)^0$	$1.038 \pm$	$0.054 \pm$	$0.097 \pm$	0.11	
$\omega(782)$	$0.360 \pm$	$0.016 \pm$	$0.034 \pm$	0.016	
$\rho(1450)^0$	$3.86 \pm$	$0.15 \pm$	$0.14 \pm$	2.0	
$\rho(1700)^0$	$0.365 \pm$	$0.050 \pm$	$0.045 \pm$	0.34	
combined	$6.14 \pm$	$0.27 \pm$	$0.34 \pm$	1.9	
$f_2(1270)$	$13.69 \pm$	$0.14 \pm$	$0.22 \pm$	0.49	
$f'_2(1525)$	$0.0528 \pm$	$0.0070 \pm$	$0.015 \pm$	0.0087	

Table 11 – Interference fractions (%) between amplitude components for model PWA-1.

	$\omega(782)$	$\rho(770)^0$	$\rho(1450)^0$	$\rho(1700)^0$	$f_2(1270)$	$f_2'(1525)$	S -wave
$\omega(782)$	0.360 ± 0.016						
$\rho(770)^0$	0.128 ± 0.013	1.038 ± 0.054					
$\rho(1450)^0$	0.36 ± 0.14	0.148 ± 0.14	3.86 ± 0.15				
$\rho(1700)^0$	0.089 ± 0.010	-0.307 ± 0.055	1.92 ± 0.20	0.365 ± 0.050			
$f_2(1270)$	-0.1540 ± 0.0040	0.280 ± 0.029	-1.10 ± 0.047	-0.376 ± 0.047	13.69 ± 0.14		
$f_2'(1525)$	0.00827 ± 0.00063	0.00283 ± 0.0038	0.066 ± 0.0021	0.0200 ± 0.0021	-0.429 ± 0.072	0.0455 ± 0.0070	
S -wave	-0.053 ± 0.0099	0.804 ± 0.076	-1.520 ± 0.086	-0.934 ± 0.086	-3.460 ± 0.092	0.20 ± 0.013	84.97 ± 0.14

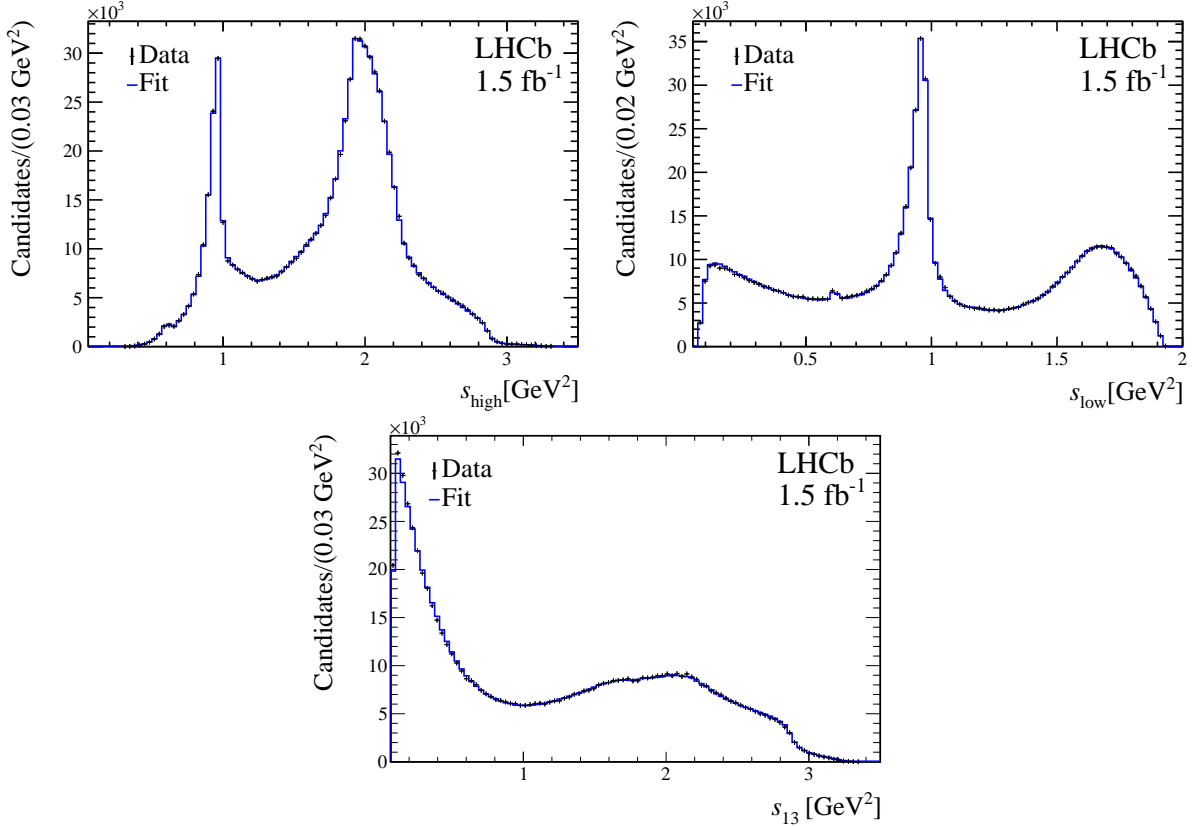


Figure 44 – Fit results from model PWA-1: the projections of the lowest (top-right) and the highest (top-left) of the two $\pi^+ \pi^-$ invariant masses squared. In the bottom the $s_{\pi^+ \pi^+}$ projection.

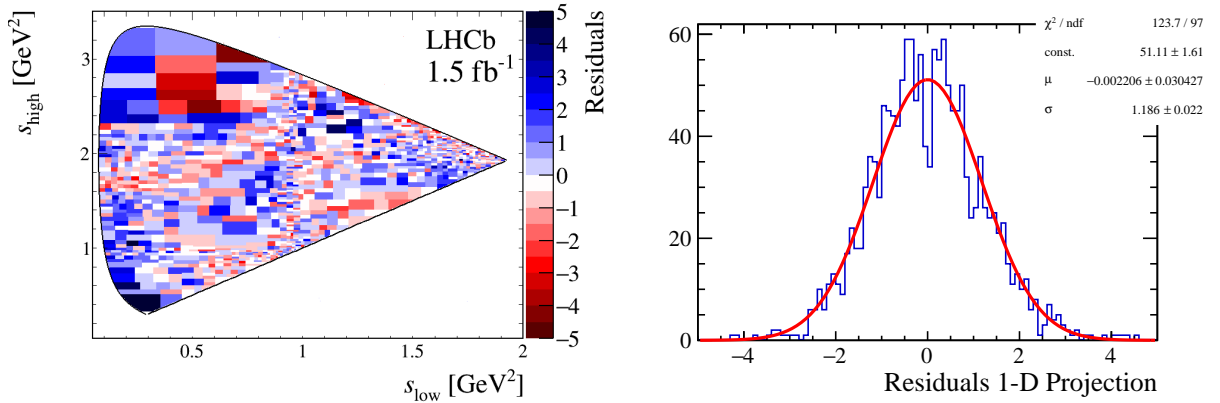


Figure 45 – Fit results from model PWA-1: distribution of the normalised residuals across the Dalitz plot (left) and as 1D projection (right).

There are some regions where the model either underestimates or overestimates the data. At the upper corner of the Dalitz plot ($s_{\text{high}} > 2.8 \text{ GeV}^2$), there is a more significant contribution from the background. There is also a significant efficiency variation in the same region, as seen in Fig.41. This behaviour also occurs at the lower corner of the Dalitz plot ($s_{\text{high}} < 0.5 \text{ GeV}^2$). In Sec. C, a fit is performed vetoing these regions, showing that they have no impact on the overall result.

The main features of the default result are:

- The resonant structure is largely dominated by the S -wave, in agreement with previous determinations.
- The magnitude of the S -wave near the threshold is small and nearly constant, indicating a very small contribution from the $f_0(500)$ (aka σ).
- The large phase variation and the peak in the magnitude near $m(\pi^+ \pi^-) \sim 1$ GeV are the signatures of a prominent contribution of the $f_0(980)$.
- The rapid growth of the S -wave phase towards the end of the spectrum indicates the presence of at least one more scalar resonance, which could be the $f_0(1370)$, the $f_0(1500)$ or a combination of both.
- The $D_s^+ \rightarrow \omega(782)^0 \pi^+$, $D_s^+ \rightarrow \rho(1700)^0 \pi^+$ and $D_s^+ \rightarrow f_2'(1525) \pi^+$ channels are observed for the first time in the $D_s^+ \rightarrow \pi^- \pi^+ \pi^+$ decay.
- The lack of a significant contribution of the $\rho(770)^0$, which is in agreement with previous analyses, is a remarkable feature, in contrast with the D^+ decay, where the contribution of this state is at the $\sim 25\%$ level.
- the combined fit fraction of the $\rho(1450)^0$ and $\rho(1700)^0$ is about six times larger than that of the $\rho(770)^0$.

A comparison between the S -wave from this analysis (only statistical uncertainties) with those from the BaBar [22] and BESIII [23] analyses is displayed in Fig. 47. There is a good agreement between the three measurements.

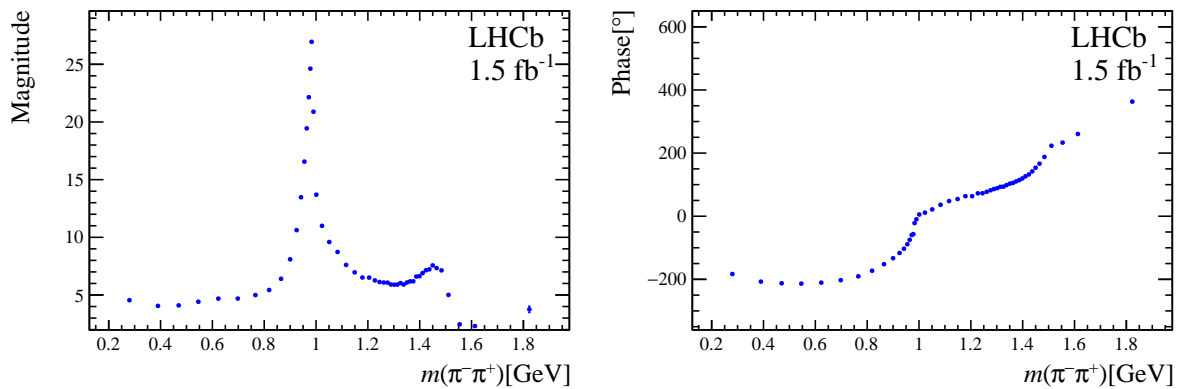


Figure 46 – (Left) Magnitude and (right) phase of the S -wave amplitude as a function of $m(\pi^+ \pi^-)$. The uncertainties are statistical.

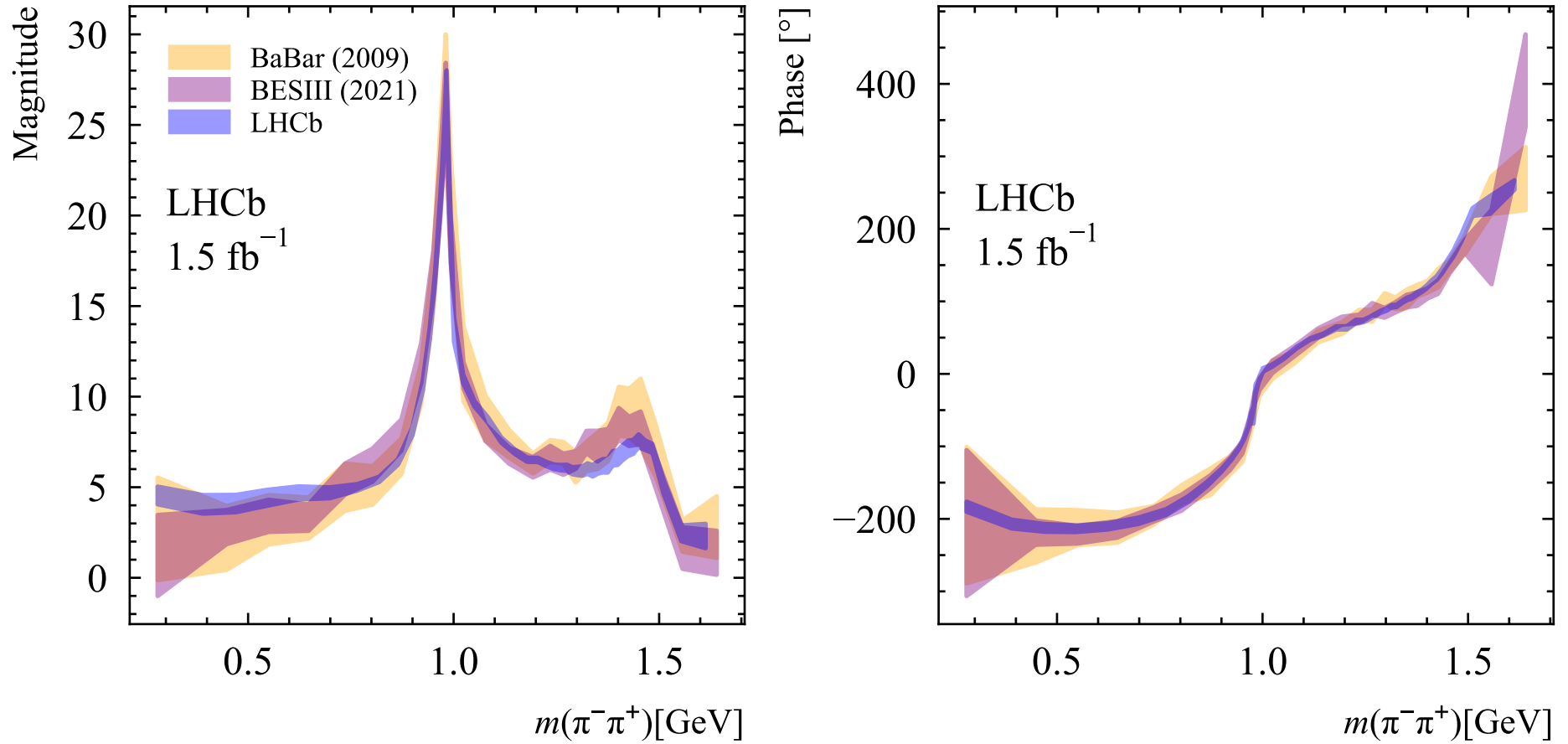
Figure 47 – The comparison of $\pi^- \pi^+$ S -wave of the $D_s^+ \rightarrow \pi^- \pi^+ \pi^+$ with previous results from BaBar and BESIII.

Table 12 – Magnitude and phase of the S-wave amplitude as a function of $\pi^- \pi^+$ invariant mass. The uncertainties are statistical, experimental and model, respectively. The $\pi^+ \pi^-$ invariant mass is expressed in GeV.

$m_{\pi\pi}$	Magnitude			Phase [°]		
0.280	4.54 ± 0.15 ± 0.24 ± 0.46			176.8 ± 2.0 ± 3.5 ± 6.6		
0.390	4.05 ± 0.12 ± 0.11 ± 0.50			152.8 ± 1.5 ± 2.3 ± 5.8		
0.470	4.10 ± 0.12 ± 0.11 ± 0.46			147.6 ± 1.4 ± 2.1 ± 5.1		
0.546	4.41 ± 0.11 ± 0.11 ± 0.42			146.4 ± 1.1 ± 1.7 ± 4.4		
0.623	4.69 ± 0.10 ± 0.13 ± 0.34			149.6 ± 1.0 ± 1.3 ± 4.2		
0.698	4.691 ± 0.092 ± 0.14 ± 0.28			157.4 ± 1.0 ± 1.4 ± 4.3		
0.766	4.994 ± 0.079 ± 0.074 ± 0.16			169.5 ± 1.1 ± 1.1 ± 3.8		
0.819	5.43 ± 0.072 ± 0.077 ± 0.13			-172.8 ± 1.3 ± 1.3 ± 3.7		
0.865	6.405 ± 0.066 ± 0.068 ± 0.14			-152.0 ± 1.2 ± 1.5 ± 2.7		
0.900	8.096 ± 0.069 ± 0.088 ± 0.20			-133.0 ± 1.1 ± 2.3 ± 1.6		
0.925	10.624 ± 0.082 ± 0.090 ± 0.25			-116.5 ± 1.0 ± 1.8 ± 1.2		
0.942	13.47 ± 0.10 ± 0.10 ± 0.29			-103.0 ± 1.0 ± 1.7 ± 0.8		
0.955	16.56 ± 0.12 ± 0.13 ± 0.32			-88.8 ± 1.2 ± 1.6 ± 1.1		
0.964	19.45 ± 0.14 ± 0.19 ± 0.42			-74.9 ± 1.2 ± 2.0 ± 0.95		
0.972	22.15 ± 0.16 ± 0.27 ± 0.40			-59.5 ± 1.4 ± 1.5 ± 5.7		
0.978	24.62 ± 0.17 ± 0.46 ± 0.68			-56.7 ± 1.4 ± 6.7 ± 11.8		
0.983	26.95 ± 0.17 ± 0.42 ± 1.04			-21.8 ± 1.2 ± 4.2 ± 6.9		
0.990	20.89 ± 0.14 ± 0.20 ± 0.90			-9.8 ± 1.1 ± 1.6 ± 2.8		
1.001	13.695 ± 0.091 ± 0.13 ± 0.66			5.45 ± 0.92 ± 1.5 ± 2.3		
1.023	10.995 ± 0.073 ± 0.10 ± 0.22			11.28 ± 0.76 ± 1.4 ± 1.3		
1.051	9.593 ± 0.063 ± 0.11 ± 0.13			21.57 ± 0.72 ± 1.3 ± 0.93		
1.083	8.731 ± 0.059 ± 0.072 ± 0.14			36.27 ± 0.65 ± 1.4 ± 0.80		
1.116	7.606 ± 0.059 ± 0.038 ± 0.13			48.02 ± 0.68 ± 1.3 ± 0.66		
1.149	6.961 ± 0.060 ± 0.043 ± 0.11			54.42 ± 0.71 ± 0.93 ± 1.2		
1.179	6.515 ± 0.058 ± 0.043 ± 0.10			63.46 ± 0.79 ± 0.82 ± 2.0		
1.205	6.506 ± 0.062 ± 0.033 ± 0.096			63.47 ± 0.79 ± 0.66 ± 2.05		
1.227	6.264 ± 0.064 ± 0.034 ± 0.097			72.45 ± 0.89 ± 0.78 ± 2.0		
1.245	6.125 ± 0.068 ± 0.025 ± 0.11			72.80 ± 0.94 ± 0.68 ± 1.4		
1.261	6.081 ± 0.069 ± 0.034 ± 0.13			77.2 ± 1.0 ± 0.78 ± 1.07		
1.276	6.071 ± 0.072 ± 0.036 ± 0.15			82.2 ± 1.0 ± 0.43 ± 0.95		
1.289	5.912 ± 0.074 ± 0.067 ± 0.18			86.1 ± 1.0 ± 0.59 ± 1.1		
1.302	5.893 ± 0.078 ± 0.099 ± 0.22			88.8 ± 1.0 ± 0.48 ± 1.1		
1.314	5.901 ± 0.080 ± 0.12 ± 0.25			93.2 ± 1.1 ± 0.55 ± 1.3		
1.326	6.031 ± 0.082 ± 0.095 ± 0.28			93.8 ± 1.1 ± 0.48 ± 1.06		
1.338	5.904 ± 0.083 ± 0.067 ± 0.30			98.7 ± 1.1 ± 0.61 ± 1.1		
1.351	6.086 ± 0.085 ± 0.056 ± 0.32			103.3 ± 1.0 ± 0.50 ± 1.3		
1.363	6.181 ± 0.089 ± 0.075 ± 0.35			105.7 ± 1.1 ± 0.65 ± 1.5		
1.375	6.185 ± 0.093 ± 0.087 ± 0.36			110.4 ± 1.1 ± 0.55 ± 1.6		
1.387	6.60 ± 0.10 ± 0.091 ± 0.38			114.5 ± 1.0 ± 0.46 ± 1.4		
1.399	6.63 ± 0.10 ± 0.085 ± 0.39			119.7 ± 1.0 ± 0.46 ± 1.7		
1.411	6.90 ± 0.11 ± 0.080 ± 0.39			126.5 ± 1.0 ± 0.33 ± 2.0		
1.424	7.14 ± 0.11 ± 0.11 ± 0.41			132.3 ± 1.0 ± 0.37 ± 2.4		
1.437	7.22 ± 0.11 ± 0.11 ± 0.37			142.03 ± 0.92 ± 0.47 ± 3.0		
1.450	7.56 ± 0.11 ± 0.12 ± 0.33			153.74 ± 0.86 ± 0.60 ± 3.5		
1.465	7.33 ± 0.11 ± 0.13 ± 0.24			166.50 ± 0.83 ± 0.68 ± 4.1		
1.484	7.13 ± 0.10 ± 0.15 ± 0.23			-172.15 ± 0.82 ± 0.81 ± 4.9		
1.511	5.009 ± 0.078 ± 0.13 ± 0.37			-136.8 ± 1.1 ± 1.4 ± 5.2		
1.554	2.456 ± 0.073 ± 0.14 ± 0.43			-126.8 ± 2.7 ± 2.9 ± 12.0		
1.613	2.31 ± 0.11 ± 0.14 ± 0.66			-99.5 ± 2.8 ± 5.9 ± 5.8		
1.823	3.75 ± 0.27 ± 0.32 ± 0.63			3.0 ± 4.2 ± 6.3 ± 17		

6 Introduction to the Dalitz plot analysis of the $D^+ \rightarrow \pi^- \pi^+ \pi^+$ decay results

The results of the Dalitz plot analysis of $D^+ \rightarrow \pi^- \pi^+ \pi^+$ [14] are briefly introduced in this chapter. The intention is to summarize the main results before going to section 7, where the $D^+ \rightarrow \pi^- \pi^+ \pi^+$ analysis will be mentioned constantly.

The analysis was performed concurrently with the $D_s^+ \rightarrow \pi^- \pi^+ \pi^+$. It was based on 1.5fb^{-1} of pp collision data at 8 TeV centre-of-mass energy, collected by the LHCb experiment in 2012. The main goal was to determine the resonant structure of the decay and perform a study of the S-wave component. The QMIPWA approach, presented in Chapter 5 for the $D_s^+ \rightarrow \pi^- \pi^+ \pi^+$, was used to model the Dalitz decay plot. It was the first time that QMIPWA was used for this channel.

6.1 Selection

The selection of candidates (data and simulation) for this analysis proceeded by the same steps detailed in section 5.1. It started including requirements on all trigger levels. The events were restricted to those triggered independent of signal (TIS) at the L0 trigger. The HLT1 and HLT2 requirements are the same presented to D_s^+ at tables 4 and 5, as the stripping line. After the trigger, the events were restricted to those after the pos-technical stop.

The specific backgrounds expected to $D^+ \rightarrow \pi^- \pi^+ \pi^+$ and how they were reduced are listed below:

- $D^+ \rightarrow \pi^- \pi^+ \mu^+ \nu_\mu$ - removed by requiring a muon veto (isMuon==0).
- MisID: $D^0 \rightarrow K^- \pi^+$, $D^0 \rightarrow K^- \pi^+$, $\Lambda_c \rightarrow p \pi^+ \pi^-$ and $D^+ \rightarrow K^- \pi^+ \pi^+$ - reduced by applying a more stringent PID requirement (PIDK<-2). This requirement is applied to simulation using weights from PIDCalib.
- Irreducible background $D_s^+ \rightarrow \eta' \pi^+$ - reduced by MVA
- The decay of $D^+ \rightarrow K_s \pi^+$ can be visualized in the Dalitz plot as a thin line near $0.25 \text{ GeV}^2/c^4$. For this analysis, it was decided to apply a veto on s_{12} and s_{13} at this region after performing MVA.

The simulation was selected following the same steps of the data, except for the PID requirement that was included using the PIDCalib weights. Before performing the MVA,

corrections were applied to the simulation sample following the same stages of section **Simulation corrections** in 5.1. The MVA was performed using the cross-validation approach. The BDTG classifier was used to learn how to distinguish signal and background. A positive cut on the predicted classifier variable was applied to produce a 95% purity sample. The invariant mass fit determined the yields and the signal window. See the left plot in figure 48. The analysis candidates were selected within $2\sigma_{eff}$ ($\sigma_{eff} = 8.7$ MeV). The corresponding mass interval is $[1854.1, 1889.0]$ MeV/ c^2 . About 600k $D^+ \rightarrow \pi^- \pi^+ \pi^+$ candidates were selected from data and simulation. See figure 48 right.

The Dalitz plot exhibits complex dynamics. At 0.25 GeV $^2/c^4$ on s_{12} and s_{13} , the white narrow lines show the veto on the $D^+ \rightarrow K_s \pi^+$. At 0.6 GeV/ c^2 , it is possible to see the interference between $\rho(770)^0$ and $\omega(782)$. The $f_0(980)^0$ at ~ 0.98 GeV/ c^2 is less prominent when compared to that in the $D_s^+ \rightarrow \pi^- \pi^+ \pi^+$ channel. The concentration of events at the up diagonal, the beginning of $s_{\pi^+ \pi^+}$, have contributions of $\rho(1450)^0$, $\rho(1700)^0$ and $f_2(1270)$.

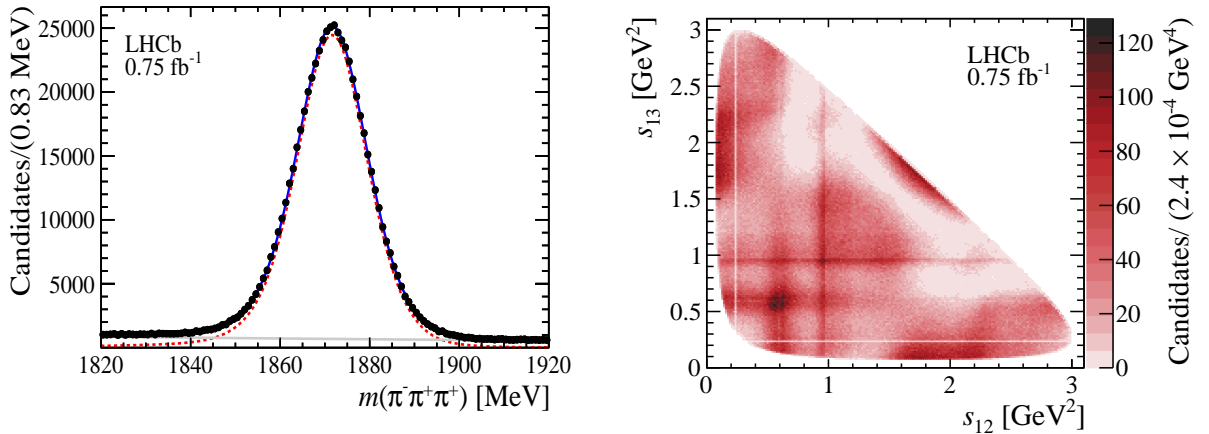


Figure 48 – (Left) Invariant-mass distribution of $D^+ \rightarrow \pi^- \pi^+ \pi^+$ candidates after final selection, with the fit result superimposed (blue solid line). The dashed red line and the solid gray line correspond to the signal and background components of the fit, respectively. (Right) Dalitz plot distribution of the final $D^+ \rightarrow \pi^- \pi^+ \pi^+$ sample. The lines in the interval $[0.235, 0.250]$ GeV 2 correspond to the veto applied to remove $D^+ \rightarrow K_s^0 \pi^+$ decays.

The efficiency map was built from the corrected simulation after MVA selection, and the background was inferred from the sidebands of the $D^+ \rightarrow \pi^- \pi^+ \pi^+$ invariant-mass signal region, specifically, the intervals $[1810, 1830]$ MeV and $[1910, 1930]$ MeV. Fig. 49 shows the efficiency and background.

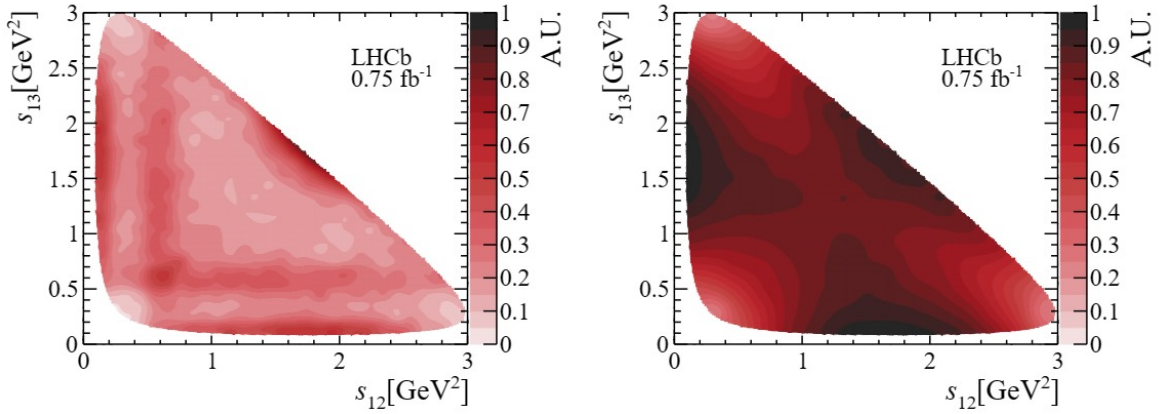


Figure 49 – Models for (left) background distribution and (right) signal efficiency across the Dalitz plot, where the z -axis scale is arbitrary.

6.2 Dalitz plot fit

In addition to the S-wave, the nominal model of this analysis consists of the resonances: $\rho(770)^0$, $\omega(782)$, $\rho(1450)^0$, $\rho(1700)^0$ and $f_2(1270)$. P-wave ρ -types were described using Gounaris-Sakurai lineshapes. The $\omega(782)$ and the $f_2(1270)$ were described using Relativistic Breit-Wigner. The S-wave was included using the same QMIPWA formalism of the $D_s^+ \rightarrow \pi^- \pi^+ \pi^+$. The reference resonance was the $\rho(770)^0$.

The $\omega(782) \rightarrow \pi^- \pi^+$ is an isospin-violating decay. There is an open discussion about the mechanism of this decay, whether by the direct decay, by the mixing with the $\rho(770)^0$ state, or both. This analysis parameterized the combined contribution of these states through the $\rho - \omega$ mixing lineshape [73]. The equation below introduces the mixing lineshape.

$$T_{\rho-\omega} = T_\rho \frac{1 + \Delta |B| e^{i\phi_B} T_\omega}{1 - \Delta^2 T_\rho T_\omega} \quad (6.1)$$

T_ρ and T_ω are the lineshapes for the $\rho(770)^0$ and $\omega(782)^0$, respectively. The magnitude $|B|$ and the phase ϕ_B quantify the relative magnitude and phase of the $\omega(782)^0$ and the $\rho(770)^0$ resonances, and are free parameters in the fit. The factor $\Delta = \delta(m_\rho + m_\omega)$ governs the electromagnetic mixing of these states, where the value of δ is fixed to 2.15 MeV and m_ρ and m_ω are the known masses. This parameterization is equivalent to that used in ref. [74] given that Δ^2 is small, and therefore, the term where it appears in the denominator can be neglected.

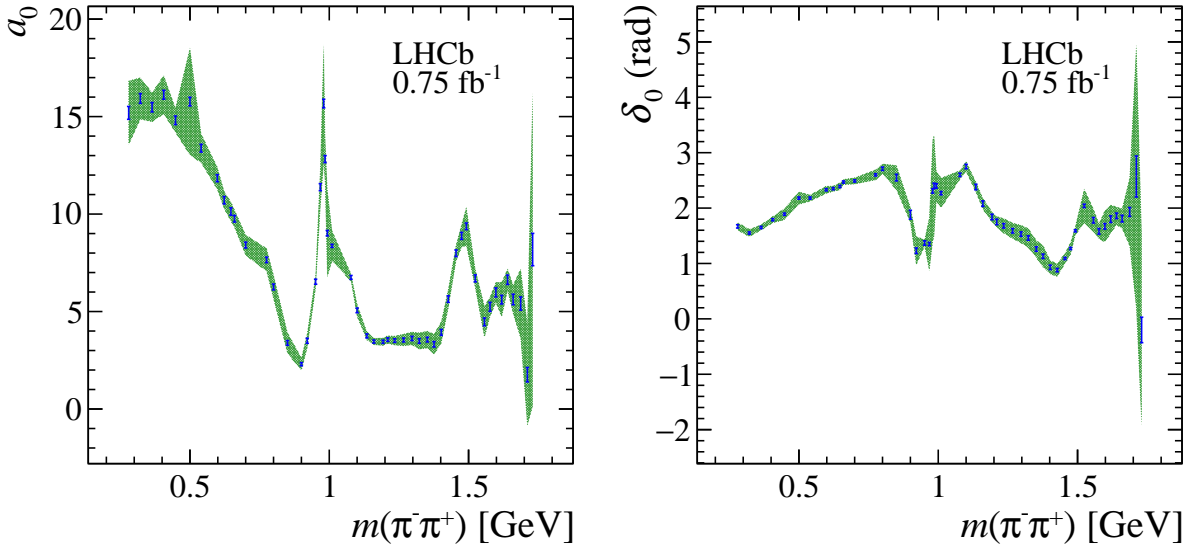
The fit results are summarised in Table 13 and Figs. 51. The interference fit fractions are collected in Table 14. The S-wave magnitude and phase at each edge of $\pi^- \pi^+$ mass squared intervals can be visualised in Fig. 50. The model provides a good description of the data, with χ^2/ndof in the range of [1.47 - 1.78].

Table 13 – Dalitz fit results for magnitudes, phases and fit fractions (%) of the spin-1 and spin-2 components, and the S-wave fit fraction. The uncertainties quoted are, in order, statistical, experimental systematics, and model systematics.

Component	Magnitude	Phase [°]	Fit fraction [%]			
$\rho(770)^0 \pi^+$	1 [fixed]	0 [fixed]	26.0	± 0.3	± 1.6	± 0.3
$\omega(782) \pi^+$	$(1.68 \pm 0.06 \pm 0.15 \pm 0.02) \times 10^{-2}$	$-103.3 \pm 2.1 \pm 2.6 \pm 0.4$	$0.103 \pm 0.008 \pm 0.014 \pm 0.002$			
$\rho(1450)^0 \pi^+$	$2.66 \pm 0.07 \pm 0.24 \pm 0.22$	$47.0 \pm 1.5 \pm 5.5 \pm 4.1$	5.4	± 0.4	± 1.3	± 0.8
$\rho(1700)^0 \pi^+$	$7.41 \pm 0.18 \pm 0.47 \pm 0.71$	$-65.7 \pm 1.5 \pm 3.8 \pm 4.6$	5.7	± 0.5	± 1.0	± 1.0
$f_2(1270) \pi^+$	$2.16 \pm 0.02 \pm 0.10 \pm 0.02$	$-100.9 \pm 0.7 \pm 2.0 \pm 0.4$	13.8	± 0.2	± 0.4	± 0.2
S-wave			61.8	± 0.5	± 0.6	± 0.5
$\sum_i FF_i$			112.8			
χ^2/ndof (range)	[1.47 - 1.78]		$-2 \log \mathcal{L} = 805622$			

Table 14 – Dalitz fit results for the interference fit fractions (%) (statistical uncertainties only).

	$\omega(782) \pi^+$	$\rho(1450)^0 \pi^+$	$\rho(1700)^0 \pi^+$	$f_2(1270) \pi^+$	S-wave
$\rho(770)^0 \pi^+$	-0.24 ± 0.06	5.1 ± 0.3	-5.8 ± 0.4	-0.3 ± 0.1	1.8 ± 0.4
$\omega(782) \pi^+$		0.05 ± 0.01	0.05 ± 0.01	0.046 ± 0.004	-0.04 ± 0.01
$\rho(1450)^0 \pi^+$			-4.0 ± 0.5	1.1 ± 0.1	1.7 ± 0.2
$\rho(1700)^0 \pi^+$				-0.8 ± 0.1	-3.4 ± 0.5
$f_2(1270) \pi^+$					-1.6 ± 0.1

Figure 50 – Fitted (left) magnitude and (right) phase of the $\pi^- \pi^+$ S-wave amplitude with statistical uncertainties as the blue bars and the total uncertainties (combined statistical, experimental and model systematics) as the green bands.

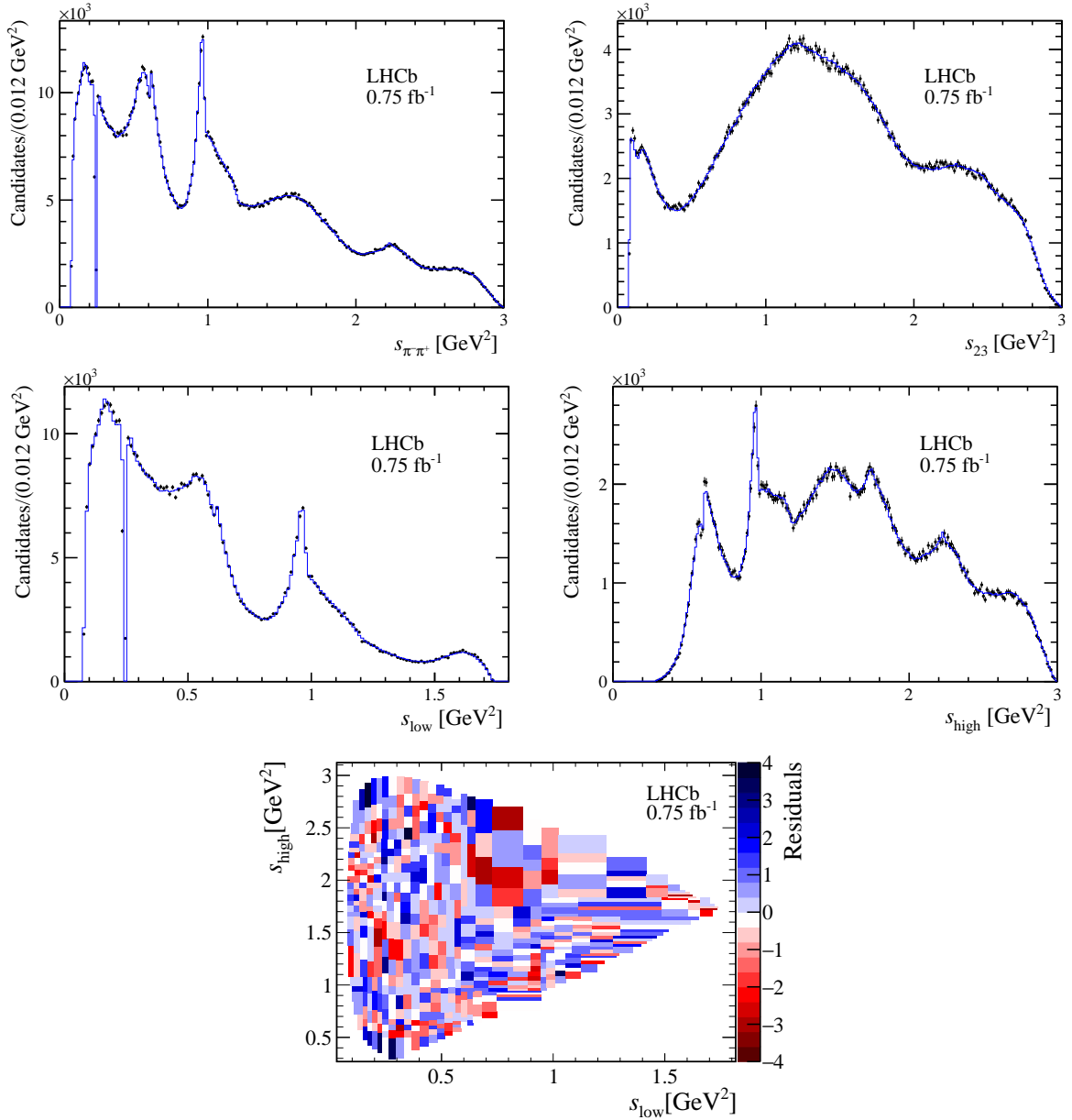


Figure 51 – Dalitz plot projections of (top left) $s_{\pi^- \pi^+}$, (top right) s_{23} , (middle left) s_{low} , and (middle right) s_{high} projections, where the (red) points are data and the (blue) line is the fit model result, with the fit normalised residuals displayed in the bottom plot.

6.3 Summary of the results

The fit result shows the dominant contribution of the S-wave (61.8%) in agreement with previous determinations based on the Isobar Model and K-Matrix. The S-wave magnitude plot on Fig. 50 shows a significant contribution of $f_0(500)$ at the beginning of the spectrum $m(\pi^- \pi^+)$. The next contribution comes from $f_0(980)$. The variation in the magnitude and phase near $m(\pi^- \pi^+) \sim 1$ GeV confirms its signature. The bump and the phase variation near $m(\pi^- \pi^+) \sim 1.5$ GeV indicates the presence of at least one scalar resonance, which could be the $f_0(1370)$ or/and $f_0(1500)$.

The P-wave is dominated by the $\rho(770)^0$ (26%), followed by a combined contribution of the high masses ρ 's, which account for $\sim 6\%$. While $\rho(1450)^0$ was already used in the previous analysis, it was the first time the $\rho(1700)^0$ was included. It was necessary to improve the determination of the P-wave at the high-mass region, resulting in an enhancement of the FCN in -488 units, a significant improvement. The small but significant contribution of $\omega(782)^0 \rightarrow \pi^- \pi^+$ was observed for the first time in this analysis for this decay channel. It's possible to see the mixing pattern in Fig. 51 (top left), which was impossible in the previous analysis due to the limited signal yields. The D-wave composed only by $f_2(1270)$ has the third more significant contribution, accounting for 13.8%.

7 Intepretation of the results

A detailed discussion of the $D_s^+ \rightarrow \pi^- \pi^+ \pi^+$ amplitude analysis results is introduced in this chapter. The chapter is divided into S-, P- and D-wave discussions. At the end of each section, a summary of the results and conclusions is provided, along with comparisons between this analysis and the $D^+ \rightarrow \pi^- \pi^+ \pi^+$.

Table 15 – Fit fractions (%) from the $D_s^+ \rightarrow \pi^- \pi^+ \pi^+$ and $D^+ \rightarrow \pi^- \pi^+ \pi^+$ decays. Uncertainties are statistical.

Resonance	$D_s^+ \rightarrow \pi^- \pi^+ \pi^+$	$D^+ \rightarrow \pi^- \pi^+ \pi^+$
$\rho(770)^0$	1.038 ± 0.055	26.04 ± 0.3
$\omega(782)$	0.360 ± 0.016	0.10 ± 0.01
$\rho(1450)^0$	3.86 ± 0.15	5.35 ± 0.3
$\rho(1700)^0$	0.365 ± 0.050	5.66 ± 0.4
$f_2(1270)$	13.69 ± 0.14	13.80 ± 0.2
$f_2'(1525)$	0.0455 ± 0.0070	-
<i>S</i> -wave	84.97 ± 0.14	61.82 ± 0.5
<i>P</i> -wave	8.55 ± 0.44	32.31 ± 0.64
<i>D</i> -wave	13.12 ± 0.02	13.8 ± 0.2

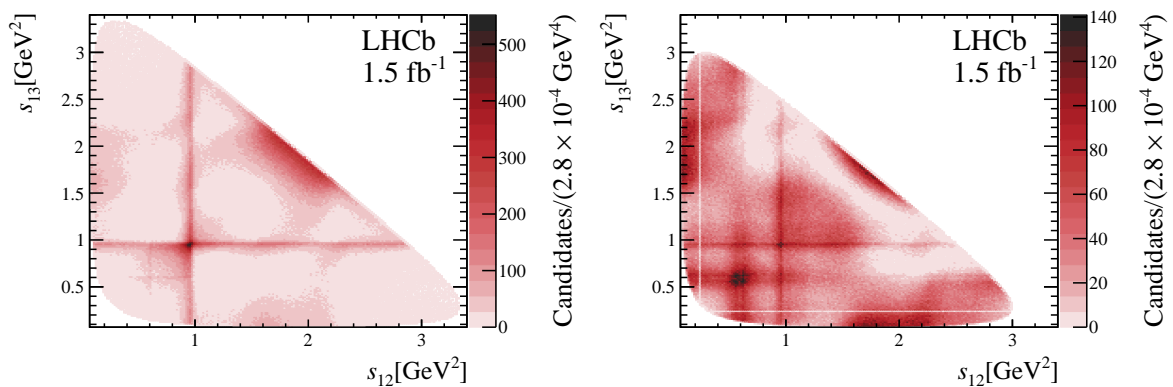


Figure 52 – (Left) Dalitz plot of the $D_s^+ \rightarrow \pi^- \pi^+ \pi^+$ and (right) $D^+ \rightarrow \pi^- \pi^+ \pi^+$ decays [14]. The colour scale indicates the density of candidates.

7.1 The $\pi^+ \pi^-$ *S*-wave

The resonant structure of the $D_s^+ \rightarrow \pi^- \pi^+ \pi^+$ and $D^+ \rightarrow \pi^- \pi^+ \pi^+$ decays are very different, despite the same final state and the slight mass difference between D_s^+ and D^+ of only 100 MeV. For comparison, the Dalitz plots of the two decays are shown in Fig. 52. In both cases, the decay rate is dominated by the *S*-wave, but with very different compositions (see Fig. 53), leading to the conclusion that scalar resonances are produced by different mechanisms in these decays.

Model-dependent analyses of the $D^+ \rightarrow \pi^- \pi^+ \pi^+$ decay channels [75, 24, 25, 22, 23] found that the resonant mode $f_0(500)\pi^+$ accounts for nearly half of the $D^+ \rightarrow \pi^- \pi^+ \pi^+$ decay rate, but it is consistent with zero in the $D_s^+ \rightarrow \pi^- \pi^+ \pi^+$ decay. In the latter, the dominant mode is the $f_0(980)\pi^+$, corresponding to approximately half of the decay rate.

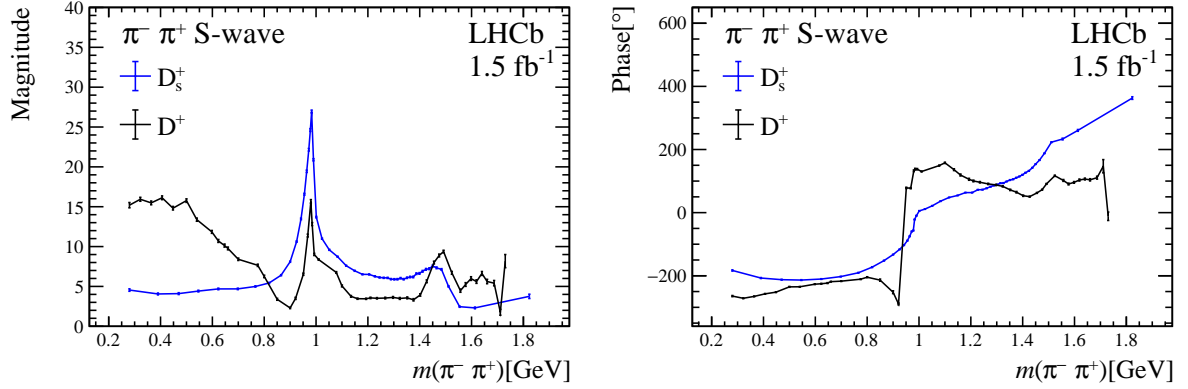


Figure 53 – (Left) Magnitude and (right) phase of the $\pi^- \pi^+$ S-wave amplitude for the $D^+ \rightarrow \pi^- \pi^+ \pi^+$ (black line) and $D_s^+ \rightarrow \pi^- \pi^+ \pi^+$ decays (blue dot).

Similar differences in the resonant structure are observed in the $B_{(s)}^0 \rightarrow J/\psi \pi^+ \pi^-$ decays [16, 15]. In these decays, the J/ψ recoils against a $d\bar{d}$ pair, in the case of the B^0 , and against an $s\bar{s}$ pair, in the case of the B_s^0 . To an excellent approximation, the interaction between the J/ψ and the $\pi^+ \pi^-$ system can be ignored. The production of the $\pi^+ \pi^-$ system from $s\bar{s}$ and $d\bar{d}$ sources results in a somewhat different resonant structure, as shown in Fig. 54.

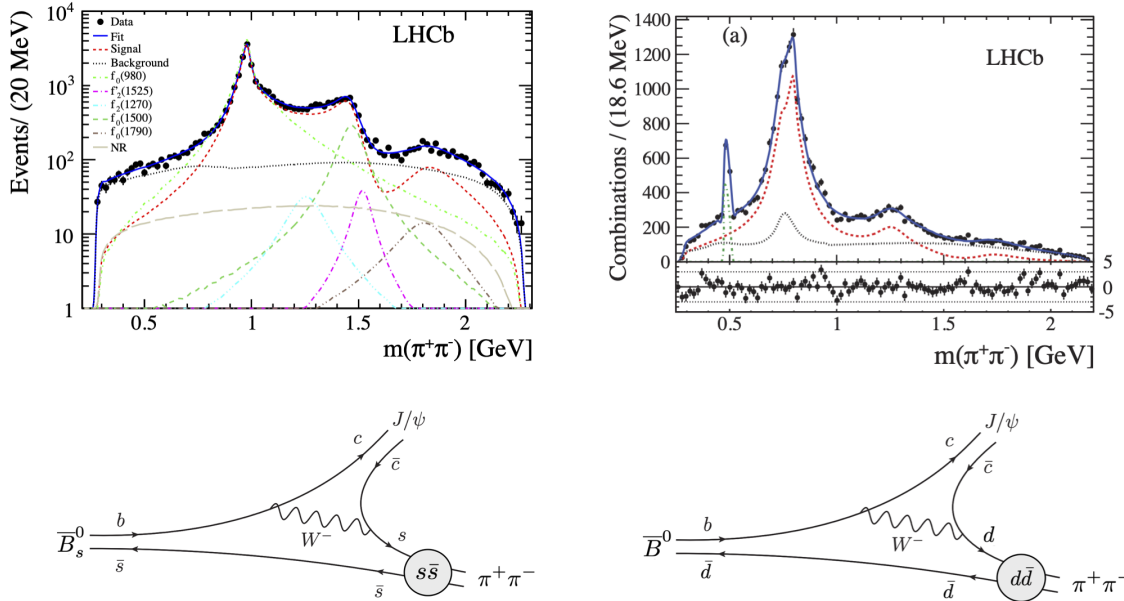


Figure 54 – The $\pi^+ \pi^-$ spectrum from $\bar{B}_s^0 \rightarrow J/\psi \pi^+ \pi^-$ decay [15], on the left, and from $\bar{B}^0 \rightarrow J/\psi \pi^+ \pi^-$ decay [16], on the right.

$f_0(1370)$ and $f_0(1500)$

The Argand plot of the S -wave amplitude from the $D_s^+ \rightarrow \pi^- \pi^+ \pi^+$ is displayed in Fig. 55. The amplitude evolves counterclockwise, describing two circles. The amplitude is purely imaginary at $m_{\pi^- \pi^+} = 0.955, 1.302$ and 1.613 GeV, which could indicate the presence of three scalar resonances. In addition to $f_0(980)$, the scalars would be the $f_0(1500)$ and the controversial $f_0(1370)$.

The quark model predicts the existence of two f_0 states above 1 GeV, but three are observed: the $f_0(1370)$, $f_0(1500)$ and the $f_0(1710)$. The lightest and long-sought glueball is expected to have a mass in the range $1.5 - 2$ GeV [76], with the same quantum numbers as the scalars, $J^{PC} = 0^{++}$. In a possible interpretation [77, 17], the physical particles would result from the mixing of the two $q\bar{q}$ states and the glueball, with different proportions in each wave function. The $f_0(1500)$ is the only scalar state with measured branching fractions.:

$$\frac{\Gamma(f_0(1500) \rightarrow \pi\pi)}{\Gamma(f_0(1500) \rightarrow K\bar{K})} = \frac{34.9 \pm 2.3}{8.6 \pm 1.0}$$

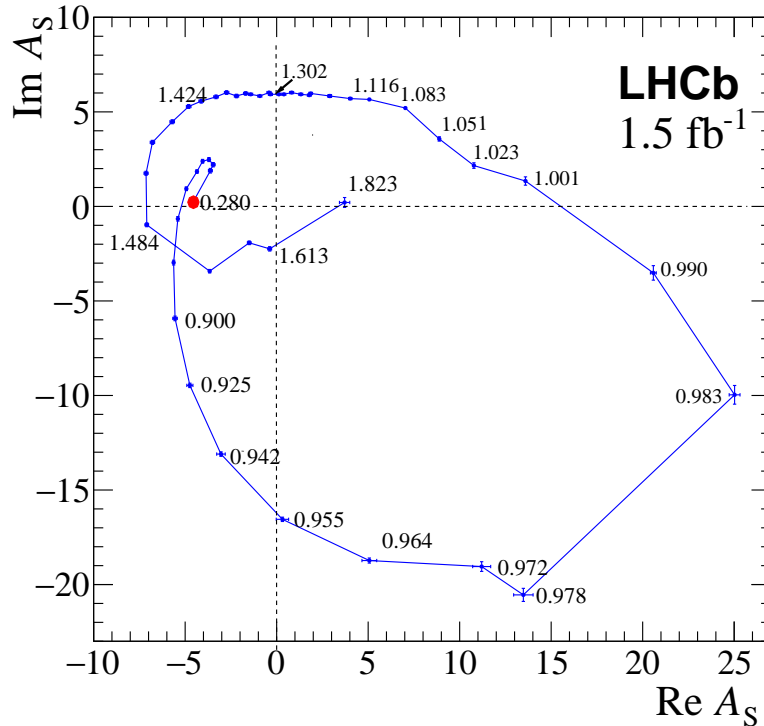


Figure 55 – The $D_s^+ \rightarrow \pi^- \pi^+ \pi^+$ Argand plot of the $\pi^+ \pi^-$ S -wave amplitude. The values of $m(\pi^+ \pi^-)$ at the edge of each interval are indicated next to the corresponding experimental point. The amplitude starts at the point circled in red and undergoes two counterclockwise circles.

The structure in the region 1.2-1.5 GeV in $D_s^+ \rightarrow \pi^- \pi^+ \pi^+$ decay was also observed in decays of B mesons, such as $B^+ \rightarrow K^+ K^+ K^-$ [78, 79], $B^+ \rightarrow K^+ \pi^+ \pi^-$ [80], $B^0 \rightarrow$

$K_S^0\pi^+\pi^-$ [81], but no conclusions can be drawn. In the decay $B^+ \rightarrow K^+K^+K^-$, BaBar found one single scalar at 1.540 GeV, with a width of 260 GeV, whereas Belle found one state nearly at the same mass but with a smaller width, 140 GeV. In the decay $B^+ \rightarrow K^+\pi^+\pi^-$, Belle found one single state at ~ 1.5 GeV, with a width of 140 GeV, close to the state observed in the decay $B^0 \rightarrow K_S^0\pi^+\pi^-$, with mass at 1.450 GeV and width of 126 GeV.

The D_s^+ and D^+ S -waves

A possible explanation for the observed differences in the resonance structure derives from the assumption that the dominant amplitude leading to the $D_{(s)}^+ \rightarrow \pi^-\pi^+\pi^+$ decays is the tree-level external W -emission shown in Fig. 1. In this case, the scalar resonances would be produced from a $d\bar{d}$ source in $D^+ \rightarrow \pi^-\pi^+\pi^+$, and from an $s\bar{s}$ source in $D_s^+ \rightarrow \pi^-\pi^+\pi^+$.

The vector and tensor resonances are well-fitted to the predicted $q\bar{q}$ states of the quark model. These resonances could couple directly to the D meson. In other words, there would be a direct association of vector and tensor mesons with the $q\bar{q}$ source. But this would not be the case for the scalar mesons, where the supernumerary states below 2 GeV lead to the conclusion that at least some of these resonances would not be regular $q\bar{q}$ states. The $f_0(980)$ and the $a_0(980)$, for instance, are often interpreted as compact tetra-quark states (see Note on Scalar Mesons Below 2 GeV in [21]), while the $f_0(500)$ and the $K^*(800)$ would be dynamically generated poles of the $\pi\pi$ and $K\pi$ scattering [82], respectively, with tiny, if any, $s\bar{s}$ component in the wave function.

In ground-state vector mesons, the valence quarks have orbital angular momentum $L = 0$. If the scalars were pure $q\bar{q}$ states, the quark and antiquark would be in a $L = 1$ state. Given the relatively low energy available in the D decays, a more likely mechanism would be the production of a pair of pseudo-scalar particles a, b ($a, b = \pi, K, \eta$) in a $L = 0$ state, as illustrated in Fig. 56. The scalar mesons would emerge from the $ab \rightarrow \pi^+\pi^-$ scattering. In this picture, the $d\bar{d}$ and $s\bar{s}$ pairs would give rise to different sets of pseudo-scalar mesons and, therefore, to different S -wave amplitudes.

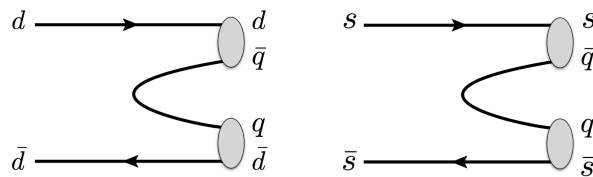


Figure 56 – The scalar mesons are formed by rescattering of the pseudo-scalar mesons a' and b' , formed by the $d\bar{d}$ pair from the D^+ decay and a $q\bar{q}$ pair from the vacuum.

Rescattering of the three pions in the final state could result in a slowly varying

phase, but it is hard to say that this effect explains the observed differences in the S -wave amplitudes. A study performed with the $D^+ \rightarrow K^- \pi^+ \pi^+$ decay [83] indicates that three-body interactions could amount up to a $\sim 20\%$ correction on the S -wave phase.

The $\pi^- \pi^+ \pi^+$ final state could also be formed by three-body rescattering connecting decay modes with the same quantum numbers, such as $K^- K^+ \pi^+$, $\pi^+ \pi^0 \pi^0$, $\pi^+ \eta \pi^0$ or $\pi^+ \eta \eta$. In Fig. 57, some possible rescattering diagrams are shown. These rescattering amplitudes involve loops and are suppressed by two orders of magnitude compared to the tree-level amplitudes [84].

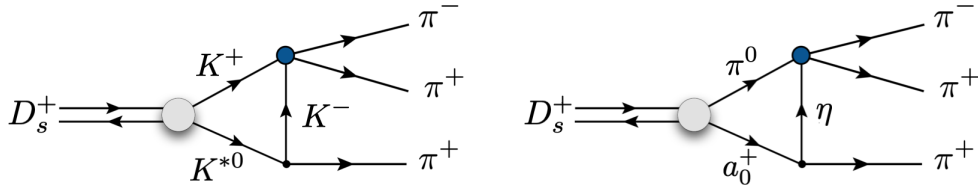


Figure 57 – Examples of three-body FSI connecting different channels with the vacuum quantum numbers. These amplitudes involve loops and are suppressed w.r.t tree-level diagrams.

An attempt to understand the impact of the different sources of the $\pi^- \pi^+$ pair on the resulting S -wave can be made in the framework of the so-called unitary chiral approach [85]. This approach establishes a connection between quark and hadron degrees of freedom, as illustrated in Fig. 56. Pseudo-scalar and vector mesons are well-established $q\bar{q}$ states. A $q\bar{q}$ pair ($u\bar{u}$, $d\bar{d}$, or $s\bar{s}$) from the vacuum combines with the $s\bar{s}$ ($d\bar{d}$) pair producing the pseudo-scalar mesons a and b (a' and b') from Fig. 1, which rescatter producing the particles that we detect.

According to the Quark Model, the SU(3) quark matrix M is given by

$$M = \begin{pmatrix} u \\ d \\ s \end{pmatrix} (\bar{u} \ \bar{d} \ \bar{s}) = \begin{pmatrix} u\bar{u} & u\bar{d} & u\bar{s} \\ d\bar{u} & d\bar{d} & d\bar{s} \\ s\bar{u} & s\bar{d} & s\bar{s} \end{pmatrix}. \quad (7.1)$$

Recalling that $|\pi^0\rangle = \frac{1}{\sqrt{2}}(u\bar{u} - d\bar{d})$ and $|\eta\rangle = \frac{1}{\sqrt{2}}(u\bar{u} + d\bar{d} - 2s\bar{s})$, the M matrix can be written in terms of SU(3) pseudo-scalar mesons,

$$M = \begin{pmatrix} \frac{1}{\sqrt{2}}\pi^0 + \frac{1}{\sqrt{6}}\eta & \pi^+ & K^+ \\ \pi^- & -\frac{1}{\sqrt{2}}\pi^0 + \frac{1}{\sqrt{6}}\eta & K^0 \\ K^- & \bar{K}^0 & -\frac{2}{\sqrt{6}}\eta \end{pmatrix}. \quad (7.2)$$

Considering the three possible light-quark pairs from the vacuum inserted between the $d\bar{d}$ pair, in the D^+ decay, one has

$$d(\bar{u}u + \bar{d}d + \bar{s}s)d = d\bar{u} u\bar{d} + d\bar{d} d\bar{d} + d\bar{s} s\bar{d}, \quad (7.3)$$

which, in terms of the pseudo-scalar mesons, corresponds to

$$\sum_i d\bar{q}_i q_i \bar{d} = \pi^+ \pi^- + \frac{1}{2} \pi^0 \pi^0 - \frac{1}{\sqrt{3}} \pi^0 \eta + K^0 \bar{K}^0 + \frac{1}{6} \eta \eta \quad (7.4)$$

where the numerical factors are the Clebsch–Gordan factors.

In the $D^+ \rightarrow \pi^- \pi^+ \pi^+$ decay, the S -wave would be formed by the reactions $a'b' \rightarrow \pi^+ \pi^-$, with $a'b' = \pi^+ \pi^-, \pi^0 \pi^0, \pi^0 \eta, K^0 \bar{K}^0$ and $\eta \eta$. In the $D_s^+ \rightarrow \pi^- \pi^+ \pi^+$ decay, on the other hand, one would have $s(\bar{u}u + \bar{d}d + \bar{s}s)\bar{s}$, which corresponds to

$$\sum_i s\bar{q}_i q_i \bar{s} = K^+ K^- + K^0 \bar{K}^0 + \frac{1}{3} \eta \eta, \quad (7.5)$$

leading to a different set of reactions $ab \rightarrow \pi^- \pi^+$ and, therefore, to different S -wave amplitudes. In this picture, the lack of an $f_0(500)$ contribution in the D_s^+ decay reinforces the interpretation of this resonance as a dynamical pole of the $\pi\pi$ scattering. The $f_0(980)$ is known to couple strongly to $K\bar{K}$, and that would explain why this state is much more prominent in D_s^+ than in D^+ .

All the above aspects can be seen in Fig. 53, where the $\pi^+ \pi^-$ S -wave amplitude obtained from the $D_s^+ \rightarrow \pi^- \pi^+ \pi^+$ decay is compared to that obtained by the QMIPWA fit of the $D^+ \rightarrow \pi^- \pi^+ \pi^+$. The results of QMIPWA of the two channels confirm the conclusions from the model-dependent analyses: in both D^+ and D_s^+ decays, there is a significant dominance of the S -wave, but with very different composition in each case. The only source for the observed differences is the quark content of the initial state after the decay of the c quark.

The $\pi\pi$ S -wave: decay and scattering

In Figure 58, the phase of the S -wave amplitude from the $D_s^+ \rightarrow \pi^- \pi^+ \pi^+$ decay is compared to the scalar-isoscalar phase shift δ_0^0 from $\pi^+ \pi^- \rightarrow \pi^+ \pi^-$ scattering [17]. The phase of the $\pi\pi$ scattering amplitude starts from zero at the threshold, as chiral symmetry requires. The scattering is elastic up to the opening of the $K\bar{K}$ threshold (~ 1 GeV). In the D_s^+ case, the phase starts at $\sim -200^\circ$, which could be a heritage of the production amplitude. The difference in the shape below 1 GeV is more evident when the phase D_s^+ decay is shifted by 210° . From 1 GeV up to 1.2 GeV, the shape of the two phases is in qualitative agreement. This is expected since this region is dominated by the $f_0(980)$. But below 1 GeV and above 1.4 GeV the two phases are clearly incompatible.

After the opening of the $K\bar{K}$ channel, in the inelastic regime, the two phases can no longer be compared. Nevertheless, in both cases, an acceleration of the phase motion at higher values of $m(\pi^+ \pi^-)$ is observed, indicating the presence of one or more scalar resonances. One should keep in mind that the scattering data are $\pi\pi \rightarrow \pi\pi$, whereas the phase in $D_s^+ \rightarrow \pi^- \pi^+ \pi^+$ would include all possible coupled channels, $ab \rightarrow \pi\pi$, as

discussed above. The comparison between the S -wave phases indicates that phases from scattering experiments could not be used directly in decay amplitudes. A production amplitude needs to be accounted for.

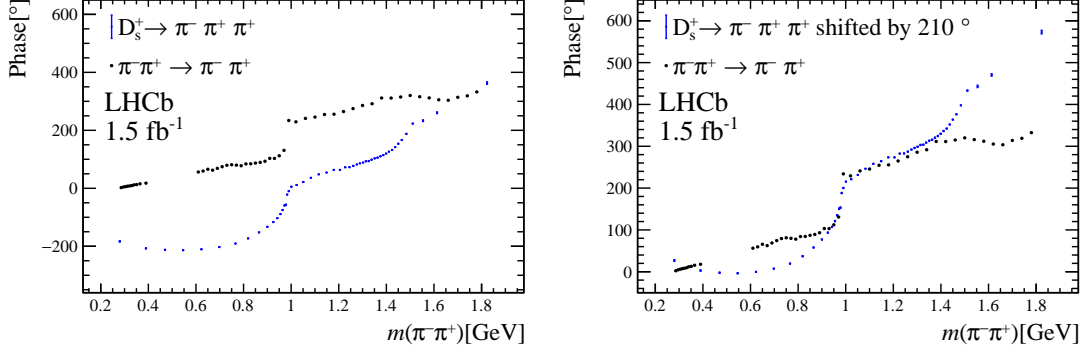


Figure 58 – (Left) Comparison of the $\pi^+\pi^-$ S -wave phase from $D_s^+ \rightarrow \pi^-\pi^+\pi^+$ decays and the phase from $\pi^+\pi^- \rightarrow \pi^+\pi^-$ scattering. Data on $\pi^+\pi^- \rightarrow \pi^+\pi^-$ scattering above 0.6 GeV are from a re-analysis [17] of original data from [18], and below 0.4 GeV are from K_{e4} decays [19]. (Right) The S -wave phase from the $D_s^+ \rightarrow \pi^-\pi^+\pi^+$ decay is shifted by 210° .

7.2 The $\pi^+\pi^-$ P -wave

$\rho(770)^0$ and $\omega(782)$

One remarkable result of this analysis is the first observation of the decay $D_s^+ \rightarrow \omega(782)\pi^+$ in the $\pi^-\pi^+\pi^+$ final state. A fit without the $\omega(782)$ is significantly worse than the default one (see model PWA-3 in Appendix C). The $\pi^+\pi^-$ mass spectrum of candidates from the $D_s^+ \rightarrow \pi^-\pi^+\pi^+$ signal region is shown in Figs. 39 and 59. The plot shows candidates after (left) and before (right) the $f_0(980)$ band. The $\omega(782)$ signal is very clear, the presence of the $\rho(770)^0$ is barely seen in the lower side of the $\omega(782)$ mass peak.

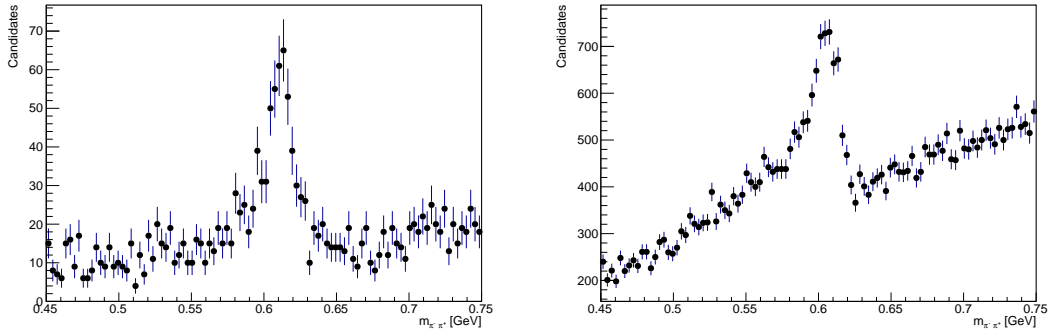


Figure 59 – The $m(\pi^+\pi^-)$ spectrum near the $\rho(770)^0$. The spectrum is divided into two regions, after (left) and before (right) the $f_0(980)$ band in the crossed channel.

The possibility that the $\omega(782)$ signal is part of the background was investigated by plotting the $\pi^+\pi^-$ invariant mass of candidates from the sidebands. The invariant mass distributions are shown in Fig. 61. The plots on the top panel contain the distribution of the $\pi^+\pi^-$ invariant mass of candidates from the left sideband. The lower panel shows the distribution of $m(\pi^+\pi^-)$ from the right sideband. The plots on the left (right) are of candidates before (after) the $f_0(980)$ band in the Dalitz plot. No mass peak at $\omega(782)$ mass can be seen in these plots, demonstrating that the observed $\omega(782)$ signal does not come from the background.

The $\omega(782) \rightarrow \pi^+\pi^-$ decay is observed in different reactions, always in conjunction with a prominent $\rho(770)^0$ signal, with the $\rho - \omega$ mixing assumed to be the dominant mechanism for the $\omega(782)$ production. The $\omega(782)$ is observed both in $e^+e^- \rightarrow \pi^+\pi^-$ and in decays having a $\pi^+\pi^-$ pair in the final state, such as $D^+ \rightarrow \pi^-\pi^+\pi^+$, $B^0 \rightarrow J/\psi\pi^+\pi^-$ [16] or $B^+ \rightarrow \pi^+\pi^+\pi^-$ [86]. The interference with the small $\omega(782)$ component distorts the lineshape of the $\rho(770)^0$. In decays, the $\omega(782)$ signal arises as a second peak close to that of the $\rho(770)^0$, instead of the depletion of the $\rho(770)^0$ peak observed in the pion electromagnetic form factor [87].

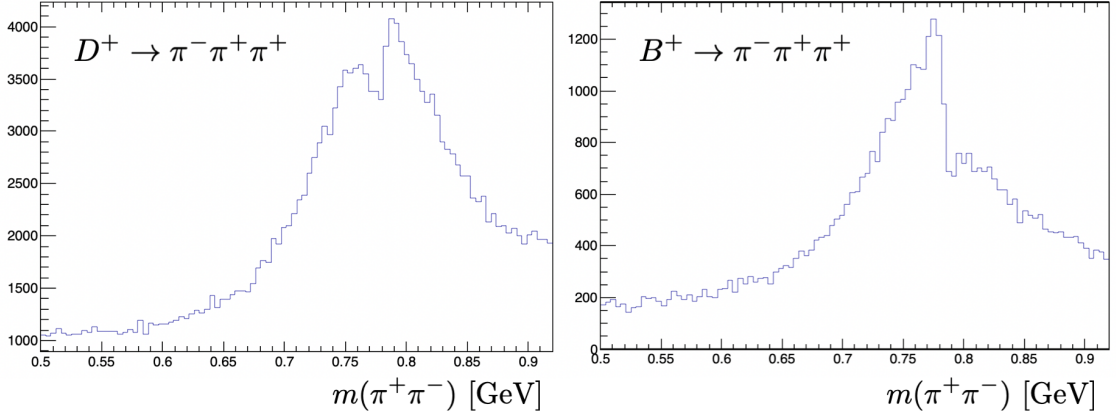
The difference in the interference pattern between the $\rho(770)^0$ and $\omega(782)$ can be understood considering that in $e^+e^- \rightarrow \pi^+\pi^-$ the photon couples to the charges of the quark-antiquark pair,

$$j_{EM}^\mu = \frac{2}{3}\bar{u}\gamma^\mu u - \frac{1}{3}\bar{d}\gamma^\mu d = \frac{1}{2}(\bar{u}\gamma^\mu u - \bar{d}\gamma^\mu d) + \frac{1}{6}(\bar{u}\gamma^\mu u + \bar{d}\gamma^\mu d),$$

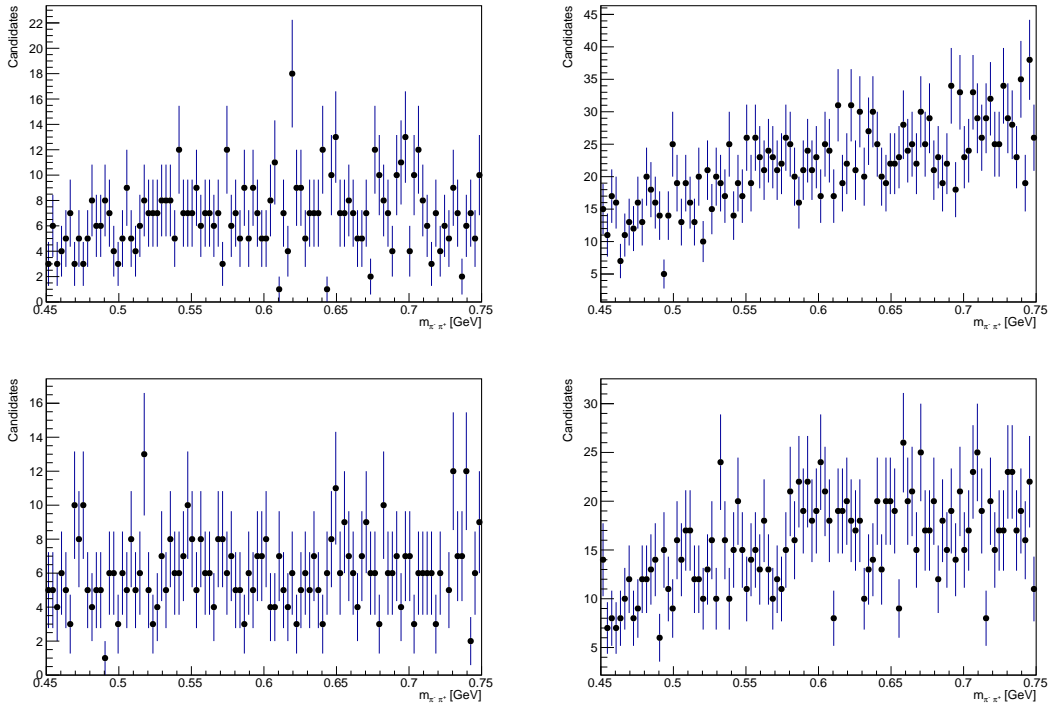
whilst in the $D^+ \rightarrow \pi^-\pi^+\pi^+$ decay, the $\rho(770)^0$ is produced from a $d\bar{d}$ source,

$$\bar{d}\gamma^\mu d = -\frac{1}{2}(\bar{u}\gamma^\mu u - \bar{d}\gamma^\mu d) + \frac{1}{2}(\bar{u}\gamma^\mu u + \bar{d}\gamma^\mu d).$$

It is remarkable, though, that in the case of the $B^+ \rightarrow \pi^+\pi^+\pi^-$, the effect of the $\rho - \omega$ mixing is similar to that observed in $e^+e^- \rightarrow \pi^+\pi^-$, as shown in Fig. 60. This intriguing feature could be associated with CP violation effects. However, according to LHCb-ANA-2019-052 [88], there is no CP violation when the data is integrated over the helicity angle, although small CP violation signals of opposite sign are observed in the cross-channel projection, the turning point being the zero of the $\rho(770)^0$ angular distribution.

Figure 60 – The $m(\pi^+\pi^-)$ spectrum near the $\rho(770)^0$.

In the $D^+ \rightarrow \pi^-\pi^+\pi^+$ decay, as well as in $e^+e^- \rightarrow \pi^+\pi^-$ and the B decays discussed above, the fit fraction of the $\omega(782)$ is less than 1% of that of the $\rho(770)^0$. In the $D_s^+ \rightarrow \pi^-\pi^+\pi^+$ decay, the contribution of the $\rho(770)^0\pi^+$ amplitude is minimal and the ratio between the fit fractions of the $\omega(782)\pi^+$ and $\rho(770)^0\pi^+$, $R_{\omega/\rho}$, is about 1/3 compared to 1/250 in $D^+ \rightarrow \pi^-\pi^+\pi^+$. The significant value of $R_{\omega/\rho}$ is a unique feature of the $D_s^+ \rightarrow \pi^-\pi^+\pi^+$ decay. It means that these resonances are produced by different mechanisms in $D_s^+ \rightarrow \pi^-\pi^+\pi^+$ and $D^+ \rightarrow \pi^-\pi^+\pi^+$ decays. With the present data set, it is not possible to identify the contributions from the direct production of the $\omega(782)$ and its production through $\rho - \omega$ mixing.

Figure 61 – The $m(\pi^+\pi^-)$ spectrum near the $\rho(770)^0$ for background sidebands. The spectrum is divided into two regions, before (left) and after (right) the $f_0(980)$ band in the crossed channel for the left (top) and the right (bottom) sidebands.

In the quark model, the physical states $\omega(782)$ and the $\phi(1020)$ are isoscalar states with the same J^{PC} and therefore mix. The SU(3) wave functions are

$$\psi_1 = \frac{1}{\sqrt{3}}(u\bar{u} + d\bar{d} + s\bar{s}), \quad \psi_8 = \frac{1}{\sqrt{6}}(u\bar{u} + d\bar{d} - 2s\bar{s}).$$

The $\phi(1020)$ is the octet state, $\phi = \psi_8 \cos \theta - \psi_1 \sin \theta$, whereas the $\omega(782)$ is the singlet state, $\omega = \psi_8 \sin \theta + \psi_1 \cos \theta$, with SU(3) nonet mixing angle θ being in the range [36-42°]. This means that the $\omega(782)$ has a small $s\bar{s}$ component in the wave function, so in the $D_s^+ \rightarrow \pi^- \pi^+ \pi^+$ decay it could be produced directly from the $s\bar{s}$ source and then decay into $\pi^+ \pi^-$ through the OZI allowed direct decay, as depicted in Fig 62. This mechanism, however, would be more relevant in the $D^+ \rightarrow \pi^- \pi^+ \pi^+$ decay since the $\omega(782)$ has a larger $n\bar{n}$ component in his wave function.

The $\rho(770)^0$ is a $\frac{1}{\sqrt{2}}(d\bar{d} - u\bar{u})$ state and could also be produced directly from the $d\bar{d}$ source in the $D^+ \rightarrow \pi^- \pi^+ \pi^+$ decay. This could not happen from the $s\bar{s}$ source in $D_s^+ \rightarrow \pi^- \pi^+ \pi^+$. At tree-level, the only alternative for the $\rho(770)^0$ production in the $D_s^+ \rightarrow \pi^- \pi^+ \pi^+$ decay would be the W-annihilation amplitude, shown in Fig. 63. The annihilation diagram is suppressed compared to the external W-emission, which could explain the large difference in the $\rho(770)^0$ fit fraction measured in the two decays. However, if it was the mechanism for the $\omega(782)$ production in $D_s^+ \rightarrow \pi^- \pi^+ \pi^+$, one would have the ratio $R_{\omega/\rho}$ similar to that of the $D^+ \rightarrow \pi^- \pi^+ \pi^+$ decay.

There is another alternative, pointed out by Cheng and Chian [20] and Yu, Hsiao and Ke [89]. The $\omega(782)$ could also be produced by G-parity conserving, long-distance, final-state rescattering, as shown in Fig. 64. Amplitudes with loops such as that of Fig. 64 are suppressed, but there is a compensation from the large branching fractions $\mathcal{B}(D_s^+ \rightarrow \eta \rho^+) = (8.9 \pm 0.8)\%$ and $\mathcal{B}(D_s^+ \rightarrow \eta' \rho^+) = (5.8 \pm 1.5)\%$ [21]. Owing to G-parity conservation, this mechanism would not be possible for the $\rho(770)^0$ production since the $\eta^{(\prime)} \rho(770)^+$ cannot rescatter into $\pi^+ \rho(770)^0$. The FSI would be a good candidate for the dominant process for the $\omega(782)$ production in $D_s^+ \rightarrow \pi^- \pi^+ \pi^+$ decay, providing a qualitative explanation for the significant value of $R_{\omega/\rho}$ ratio.

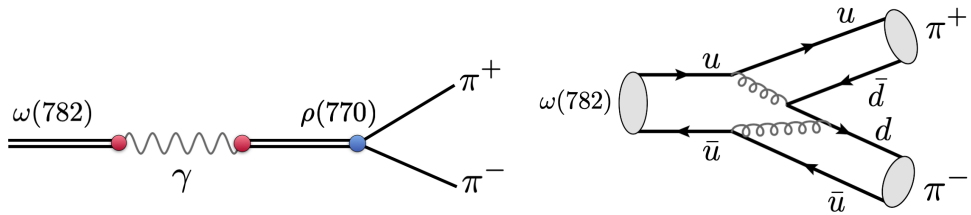


Figure 62 – The mechanisms for the $\omega(782) \rightarrow \pi^+ \pi^-$ decay: the $\omega - \rho$ mixing, on the left, and the “direct” decay.

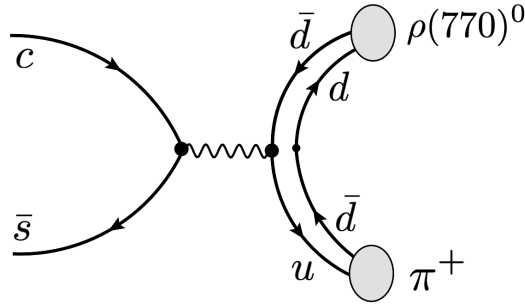


Figure 63 – The annihilation diagram of $D_s^+ \rightarrow \pi^- \pi^+ \pi^+$ decay, showing how the $\rho(770)^0$ could be formed.

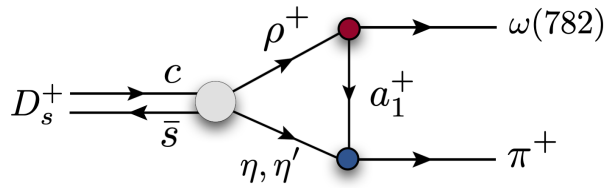


Figure 64 – A mechanism for $\omega(782)$ production in $D_s^+ \rightarrow \pi^- \pi^+ \pi^+$ decays, proposed by the Cheng and Chiang [20].

$\rho(1450)^0$ and $\rho(1700)^0$

The data description requires two ρ -like resonances in the region $1.4 \lesssim m(\pi^+ \pi^-) \lesssim 1.8$ GeV, with comparable contributions to the decay amplitude. The combination of two overlapping ρ -like states in this region is also required to explain some different sets of data, such as $p\bar{p}$ [90] and pn [91] annihilation at rest, $\tau^- \rightarrow \pi^- \pi^0 \nu_\tau$ decays [92] or $e^+ e^- \rightarrow \pi^+ \pi^- \gamma$ cross-section with initial state radiation [93].

These states are identified as the $\rho(1450)^0$ and $\rho(1700)^0$ mesons. The existence of both resonances is established, although their structures are still uncertain. In the PDG review “Quark Model”, it is suggested that the two vector mesons have the same structure as the ground state $\rho(770)^0$: both would be $\frac{1}{\sqrt{2}}(d\bar{d} - u\bar{u})$ states, the $\rho(1450)^0$ being the first radial and $\rho(1700)^0$ the first orbital excitation. Both decays into two and four pions, but the $K\bar{K}$ channel was observed only in $\rho(1700)^0$ decays.

As discussed previously, in the $D_s^+ \rightarrow \pi^- \pi^+ \pi^+$ decay, states with no strange quarks could be produced, at tree level, only through the suppressed W -annihilation amplitude (Fig. 63). If the two ρ -like resonances are indeed $(d\bar{d} - u\bar{u})$ states, this could explain the small fit fraction of the P -wave. But this explanation would raise another problem. If the $\rho(1450)^0$ and $\rho(1700)^0$ are indeed excited states and lying close to the edge of the phase space, it is rather surprising that the combined fit fraction of the two ρ -like resonances is five times larger than that of the $\rho(770)^0$, the ground state meson. Whilst the existence of these states is established, their nature and production mechanisms are still uncertain.

A strong correlation exists between the fit fractions and the masses and widths of these states, implying larger uncertainties on the individual contributions. However, the fit fraction of the combination of the $\rho(1450)^0$ and $\rho(1700)^0$ is a stable quantity, found to be $(6.14 \pm 0.27)\%$. This result is comparable with that from the $D^+ \rightarrow \pi^- \pi^+ \pi^+$ decay, $(7.1 \pm 0.9)\%$. The combined contribution of the two ρ -like resonances is surprisingly high if these states are to be interpreted as excitations of the $\rho(770)^0$. The agreement between the combined contribution in $D_s^+ \rightarrow \pi^- \pi^+ \pi^+$ and $D^+ \rightarrow \pi^- \pi^+ \pi^+$ decays is intriguing, given that the fit fraction of the $\rho(770)^0$ is only $(1.038 \pm 0.054)\%$, in sharp contrast with the value $(26.0 \pm 0.3)\%$ found in the $D^+ \rightarrow \pi^- \pi^+ \pi^+$ decay.

7.3 The $\pi^+ \pi^-$ D -wave

The D -wave contains two states, the $f_2(1270)$ and the $f_2'(1525)$. As is the case of the vector mesons, there are two SU(3) states with the same J^{PC} that mix and give rise to the physical mesons,

$$f_2(1270) = \psi_8 \sin \theta_T + \psi_1 \cos \theta_T, \quad f_2'(1525) = \psi_8 \cos \theta_T - \psi_1 \sin \theta_T,$$

with $\theta_T \sim 27^\circ$ and

$$\psi_1 = \frac{1}{\sqrt{3}}(u\bar{u} + d\bar{d} + s\bar{s}), \quad \psi_8 = \frac{1}{\sqrt{6}}(u\bar{u} + d\bar{d} - 2s\bar{s}).$$

After computing the numerical factors, one has

$$f_2(1270) = 1.38n\bar{n} - 0.33s\bar{s}, \quad f_2'(1525) = 0.2n\bar{n} - 0.98s\bar{s} \quad (n\bar{n} \equiv u\bar{u} + d\bar{d}).$$

Indeed, the assigned quark content of the two tensor states is consistent with the observed branching fractions,

$$\frac{\mathcal{B}(f_2(1270) \rightarrow K\bar{K})}{\mathcal{B}(f_2(1270) \rightarrow \pi\pi)} = \frac{4.6}{84.8}, \quad \frac{\mathcal{B}(f_2'(1525) \rightarrow K\bar{K})}{\mathcal{B}(f_2'(1525) \rightarrow \pi\pi)} = \frac{88.7}{10.4}.$$

The small fit fraction of the $f_2'(1525)$ in the $D_s^+ \rightarrow \pi^- \pi^+ \pi^+$ decay is consistent with this picture, but one would expect the $f_2(1270)$ to be produced at a higher rate from a $d\bar{d}$ source in the $D^+ \rightarrow \pi^- \pi^+ \pi^+$ decay, compared to the rate from an $s\bar{s}$ source, as in the $D_s^+ \rightarrow \pi^- \pi^+ \pi^+$ decay. Yet, the fit fractions of the $f_2(1270)$ are found to be the same in both cases, which is rather intriguing.

7.4 Summary and conclusions

This work performs the Dalitz plot analysis of the decay $D_s^+ \rightarrow \pi^- \pi^+ \pi^+$. Using a large sample containing over seven hundred thousand candidates, with a purity of 95%,

the resonant structure of the decay and the $\pi^+\pi^-$ amplitude in S -wave was determined using the QMIPWA approach.

The data is described by a model with contributions from S -, P - and D -waves. The P -wave has four components, corresponding to the resonances $\rho(770)^0$, $\omega(782)$, $\rho(1450)^0$ and $\rho(1700)^0$. The D -wave contains two states: the $f_2(1270)$ and the $f'_2(1525)$. Both states populate a large area of the phase space. The $f_2(1270)$ have the second largest contribution (13%), while $f'_2(1525)$ has a very tiny contribution (0.05%). The S -wave corresponds to nearly 85% of the decay rate. The contribution of each amplitude, expressed as fit fractions (in %), are summarised in Table 16.

Table 16 – The resonant structure of the $D_s^+ \rightarrow \pi^-\pi^+\pi^+$ decay. The fit fractions are in %. The first uncertainty is statistical, the second experimental, and the third is the uncertainty due to the fit model.

S -wave	84.97	\pm 0.14	\pm 0.30	\pm 0.63
$\rho(770)^0\pi^+$	1.038	\pm 0.054	\pm 0.097	\pm 0.11
$\omega(782)\pi^+$	0.360	\pm 0.016	\pm 0.034	\pm 0.016
$\rho(1450)^0\pi^+$	3.86	\pm 0.15	\pm 0.14	\pm 2.0
$\rho(1700)^0\pi^+$	0.365	\pm 0.050	\pm 0.045	\pm 0.34
$(\rho(1450)^0 + \rho(1700)^0)\pi^+$	6.14	\pm 0.27	\pm 0.34	\pm 1.9
$f_2(1270)\pi^+$	13.69	\pm 0.14	\pm 0.22	\pm 0.54
$f'_2(1525)\pi^+$	0.0455	\pm 0.0070	\pm 0.015	\pm 0.017

The resonant structure of the $D_s^+ \rightarrow \pi^-\pi^+\pi^+$ decay from this analysis agrees with previous determinations from BaBar [22] and BESIII [23], as summarized in Table 17. The fit fractions are expressed in %, and the statistical and systematic uncertainties are added in quadrature.

Table 17 – The resonant structure of the $D_s^+ \rightarrow \pi^-\pi^+\pi^+$ decay from this analysis compared to previous determinations from BaBar [22] and BESIII [23]. The fit fractions are given in %. The statistical and systematic uncertainties are added in quadrature.

mode	this result	BaBar	BESIII
S -wave	84.97 \pm 0.64	83.0 \pm 2.1	84.2 \pm 1.4
$\rho(770)^0\pi^+$	1.038 \pm 0.12	1.8 \pm 1.1	0.9 \pm 0.8
$\omega(782)\pi^+$	0.360 \pm 0.022	-	-
$\rho(1450)^0\pi^+$	3.86 \pm 2.0	2.3 \pm 1.9	1.3 \pm 0.8
$\rho(1700)^0\pi^+$	0.37 \pm 0.34	-	-
$(\rho(1450)^0 + \rho(1700)^0)\pi^+$	6.14 \pm 1.9	-	-
$f_2(1270)\pi^+$	13.60 \pm 0.51	10.1 \pm 1.9	10.5 \pm 1.4
$f'_2(1525)\pi^+$	0.0455 \pm 0.0011	-	-

Remarkable differences between the D^+ and D_s^+ decays are observed in the S -wave, as shown in Fig. 53. The broad structure near the threshold observed in the $D^+ \rightarrow \pi^-\pi^+\pi^+$

decay, associated with the $f_0(500)$ resonance according to model-dependent analyses, is absent in the $D_s^+ \rightarrow \pi^- \pi^+ \pi^+$ Dalitz plot. On the other hand, in the D_s^+ decay, the peak corresponding to the $f_0(980)$ is much more prominent in the D_s^+ decay. Despite the striking differences observed in the phase motion, in both cases, there is an activity at $m(\pi^+ \pi^-) \sim 1.45$ GeV, indicating the presence of at least one scalar state in this region. In fact, the inspection of the $D_s^+ \rightarrow \pi^- \pi^+ \pi^+$ Dalitz plot in Fig. 38, shows a typical interference pattern between the $f_0(980)$ and another scalar resonance at $s_{\pi^+ \pi^-} \sim 2.2$ GeV². The measured S -wave amplitude is in good agreement with previous determinations, as shown in Fig. 47, where the result of this analysis is represented in blue, with all uncertainties included.

The features discussed above support the idea of the $\pi^+ \pi^-$ system in S -wave being produced by rescattering of pseudo-scalar mesons originated from a $d\bar{d}$ source, in the case of the D^+ decay and from an $s\bar{s}$ source in the case of the D_s^+ decay. This mechanism would result in different sets of coupled channels in each decay, which would qualitatively explain the discrepancies between the resonant structures, as well as the differences to the $\delta_{I=0}^0$ phase of $\pi^+ \pi^-$ scattering. A similar pattern is observed in decays of neutral B mesons into J/ψ and two charged pions.

Many different data sets require the presence of two broad vector resonances interfering in the region 1.4-1.8 GeV, identified as the $\rho(1450)^0$ and $\rho(1700)^0$. These states have significant uncertainties regarding their masses and widths. The attempt to determine the resonance parameters revealed a strong correlation between masses and widths, and fit fractions, preventing a precise measurement of the individual contribution of each state. However, the fit fraction of the combined ρ -like amplitudes, amounting to approximately 6%, is stable and does not depend on the precise values of the $\rho(1450)^0$ and $\rho(1700)^0$ masses and widths. The uncertainty on these parameters has a small impact on the S - and D -waves.

At tree level in the $D_s^+ \rightarrow \pi^- \pi^+ \pi^+$ decay, resonances with no strange quarks in the wave function, such as the $\rho(770)^0$, could be produced only through the suppressed W -annihilation amplitude. The small contribution of the $\rho(770)^0$ could be interpreted as an indication of the magnitude of W -annihilation amplitude relative to the W -radiation. An intriguing aspect is the combined $\rho(1450)^0$ and $\rho(1700)^0$ fit fraction, almost five times larger than that of the $\rho(770)^0$, which challenge the interpretation of these resonances as $\rho(770)^0$ excited states.

The decay $D_s^+ \rightarrow \omega(782)\pi^+$ is observed for the first time in the $D_s^+ \rightarrow \pi^- \pi^+ \pi^+$ decay. The $\omega(782) \rightarrow \pi^+ \pi^-$ decay has been observed in different reactions through the $\rho - \omega$ mixing mechanism. In all cases, the $\omega(782)$ is a small fraction of the $\rho(770)^0$ signal. The unique feature of the $D_s^+ \rightarrow \pi^- \pi^+ \pi^+$ decays is the relatively large ratio $R_{\omega/\rho}$ of the $\omega(782)$ and $\rho(770)^0$ contributions, approximately thirty times larger than in $D^+ \rightarrow \pi^- \pi^+ \pi^+$

decay or any other reactions.

The large value of $R_{\omega/\rho}$ indicates different $\omega(782)$ production mechanisms in $D_s^+ \rightarrow \pi^- \pi^+ \pi^+$ and $D^+ \rightarrow \pi^- \pi^+ \pi^+$ decays. The authors of Ref. [20] suggest that the long-distance rescattering, depicted in Fig. 64, is the most important process for the $\omega(782)$ production in $D_s^+ \rightarrow \pi^- \pi^+ \pi^+$ decays. This mechanism could not produce $\rho(770)^0$ due to G-parity conservation.

The S -wave determination is an essential input to phenomenological analyses. The $D_{(s)}^+ \rightarrow \pi^- \pi^+ \pi^+$ decays are the only processes in which the $\pi^+ \pi^-$ scattering amplitude can be obtained continuously from threshold up to energies of 1.7-1.8 GeV, once the role of three-body FSI is understood. Moreover, the present analysis results demonstrate that scattering amplitudes should not be used directly in models of decay amplitudes.

8 Thechnical contributions for LHCb Upgrade

This chapter comprises the contributions to the LHCb Upgrade. The contributions are related to the HLT1 GPU trigger and Ecal software calibration.

8.1 HLT1 GPU trigger lines

The contribution to the HLT1 GPU trigger consists of the implementation of the two radioactive trigger lines: The $B_{(s)}^0 \rightarrow \gamma\gamma$ and $\pi^0 \rightarrow \gamma\gamma$. Both lines were implemented in cooperation with Murilo Santana Rangel and Lucas Meyer from Universidade Federal do Rio de Janeiro (UFRJ). This project was a contribution of RTA-Rio to the LHCb RTA.

The lines were implemented and merged to the Allen project in the GitLab [94]. The software consists of a series of CUDA, C++ and Python scripts. The latter is used to configure the parameters of the trigger lines.

The decays $B^0 \rightarrow \gamma\gamma$ and $B_s^0 \rightarrow \gamma\gamma$ are of particular interest for searching physics beyond the Standard Model [95, 96]. The former is theoretically interesting because it allows for a study of the non-trivial QCD effects of the B decay. Additionally, since the two-photon final state can be in a CP-even or CP-odd final state, this decay could be a non-traditional channel to study CP violation. The latter is induced by flavour-changing neutral current FCNC at the loop level in the standard model SM. Therefore, it allows us to test the flavour structure of the SM.

These channels have not been observed yet; however, their experimental upper limits were reported by BaBar [97] and Belle[98] collaborations

$$\begin{aligned}\mathcal{B}(B^0 \rightarrow \gamma\gamma) &< 3.2 \times 10^{-7} \quad \text{at 90\% CL,} \\ \mathcal{B}(B_s^0 \rightarrow \gamma\gamma) &< 3.2 \times 10^{-7} \quad \text{at 90\% CL}\end{aligned}$$

about one order of magnitude above SM prediction [99, 100]

$$\begin{aligned}\mathcal{B}(B^0 \rightarrow \gamma\gamma) &= 1.5_{-0.7}^{+1.4} \times 10^{-8}, \\ \mathcal{B}(B^0 \rightarrow \gamma\gamma) &= 3.0_{-1.6}^{+1.8} \times 10^{-7}\end{aligned}$$

motivating a dedicated search at the LHCb experiment.

The $\pi^0 \rightarrow \gamma\gamma$ decay has a branching fraction of 98.8% [21]. Due to this large production, it is used to perform the fine calibration of ECAL cells. The fine calibration of ECAL is essential to ensure precise measurements of radioactive decays such as the $B_{(s)}^0 \rightarrow \gamma\gamma$, $B^0 \rightarrow K^{*0}\gamma$ and $B_s^0 \rightarrow \phi\gamma$.

Photons are defined as 3x3 clusters of ECAL cells in which the total energy (E_γ)¹ is consistent with the signal of a single photon. To reconstruct the $\gamma\gamma$ final state particles, pairs of clusters are combined according to the position and energy. To reduce the huge number of possible combinations, a selection is applied in the transverse energy ($E_T(\gamma)$) of each cluster and the total energy of the two clusters $E_T(\gamma_1\gamma_2)$. An additional efficient selection is applied on each cluster's E_{19} variable. The E_{19} is the ratio between the most energetic cell of the cluster, called *seed* cell, and the total energy of the cluster. An additional selection is applied to the invariant mass of the two clusters $m(\gamma_1\gamma_2)$, which is calculated using the energy and position.

$$m(\gamma_1\gamma_2)^2 = 2E_1^\gamma E_2^\gamma \cos(\theta_{\gamma_1\gamma_2}) \quad (8.1)$$

A final selection is performed on the transverse momentum $p_T(\gamma_1\gamma_2)$ of the reconstructed particle candidate. Table 18 shows the selection applied in each trigger line. The selections were decided using simulation samples. Figure 65 left shows simulated candidates of $B_s^0 \rightarrow \gamma\gamma$ selected by the $B_s^0 \rightarrow \gamma\gamma$ HLT1 trigger line. The right plot shows real data candidates of π^0 selected by the $\pi^0 \rightarrow \gamma\gamma$ line.

Variable	B_s^0 selection	π^0 selection
min_ $m(\gamma_1\gamma_2)$	>3000 MeV	>50 MeV
max_ $m(\gamma_1\gamma_2)$	>8000 MeV	>300 MeV
min_ $p_T(\gamma_1\gamma_2)$	>1000 MeV	>1000 MeV
min_ $E_T(\gamma)$	>2500 MeV	>200 MeV
min_ $E_T(\gamma_1\gamma_2)$	>0	>400 MeV
min_ E_{19}	>0.6	>0.7

Table 18 – The trigger requirements of $B_s^0 \rightarrow \gamma\gamma$ and $\pi^0 \rightarrow \gamma\gamma$ respectively.

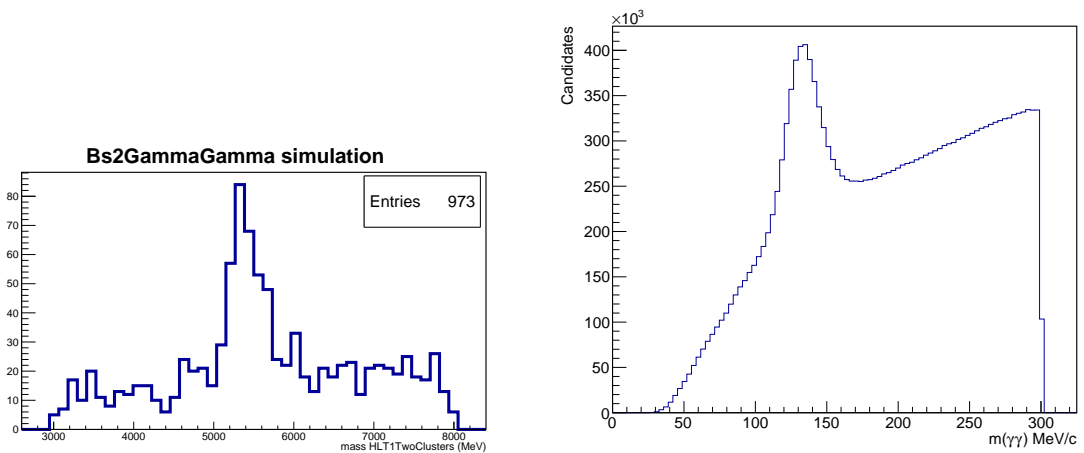


Figure 65 – (Left) The invariant mass $B_s^0 \rightarrow \gamma\gamma$ (simulation). (Right) The invariant mass of $\pi^0 \rightarrow \gamma\gamma$ (real data).

¹ $E_\gamma = \sum_i E_i$, where E_i is the energy of each cell of the cluster

8.2 The ECAL π^0 Calibration

The ECAL calibration is divided into the following steps: the adjustment of the energy scale, energy flow calibration and fine calibration of the ECAL cells [101].

The energy scale of an ECAL cell is defined by adjusting the PMT gain to the nominal operational value $G_{nominal}$, which is determined by the LED monitoring system. Light flashes of known intensity are emitted by LED and transported to the cell PMT and a PIN-diode. The intensity of the signal of the PMT is normalised by the PIN-diode response so that the average PMT gain can be determined. The PMT gain is then adjusted by the value of HV supplied to the PMT.

The energy flow calibration equalizes the gain of cell PMTs in each of the 3 ECAL zones. Fluctuations of the flux among neighbouring cells due to initial miscalibration are smoothed by averaging the energy flow over clusters of 3×3 cells and exploiting the symmetry of the energy flow over the calorimeter surface. This procedure allows to equalise the calibration and give calibration coefficients, but the π^0 response is used for the absolute calibration.

The fine-tuning of ECAL PMT is performed using the $\pi^0 \rightarrow \gamma\gamma$ decay. This was my main contribution to the Upgrade. During seven months in 2023 hosted at CERN, I contributed to developing the π^0 calibration package. This project was supervised by Ulrich Uwer (Heidelberg) and Rosen Matev (CERN). Yang Gao (Central China Normal University) performed the π^0 selection studies.

Figure 66 shows the steps of the π^0 calibration. The π^0 candidates are reconstructed as mentioned in the previous section and then selected following the requirements of table 18. In Run 1 and Run 2, the calibration used π^0 candidates reconstructed from simulated minimum bias samples, requiring both HLT1 and HLT2 steps. Thanks to the effort in developing a dedicated π^0 line in the HLT1 trigger, the Run 3 calibration can collect and use candidates just after HLT1. The output candidates are saved in the storage in a ROOT format during the tupling step.

Invariant mass histograms are built for each ECAL cell (a total of 6016). Each of these histograms is fitted by a Gaussian function representing the π^0 signal plus a second-degree polynomial function representing the noise. The free parameters of the fit are the polynomial coefficients ($c_i, i = 0, \dots, 2$), and the mean μ and the standard deviation σ of the Gaussian. The μ parameter is allowed to vary around the nominal mass of the π^0 , and the σ is allowed to vary in the interval $4 < \sigma < 15$ MeV. This process is repeated six times. In each iteration, new calibration constants λ are determined for each cell according to the expression

$$\lambda = 1.0 - \frac{\delta M_{\pi^0}}{M_{\pi^0}}, \quad (8.2)$$

where δM_{π^0} is the difference between the fitted mass and the nominal mass M_{π^0} . After the six iterations, a set of calibration constants λ_1 is saved and applied to the Condition DataBase, where the alignment and calibration information of LHCb detectors are saved. This is the end of the called *First Pass* of the calibration.

The role process is repeated once. The only difference is that the reconstruction starts with the calibration information of the First Pass. At the end of the now called *Second Pass*, a set of calibration constants λ_2 is determined. The final calibration constants are given by the product $\lambda_1 \times \lambda_2$ of each cell and are directly applied to the reference used to obtain the new HV values for the PMTs from the LED system.

Two loops

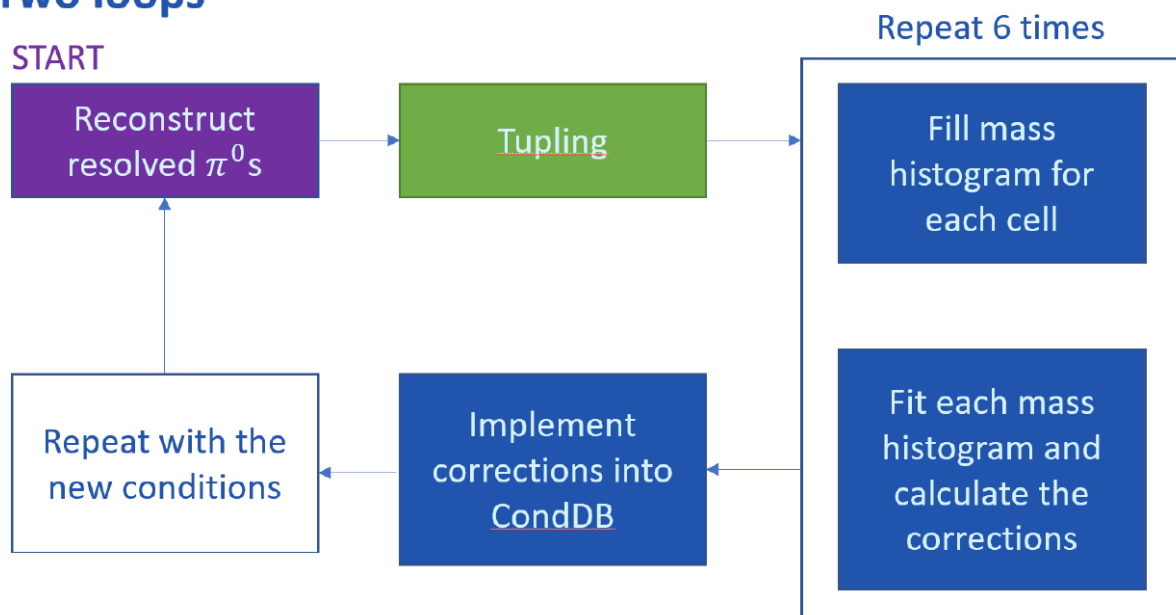


Figure 66 – The π^0 calibration flow.

The new calibration package was tested locally using 50M minimum bias events², see figure 67. Figure 68 shows the fitted mean values of the π^0 masses in each ECAL zone before and after the calibration. The values before the calibration are dispersed. After the calibration, almost all values converged to the π^0 nominal mass.

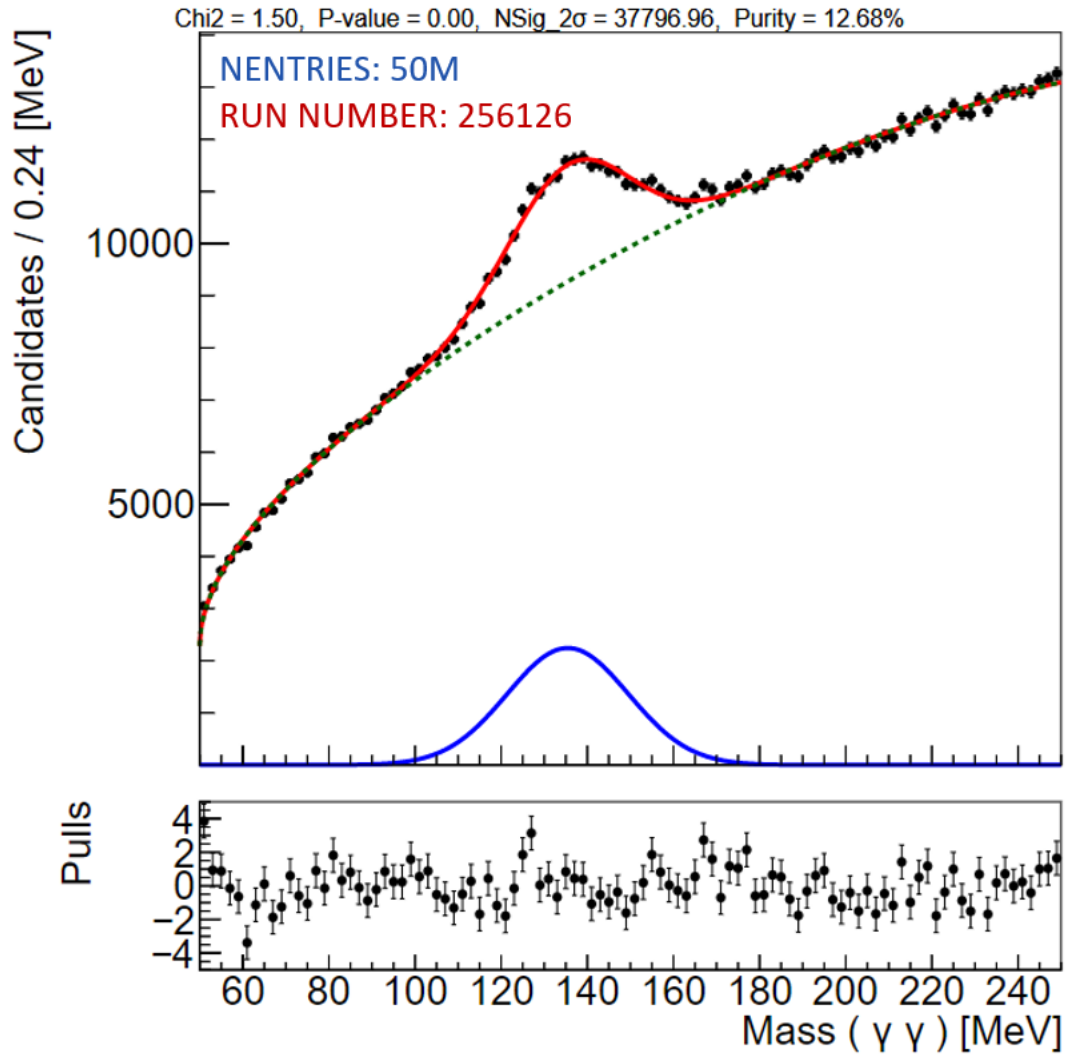
The full integration of the π^0 calibration to the LHCb environment requires the implementation of the calibration routines in the Online system software. It allows the π^0 calibration to use the various computing nodes of EFF and be executed by the Experiment Control System (ECS)³. This task was performed during my last month at CERN and is still being tested.

Therefore, the next steps include:

² Real data was not used because the HLT1 line was implemented close to the end of my stay at CERN. After the tests.

³ The ECS is in charge of the configuration, control and monitoring of all the components of the online system.

- Collect a data sample with about 300M π^0 candidates selected by the HLT1 π^0 trigger line.
- Test the π^0 package integrated to the Online system.
- Perform the first π^0 calibration of Run 3.

Figure 67 – Minimum bias π^0 candidates.

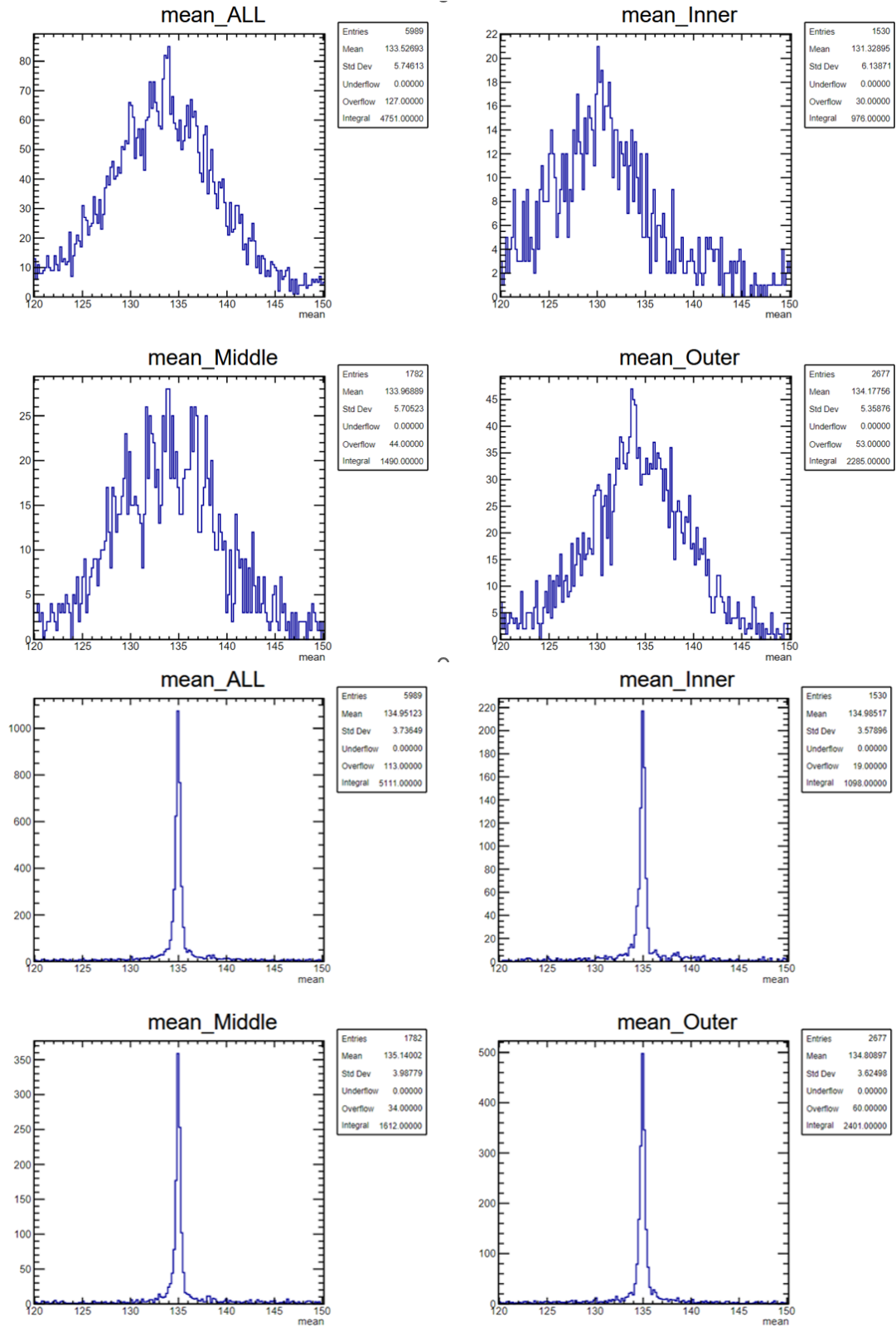


Figure 68 – The histograms of the fitted mean values of the π^0 mass for each ECAL cell and each ECAL zone, (top) before and (bottom) after the calibration. The ALL histograms are the result of merging the three zones.

9 Conclusions

In this thesis, we have presented the amplitude analysis of the $D_s^+ \rightarrow \pi^- \pi^+ \pi^+$ decay. The analysis was performed using $\sim 700k$ candidates with purity of 95%. The resonant structure was determined using a QMIPWA approach. The model consists of contributions from the S-, P- and D-waves. The P-wave component consists of four isobars: $\rho(770)^0$ (1.038%), $\omega(782)$ (0.360%), $\rho(1450)^0$ (3.86%) and $\rho(1700)^0$ (0.365%). The D-wave contains two: $f_2(1270)$ (13.69%) and $f_2(1525)$ (0.0455%). The parenthesized numbers are the fit fractions. The S-wave corresponds to nearly 85% of the decay rate, and is the largest contribution.

The decay channels $D_s^+ \rightarrow \omega(782)\pi^+$, $D_s^+ \rightarrow \rho(1700)^0\pi^+$ and $D_s^+ \rightarrow f_2'(1525)\pi^+$ were observed for the first time in the $D_s^+ \rightarrow \pi^- \pi^+ \pi^+$ decay. The analysis also provided the most precise measurement of the $\pi^- \pi^+$ S-wave decay amplitude, an important input to phenomenological models.

Remarkable differences between D_s^+ and D^+ decays were observed in all components:

- The $\pi^- \pi^+$ S-wave of D_s^+ has no contribution of $f_0(500)$ at the beginning of the threshold, while the D^+ shows a prominent contribution of this particle. The unitarity chiral approach, introduced in Chapter 7, interprets the $f_0(500)$ as a dynamic pole of the $\pi\pi$ scattering. It explains the lack of $f_0(500)$ in the D_s^+ . The following contribution is given by the prominent $f_0(980)$ signal around 0.955 GeV^2 , which is less prominent in the D^+ . The $f_0(980)$ couples strongly to the $K\bar{K}$ channel, and the unitarity chiral approach shows that the $K\bar{K}$ impacts more the D_s^+ S-wave. Finally, between 1.4 and 1.6 GeV, there is an indication of at least two scalars. The argand plot of the D_s^+ and D^+ S-waves indicates that they are the $f_0(1340)$ with a mass value of 1.302 GeV and the $f_0(1500)$ with a mass value of 1.613 GeV.
- The P-waves of D_s^+ and D^+ have the same resonant structure but very different contributions. The omega was observed for the first time in both $D_s^+ \rightarrow \pi^- \pi^+ \pi^+$ and $D^+ \rightarrow \pi^- \pi^+ \pi^+$ channels. The $\omega(782) \rightarrow \pi^- \pi^+$ isospin violating has been observed in association with the $\rho(770)^0 \rightarrow \pi^- \pi^+$. The Ratio of the fit fractions $R_{\omega/\rho}$ for the D_s^+ is about 1/3 compared to 1/250 for the D^+ , which indicates different production mechanisms for these resonances. In the high-mass region, it was found that the contribution of both $\rho(1450)^0$ and $\rho(1700)^0$ is required. These resonances have considerable uncertainties regarding their masses and widths, implying significant uncertainties on individual contributions. However, the combined fit fraction of these states is stable, about 6.14%. This combined contribution is 6 times larger than their ground state $\rho(770)^0$, which casts suspicion about the nature of these particles.

A similar combined FF is found in the D^+ . The $\rho(1700)^0$ was also observed for the first time in both D_s^+ and D^+ .

- The D-wave of D_s^+ comprises of the $f_2(1270)$ and $f_2'(1525)$. The $f_2(1270)$ is present in both D_s^+ and D^+ models and contributes similarly: 13.69% and 13.80%, respectively. The $f_2(1270)$ coupling to the $d\bar{d}$ is expected to be stronger than to $s\bar{s}$. Thus, one may expect a more likely production in the D^+ . The same contribution is rather intriguing. The $f_2'(1525)$ is expected to couple strongly to the $s\bar{s}$. The small contribution of 0.045% is consistent with this picture. The $f_2'(1525)$ was also observed for the first time in the D_s^+ . It is absent in the D^+ .

The technical contributions consists of the HLT1 trigger lines $B_{(s)}^0 \rightarrow \gamma\gamma$ and $\pi^0 \rightarrow \gamma\gamma$, and the implementation of the π^0 calibration. The $B_{(s)}^0 \rightarrow \gamma\gamma$ trigger lines are of particular for searching physics beyond the Standard Model. The $\pi^0 \rightarrow \gamma\gamma$ line has been used to collect π^0 candidates for performing the π^0 calibration. The latter is essential for improving the measurements involving radioactive decay. Both trigger lines and the π^0 calibration package were pushed for the respective LHCb projects GitLab.

A MVA

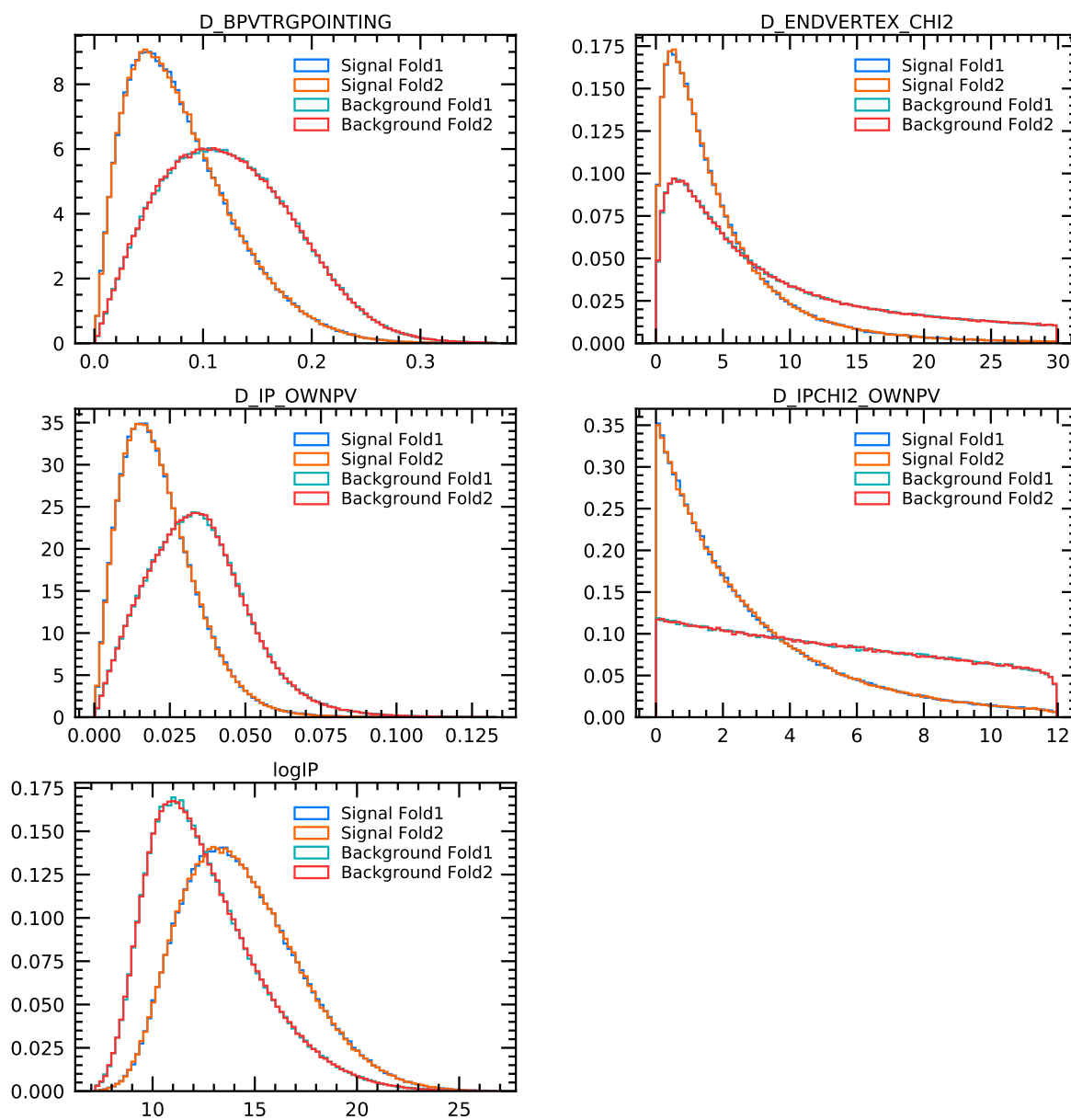
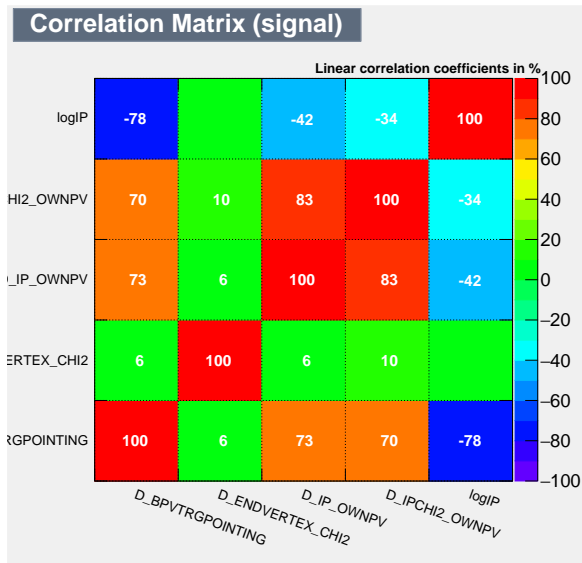
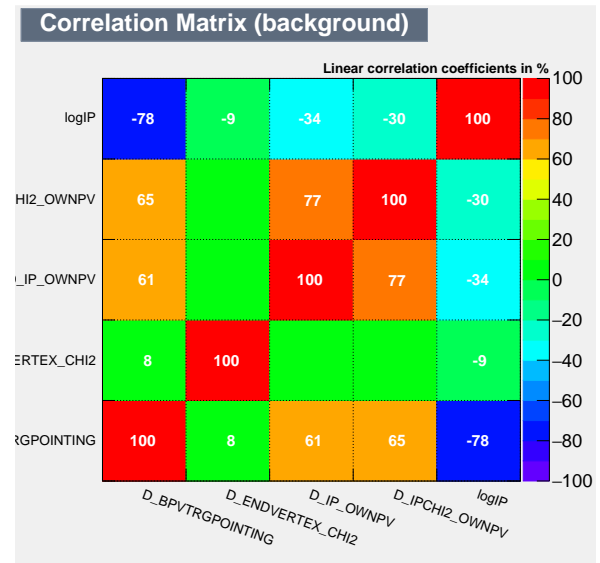


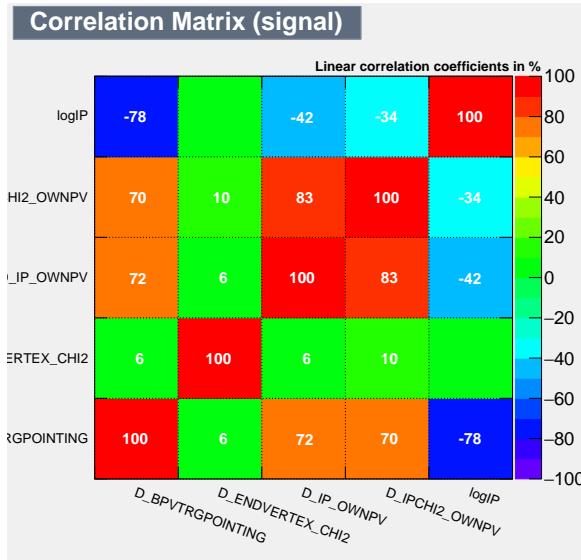
Figure 69 – Set of input variables used for the MVA training.



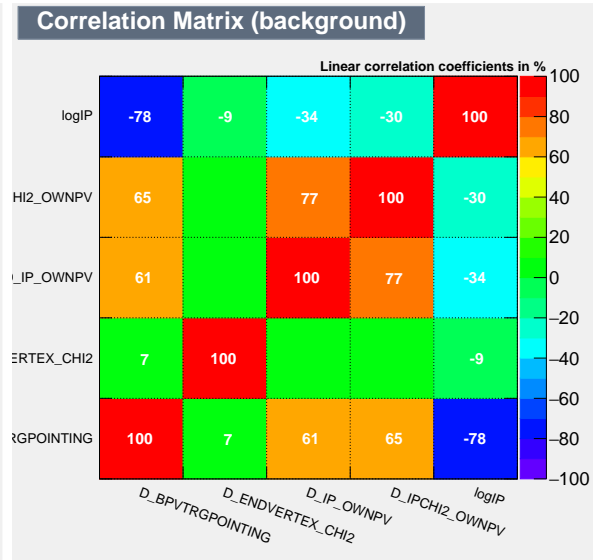
(a) The linear Correlation Matrix for Signal Fold 1.



(b) The linear Correlation Matrix for Background Fold 1.



(c) The linear Correlation Matrix for Signal Fold 2.



(d) The linear Correlation Matrix for Background Fold 2.

Figure 70 – The linear correlation matrix for signal and background from fold 1 and fold 2 used to train the classifier.

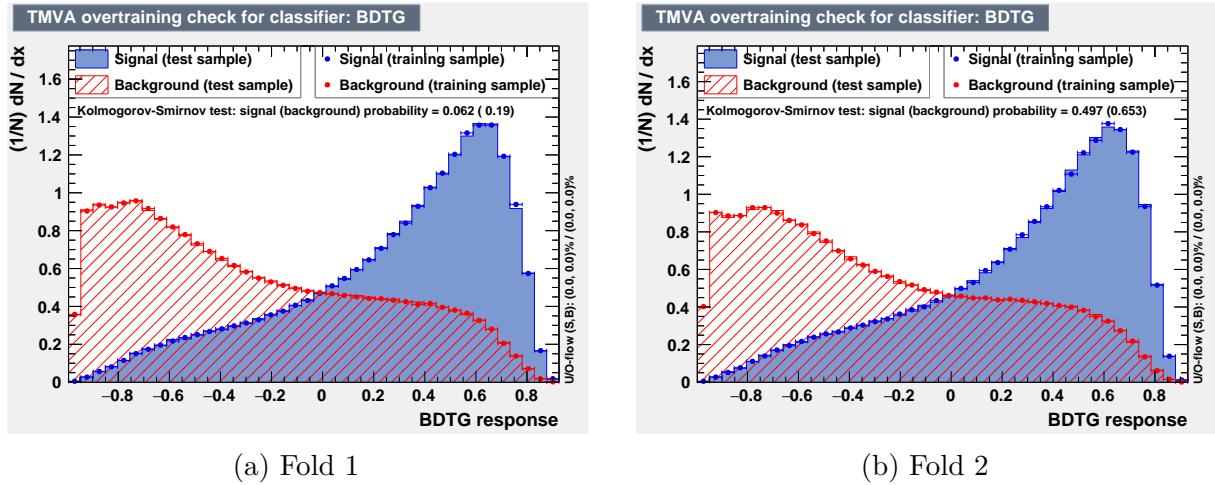


Figure 71 – Overfitting test

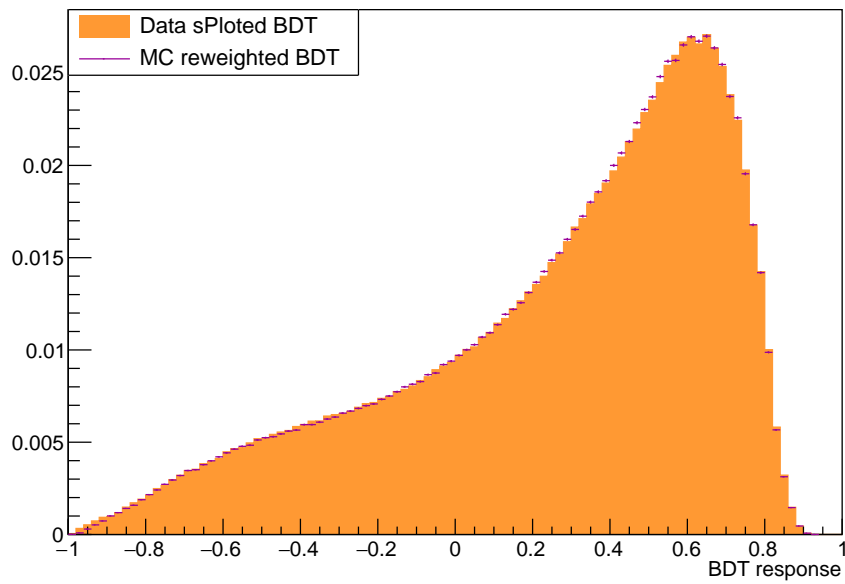
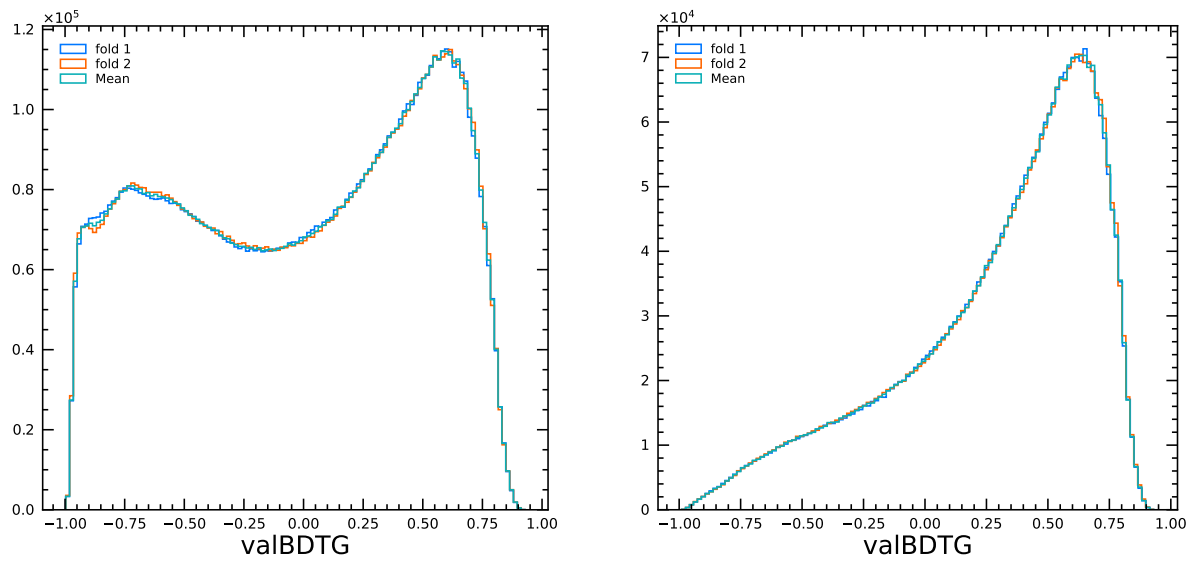


Figure 72 – Comparison of the BDTG variable for Data sPloted and for MC reweighted. Compatibility shows that MC reweighted models this variable well.



(a) Distribution of the BDTG variable for Data (b) Distribution of the BDTG variable for MC

Figure 73 – The BDTG variables predicted with the two classifiers trained: (a) the predicted variables for data and their mean; (b) the predicted variables for MC and their mean. The mean variable of these samples is used in the rest of analysis.

B Systematics

The systematic uncertainties are divided into two categories: experimental aspects such as efficiency correction, background parameterisation and fit procedure; model systematics, corresponding to the uncertainties in resonance parameters, such as masses and widths, as well as to other parameters that are fixed in the fit model.

Efficiency correction

The efficiency map is obtained from a series of steps, each resulting in a 2D histogram. The final efficiency includes the effect of the selection, determined from simulated events (no PID applied), ϵ^{sel} , and of the PID, ϵ^{PID} , determined from the PIDCalib tables. In the case of the correction for PID efficiency, weights – the per-track efficiency – are applied to the simulated events that pass the MVA selection. The final efficiency map histogram is obtained by a smoothing procedure that uses a 2D cubic spline, yielding a high-resolution histogram (300x300 bins).

The considered sources of systematic uncertainty associated with the efficiency map are:

- the correction for the PID efficiency;
- tracking efficiency correction;
- the finite size of the simulated sample;
- the binning scheme of the efficiency map before the smoothing procedure.

PID efficiency

The PID efficiency tables are 3D histograms which contain the average efficiency in the corresponding bin and its uncertainty. The PID efficiency is given as a function of the particle momentum, pseudo-rapidity and track multiplicity of the event. The calibration samples used to create these tables are composed of kaons and pions from $D^0 \rightarrow K^- \pi^+$ from the $D^{*+} \rightarrow D^0 \pi^+$ decays, with default binning: momentum from 0 to 100 GeV, divided into 19 bins with edges [0,3], [3,9.3], [9.3,15.6], [15.6,19.0] and 15 equal-size bins from 19 to 100 GeV; pseudo-rapidity from 1.5 to 5, with 4 equal-size bins; and `Ntracks` with 4 bins: [0,50], [50,200], [200,300] and [300,500].

Systematic uncertainties related to the PID efficiency considered here are due to the finite size of the calibration samples, the choice of a specific binning and the treatment of the muon veto, as recommended in the PIDCalib twiki page [102].

The systematic uncertainty due to the finite size of the calibration samples is assessed using toys. A set of 100 alternative efficiency maps is generated varying the PID efficiency tables according to their uncertainties. In each bin of the `PIDCalib` tables, the values of the efficiencies are fluctuated according to a Gaussian centred in the nominal value with a width equal to the uncertainty. Then an efficiency map is produced, smoothed by the 2D cubic spline and used to fit the data. For each fit parameter, the r.m.s. of the distribution of fitted values is assigned as systematic uncertainty. The PID calibration samples are large, and the uncertainty on the PID efficiency is expected to be small. Thus, the resulting systematic uncertainties due to the PID efficiency are also expected to be very small compared to other sources.

Decays in the flight of the pions would cause a difference in the track efficiency. Alternative efficiency tables were produced including the flag `isMuon=0`. For each fit parameter, the difference between the nominal value and that obtained with the alternative tables is taken as a systematic uncertainty.

A similar procedure is used to assess the impact of a different binning scheme. Alternative tables were produced dividing the momentum spectrum into nine bins with edges $[3.0,15.6],[15.6,24.4]$ plus seven equal-size bins from 24.4 to 100 GeV. The difference between the nominal fit and the one with this alternative `PIDCalib` tables is considered systematic uncertainty.

Compared to other sources, the systematic uncertainties related to the PID efficiency correction are very small. The different sources are added in quadrature, and the result is shown in the column "PID" in Table 21.

Tracking efficiency

There is a small difference in the tracking efficiency between data and MC. The available tables for correcting for this difference do not cover the entire kinematic of the $D_s^+ \rightarrow \pi^- \pi^+ \pi^+$ decay products: momentum starts at 5 GeV and pseudo-rapidity at 1.9. Approximately 15% of the $D_s^+ \rightarrow \pi^- \pi^+ \pi^+$ candidates have at least one track outside the fiducial volume of the tracking efficiency correction tables. The correction could therefore be applied only to a fraction of the data set. For this reason, the nominal result of this analysis does not include tracking efficiency correction. To assess the impact of this correction, an alternative efficiency map was produced applying the correction whenever possible. For each fit parameter, the difference between the nominal value and that obtained with the alternative map is taken as systematic uncertainty, which, as for the PID, is also very small.

MC statistics

The finite size of the simulated sample is also a source of systematic uncertainty. An extensive set of histograms is generated from the selection efficiency map before smoothing, ϵ^{sel} , in which the bin content is varied according to a Poisson distribution with a mean value equal to the nominal bin content. After including the PID efficiency, the toy efficiency map is smoothed and used to fit the data. For each parameter, the r.m.s. of the distribution of fitted values is assigned as a systematic uncertainty.

MC binning

The efficiency map is a smoothed 2D histogram. To account for possible effects due to the choice of the binning before the smoothing, alternative efficiency maps are produced varying the binning schemes of the input 2D histogram. The variations included efficiency maps of $n \times n$ bins, where $n = 20$ and 25 . The data is fitted using the alternative efficiency maps and the largest deviation from the nominal value of each fit parameter is taken as systematic uncertainty.

Background model

The background corresponds to approximately 5% of candidates within the signal region. As for the efficiency, the background model is a smoothed 2D histogram made from a weighted average of the right and left sidebands. There are uncertainties related to the background level, the fraction of each sideband, and the histogram's binning before the smoothing procedure. The background level is varied according to the uncertainty from the mass plot fit. The Dalitz plot is fitted, changing the background level by $\pm 1\sigma$. The largest variation in the value of the fit parameters is considered as a systematic uncertainty.

The Dalitz plot of candidates from the left and right sidebands have different structures. The background in the signal region is assumed to be a weighted average of the two sidebands. The model is built by assigning equal weights to both sidebands. The fit is repeated assuming weights 1.0-0.0, 0.8-0.2, 0.6-0.4, 0.4-0.6, 0.2-0.8 and 0.0-1.0 for the left-right sidebands, respectively. The deviation from the nominal value is computed for each parameter, and the r.m.s is considered a systematic uncertainty.

For account the effect of the binning, the background histogram is made with 20×20 and 25×25 bins. Each histogram is smoothed, and the data is fitted using these alternative models. The largest deviation from the nominal value of each fit parameter is taken as a systematic uncertainty.

Fit biases

Systematic uncertainties assigned to biases in the fit algorithm are also estimated. An ensemble of 1000 toy samples is generated according to the fitted values of the parameters. The simulations include background and efficiency. Each toy is fitted independently, resulting in a distribution of fitted values for each parameter and its respective statistical uncertainty. For each parameter, the mean of the distribution of fitted values is compared to the input. The difference is assigned as the systematic uncertainty due to the fit bias (tables 23 and 30). As a sanity check, the statistical uncertainties from MINUIT are compared to the mean value of the distribution of fitted parameter uncertainties.

Table 19 – Summary of the sanity check for the uncertainties on the fit parameters. The column “stat“ has the statistical errors from MINUIT. The column “ σ “ has the standard deviation for the parameter distribution.

parameter	stat	σ
$\rho(770)^0$ mag.	0.0030	0.0031
$\rho(770)^0$ ph.	1.8	1.8
$\omega(782)$ mag.	0.00090	0.00093
$\omega(782)$ ph.	1.7	1.7
$\rho(1450)^0$ mag.	0.026	0.026
$\rho(1450)^0$ ph.	2.6	2.7
$\rho(1700)^0$ mag.	0.061	0.060
$\rho(1700)^0$ ph.	6.1	6.5
$f_2'(1525)^0$ mag.	0.0069	0.0080
$f_2'(1525)^0$ ph.	4.2	4.4

Mass resolution

The mass resolution in the region around the $\omega(782)$ is 2.3 MeV. The default result is obtained with a convolution of the Gaussian mass resolution with the RBW representing the $\omega(782)$ line shape. A systematic uncertainty is assigned by varying the width of the mass resolution function (\pm one standard deviation) used for this convolution. The differences with respect to the nominal fit are taken as systematic uncertainties.

Model systematics

Regarding model systematics, uncertainties from lineshape of the spin-1 and -2 resonances are considered. The masses and widths of each contribution are varied according to the uncertainty on their PDG average ($\pm 1\sigma$); the Blatt-Weisskopf parameter are varied ($r_D = 4.0, 6.0\text{GeV}^{-1}$ and $r_R = 1.0, 2.0\text{GeV}^{-1}$, instead of 5.0GeV^{-1} and 1.5GeV^{-1} , respectively). The largest deviation from the nominal value is taken as the systematic uncertainty for each parameter.

In the QMIPWA, the choice of the number of points in which the mass spectrum is binned is also a source of uncertainties. The fit is repeated dividing the data into 45 and 55 intervals for the S -wave. For each parameter, the largest deviation is taken as the systematic uncertainty.

The systematic uncertainties are summarised in Tables 20-31. In all Tables, a column named "stat." has the corresponding statistical uncertainty on the fit parameter for comparison.

Table 20 – Systematic uncertainties related to the background parameterisation. The column "total" contains the sum in quadrature of the values in the previous columns. Phases are in degrees.

parameter	composition	level	binning	total	stat.
$\rho(770)^0$ mag.	0.0027	0.000030	0.0020	0.0034	0.0030
$\rho(770)^0$ ph.	5.9	0.057	1.6	6.1	1.8
$\omega(782)$ mag.	0.0016	0.000013	0.00021	0.0017	0.00090
$\omega(782)$ ph.	0.71	0.018	0.072	0.71	1.7
$\rho(1450)^0$ mag.	0.0040	0.000010	0.011	0.011	0.026
$\rho(1450)^0$ ph.	0.68	0.060	0.99	1.20	2.6
$\rho(1700)^0$ mag.	0.014	0.0027	0.038	0.041	0.061
$\rho(1700)^0$ ph.	2.8	0.27	1.3	3.1	6.1
$f'_2(1525)$ mag.	0.0063	0.000075	0.0049	0.0080	0.0069
$f'_2(1525)$ ph.	8.2	0.0020	2.2	8.5	4.2

Table 21 – Systematic uncertainties related to the efficiency correction. The column "total" contains the sum in quadrature of the values in the previous columns. Phases are in degree

parameter	binning	PID	MC stat.	tracking	total	Stat.
$\rho(770)^0$ mag.	0.0023	0.0016	0.00083	0.00033	0.0030	0.0030
$\rho(770)^0$ ph.	4.5	1.1	0.13	0.25	4.6	1.8
$\omega(782)$ mag.	0.00041	0.00023	0.000048	0.000011	0.00047	0.00090
$\omega(782)$ ph.	0.41	0.30	0.057	0.14	0.53	1.7
$\rho(1450)^0$ mag.	0.0096	0.011	0.0044	0.0049	0.016	0.026
$\rho(1450)^0$ ph.	0.65	0.21	0.047	0.22	0.72	2.6
$\rho(1700)^0$ mag.	0.024	0.016	0.013	0.0041	0.032	0.061
$\rho(1700)^0$ ph.	1.5	3.0	0.71	0.89	3.5	6.1
$f'_2(1525)$ mag.	0.015	0.0062	0.00098	0.0018	0.017	0.0
$f'_2(1525)$ ph.	7.2	2.9	0.38	0.71	7.9	4.2

Table 22 – Systematic uncertainties related to the model parameters. The column “model” has the sum in quadrature of the individual items.

parameter	m_0, Γ_0	r_D, r_R	S -wave bin.	model	stat.
$\rho(770)^0$ mag.	0.0052	0.0027	0.0020	0.0062	0.0030
$\rho(770)^0$ ph.	4.1	0.97	1.3	4.4	1.8
$\omega(782)$ mag.	0.00072	0.00032	0.00035	0.00086	0.00090
$\omega(782)$ ph.	0.90	0.67	0.86	1.4	1.7
$\rho(1450)^0$ mag.	0.47	0.10	0.021	0.48	0.026
$\rho(1450)^0$ ph.	10.1	0.84	2.1	10.4	2.6
$\rho(1700)^0$ mag.	0.62	0.030	0.031	0.62	0.061
$\rho(1700)^0$ ph.	9.1	6.2	5.5	12.4	6.1
$f'_2(1525)$ mag.	0.0099	0.0093	0.0054	0.015	0.0069
$f'_2(1525)$ ph.	4.5	4.4	3.0	7.0	4.2

Table 23 – Systematic uncertainties related to the fit bias.

parameter	Fit bias	stat.
$\rho(770)^0$ mag.	0.0021	0.0030
$\rho(770)^0$ ph.	1.1	1.8
$\omega(782)$ mag.	0.00041	0.00090
$\omega(782)$ ph.	0.32	1.7
$\rho(1450)^0$ mag.	0.013	0.026
$\rho(1450)^0$ ph.	2.5	2.6
$\rho(1700)^0$ mag.	0.014	0.061
$\rho(1700)^0$ ph.	4.7	6.1
$f'_2(1525)$ mag.	0.0031	0.0069
$f'_2(1525)$ ph.	1.2	4.2

Table 24 – Systematic uncertainties related to the mass resolution.

parameter	mass res.	stat.
$\rho(770)^0$ mag.	0.000010	0.0030
$\rho(770)^0$ ph.	0.016	1.8
$\omega(782)$ mag.	0.000030	0.00090
$\omega(782)$ ph.	0.0030	1.7
$\rho(1450)^0$ mag.	0.000040	0.026
$\rho(1450)^0$ ph.	0.011	2.6
$\rho(1700)^0$ mag.	0.00014	0.061
$\rho(1700)^0$ ph.	0.017	6.1
$f'_2(1525)$ mag.	0.0000020	0.0069
$f'_2(1525)$ ph.	0.012	4.2

Table 25 – Summary of the systematic uncertainties. The column “total exp.” has the sum in quadrature of the first four columns.

parameter	back.	eff.	fit bias	res.	total	model	stat.
$\rho(770)^0$ mag.	0.0034	0.0030	0.0021	0.000010	0.0050	0.0062	0.0030
$\rho(770)^0$ ph.	6.12	4.6	1.1	0.016	7.8	4.4	1.8
$\omega(782)$ mag.	0.0017	0.00047	0.00041	0.000030	0.0018	0.00086	0.00090
$\omega(782)$ ph.	0.71	0.53	0.32	0.0030	0.94	1.4	1.68
$\rho(1450)^0$ mag.	0.011	0.016	0.013	0.000040	0.023	0.48	0.026
$\rho(1450)^0$ ph.	1.2	0.72	2.5	0.011	2.83	10.4	2.57
$\rho(1700)^0$ mag.	0.041	0.032	0.014	0.00014	0.054	0.62	0.061
$\rho(1700)^0$ ph.	3.1	3.5	4.7	0.017	6.7	12.4	6.14
$f_2'(1525)$ mag.	0.0080	0.017	0.0031	0.0000020	0.019	0.015	0.0069
$f_2'(1525)$ ph.	8.5	7.9	1.2	0.012	11.7	7.0	4.20

Table 26 – Systematic uncertainties on the fit fractions, in %

amplitude	back.	eff.	fit bias	mass res.	total	model	stat.
S -wave	0.28	0.085	0.082	0.00050	0.30	0.63	0.14
$\rho(770)^0\pi^+$	0.066	0.061	0.037	0.00018	0.097	0.11	0.054
$\omega(782)\pi^+$	0.031	0.013	0.0072	0.00019	0.034	0.016	0.016
$\rho(1450)^0\pi^+$	0.041	0.10	0.078	0.00023	0.14	2.0	0.15
$\rho(1700)^0\pi^+$	0.035	0.027	0.0095	0.00012	0.045	0.34	0.050
combined	0.035	0.027	0.0095	0.00012	0.045	0.34	0.27
$f_2(1270)\pi^+$	0.12	0.19	0.0026	0.00010	0.22	0.49	0.14
$f_2'(1525)\pi^+$	0.007	0.013	0.0029	0.0000016	0.015	0.0087	0.0070

Table 27 – Systematic uncertainty on the S -wave due the background parameterization. Phases are in degrees.

interval	magnitude	stat.	phase	stat.	interval	magnitude	stat.	phase	stat.
1	0.11	0.15	1.3	2.0	26	0.022	0.062	0.27	0.79
2	0.068	0.12	1.4	1.5	27	0.027	0.064	0.30	0.89
3	0.024	0.12	1.4	1.4	28	0.023	0.068	0.48	0.94
4	0.045	0.11	0.92	1.1	29	0.022	0.069	0.45	1.0
5	0.10	0.10	0.62	1.0	30	0.019	0.072	0.34	1.0
6	0.095	0.092	1.1	1.0	31	0.019	0.074	0.31	1.0
7	0.040	0.079	0.65	1.1	32	0.020	0.078	0.33	1.0
8	0.051	0.072	1.0	1.3	33	0.024	0.080	0.28	1.1
9	0.064	0.066	0.90	1.2	34	0.027	0.082	0.31	1.1
10	0.072	0.069	1.1	1.1	35	0.033	0.083	0.31	1.1
11	0.055	0.082	0.94	1.0	36	0.040	0.085	0.24	1.0
12	0.050	0.10	0.92	1.0	37	0.043	0.089	0.23	1.1
13	0.054	0.12	1.0	1.2	38	0.047	0.093	0.20	1.1
14	0.065	0.14	1.0	1.2	39	0.049	0.10	0.14	1.0
15	0.078	0.16	1.0	1.4	40	0.049	0.10	0.12	1.0
16	0.088	0.17	1.0	1.4	41	0.052	0.11	0.14	1.0
17	0.095	0.17	0.94	1.2	42	0.055	0.11	0.21	1.0
18	0.066	0.14	0.92	1.1	43	0.061	0.11	0.22	0.92
19	0.035	0.091	0.75	0.92	44	0.071	0.11	0.28	0.86
20	0.054	0.073	0.72	0.76	45	0.076	0.11	0.32	0.83
21	0.075	0.063	0.61	0.72	46	0.079	0.10	0.52	0.82
22	0.048	0.059	0.33	0.65	47	0.090	0.078	1.2	1.1
23	0.020	0.059	0.32	0.68	48	0.084	0.073	2.1	2.7
24	0.020	0.060	0.19	0.71	49	0.13	0.11	4.7	2.8
25	0.023	0.058	0.16	0.79	50	0.16	0.27	2.5	4.2

Table 28 – Systematic uncertainty on the S -wave due the efficiency correction. Phases are in degrees.

interval	magnitude	stat.	phase	stat.	interval	magnitude	stat.	phase	stat.
1	0.063	0.15	2.4	2.0	26	0.023	0.062	0.60	0.79
2	0.055	0.12	1.8	1.5	27	0.020	0.064	0.52	0.89
3	0.040	0.12	1.6	1.4	28	0.0059	0.068	0.49	0.94
4	0.049	0.11	1.3	1.1	29	0.016	0.069	0.34	1.0
5	0.032	0.10	1.1	1.0	30	0.023	0.072	0.26	1.0
6	0.019	0.092	0.85	1.0	31	0.051	0.074	0.29	1.0
7	0.031	0.079	0.82	1.1	32	0.097	0.078	0.32	1.0
8	0.017	0.072	0.68	1.3	33	0.11	0.080	0.34	1.1
9	0.017	0.066	1.2	1.2	34	0.091	0.082	0.30	1.1
10	0.048	0.069	2.0	1.1	35	0.045	0.083	0.29	1.1
11	0.069	0.082	1.6	1.0	36	0.023	0.085	0.38	1.0
12	0.088	0.10	1.4	1.0	37	0.045	0.089	0.45	1.1
13	0.11	0.12	1.2	1.2	38	0.060	0.093	0.39	1.1
14	0.15	0.14	1.1	1.2	39	0.060	0.10	0.32	1.0
15	0.17	0.16	1.1	1.4	40	0.048	0.10	0.29	1.0
16	0.22	0.17	1.1	1.4	41	0.051	0.11	0.24	1.0
17	0.24	0.17	1.3	1.2	42	0.071	0.11	0.25	1.0
18	0.18	0.14	1.3	1.1	43	0.071	0.11	0.38	0.92
19	0.11	0.091	1.3	0.92	44	0.063	0.11	0.53	0.86
20	0.085	0.073	1.1	0.76	45	0.065	0.11	0.61	0.83
21	0.073	0.063	1.2	0.72	46	0.11	0.10	0.51	0.82
22	0.053	0.059	1.3	0.65	47	0.098	0.078	0.58	1.1
23	0.028	0.059	1.2	0.68	48	0.11	0.073	0.59	2.7
24	0.038	0.060	0.91	0.71	49	0.040	0.11	2.86	2.8
25	0.036	0.058	0.79	0.79	50	0.15	0.27	4.1	4.2

Table 29 – Systematic uncertainty on the S -wave due the fit model. Phases are in degrees.

interval	magnitude	stat	phase	stat.	interval	magnitude	stat.	phase	stat.
1	0.45	0.15	5.6	1.8	26	0.096	0.062	2.0	0.79
2	0.51	0.12	4.9	1.4	27	0.097	0.064	2.0	0.89
3	0.48	0.11	4.2	1.3	28	0.11	0.068	1.4	0.94
4	0.44	0.11	3.8	1.09	29	0.13	0.069	1.1	1.0
5	0.38	0.10	3.6	1.0	30	0.15	0.072	0.95	1.0
6	0.32	0.094	3.9	0.94	31	0.18	0.074	1.1	1.0
7	0.20	0.081	3.7	1.0	32	0.22	0.078	1.1	1.0
8	0.17	0.069	3.7	1.2	33	0.25	0.080	1.3	1.1
9	0.15	0.059	2.9	1.2	34	0.28	0.082	1.1	1.1
10	0.19	0.059	1.8	1.1	35	0.30	0.083	1.1	1.1
11	0.23	0.068	1.03	1.0	36	0.32	0.085	1.3	1.0
12	0.27	0.083	1.0	1.04	37	0.35	0.089	1.5	1.1
13	0.31	0.10	1.5	1.1	38	0.36	0.093	1.6	1.1
14	0.46	0.12	2.2	1.2	39	0.38	0.10	1.4	1.0
15	0.42	0.14	1.8	1.2	40	0.39	0.10	1.7	1.0
16	0.38	0.15	1.7	1.2	41	0.39	0.11	2.0	1.0
17	0.57	0.16	1.06	0.89	42	0.41	0.11	2.4	1.0
18	0.72	0.13	1.5	1.0	43	0.37	0.11	3.0	0.92
19	0.78	0.090	2.3	0.85	44	0.33	0.11	3.5	0.86
20	0.21	0.068	1.1	0.73	45	0.24	0.11	4.1	0.83
21	0.15	0.060	0.94	0.64	46	0.23	0.10	4.9	0.82
22	0.15	0.055	0.80	0.58	47	0.37	0.078	5.2	1.1
23	0.14	0.058	1.0	0.67	48	0.43	0.073	12.0	2.7
24	0.13	0.059	0.78	0.71	49	0.66	0.11	5.8	2.8
25	0.10	0.057	1.7	0.75	50	0.63	0.27	17.2	4.2

Table 30 – Systematic uncertainty on the S -wave due the fit bias. Phases are in degrees.

interval	magnitude	stat	phase	stat.	interval	magnitude	stat.	phase	stat.
1	0.20	0.15	2.3	2.0	26	0.0062	0.06	0.0428	0.79
2	0.070	0.12	0.14	1.5	27	0.0027	0.06	0.495	0.89
3	0.10	0.12	0.26	1.4	28	0.008	0.07	0.0160	0.94
4	0.083	0.11	0.37	1.1	29	0.021	0.07	0.535	1.0
5	0.077	0.10	0.28	1.0	30	0.020	0.07	0.021	1.0
6	0.099	0.09	0.26	1.0	31	0.039	0.07	0.41	1.0
7	0.053	0.08	0.33	1.1	32	0.010	0.08	0.150	1.0
8	0.055	0.07	0.58	1.3	33	0.030	0.08	0.326	1.1
9	0.016	0.07	0.30	1.2	34	0.0015	0.08	0.216	1.1
10	0.020	0.07	0.43	1.1	35	0.038	0.08	0.430	1.1
11	0.015	0.08	0.13	1.0	36	0.033	0.09	0.215	1.0
12	0.024	0.10	0.45	1.0	37	0.043	0.09	0.407	1.1
13	0.025	0.12	0.26	1.2	38	0.041	0.09	0.326	1.1
14	0.11	0.14	1.3	1.2	39	0.049	0.10	0.310	1.0
15	0.19	0.16	0.17	1.4	40	0.049	0.10	0.329	1.0
16	0.40	0.17	6.5	1.4	41	0.032	0.11	0.174	1.0
17	0.33	0.17	3.9	1.2	42	0.070	0.11	0.18	1.0
18	0.06	0.14	0.21	1.1	43	0.065	0.11	0.179	0.92
19	0.058	0.09	0.0041	0.92	44	0.066	0.11	0.085	0.86
20	0.0016	0.07	0.030	0.76	45	0.077	0.11	0.02	0.83
21	0.020	0.06	0.21	0.72	46	0.059	0.10	0.36	0.82
22	0.012	0.06	0.13	0.65	47	0.0177	0.08	0.58	1.1
23	0.016	0.06	0.036	0.68	48	0.0160	0.07	1.90	2.7
24	0.00094	0.06	0.038	0.71	49	0.025	0.11	2.02	2.8
25	0.0054	0.06	0.15	0.79	50	0.236	0.27	4.2	4.2

Table 31 – Systematic uncertainty on the S -wave due the mass resolution. Phases are in degrees.

interval	magnitude	stat	phase	stat.	interval	magnitude	stat.	phase	stat.
1	0.00052	0.15	0.011	2.0	26	0.0000	0.06	0.00	0.79
2	0.00037	0.12	0.0050	1.5	27	0.0000	0.06	0.00	0.89
3	0.00034	0.12	0.0010	1.4	28	0.0001	0.07	0.00	0.94
4	0.00032	0.11	0.0080	1.1	29	0.0000	0.07	0.00	1.0
5	0.00039	0.10	0.0010	1.0	30	0.0001	0.07	0.00	1.0
6	0.00041	0.092	0.0060	1.0	31	0.0000	0.07	0.00	1.0
7	0.00026	0.079	0.010	1.1	32	0.0000	0.08	0.00	1.0
8	0.00032	0.072	0.0030	1.3	33	0.0000	0.08	0.00	1.1
9	0.00019	0.066	0.020	1.2	34	0.0001	0.08	0.00	1.1
10	0.00014	0.069	0.055	1.1	35	0.0001	0.08	0.00	1.1
11	0.00060	0.082	0.065	1.0	36	0.0001	0.09	0.01	1.0
12	0.00050	0.10	0.069	1.0	37	0.0002	0.09	0.00	1.1
13	0.00050	0.12	0.00020	1.2	38	0.0001	0.09	0.00	1.1
14	0.00090	0.14	0.00040	1.2	39	0.0001	0.10	0.00	1.0
15	0.00050	0.16	0.0011	1.4	40	0.0002	0.10	0.01	1.0
16	0.00070	0.17	0.0078	1.4	41	0.0003	0.11	0.01	1.0
17	0.00060	0.17	0.00040	1.2	42	0.0003	0.11	0.01	1.0
18	0.00050	0.14	0.00059	1.1	43	0.0003	0.11	0.01	0.92
19	0.00020	0.091	0.0010	0.92	44	0.0004	0.11	0.01	0.86
20	0.00040	0.073	0.0017	0.76	45	0.0004	0.11	0.01	0.83
21	0.00011	0.063	0.0011	0.72	46	0.0003	0.10	0.05	0.82
22	0.000080	0.059	0.00020	0.65	47	0.0002	0.08	0.09	1.1
23	0.000020	0.059	0.00030	0.68	48	0.0003	0.07	0.04	2.7
24	0.000050	0.060	0.00080	0.71	49	0.0002	0.11	0.02	2.8
25	0.000070	0.058	0.00080	0.79	50	0.0007	0.27	0.01	4.2

C Alternative models

In this section, alternative models are presented to check the nominal model PWA-1. The significance of resonances in the model is tested, followed by testing the impact of the lower efficiency regions on the fit quality. In the end, an alternative parameterisation to the $\rho(770)^0$ and $\omega(782)$ is tested, and the Bose-Einstein correlation is introduced to the fit model.

C.1 PWA-2 - Fit without $\rho(770)^0$

The lack of a visible $\rho(770)^0$ signal is one of the remarkable differences between $D_s^+ \rightarrow \pi^- \pi^+ \pi^+$ and $D^+ \rightarrow \pi^- \pi^+ \pi^+$ decays. In this exercise, the data is fitted removing the $\rho(770)^0$ from the amplitude model. The result is a fit with significantly worse quality, with an increase of 761 units in FCN and $\chi^2/\text{ndof} \in [2.1 - 2.3]$. The fit fractions are presented in Tables 32 and 33, and the S -wave, the fit projections and normalised residuals are shown in Fig. 74 and 75. This fit demonstrates that the $\rho(770)^0$ is required to describe the data, even with a small contribution.

Table 32 – Fit results for model PWA-2. Phases in degrees and fit fractions (FF) in %.

Resonance	Magnitude	Phase	FF PWA-2	FF PWA-1
S -wave			87.56	84.97 ± 0.14
$\omega(782)$	0.04983 ± 0.00087	-134.3 ± 1.2	0.527	0.360 ± 0.016
$\rho(1450)^0$	1.937 ± 0.037	-93.5 ± 1.2	8.37	3.86 ± 0.15
$\rho(1700)^0$	1.271 ± 0.073	-129.2 ± 2.6	0.729	0.365 ± 0.050
$\rho(1450)^0 + \rho(1700)^0$			10.44	6.14 ± 0.27
$f_2(1270)$	1 [Fixed]	0 [Fixed]	12.90	13.69 ± 0.14
$f_2'(1525)$	0.1535 ± 0.0068	122.1 ± 2.8	0.0838	0.0455 ± 0.0070
\sum FF			116.4	104.3
χ^2/ndof (range):	[2.1-2.3]	Δ FCN:	+761	

Table 33 – Interference fractions (%) between amplitude components for model PWA-2.

	$\omega(782)$	$\rho(1450)^0$	$\rho(1700)^0$	$f_2(1270)$	$f_2'(1525)$	S -wave
$\omega(782)$	0.53					
$\rho(1450)^0$	0.51	8.4				
$\rho(1700)^0$	0.17	1.3	0.73			
$f_2(1270)$	-0.13	-2.3	0.34	12.9		
$f_2'(1525)$	0.012	0.12	0.033	0.41	0.084	
S -wave	-0.014	-8.1	0.018	-2.8	0.18	87.6

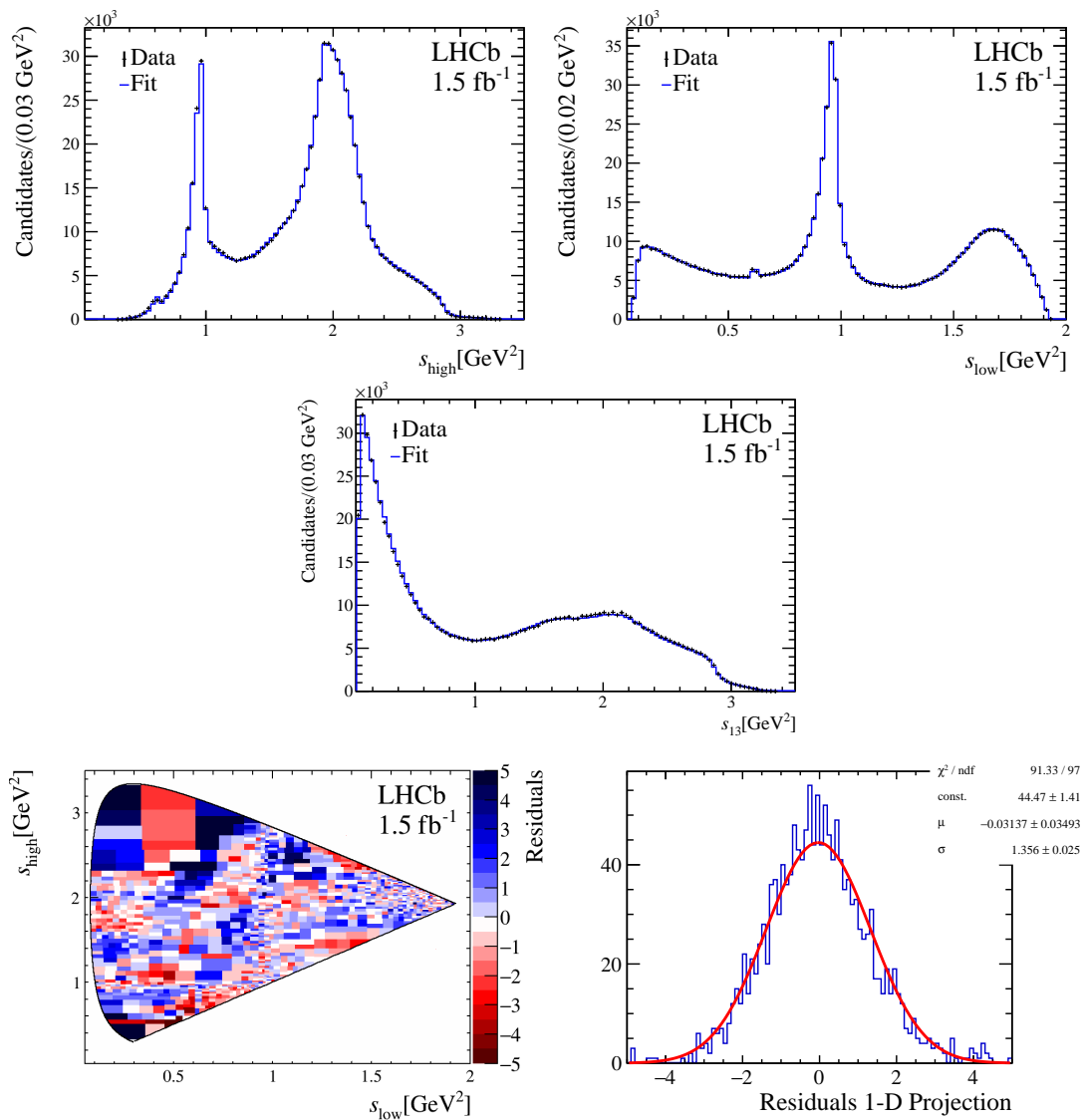


Figure 74 – Fit results from model PWA-2: the projections of the lowest (top left) and the highest (top right) of the two $\pi^+\pi^-$ invariant masses squared; the $\pi^+\pi^-$ projection (mid left) and the helicity angle (mid right, with two entries per event); distribution of the normalised residuals across the Dalitz plot (bottom left) and as 1D projection (bottom right). The data is represented by the red dots whilst the fit result is the histogram in black.

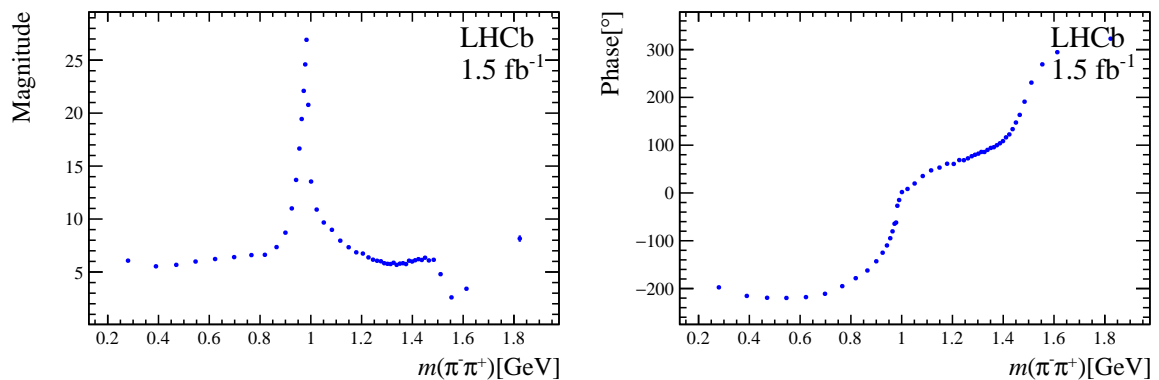


Figure 75 – Fitted S -wave for model PWA-2.

C.2 PWA-3 - Fit without $\omega(782)$

An amplitude model excluding the $\omega(782)$ also renders a poor fit, increasing 849 FCN units to the default solution. The χ^2/ndof is in the range $[1.90 - 2.05]$. The impact on the S -wave is small, as expected, and this fit demonstrates that the $\omega(782)$ resonance is necessary to describe the $D_s^+ \rightarrow \pi^- \pi^+ \pi^+$ Dalitz plot. The results for this model are presented in Tables 34 and 35, and in Figs. 77 and 76.

Table 34 – Results from the Dalitz plot fit with model PWA-3.

Resonance	Magnitude	Phase	FF PWA-3	FF PWA-1
S -Wave	-	-	84.8	84.97 ± 0.14
$\rho(770)^0$	0.1417 ± 0.0026	114.2 ± 1.4	1.45	1.038 ± 0.054
$\rho(1450)^0$	1.348 ± 0.024	-132.9 ± 2.4	4.32	3.86 ± 0.15
$\rho(1700)^0$	0.509 ± 0.073	-7.6 ± 8.5	0.12	0.365 ± 0.050
$\rho(1450)^0 + \rho(1700)^0$			4.45	6.14 ± 0.27
$f_2(1270)$	1 [Fixed]	0 [Fixed]	13.76	13.69 ± 0.14
$f_2'(1525)$	0.1176 ± 0.0069	176.4 ± 3.9	0.052	0.0455 ± 0.0070
Σ FF			103.83	104.3
χ^2/ndof (range):	$[1.90 - 2.05]$	Δ FCN:	+849	

Table 35 – Interference fractions between amplitude components for model PWA-3.

	$\rho(770)^0$	$\rho(1450)^0$	$\rho(1700)^0$	$f_2(1270)$	$f_2'(1525)$	S -wave
$\rho(770)^0$	1.45					
$\rho(1450)^0$	2.1	4.32				
$\rho(1700)^0$	-0.30	0.0084	0.12			
$f_2(1270)$	-0.31	-0.62	-0.33	13.76		
$f_2'(1525)$	0.036	0.057	0.013	-0.44	0.052	
S -wave	-0.17	-0.49	-0.36	-4.0	0.23	84.8

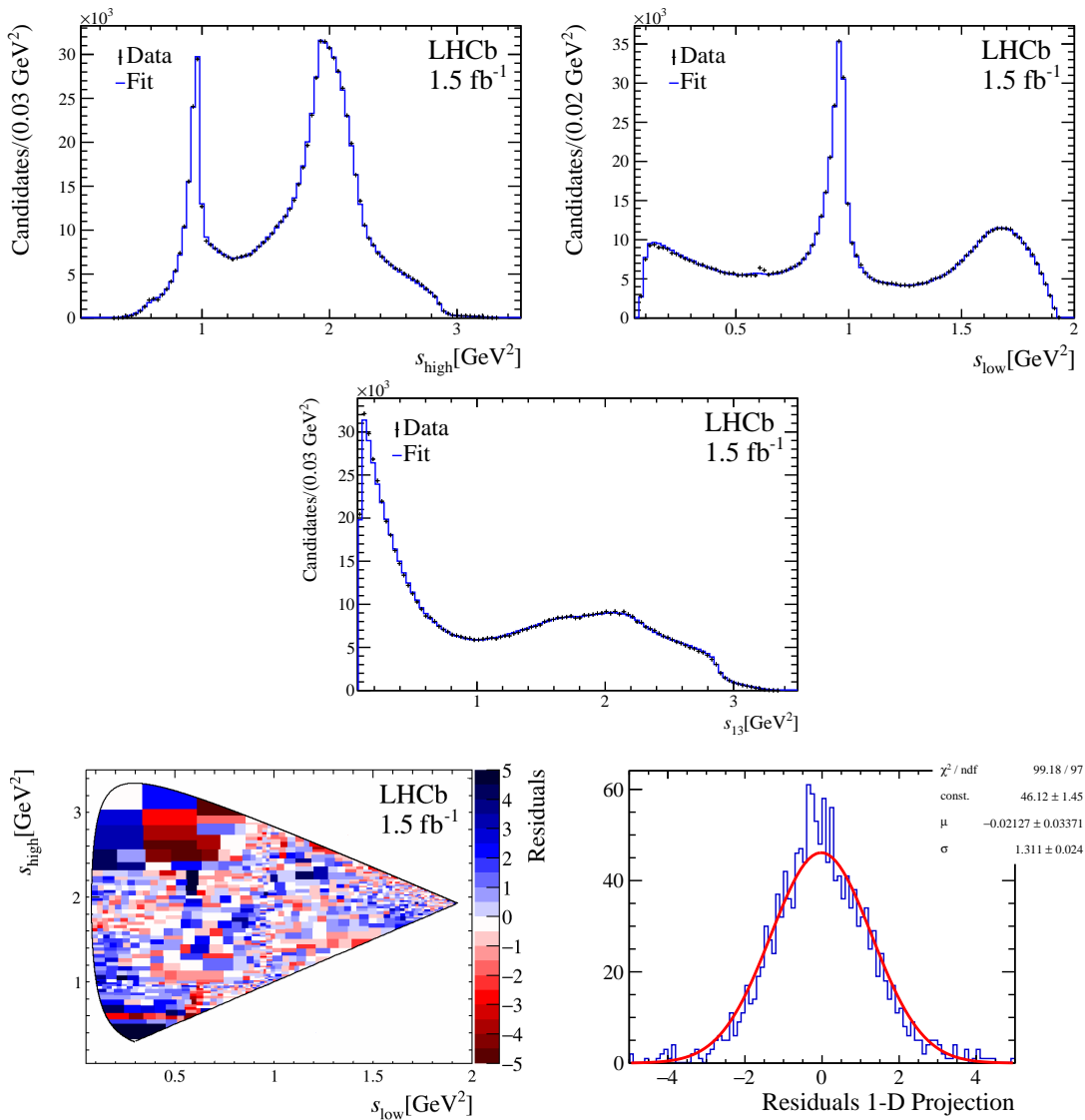


Figure 76 – Fit results from model PWA-3: the projections of the lowest (top left) and the highest (top right) of the two $\pi^+\pi^-$ invariant masses squared; the $\pi^+\pi^-$ projection (mid left) and the helicity angle (mid right, with two entries per event); distribution of the normalised residuals across the Dalitz plot (bottom left) and as 1D projection (bottom right). The data is represented by the red dots whilst the fit result is the histogram in black.

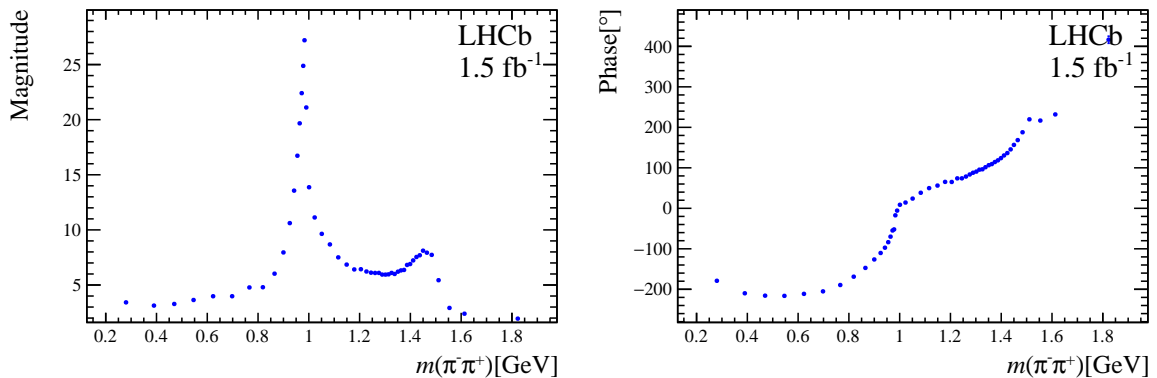


Figure 77 – Fitted S -wave for model PWA-3.

C.3 PWA-4 - Excluding $f'_2(1525)$

The tensor resonance $f'_2(1525)$ has a dominant $s\bar{s}$ component in its wave function, which implies a small branching fraction for the $\pi^+\pi^-$ mode: $(8.2 \pm 1.5) \times 10^{-3}$ [21]. Moreover, it is a spin-2 state with a mass close to the kinematic limit, and these facts explain the minute fit fraction of the $f'_2(1525)$.

In this fit, the $f'_2(1525)$ is excluded from the decay amplitude. The results are presented in Tables 36 and 37, and in Figs. 79 and 78. The exclusion of the $f'_2(1525)$ results in a fit with worse quality. The $\chi^2/ndof$ is in the range [1.54-1.66]. The S -wave and the contribution of the other resonances remain unaltered.

Table 36 – Results from the Dalitz plot fit with model PWA-4.

Resonance	Magnitude	Phase	FF PWA-4	FF PWA-1
S -Wave	-	-	85.51	84.97 ± 0.14
$\rho(770)^0$	0.04064 ± 0.00088	-107.6 ± 1.7	1.13	1.038 ± 0.054
$\omega(782)$	0.1255 ± 0.0028	79.8 ± 1.8	0.37	0.360 ± 0.016
$\rho(1450)^0$	1.275 ± 0.030	-108.9 ± 2.6	3.8	3.86 ± 0.15
$\rho(1700)^0$	1.041 ± 0.066	-67.4 ± 5.0	0.33	0.365 ± 0.050
$\rho(1450)^0 + \rho(1700)^0$			6.72	6.14 ± 0.27
$f_2(1270)$	1 [Fixed]	0 [Fixed]	13.61	13.69 ± 0.14
Σ FF			104.25	104.3
$\chi^2/ndof$ (range):	[1.54 - 1.66]	Δ FCN:	+102	

Table 37 – Interference fractions between amplitude components for model PWA-4.

	$\omega(782)$	$\rho(770)^0$	$\rho(1450)^0$	$\rho(1700)^0$	$f_2(1270)$	S -wave
$\omega(782)$	0.37					
$\rho(770)^0$	0.12	1.13				
$\rho(1450)^0$	0.37	-0.063	3.8			
$\rho(1700)^0$	0.037	-0.30	2.4	0.33		
$f_2(1270)$	-0.16	0.28	-1.3	-0.39	13.6	
S -wave	-0.081	0.98	-2.2	-1.2	-3.6	85.5

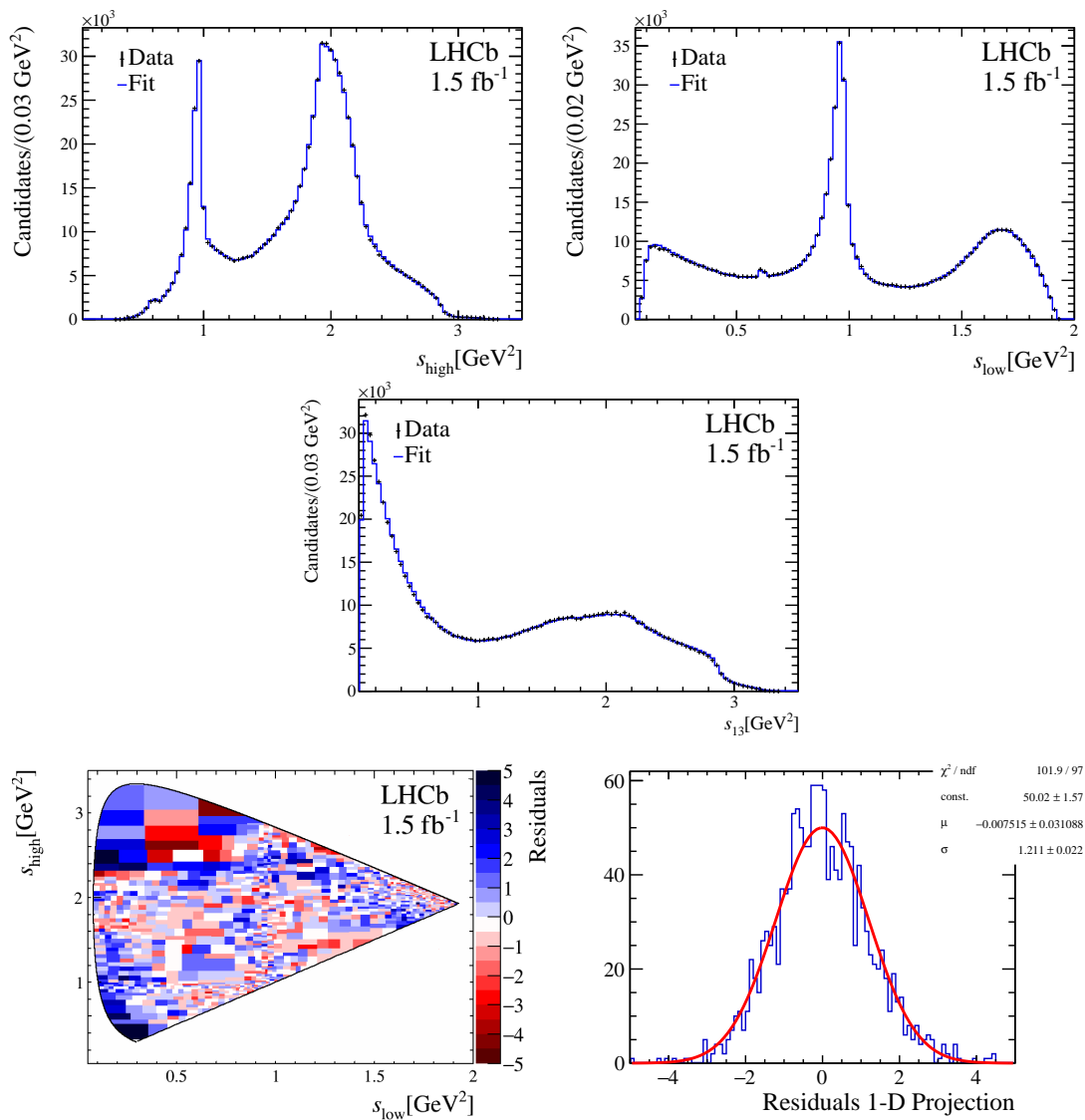


Figure 78 – Fit results from model PWA-4: the projections of the lowest (top left) and the highest (top right) of the two $\pi^+\pi^-$ invariant masses squared; the $\pi^+\pi^-$ projection (mid left) and the helicity angle (mid right, with two entries per event); distribution of the normalised residuals across the Dalitz plot (bottom left) and as 1D projection (bottom right). The data is represented by the red dots whilst the fit result is the histogram in black.

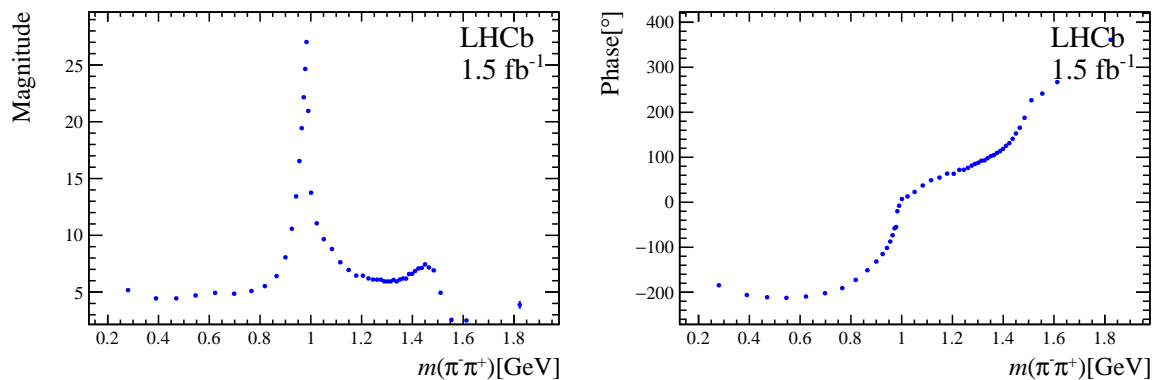


Figure 79 – Fitted S -wave for model PWA-4.

C.4 PWA-5 - Fit without $\rho(1700)^0$

An amplitude model excluding the $\rho(1700)^0$ yields a result worst than PWA-1 by 96 units of FCN. The results are shown in Tables 38 and 39, and in Figs. 81 and 80. This state is necessary for a better description of the region between 1.8-2.4 GeV². The $\chi^2/ndof$ is in the range [1.54 - 1.66].

Table 38 – Results from the Dalitz plot fit with model PWA-5.

Resonance	Magnitude	Phase	FF PWA-5	FF PWA-1
S -wave	-	-	84.55	84.97 ± 0.14
$\rho(770)^0$	0.1232 ± 0.0025	89.9 ± 1.5	0.88	1.038 ± 0.054
$\omega(782)$	0.03828 ± 0.00085	111.3 ± 1.7	0.32	0.360 ± 0.016
$\rho(1450)^0$	1.524 ± 0.015	-118.3 ± 1.0	5.35	3.86 ± 0.15
$f_2(1270)$	1 [Fixed]	0 [Fixed]	13.34	13.69 ± 0.14
$f'_2(1525)$	0.1241 ± 0.0063	167.8 ± 3.0	0.057	0.0455 ± 0.0070
Σ FF			105.0	104.3
$\chi^2/ndof$ (range):	[1.54 - 1.66]	Δ FCN:	+96	

Table 39 – Interference fit fractions between components of model PWA-5.

	$\omega(782)$	$\rho(770)^0$	$\rho(1450)^0$	$f_2(1270)$	$f'_2(1525)$	S -wave
$\omega(782)$	0.32					
$\rho(770)^0$	0.20	0.88				
$\rho(1450)^0$	0.40	0.63	5.35			
$f_2(1270)$	-0.14	0.12	-1.18	13.34		
$f'_2(1525)$	-0.0087	0.018	0.093	-0.33	0.057	
S -wave	-0.058	0.30	-1.46	-3.31	0.22	84.6

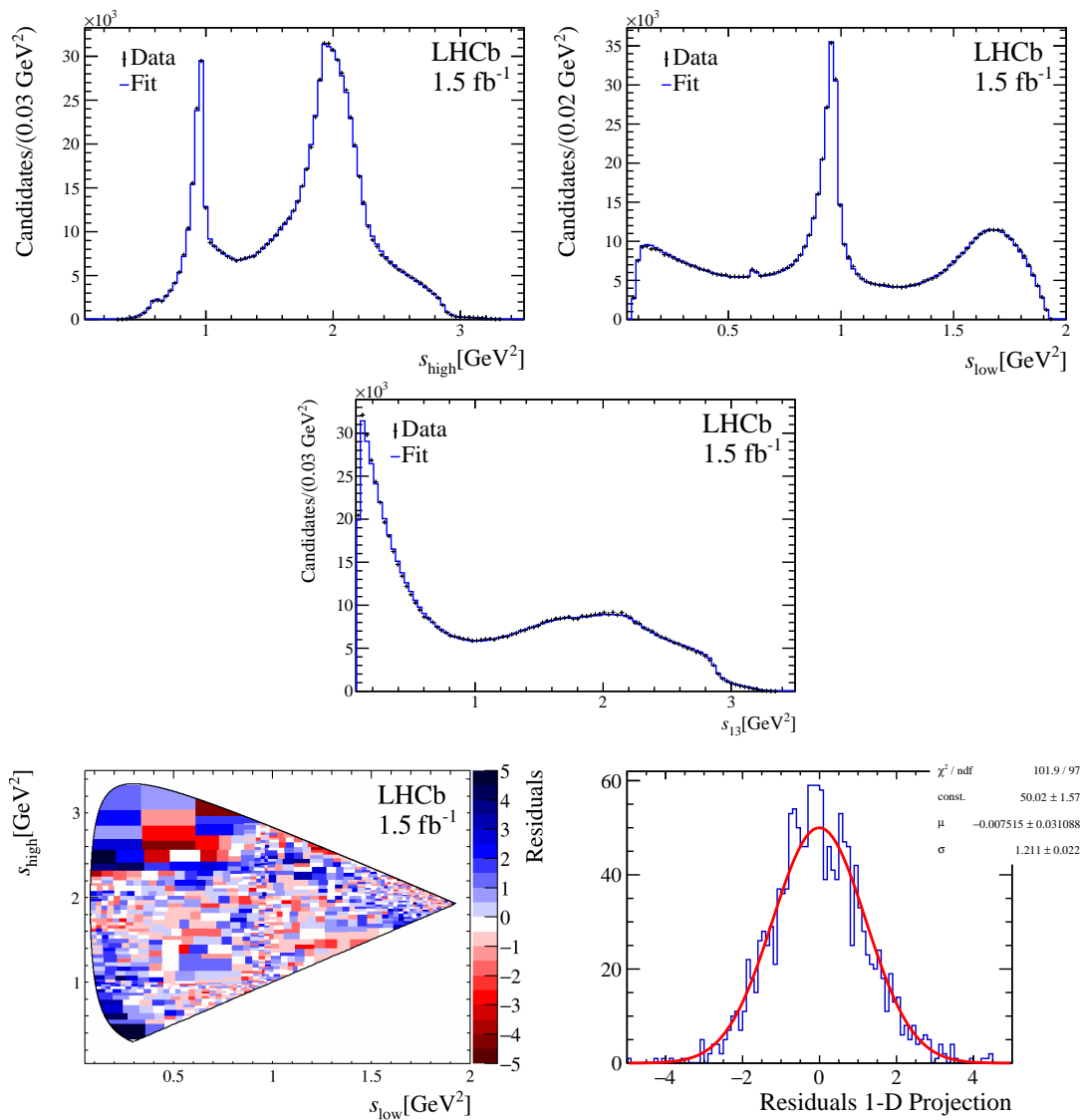


Figure 80 – Fit results from model PWA-5: the projections of the lowest (top left) and the highest (top right) of the two $\pi^+\pi^-$ invariant masses squared; the $\pi^+\pi^+$ projection (mid left) and the helicity angle (mid right, with two entries per event); distribution of the normalised residuals across the Dalitz plot (bottom left) and as 1D projection (bottom right). The data is represented by the red dots whilst the fit result is the histogram in black.

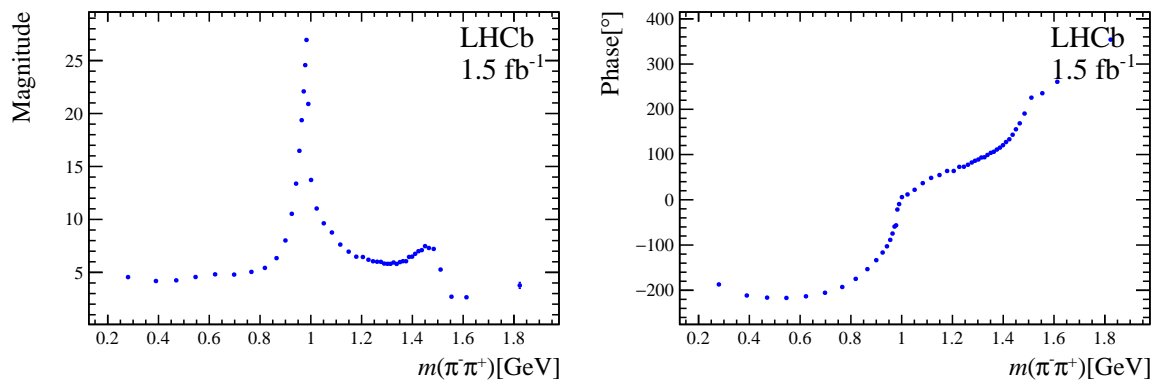


Figure 81 – Fitted S -wave for model PWA-5.

C.5 PWA-6 - Fit with $\rho - \omega$ mixing amplitude

In various data sets with a $\pi^+\pi^-$ pair in the final state, a large $\rho(770)^0$ signal is observed, and the $\omega(782)$ appears either as a dip or as a second peak above the $\rho(770)^0$ mass. In this respect, the $D_s^+ \rightarrow \pi^-\pi^+\pi^+$ decay is unique: a clear signal of $\omega(782)$ and a tiny $\rho(770)^0$ signal are observed. This fact may indicate that the mechanisms for the $\omega(782)$ production in $D_s^+ \rightarrow \pi^-\pi^+\pi^+$ decays are different from other reactions. This feature is further explored in this fit by varying the parameterisation of both amplitudes. Instead of a sum of individual components for the $\rho(770)^0$ and $\omega(782)$, the $\rho - \omega$ mixing amplitude is used, following the parameterisation from [103],

$$R_{\rho-\omega}(m) = R_\rho(m) \left[\frac{1 + R_\omega(m)\Delta\zeta}{1 - \Delta^2 R_\rho(m)R_\omega(m)} \right], \quad (\text{C.1})$$

where ζ is a complex parameter representing the intensity of the $\omega(782)$ production through mixing. In this fit, ζ is a free parameter. The functions $R_\rho(m)$ and $R_\omega(m)$ are the GS and RBW functions for the $\rho(770)^0$ $\omega(782)$ lineshapes, respectively. The quantity $\Delta = \delta(m_\rho + m_\omega)$ is related to the strength of the electromagnetic transition between the $\rho(770)^0$ and the $\omega(782)$. The parameter δ is also allowed to float in this fit (to the best of our knowledge, there is no expectation value for this parameter based on first principles). Its value is small ($\mathcal{O}(10^{-3})$), so the term Δ^2 in the denominator has no influence. Note that this parameterisation assumes the direct decay $\omega \rightarrow \pi^+\pi^-$ plays no role in the $\omega(782)$ production. This fit has equivalent quality as the default one, and the results are shown in Tables 40, 41 and 42, and in Figs. 83 and 82.

Replacing the default model by the $\rho - \omega$ mixing amplitude has a minor impact on the S - and D -waves. The combined fit fraction of the $\rho(770)^0$ and $\omega(782)$ in the default result agrees with the fit fraction of the $\rho - \omega$ amplitude. As expected, some variation on the fit fraction of the other P -wave amplitudes is observed.

The parameters of the $\rho - \omega$ mixing amplitude are very different from corresponding values from the $D^+ \rightarrow \pi^-\pi^+\pi^+$ analysis, also summarised in Table 42. The phase ϕ_ζ differs by approximately 100 degrees, whilst the magnitude $|\zeta|$ is nearly eight times larger in the $D_s^+ \rightarrow \pi^-\pi^+\pi^+$ decay. The fit with the $\rho - \omega$ mixing amplitude becomes significantly worse (over 350 FCN units) when the parameter δ is fixed at the same value as in [103], a value that is also used in the $D^+ \rightarrow \pi^-\pi^+\pi^+$ analysis. The significant difference in the parameters of $\rho - \omega$ mixing amplitude reinforces the interpretation that the $\omega(782)$ is produced through different mechanisms in $D_s^+ \rightarrow \pi^-\pi^+\pi^+$ and $D^+ \rightarrow \pi^-\pi^+\pi^+$ decays.

Table 40 – Fit results for model PWA-6. Phases in degrees and fit fractions (FF) in %.

Resonance	Magnitude	Phase	FF PWA-6	FF PWA1
S -wave			85.00	84.97 ± 0.14
$\rho - \omega$	0.1177 ± 0.0026	85.0 ± 1.7	1.46	1.53 ± 0.24
$\rho(1450)^0$	1.749 ± 0.028	-110.9 ± 1.4	5.57	3.86 ± 0.15
$\rho(1700)^0$	0.509 ± 0.058	-68.9 ± 7.5	0.13	0.365 ± 0.050
$\rho(1450)^0 + \rho(1700)^0$			7.14	6.14 ± 0.27
$f_2(1270)$	1 [Fixed]	0 [Fixed]	13.7	13.69 ± 0.14
$f_2'(1525)$	0.1118 ± 0.0076	175.0 ± 4.4	0.047	0.0528 ± 0.0070
\sum FF			105.9	104.3
χ^2/ndof (range):	[1.38 - 1.49]	ΔFCN :	-24	

Table 41 – Interference fractions (%) between amplitude components for model PWA-6.

	$\rho - \omega$	$\rho(1450)^0$	$\rho(1700)^0$	$f_2(1270)$	$f_2'(1525)$	S -wave
$\rho - \omega$	1.46					
$\rho(1450)^0$	0.29	5.57				
$\rho(1700)^0$	-0.10	1.44	0.12			
$f_2(1270)$	0.16	-1.39	-0.18	13.7		
$f_2'(1525)$	0.011	0.084	0.011	-0.39	0.047	
S -wave	0.75	-2.71	-0.56	-3.47	0.21	85.0

 Table 42 – Fitted parameters of the $\rho - \omega$ mixing amplitude.

Parameter	$D_s^+ \rightarrow \pi^- \pi^+ \pi^+$	$D^+ \rightarrow \pi^- \pi^+ \pi^+$
$ \zeta $	4.44 ± 0.97	0.544 ± 0.021
ϕ_ζ	$(68.9 \pm 2.4)^\circ$	$(166.8 \pm 2.3)^\circ$
δ [MeV]	5.06 ± 1.10	2.15 (fixed)

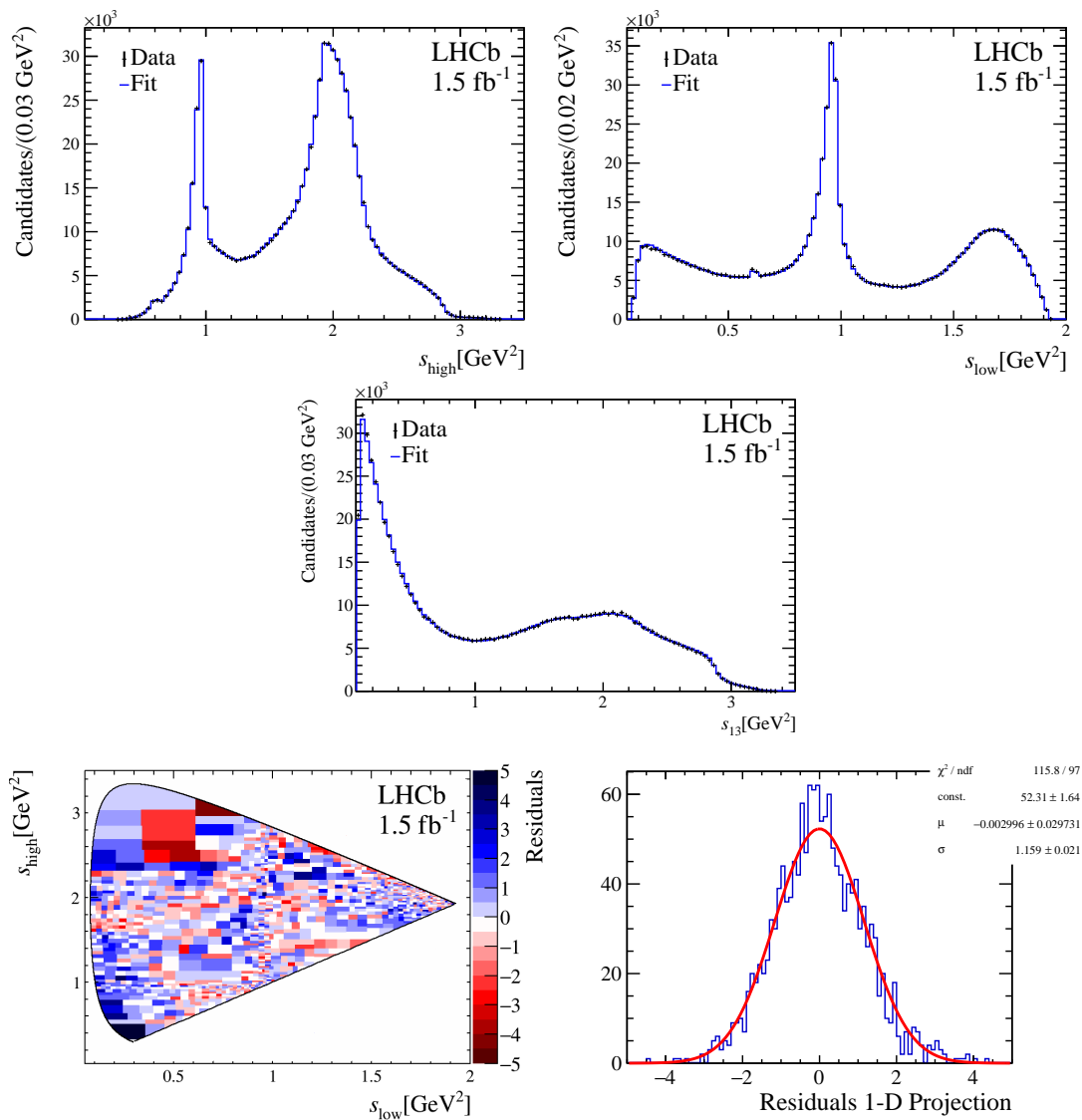


Figure 82 – Fit results from model PWA-6: the projections of the lowest (top left) and the highest (top right) of the two $\pi^+\pi^-$ invariant masses squared; the $\pi^+\pi^+$ projection (mid left) and the helicity angle (mid right, with two entries per event); distribution of the normalised residuals across the Dalitz plot (bottom left) and as 1D projection (bottom right). The data is represented by the red dots whilst the fit result is the histogram in black.

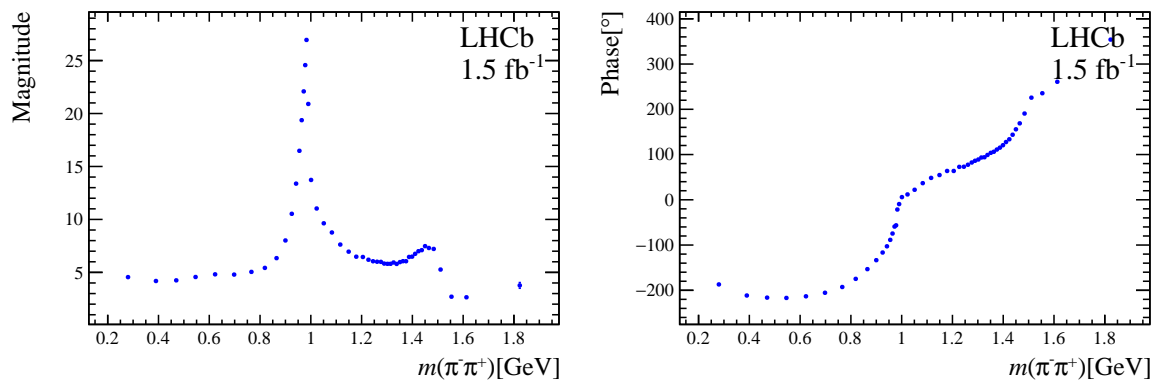


Figure 83 – Fitted S -wave for model PWA-6.

C.6 PWA-7 - Vetoing regions with low efficiency

In this fit, data from the edges of the Dalitz plot are discarded. In these regions, the fit quality is worse. The edges are defined as $s_{12} > 3.0$ and $s_{13} > 3.0$ GeV²; $s_{12} < 0.5$ and $s_{13} < 0.5$ GeV². The idea is to test the influence of these regions in the fit. The results are in Tables 43 and 44, and in Figs. 84 and 85. The exclusion of these regions made very little difference concerning the fit of the full phase space.

Table 43 – Fit results for model PWA-7. Phases in degrees and fit fractions (FF) in %.

Resonance	Magnitude	Phase	FF PWA-7	FF PWA1
S -wave			84.8	84.97 ± 0.14
$\rho(770)$	0.1268 ± 0.0029	84.8 ± 2.0	0.99	1.038 ± 0.054
$\omega(782)$	0.0388 ± 0.0010	-108.7 ± 1.8	0.339	0.360 ± 0.016
$\rho(1450)^0$	1.313 ± 0.028	-114.8 ± 2.7	4.01	3.86 ± 0.15
$\rho(1700)^0$	0.928 ± 0.075	-69.2 ± 6.4	0.405	0.365 ± 0.050
$\rho(1450)^0 + \rho(1700)^0$	0.983 ± 0.072	-71.1 ± 5.7	6.56	6.14 ± 0.27
$f_2(1270)$	1 [Fixed]	0 [Fixed]	13.46	13.69 ± 0.14
$f_2'(1525)$	0.1078 ± 0.0069	175.729 ± 4.44606	0.043	0.0455 ± 0.0070
Σ FF			104.0	104.3
χ^2/ndof (range):	[1.42 - 1.53]			

Table 44 – Interference fractions (%) between amplitude components for model PWA-7.

	$\omega(782)$	$\rho(770)^0$	$\rho(1450)^0$	$\rho(1700)^0$	$f_2(1270)$	$f_2'(1525)$	S -wave
$\omega(782)$	0.334						
$\rho(770)^0$	0.15	0.99					
$\rho(1450)^0$	0.36	0.27	4.01				
$\rho(1700)^0$	0.097	-0.20	2.14	0.405			
$f_2(1270)$	-0.15	0.21	-1.13	-0.33	13.46		
$f_2'(1525)$	-0.0078	0.0074	0.067	0.019	-0.39	0.043	
S -wave	-0.065	0.85	-1.96	-0.99	-3.19	0.19	84.8

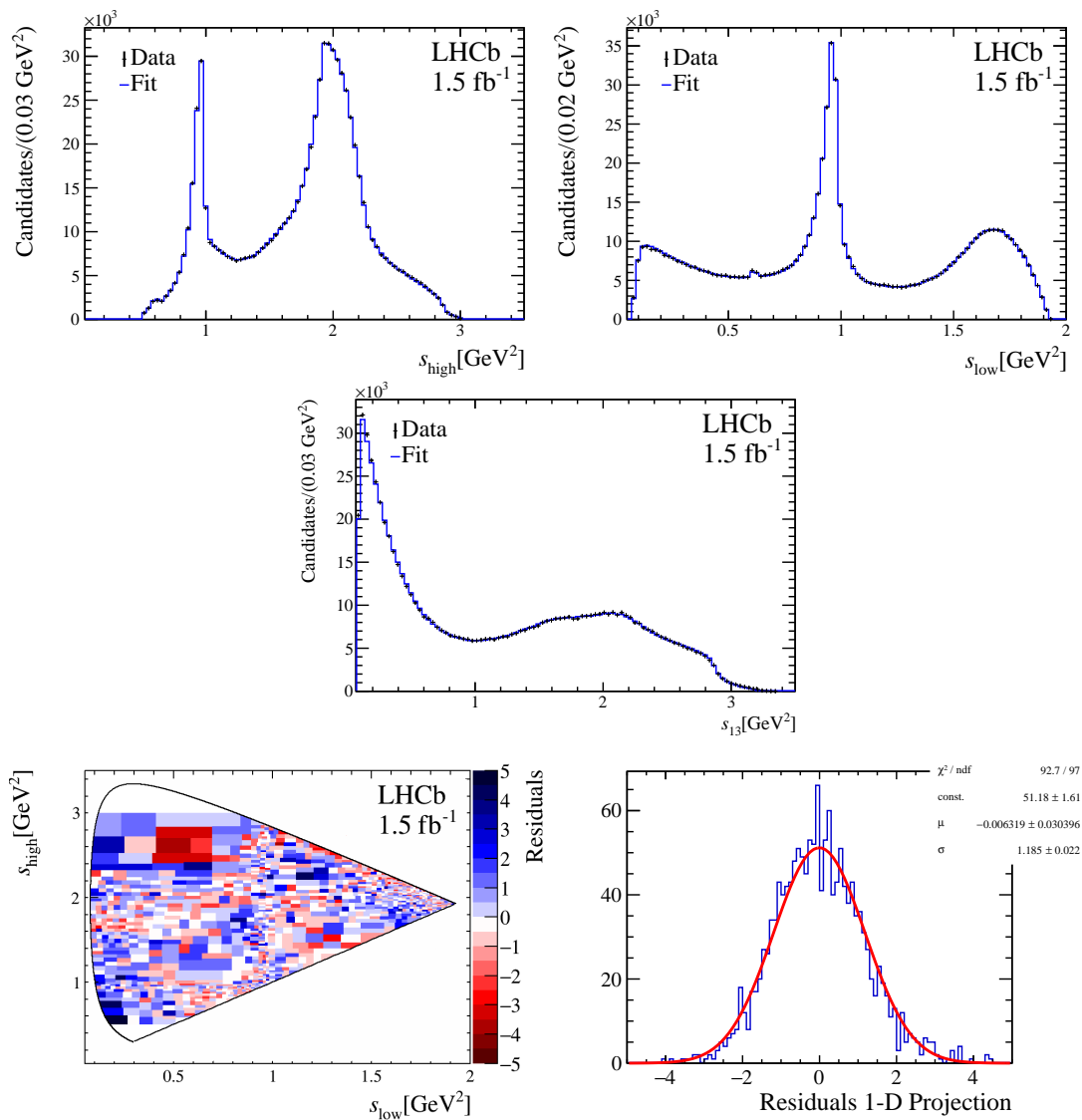


Figure 84 – Fit results from model PWA-7: the projections of the lowest (top left) and the highest (top right) of the two $\pi^+\pi^-$ invariant masses squared; the $\pi^+\pi^-$ projection (mid left) and the helicity angle (mid right, with two entries per event); distribution of the normalised residuals across the Dalitz plot (bottom left) and as 1D projection (bottom right). The data is represented by the red dots whilst the fit result is the histogram in black.

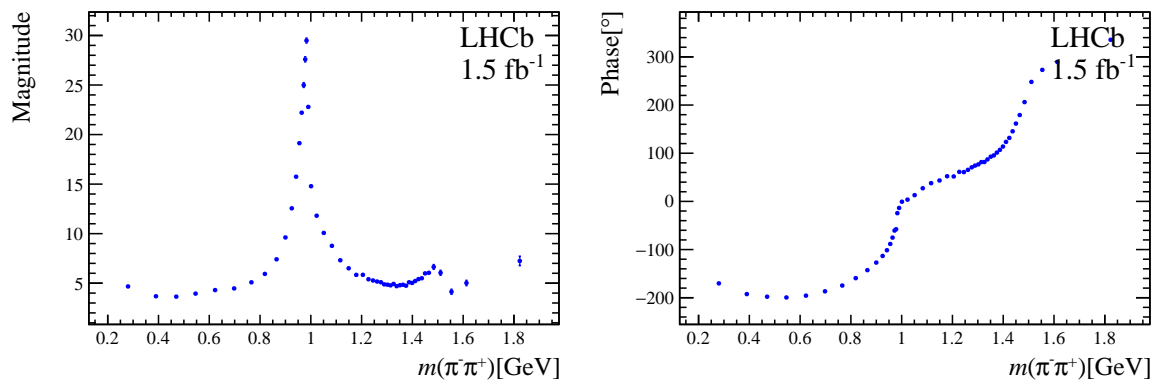


Figure 85 – Fitted S -wave for model PWA-7.

C.7 PWA-8 - Fit including Bose-Einstein correlation

Murray Gell-Mann used to say “in quantum mechanics, everything not forbidden is mandatory”. In this spirit, we considered a possible contribution from the Bose-Einstein correlation (BEC) since the final state contains two identical bosons. The BEC effect has been observed in many reactions since the 1960s but never in decays, perhaps because no one ever searched for it. The BEC effect consists of an enhancement of the two-particle correlation function when both identical pions are very close in the momentum space. Defining the variable $Q = \sqrt{-(q_2 - q_3)^2} = \sqrt{s_{23} - 4m_\pi^2}$, where q_2 and q_3 are the four-momenta of the π_2^+ and π_3^+ , the BEC effect manifests as a peak at the threshold of the $\pi^+\pi^+$ mass spectrum, $s_{23} = 4m_\pi^2$ or $Q \approx 0$.

The two-particle density function for like-sign pair of indistinguishable particles is defined as [104]

$$\rho_2(Q) = N(1 + \lambda e^{-QR}), \quad (\text{C.2})$$

where N is a normalization factor, λ is the chaoticity parameter related to the coherence of the emitting source, and R is the correlation radius. The actual BEC effect is the second term in the above equation. In this alternative model, the BEC effect is added as an additional amplitude, parameterised as $A_{BEC}(s_{23}) = c_{BEC}e^{-QR}$, similar to the parameterization used in the LHCb publication [105]. The complex coefficient c_{BEC} is a free parameter that absorbs the constant λ . In pp collisions the parameter R depends on the multiplicity of particles in the event. In this fit, the parameter R is fixed at 1.0 fm, the value measured for low multiplicity events in the LHCb publication.

The results from this alternative model are summarised in Tables 45 and 46, and in Figs. 86 and 87. The model with the BEC amplitude yields a good description of the data, with similar fit quality ($\chi^2/\text{ndof} \in [1.26 - 1.36]$) as the nominal result. The BEC amplitude competes with the two ρ -like and with the $f_2(1270)$ amplitudes, causing a small reduction of these contributions. The agreement between the model and data is improved in the low s_{23} region. This is expected since the BEC amplitude is peaked at s_{23} threshold.

Table 45 – Fit results for model PWA-8. Phases in degrees and fit fractions (FF) in %.

Resonance	Magnitude	Phase	FF PWA-8	FF PWA1
<i>S</i> -wave			82.69	84.97 ± 0.14
$\rho(770)^0$	0.1284 ± 0.0034	77.5 ± 1.8	1.048	1.038 ± 0.054
$\omega(782)$	0.04269 ± 0.00095	-109.8 ± 1.7	0.363	0.360 ± 0.016
$\rho(1450)^0$	1.036 ± 0.033	-114.8 ± 4.1	2.25	3.86 ± 0.15
$\rho(1700)^0$	1.02 ± 0.10	-12.4 ± 6.6	0.439	0.365 ± 0.050
$\rho(1450)^0 + \rho(1700)^0$	0.729 ± 0.092	-20.2 ± 8.5	3.35	6.14 ± 0.27
$f_2(1270)$	1 [Fixed]	0 [Fixed]	12.10	13.60 ± 0.11
$f'_2(1525)$	0.1429 ± 0.0079	173.0 ± 4.3	0.068	0.0455 ± 0.0070
BEC	9.47 ± 0.56	114.6 ± 5.2	9.97	-
Σ FF			108.9	104.3
χ^2/ndof (range):	[1.26 - 1.36]	ΔFCN :	-146	

Table 46 – Interference fractions (%) between amplitude components for model PWA-8.

	$\omega(782)$	$\rho(770)^0$	$\rho(1450)^0$	$\rho(1700)^0$	$f_2(1270)$	$f'_2(1525)$	BEC	<i>S</i> -wave
$\omega(782)$	0.363							
$\rho(770)^0$	0.11	1.048						
$\rho(1450)^0$	0.28	0.053	2.25					
$\rho(1700)^0$	0.021	-0.62	0.67	0.44				
$f_2(1270)$	-0.14	0.29	-0.80	-0.58	12.10			
$f'_2(1525)$	-0.010	0.0066	0.065	0.027	0.43	0.068		
BEC	-0.19	-0.44	0.0066	2.75	0.87	-0.0039	9.97	
<i>S</i> -wave	0.092	1.60	-1.73	-1.72	-2.84	0.20	-7.02	82.69

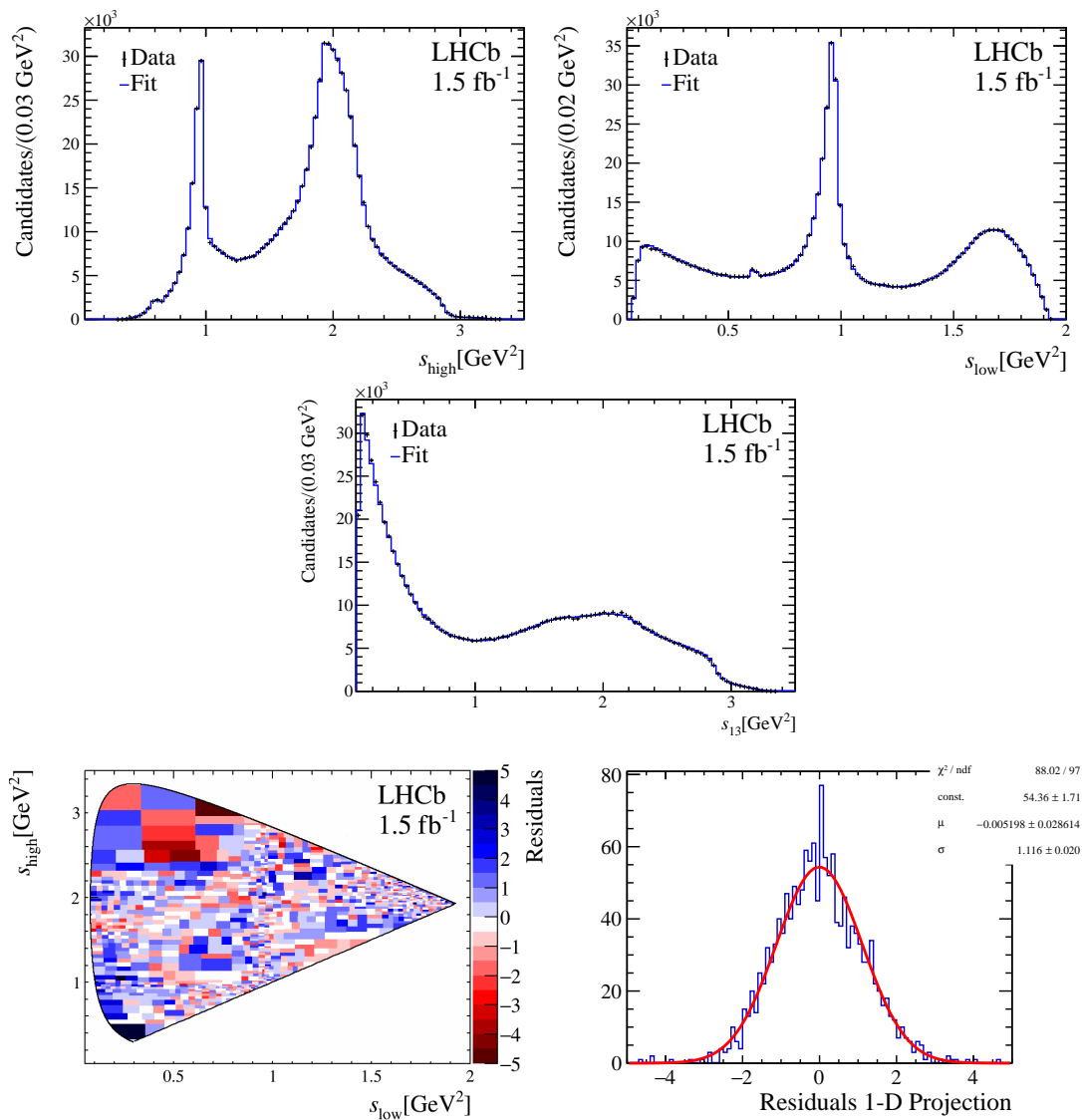


Figure 86 – Fit results from model PWA-8: the projections of the lowest (top left) and the highest (top right) of the two $\pi^+\pi^-$ invariant masses squared; the $\pi^+\pi^+$ projection (mid left) and the helicity angle (mid right, with two entries per event); distribution of the normalised residuals across the Dalitz plot (bottom left) and as 1D projection (bottom right). The data is represented by the red dots whilst the fit result is the histogram in black.

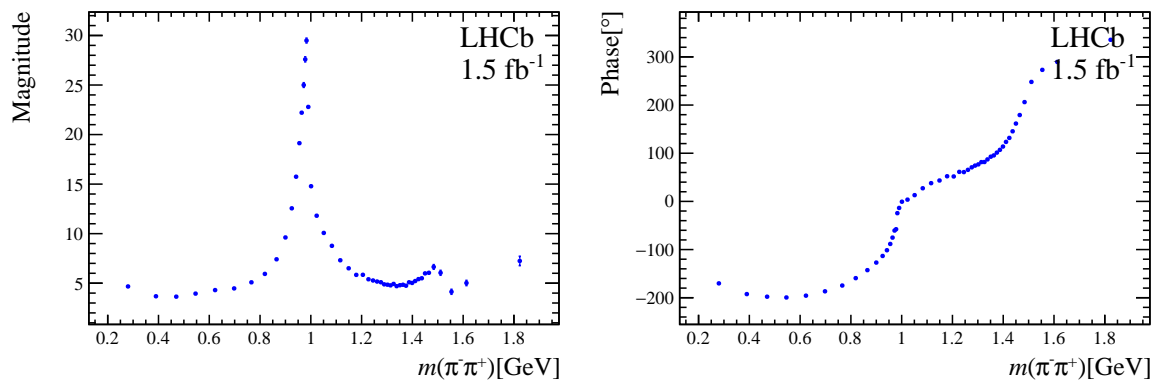


Figure 87 – Fitted S -wave for model PWA-8.

D Brief discussion about the Scalars

The Quark Model groups the mesons with light quark constituents (u,d,s) in $SU(3)$ nonets according to the J^{PC} numbers. The pseudo-scalars (0^{-+}), vectors ($1^{\pm\pm}$) and tensors (2^{++}) nonets are well identified. In contrast, identifying scalar (0^{++}) nonet has been a longstanding puzzle.

Scalar resonances are difficult to distinguish due to the lack of angular information and broad decay widths, which make them strongly overlap with each other and with the non-resonant background. The opening of decay channels within a narrow mass range can include cusps in resonance lineshape, requiring more sophisticated parameterizations than simple Breit-Wigner to extract the resonance parameters from data. Thus, it is convenient to refer to resonance pole position $\sqrt{s_{pole}} = \bar{m} + i\bar{\Gamma}/2$, which is process independent. However, it requires an analytic extrapolation of the amplitude away from the region of experimental measurements since $\sqrt{s_{pole}}$ is not directly accessible from the experiment. Furthermore, non- $q\bar{q}$ states with the same quantum numbers 0^{++} such as the lightest glueballs, multi-quark states with a quark-antiquark and an excited gluon (called hybrid mesons), tetraquarks ($q\bar{q}q\bar{q}$ or $qq\bar{q}\bar{q}$) and baryonia ($qqq\bar{q}\bar{q}$) are expected to populate the mass region of interest (up to 2 GeV).

Scalar resonances can be produced in several processes. For example, in πN scattering on (un)polarized target, $p\bar{p}$ annihilation, central hadronic production, $J/\psi(1S)$, B-, D- and K-meson decays, in $\gamma\gamma$ formation and radioactive decays of ϕ . Generally, it is expected that a resonance, being a real particle, must have the same parameters in whichever process it appears. Thus, the measuring of the scalars in different processes is fundamental for determining their nature.

The LHCb experiment has copiously produced scalar resonances through decays of D meson into 3- and 4-hadrons, permitting access to important decay channels of these particles as the $\pi\pi$, the πK and the $K\bar{K}$ channels. The advantage of D meson decays compared with scattering experiments is that they are expected to be dominated by resonances, with a small contribution of non-resonant background. Moreover, in scattering experiments, only strong interactions are involved, preserving isospin and parity. It is not the case of weak decays of D-mesons that violate isospin and parity. The quark content of the initial state determines the observed spectrum in such decays.

According to [21], the following scalars are expected up to 2 GeV: the two known isoscalars $a_0(980)$ and $a_0(1450)$. The five established isoscalars $f_0(500)/\sigma$, $f_0(980)$, $f_0(1370)$, $f_0(1500)$ and $f_0(1710)$. And, the strange companions $K_0^*(700)/\kappa$ and the $K_0^*(1430)$. Additionally, it is predicted by Lattice QCD the presence of a light scalar glueball with

a mass of around 1600 – 1700 MeV. The nature and existence of some of these states is quite controversial. For example, the $f_0(980)$ is usually referred as a tetraquark state in the literature. The determination of the light meson nonets is fundamental for the QCD and depends on correctly identifying the scalar mesons. A brief discussion about each of these states is presented below.

$f_0(500)/\sigma$ and $K_0^*(700)/\kappa$

The existence and the parameters of light scalar mesons have been an object of debate for many years. The $f_0(500)/\sigma$ was suggested in linear sigma models more than 60 years ago by Johnson and Teller [106] as a particle that couples strongly to the $\pi\pi$ channel. Later, It was incorporated by Schwinger as a singlet in the isospin picture [107]. Furthermore, 40 years ago, when extending this picture to include strangeness and SU(3) flavour symmetry, the scalar nonet below 1 GeV was proposed by Jaffe [108] including $K_0^*(700)/\kappa$ meson. Both σ and κ have very large widths, which makes them not show prominent Breit-Wigner peaks being hard to distinguish.

The $f_0(500)$

The $\pi\pi$ phase shifts extracted from Breit-Wigners strongly disagree with the scattering phase shifts, which makes Breit-Wigner parameterization not recommended to model broad decay width resonances. Dispersion relations, such “Roy equations”, have been used to determine the position of the complex mass pole by exploring the S-matrix analyticity, crossing symmetry and unitarity, and experimental information of $\pi\pi$ scattering. According to the review of scalars below 1 GeV [1], the most recent results, including only the most advanced dispersive analyses, predict the mass pole position at $\sqrt{s_{pole}^\sigma} = (449_{-16}^{+22}) - i(275 \pm 12)$ MeV. A detailed discussion about σ pole determination can be found in [17].

Indication of this state is present in $\pi\pi$ elastic scattering, where it contributes as a broad resonance with a central value of 1000 MeV when the phase passes to 90° . In decays of B_d meson as $B_d \rightarrow KK\pi$, $B_d \rightarrow K\bar{K}K$ and in the $B_s^0 \rightarrow J/\Psi\pi\pi$, it shows up as a broad background. There is also the important contribution attributed to σ at the beginning of the threshold $\pi\pi$ of the S-wave extracted from $D^+ \rightarrow \pi^-\pi^+\pi^+$, as detailed in 6 and 7. In that analysis, the σ was interpreted as a dynamic pole in the $\pi\pi$ scattering.

The $K_0^*(700)$

The κ resonance appears as a pole in the $K\pi$ scattering close to the threshold. Due to its very broad width of about 500 MeV, it is considered difficult to establish. Hadronic D- and B-meson decays provide additional data from the vicinity of the $K\pi$ threshold.

Indication of the existence of κ was found in BES II re-analysis [109], a κ -like structure was found in the decay of $J/\Psi(1S) \rightarrow K^{*0}(892)K^+\pi^-$. In the phenomenological analysis in which constraints from Chiral symmetry are included at low energies, the κ pole is also found below 800 MeV. However, some analyses do not need to include it in their fits. Thus, the existence of this particle remains controversial.

The position of the mass pole of κ can also be determined through the dispersion relations approach. The pole position given in [1] is $\sqrt{s_{pole}^\kappa} = (630 - 730) - i(260 - 340)$ MeV. A detailed discussion about the determination of $\sqrt{s_{pole}^\kappa}$ in dispersive data analysis can be found in [110].

The companion isospin-1/2 of κ , the $K_0^*(1430)$, is the least controversial of the scalar mesons. Analysis using unitarized amplitudes agrees about the presence of this resonance pole around 1410 MeV with a decay width of 300 MeV. However, other analyses with reduced model dependence found a larger width of 500 MeV. The most recent PDG estimative of mass and width are 1425 ± 50 MeV and 270 ± 40 MeV.

$f_0(980)$ and $a_0(980)$

In addition to κ and σ , the $f_0(980)$ and $a_0(980)$ are expected to form a scalar meson nonet below 1 GeV. The $f_0(980)$ couples predominantly to the $\pi\pi$ and $K\bar{K}$ channels, while the $a_0(980)$ couples to $\pi\eta$ and $K\bar{K}$ channels. The opening of decay channels within a narrow mass range includes cusps in both resonance lineshapes. The results of their masses agree to the value of 980 ± 20 MeV. In contrast, their decay widths are poorly known, varying between 50-100 MeV. The reason is that $f_0(980)$ and $a_0(980)$ behave differently depending on the reaction in which they are produced.

Coupled channel Breit-Wigner parameterization, also called Flatté [111], and K-Matrix are often used to model these states, allowing the extraction of the respective couplings. The latter is required for the determination of the decay width. The relative $K\bar{K}/\pi\eta = 1.03 \pm 0.14$ is determined from $KK\pi$ final state from $p\bar{p}$ annihilation at rest [112] for the $a_0(980)$. The relative $K\bar{K}/\pi\pi = 4.21 \pm 0.25 \pm 0.21$ is determined from coupled channel analysis of $J/\Psi \rightarrow \phi\pi\pi$ and ϕKK [113]. A detailed discussion about Flatté-like lineshapes and $f_0(980)$ and $a_0(980)$ can be found in [114].

Unitarized chiral perturbation theory and dispersion theoretical approaches were employed to extract the pole of each resonance. The values for each one in reference [1] are $\sqrt{s_{pole}^{a_0}} = (960 - 1030) - i(20 - 70)$ MeV and $\sqrt{s_{pole}^{f_0}} = (980 - 1010) - i(20 - 35)$ MeV.

The $f_0(980)$ and $a_0(980)$ are often interpreted as compact tetraquarks or $K\bar{K}$ bound states. This thesis analysis of the $D_s^+ \rightarrow \pi^-\pi^+\pi^+$ decays shows a prominent contribution of the $f_0(980)$ in the S-wave with no background from σ . In contrast, the $D^+ \rightarrow \pi^-\pi^+\pi^+$ shows a less prominent contribution of the same state. This observation shows the affinity

of $f_0(980)$ to the $s\bar{s}$ source already observed in other decays like $J/\Psi \rightarrow \phi\pi^+\pi^-$ and $\omega\pi^+\pi^-$, and $B_{(s)}^0 \rightarrow J/\Psi\pi^+\pi^-$. The $f_0(980)$ strongly couples to the $K\bar{K}$ channel. The unitarity chiral is used in section 7 to explain this difference. The approach shows that $K\bar{K}$ channel contributes more with $D_s^+ \pi\pi$ S-wave. The above situation reinforces the interpretation of this state as a 4-quark state surrounded by a $K\bar{K}$ molecular cloud. At short distances, as in D decays, we would access the $qq\bar{q}\bar{q}$ component, whereas in peripheral processes, the molecular component would manifest itself.

the f_0 states above 1 GeV

The quark model predicts the existence of two f_0 states above 1 GeV, but three are observed: $f_0(1370)$, $f_0(1500)$ and $f_0(1710)$. The first two decay mostly into pions (2π and 4π), while the $f_0(1710)$ decays mostly in $K\bar{K}$ final states. The same model assume that $f_0(1370)$, $a_0(1450)$ and $K_0^*(1430)$ are in the same $SU(3)$ flavour nonet with quark content ($u\bar{u} + d\bar{d}$), $u\bar{d}$, $u\bar{s}$, while $f_0(1710)$ is the $s\bar{s}$ state. The $f_0(1710)$ is observed in $p\bar{p}$ annihilation experiments as well the $a_0(1450)$. The latter is also observed in the decay $D^0 \rightarrow K_s^0 K^\pm \pi^\mp$ [115].

The $f_0(1500)$ is the only scalar state with measured branching fractions.

$$\frac{\Gamma(f_0(1500) \rightarrow \pi\pi)}{\Gamma(f_0(1500) \rightarrow K\bar{K})} = \frac{34.9 \pm 2.3}{8.6 \pm 1.0}$$

The upper limit from $\pi^-\pi^+$ process excludes a large $n\bar{n}$ (here n stands for the two lightest quarks) content for $f_0(1500)$ [116, 1]. Thus pointing out $f_0(1500)$ as a mainly $s\bar{s}$ state. The latter observation contradicts the small $K\bar{K}$ branching fraction, which makes the assignment of $f_0(1500)$ as a pure $q\bar{q}$ state questionable. Although, it reinforces the interpretation of $f_0(1500)$ as the ground-state scalar glueball expected to populate the mass region between 1.6-1.7 GeV.

The results of $f_0(1500)$ and $f_0(1710)$ provide a good measurement of their masses but a bit high uncertainty on the determination of the widths. In contrast, the parameters of $f_0(1370)$ are very poorly known, with very different results from the analysis. A scalar with a mass around 1470 MeV was observed in $\gamma\gamma \rightarrow \pi^0\pi^0$, but it was not conclusive if it is the $f_0(1370)$ or the $f_0(1500)$. In the $D_s^+ \rightarrow \pi^-\pi^+\pi^+$ and $D^+ \rightarrow \pi^-\pi^+\pi^+$ analysis, the argand plots of the $\pi\pi$ S-waves indicate the presence of two scalars above 1 GeV when the amplitude is purely imaginary. From the D_s^+ S-wave, we got the values 1302 MeV and 1613 MeV, indicating that they may be the $f_0(1370)$ and $f_0(1500)$, respectively.

References

- 1 WORKMAN, R. L.; OTHERS. Review of Particle Physics. *PTEP*, v. 2022, p. 083C01, 2022. Disponível em: <<https://pdg.lbl.gov/2023/web/viewer.html?file=../reviews/rpp2022-rev-kinematics.pdf>>.
- 2 HOECKER, A. et al. *TMVA - Toolkit for Multivariate Data Analysis*. 2009. Disponível em: <<https://arxiv.org/abs/physics/0703039>>.
- 3 MACHINELEARNINGMIKE.COM. *Gradient Boosting*. 2023. Disponível em: <<https://www.machinelearningmike.com/post/gradient-boosting-part-3>>.
- 4 SJÖSTRAND, T. et al. An introduction to PYTHIA 8.2. *Computer Physics Communications*, Elsevier BV, v. 191, p. 159–177, jun 2015. Disponível em: <<https://doi.org/10.1016%2Fj.cpc.2015.01.024>>.
- 5 ELSASSER, C. *$\bar{b}b$ production angle plots*. 2023. Disponível em: <https://lhcb.web.cern.ch/speakersbureau/html/bb_ProductionAngles.html>.
- 6 COLLABORATION, e. a. The lhcb detector at the lhc. *Journal of Instrumentation*, v. 3, p. S08005, 08 2008. Disponível em: <<https://cds.cern.ch/record/1129809/>>.
- 7 MCCARRON, J.; MUHEIM, F. Characterisation of hybrid photon detectors for the lhcb and an analysis of the rare decay $b_s^0 \rightarrow \phi\phi$. 08 2023. Disponível em: <<https://cds.cern.ch/record/1096861/files/CERN-THESIS-2008-031.pdf>>.
- 8 BETETA, C. A. et al. Monitoring radiation damage in the lhcb tracker turicensis. *Journal of Instrumentation*, v. 15, n. 08, p. P08016, aug 2020. Disponível em: <<https://dx.doi.org/10.1088/1748-0221/15/08/P08016>>.
- 9 HOMMELS, L. The lhcb outer tracker detector design and production. In: . [s.n.], 2004. v. 1, p. 672 – 676 Vol. 1. ISBN 0-7803-8700-7. Disponível em: <<https://ieeexplore.ieee.org/document/1462281>>.
- 10 AAIJ, R. et al. LHCb Detector Performance. *Int. J. Mod. Phys. A*, v. 30, p. 1530022, 2015. Disponível em: <<http://cds.cern.ch/record/1978280>>.
- 11 COLLABORATION, L. et al. *The LHCb upgrade I*. 2023. Disponível em: <<https://arxiv.org/abs/2305.10515>>.
- 12 COLLABORATION, L. *LHCb PID Upgrade Technical Design Report*. [S.l.], 2013. Disponível em: <<https://cds.cern.ch/record/1624074>>.
- 13 COLLABORATION, C. M. L. *LHCb Upgrade GPU High Level Trigger Technical Design Report*. Geneva, 2020. Disponível em: <<https://cds.cern.ch/record/2717938>>.
- 14 AL. and R. Aaij et. Amplitude analysis of the $d^+ \rightarrow \pi^-\pi^+\pi^+$ decay and measurement of the $\pi^-\pi^+$ s-wave amplitude. *Journal of High Energy Physics*, Springer Science and Business Media LLC, v. 2023, n. 6, jun 2023. Disponível em: <<https://doi.org/10.1007%2Fjhep06%282023%29044>>.

- 15 AAIJ, R. et al. Measurement of the resonant and CP components in $\bar{B}_s^0 \rightarrow j/\psi\pi^-\pi^+$. *Physical Review D*, American Physical Society (APS), v. 89, n. 9, may 2014. Disponível em: <<https://doi.org/10.1103/PhysRevD.89.092006>>.
- 16 AAIJ, R. et al. Measurement of the resonant and CP components in $\bar{B}^0 \rightarrow j/\psi\pi^-\pi^+$. *Physical Review D*, American Physical Society (APS), v. 90, n. 1, jul 2014. Disponível em: <<https://doi.org/10.1103/PhysRevD.90.012003>>.
- 17 OCHS, W. The status of glueballs. *Journal of Physics G: Nuclear and Particle Physics*, IOP Publishing, v. 40, n. 4, p. 043001, Feb 2013. ISSN 1361-6471. Disponível em: <<http://dx.doi.org/10.1088/0954-3899/40/4/043001>>.
- 18 HYAMS, B. et al. $\pi\pi$ phase-shift analysis from 600 to 1900 mev. *Nucl. Phys.*, B64, p. 134–162, 1973. Disponível em: <<https://doi.org/10.1063/1.2947103>>.
- 19 BATLEY, J. et al. Precise tests of low-energy qcd from k_{e4} decay properties. *Eur. Phys. J.*, C70, p. 635, 2010. Disponível em: <<https://cds.cern.ch/record/1293564/>>.
- 20 CHENG, H.; CHIANG, C. Two-body hadronic charmed meson decays. *Phys. Rev. D*, v. 81, p. 074021, 2010. Disponível em: <<https://doi.org/10.1103/PhysRevD.81.074021>>.
- 21 ZYLA, P. et al. Review of particle physics. *PTEP*, v. 2020, n. 8, p. 083C01, 2020. Disponível em: <<https://pdg.lbl.gov/2020/>>.
- 22 AUBERT, B. et al. Dalitz plot analysis of $d_s^+ \rightarrow \pi^-\pi^+\pi^+$. *Phys. Rev. D*, v. 79, p. 032003, 2009. Disponível em: <<http://dx.doi.org/10.1103/PhysRevD.79.032003>>.
- 23 ABLIKIM, M. et al. Amplitude analysis of $d_s^+ \rightarrow \pi^-\pi^+\pi^+$. *Physical Review D*, American Physical Society (APS), v. 106, n. 11, dec 2022. Disponível em: <<https://doi.org/10.1103/PhysRevD.106.112006>>.
- 24 AITALA, E. M. et al. Study of the $d_s^+ \rightarrow \pi^-\pi^+\pi^+$ decay and measurement of f_0 masses and widths. *Phys. Rev. Lett.*, American Physical Society, v. 86, p. 765–769, Jan 2001. Disponível em: <<https://link.aps.org/doi/10.1103/PhysRevLett.86.765>>.
- 25 BONVICINI, G. et al. Dalitz plot analysis of the $d^+ \rightarrow \pi^-\pi^+\pi^+$ decay. *Phys. Rev. D*, v. 76, p. 012001, 2007. Disponível em: <<https://journals.aps.org/prd/abstract/10.1103/PhysRevD.76.012001>>.
- 26 AAIJ and R. et al. Amplitude analysis of the $d_s^+ \rightarrow \pi^-\pi^+\pi^+$ decay. *Journal of High Energy Physics*, Springer Science and Business Media LLC, v. 2023, n. 7, jul 2023. Disponível em: <[https://doi.org/10.1007/JHEP07\(2023\)204](https://doi.org/10.1007/JHEP07(2023)204)>.
- 27 AAIJ, R. et al. Search for cp violation in the decay $d^+ \rightarrow \pi^-\pi^+\pi^+$. *Physics Letters B*, Elsevier BV, v. 728, p. 585–595, jan. 2014. ISSN 0370-2693. Disponível em: <<http://dx.doi.org/10.1016/j.physletb.2013.12.035>>.
- 28 BURAS, A. J. The standardmodel. In: _____. *Gauge Theory of Weak Decays: The Standard Model and the Expedition to New Physics Summits*. Cambridge University Press, 2020. p. 57–58. Disponível em: <<https://doi.org/10.1017/9781139524100>>.
- 29 KOBAYASHI, M.; MASKAWA, T. CP-Violation in the Renormalizable Theory of Weak Interaction. *Progress of Theoretical Physics*, v. 49, n. 2, p. 652–657, 02 1973. ISSN 0033-068X. Disponível em: <<https://doi.org/10.1143/PTP.49.652>>.

- 30 WEINBERG, S. *The Quantum Theory of Fields*. Cambridge University Press, 1995. v. 1. Disponível em: <<https://doi.org/10.1017/CBO9781139644167>>.
- 31 PESKIN, M. E.; SCHROEDER, D. V. *An introduction to quantum field theory*. Boulder, CO: Westview, 1995. Includes exercises. Disponível em: <<https://cds.cern.ch/record/257493>>.
- 32 DALITZ, R. H. On the analysis of tau-meson data and the nature of the tau-meson. *Phil. Mag. Ser. 7*, v. 44, p. 1068–1080, 1953. Disponível em: <<https://inspirehep.net/literature/44364>>.
- 33 BLATT, J. M.; WEISSKOPF, V. F. *Theoretical nuclear physics*. New York: Springer, 1952. ISBN 978-0-471-08019-0. Disponível em: <<https://inspirehep.net/literature/1500819>>.
- 34 GOUNARIS, G.; SAKURAI, J. Finite-width corrections to the vector-meson-dominance prediction for $\rho \rightarrow e^+e^-$. *Physical Review Letters*, APS, v. 21, n. 4, p. 244, 1968. Disponível em: <<https://doi.org/10.1103/PhysRevLett.21.244>>.
- 35 BARTOŠ, E. et al. Generalized gounaris-sakurai formula and $\rho^0(770)$, $\rho^0(1450)$ and $\rho^0(1700)$ masses and widths. In: . [S.l.: s.n.], 2018. p. 730.
- 36 ABRAROV, S.; QUINE, B. Efficient algorithmic implementation of the voigt/complex error function based on exponential series approximation. *Applied Mathematics and Computation*, v. 218, n. 5, p. 1894–1902, 2011. ISSN 0096-3003. Disponível em: <<https://www.sciencedirect.com/science/article/pii/S0096300311009179>>.
- 37 SCHREINER, H. et al. *GooFit 2.0*. 2017.
- 38 WILLIAMS, M. How good are your fits? unbinned multivariate goodness-of-fit tests in high energy physics. *Journal of Instrumentation*, v. 5, n. 09, p. P09004, sep 2010. Disponível em: <<https://dx.doi.org/10.1088/1748-0221/5/09/P09004>>.
- 39 PIVK, M.; DIBERDER, F. L. : A statistical tool to unfold data distributions. *Nuclear Instruments and Methods in Physics Research Section A: Accelerators, Spectrometers, Detectors and Associated Equipment*, Elsevier BV, v. 555, n. 1-2, p. 356–369, dec 2005. Disponível em: <<https://doi.org/10.1016%2Fj.nima.2005.08.106>>.
- 40 ROGOZHNIKOV, A. *sPlot: a technique to reconstruct components of a mixture*. 2023. Disponível em: <<https://arogozhnikov.github.io/2015/10/07/splot.html>>.
- 41 VERKERKE, W.; KIRKBY, D. *The RooFit toolkit for data modeling*. 2003. Disponível em: <<https://arxiv.org/abs/physics/0306116>>.
- 42 COADOU, Y. Boosted decision trees. In: *Artificial Intelligence for High Energy Physics*. WORLD SCIENTIFIC, 2022. p. 9–58. Disponível em: <https://doi.org/10.1142%2F9789811234033_0002>.
- 43 ROGOZHNIKOV, A. Reweighting with boosted decision trees. *Journal of Physics: Conference Series*, IOP Publishing, v. 762, p. 012036, oct 2016. Disponível em: <<https://doi.org/10.1088%2F1742-6596%2F762%2F1%2F012036>>.
- 44 ROGOZHNIKOV, A. *Reweighting with Boosted Decision Trees*. 2023. Disponível em: <<https://arogozhnikov.github.io/2015/10/09/gradient-boosted-reweighter.html>>.

- 45 LHC Machine. *JINST*, v. 3, p. S08001, 2008. Disponível em: <<https://iopscience.iop.org/article/10.1088/1748-0221/3/08/S08001>>.
- 46 BARBOSA-MARINHO, P. R. et al. *LHCb VELO (VERtEX LOcator): Technical Design Report*. Geneva: CERN, 2001. (Technical design report. LHCb). Disponível em: <<http://cds.cern.ch/record/504321>>.
- 47 AMATO, S. et al. *LHCb magnet: Technical Design Report*. Geneva: CERN, 2000. (Technical design report. LHCb). Disponível em: <<http://cds.cern.ch/record/424338>>.
- 48 GASSNER, J. et al. *Layout and Expected Performance of the LHCb TT Station*. Geneva, 2004. Disponível em: <<http://cds.cern.ch/record/728548>>.
- 49 BARBOSA-MARINHO, P. R. et al. *LHCb inner tracker: Technical Design Report*. Geneva: CERN, 2002. (Technical design report. LHCb). Revised version number 1 submitted on 2002-11-13 14:14:34. Disponível em: <<http://cds.cern.ch/record/582793>>.
- 50 BARBOSA-MARINHO, P. R. et al. *LHCb outer tracker: Technical Design Report*. Geneva: CERN, 2001. (Technical design report. LHCb). Disponível em: <<http://cds.cern.ch/record/519146>>.
- 51 CERENKOV, P. et al. Visible emission of clean liquids by action of γ radiation. *Dok Akad Nauk SSSR*, v. 2, p. 451–454, 1934. Disponível em: <https://www.researchgate.net/publication/285253557_Visible_emission_of_clean_liquids_by_action_of_g_radiation>.
- 52 MARINHO, P. et al. *LHCb calorimeters : Technical Design Report*. [s.n.], 2000. Disponível em: <https://www.researchgate.net/publication/281504305_LHCb_calorimeters_Technical_Design_Report>.
- 53 MARINHO, P. et al. *LHCb muon system: Technical Design Report*. [s.n.], 2001. Disponível em: <https://www.researchgate.net/publication/280789980_LHCb_muon_system_Technical_Design_Report>.
- 54 ALEMANY-FERNANDEZ, R. et al. Operation and Configuration of the LHC in Run 1. 2013. Disponível em: <<https://cds.cern.ch/record/1631030>>.
- 55 WENNINGER, J. Operation and Configuration of the LHC in Run 2. 2019. Disponível em: <<https://cds.cern.ch/record/2668326>>.
- 56 HEAD, T. The lhcb trigger system. *Journal of Instrumentation*, v. 9, p. C09015, 09 2014. Disponível em: <https://www.researchgate.net/publication/234404180_LHCb_trigger_system>.
- 57 BOS, E. et al. *The Trajectory Model for Track Fitting and Alignment*. Geneva, 2007. Disponível em: <<http://cds.cern.ch/record/1025826>>.
- 58 AAIJ, R. et al. Design and performance of the lhcb trigger and full real-time reconstruction in run 2 of the lhc. performance of the lhcb trigger and full real-time reconstruction in run 2 of the lhc. *JINST*, v. 14, n. 04, p. P04013, 2019. Disponível em: <<https://cds.cern.ch/record/2652801>>.
- 59 LETTER of Intent for the LHCb Upgrade. Geneva, 2011. Disponível em: <<https://cds.cern.ch/record/1333091>>.

- 60 COLLABORATION, C. M. L. *Framework TDR for the LHCb Upgrade II - Opportunities in flavour physics, and beyond, in the HL-LHC era*. Geneva, 2021. Disponível em: <<https://cds.cern.ch/record/2776420>>.
- 61 COLLABORATION, L. et al. *Physics case for an LHCb Upgrade II - Opportunities in flavour physics, and beyond, in the HL-LHC era*. 2019. Disponível em: <<https://arxiv.org/abs/1808.08865>>.
- 62 COLLABORATION, L. *LHCb VELO Upgrade Technical Design Report*. 2013. Disponível em: <<https://cds.cern.ch/record/1624070>>.
- 63 van Beuzekom, M. et al. Velopix ASIC development for LHCb VELO upgrade. *Nuclear Instruments and Methods in Physics Research Section A: Accelerators, Spectrometers, Detectors and Associated Equipment*, v. 731, p. 92–96, 2013. ISSN 0168-9002. PIXEL 2012. Disponível em: <<https://www.sciencedirect.com/science/article/pii/S0168900213004117>>.
- 64 PAPADELIS, A. *Characterisation and commissioning of the LHCb VELO detector*. 2009. Presented on 17 Jun 2009. Disponível em: <<https://cds.cern.ch/record/1186697>>.
- 65 COLLABORATION, L. *LHCb Tracker Upgrade Technical Design Report*. [S.l.], 2014. Disponível em: <<https://cds.cern.ch/record/1647400/>>.
- 66 BOETTCHER, T. *The LHCb GPU high level trigger and measurements of neutral pion and photon production with the LHCb detector*. 2021. Presented 16 Dec 2020. Disponível em: <<https://cds.cern.ch/record/2762054>>.
- 67 AAIJ, R. et al. Allen: A high-level trigger on GPUs for LHCb. *Computing and Software for Big Science*, Springer Science and Business Media LLC, v. 4, n. 1, apr 2020. Disponível em: <<https://doi.org/10.1007%2Fs41781-020-00039-7>>.
- 68 MC Tool Background Info. 2023. <<https://twiki.cern.ch/twiki/bin/view/LHCb/TupleToolMCBackgroundInfo>>. Accessed: 2023-06-19.
- 69 ANDERLINI, L. et al. *The PIDCalib package*. Geneva, 2016. Disponível em: <<https://cds.cern.ch/record/2202412>>.
- 70 AMATO, S. et al. Search for CP violation in the decays $D_s^+ \rightarrow K^- K^+ K^+$ and $D^+ \rightarrow K^- K^+ K^+$. 2021. Disponível em: <<https://cds.cern.ch/record/2779666>>.
- 71 GAISER, J. E. Other thesis, *Charmonium Spectroscopy From Radiative Decays of the J/ψ and ψ'* . 1982. Disponível em: <<https://inspirehep.net/literature/183554>>.
- 72 HULSBERGEN, W. D. Decay chain fitting with a kalman filter. *Nuclear Instruments and Methods in Physics Research Section A: Accelerators, Spectrometers, Detectors and Associated Equipment*, Elsevier, v. 552, n. 3, p. 566–575, 2005. Disponível em: <<https://arxiv.org/abs/physics/0503191>>.
- 73 O'CONNELL, H. et al. Rho-omega mixing, vector meson dominance and the pion form-factor. *Progress in Particle and Nuclear Physics*, Elsevier BV, v. 39, p. 201–252, jan 1997. Disponível em: <<https://doi.org/10.1016%2Fs0146-6410%2897%2900044-6>>.
- 74 COLLABORATION, L. et al. Amplitude analysis of the $b^+ \rightarrow \pi^+ \pi^+ \pi^-$ decay. *Physical Review. D, Particles, fields, gravitation and cosmology*, v. 101, 01 2020. Disponível em: <<https://link.aps.org/doi/10.1103/PhysRevD.101.012006>>.

- 75 AITALA, E. et al. Experimental evidence for a light and broad scalar resonance in $d^+ \rightarrow \pi^- \pi^+ \pi^+$ decay. *Phys. Rev. Lett.*, v. 86, p. 770, 2001. Disponível em: <http://dx.doi.org/10.1103/PhysRevLett.86.770>.
- 76 ATHENODOROU, A.; TEPPER, M. The glueball spectrum of $su(3)$ gauge theory in 3+1 dimensions. *J. High Energ. Phys.*, v. 2020, p. 172, 2020. Disponível em: [https://doi.org/10.1007/JHEP11\(2020\)172](https://doi.org/10.1007/JHEP11(2020)172).
- 77 CLOSE, F.; TORNQVIST, N. Scalar mesons below and above 1 gev. *J. Phys. G: Nucl. Part. Phys.*, v. 28, p. R249–R267, 2002. Disponível em: <https://10.1088/0954-3899/28/10/201>.
- 78 GARMASH, A. et al. Dalitz plot analysis of the three-body charmless decays $b^+ \rightarrow k^+ \pi^+ \pi^-$ and $b^+ \rightarrow k^+ k^+ k^-$. *Phys. Rev. D*, v. 71, p. 002003, 2005. Disponível em: [Doi={https://doi.org/10.1103/PhysRevD.71.092003}.>](https://doi.org/10.1103/PhysRevD.71.092003)
- 79 AUBERT, B. et al. Dalitz plot analysis of the decay $b^+ \rightarrow k^+ k^+ k^-$. *Phys. Rev. D*, v. 74, p. 032003, 2006. Disponível em: <https://doi.org/10.1103/PhysRevD.74.032003>.
- 80 GARMASH, A. et al. Evidence for large direct cp violation in $b^\pm \rightarrow \rho(770) k^\pm$ from analysis of the three-body charmless decay $b^\pm \rightarrow k^\pm \pi^\pm \pi^\mp$. *Phys. Rev. Lett.*, v. 96, p. 251803, 2006. Disponível em: <https://doi.org/10.1103/PhysRevLett.96.251803>.
- 81 GARMASH, A. et al. Dalitz analysis of three-body charmless decay $b^0 \rightarrow k_s^0 \pi^+ \pi^-$ decay. *Phys. Rev. D*, v. 75, p. 012006, 2007. Disponível em: <https://doi.org/10.1103/PhysRevD.75.012006>.
- 82 KAMIŃSKI, R. et al. Pion-pion scattering amplitude. iii. improving the analysis with forward dispersion relations and roy equations. *Physical Review D*, APS, v. 77, n. 5, p. 054015, 2008. Disponível em: <https://arxiv.org/abs/0710.1150>.
- 83 AES, P. M. et al. Towards three-body unitarity in $d^+ \rightarrow k^- \pi^+ \pi^+$. *Phys. Rev. D.*, v. 84, p. 094001, 2011. Disponível em: <http://dx.doi.org/10.1103/PhysRevD.84.094001>.
- 84 AES, P. M.; ROBILOTTA, M. *A study of the $D^+ \rightarrow K^- \pi^+ \pi^+$* . Tese (Doutorado) — Universidade de São Paulo, 2014. <http://www.teses.usp.br/teses/disponiveis/43/43134/tde-03112014-142936/pt-br.php>. Disponível em: <http://www.teses.usp.br/teses/disponiveis/43/43134/tde-03112014-142936/pt-br.php>.
- 85 OSET, E. et al. Weak decays of heavy hadrons into dynamically generated resonances. *Int. Journal of Modern Phys.*, v. 25, p. 1630001, 2016. Disponível em: <https://doi.org/10.1142/S0218301316300010>.
- 86 AAIJ, R. et al. Amplitude analysis of the $B^+ \rightarrow \pi^+ \pi^+ \pi^-$ decay. Amplitude analysis of the $B^+ \rightarrow \pi^+ \pi^+ \pi^-$ decay. *Phys. Rev. D*, v. 101, n. 1, p. 012006, 2020. All figures and tables, along with any supplementary material and additional information, are available at <https://cern.ch/lhcbproject/Publications/p/LHCb-PAPER-2019-017.html> (LHCb public pages). Disponível em: <https://cds.cern.ch/record/2689374>.
- 87 AKHMETSHINA, R. et al. Measurement of $e^+ e^- \rightarrow \pi^+ \pi^-$ cross section with CMD-2 around ρ -meson. *arXiv hep-ex/0112031*. Disponível em: <https://arxiv.org/abs/hep-ex/0112031>.

- 88 MACHADO, D. T. et al. Direct CP violation in $B^\pm \rightarrow h^\pm h^+ h^-$ decays using 2015-2018 data. 2019. Disponível em: <<https://cds.cern.ch/record/2702421>>.
- 89 YU, Y. et al. Study of the $d_s^+ \rightarrow a_0(980)\rho a_0(980)\omega$ decays. *The European Physical Journal C*, Springer Science and Business Media LLC, v. 81, n. 12, dec 2021. Disponível em: <<https://doi.org/10.1140%2Fepjc%2Fs10052-021-09895-y>>.
- 90 ABELE, A. et al. High mass ρ -meson states from $\bar{p}d$ annihilation at rest into $\pi^-\pi^0\pi^0 p_{\text{spectator}}$. *Physics Letters B*, Elsevier, v. 391, p. 191–196, 1997. Disponível em: <<https://cds.cern.ch/record/406469>>.
- 91 BERTIN, A. et al. Study of isovector scalar mesons ρ -meson states in the channel $\bar{p} \rightarrow k^\pm k_s^0 \pi^\mp$ at rest with initial angular momentum state selection. *Physics Letters B*, Elsevier, v. 434, p. 180–188, 1998. Disponível em: <<https://www.sciencedirect.com/science/article/pii/S0370269398007679>>.
- 92 FUJIKAWA, M. et al. High-statistics study of $\tau^- \rightarrow \pi^-\pi^0\nu_\tau$ decay. *Phys. Rev. D*, v. 78, p. 072006, 2008. Disponível em: <<https://doi.org/10.1103/PhysRevD.78.072006>>.
- 93 LEES, J. et al. Precise measurement of $e^+e^- \rightarrow \pi^+\pi^-(\gamma)$ with initial state radiations method at babar. *Phys. Rev. D*, v. 86, p. 032013, 2012. Disponível em: <<https://10.1103/PhysRevD.86.032013>>.
- 94 COLLABORATION, L. *Allen GitLab*. 2023. Disponível em: <<https://gitlab.cern.ch/lhcb/Allen>>.
- 95 HUO, W. J. et al. $B_{s,d} \rightarrow \gamma\gamma$ Decay with the Fourth Generation. 2003. Disponível em: <<https://arxiv.org/abs/hep-ph/0302177v1>>.
- 96 ALIEV, T. M.; ILTAN, E. O. $b_s^0 \rightarrow \gamma\gamma$ decay in the two higgs doublet model with flavor changing neutral currents. *Physical Review D*, American Physical Society (APS), v. 58, n. 9, oct 1998. Disponível em: <<https://doi.org/10.1103%2Fphysrevd.58.095014>>.
- 97 SANCHEZ, P. del A. et al. Search for the decay $b_s^0 \rightarrow \gamma\gamma$. *Physical Review D*, American Physical Society (APS), v. 83, n. 3, feb 2011. Disponível em: <<https://doi.org/10.1103%2Fphysrevd.83.032006>>.
- 98 DUTTA, D. et al. Search for the $b_s^0 \rightarrow \gamma\gamma$ and a measurement of the branching fraction for $b_s^0 \rightarrow \phi\gamma$. *Physical Review D*, American Physical Society (APS), v. 91, n. 1, jan 2015. Disponível em: <<https://doi.org/10.1103%2Fphysrevd.91.011101>>.
- 99 BOSCH, S. W.; BUCHALLA, G. The double radiative decays $b \rightarrow \gamma\gamma$ in the heavy quark limit. *Journal of High Energy Physics*, Springer Science and Business Media LLC, v. 2002, n. 08, p. 054–054, aug 2002. Disponível em: <<https://doi.org/10.1088%2F1126-6708%2F2002%2F08%2F054>>.
- 100 LI, D.-H. et al. Strange quark mass effect in $b_s \rightarrow \gamma\gamma, \gamma\bar{l}$ decays. *Physical Review D*, American Physical Society (APS), v. 106, n. 9, nov 2022. Disponível em: <<https://doi.org/10.1103%2Fphysrevd.106.094038>>.
- 101 BETETA, C. A. et al. *Calibration and performance of the LHCb calorimeters in Run 1 and 2 at the LHC*. 2020. Disponível em: <<https://arxiv.org/abs/2008.11556>>.

- 102 COLLABORATION, L. *PIDCalib Package*. 2023. Disponível em: <<https://twiki.cern.ch/twiki/bin/view/LHCb/PIDCalibPackage>>.
- 103 AAIJ, R. et al. Amplitude analysis of the $B^+ \rightarrow \pi^+\pi^+\pi^-$ decay. *Phys. Rev. D*, American Physical Society, v. 101, p. 012006, Jan 2020. Disponível em: <<https://link.aps.org/doi/10.1103/PhysRevD.101.012006>>.
- 104 BENGTLÖRSTAD. Boson interferometry: A review of high energy data and its interpretation. *International Journal of Modern Physics A*, v. 04, 04 2012. Disponível em: <<https://inspirehep.net/literature/268947>>.
- 105 AAIJ, R. et al. *Bose-Einstein correlations of same-sign charged pions in the forward region in pp collisions at $\sqrt{s} = 7$ TeV. Bose-Einstein correlations of same-sign charged pions in the forward region in pp collisions at $\sqrt{s} = 7$ TeV*. 2017. 025 p. All figures and tables, along with any supplementary material and additional information, are available at <https://lhcbproject.web.cern.ch/lhcbproject/Publications/LHCbProjectPublic/LHCb-PAPER-2017-025.html>. Disponível em: <<https://cds.cern.ch/record/2282719>>.
- 106 JOHNSON, M. H.; TELLER, E. Classical field theory of nuclear forces. *Phys. Rev.*, American Physical Society, v. 98, p. 783–787, May 1955. Disponível em: <<https://link.aps.org/doi/10.1103/PhysRev.98.783>>.
- 107 SCHWINGER, J. A theory of the fundamental interactions. *Annals of Physics*, v. 2, n. 5, p. 407–434, 1957. ISSN 0003-4916. Disponível em: <<https://www.sciencedirect.com/science/article/pii/0003491657900155>>.
- 108 JAFFE, R. J. Multiquark hadrons. i. phenomenology of $Q^2\bar{q}^2$ mesons. *Phys. Rev. D*, American Physical Society, v. 15, p. 267–280, Jan 1977. Disponível em: <<https://link.aps.org/doi/10.1103/PhysRevD.15.267>>.
- 109 GUO, F.-K. et al. S wave $k\pi$ scattering and effects of κ in. *Nuclear Physics A*, Elsevier BV, v. 773, n. 1-2, p. 78–94, jul 2006. Disponível em: <<https://doi.org/10.1016%2Fj.nuclphysa.2006.04.008>>.
- 110 PELÁEZ, J.; RODAS, A. Determination of the lightest strange resonance $k_0^*(700)$ or κ from a dispersive data analysis. *Physical Review Letters*, American Physical Society (APS), v. 124, n. 17, apr 2020. Disponível em: <<https://doi.org/10.1103%2Fphysrevlett.124.172001>>.
- 111 FLATTÉ, S. Coupled-channel analysis of the $\pi\eta$ and $k\bar{K}$ systems near kk threshold. *Physics Letters B*, v. 63, n. 2, p. 224–227, 1976. ISSN 0370-2693. Disponível em: <<https://www.sciencedirect.com/science/article/pii/0370269376906547>>.
- 112 ABELE, A. et al. $\bar{p}p$ annihilation at rest into $K_L K^\pm \pi^\mp$. *Phys. Rev. D*, American Physical Society, v. 57, p. 3860–3872, Apr 1998. Disponível em: <<https://link.aps.org/doi/10.1103/PhysRevD.57.3860>>.
- 113 ABLIKIM, M. et al. Resonances in and. *Physics Letters B*, Elsevier BV, v. 607, n. 3-4, p. 243–253, feb 2005. Disponível em: <<https://doi.org/10.1016%2Fj.physletb.2004.12.041>>.
- 114 BARU, V. et al. Flatté-like distributions and the $a_0(980)/f_0(980)$ mesons. *The European Physical Journal A*, Springer Science and Business Media LLC, v. 23, n. 3, p. 523–533, jan 2005. Disponível em: <<https://doi.org/10.1140%2Fepja%2Fi2004-10105-x>>.

- 115 AAIJ, R. et al. Studies of the resonance structure in $d^0 \rightarrow k_s^0 k^\pm \pi^\mp$ decays. *Physical Review D*, American Physical Society (APS), v. 93, n. 5, mar 2016. Disponível em: <https://doi.org/10.1103/PhysRevD.93.052018>.
- 116 UEHARA, S. et al. High-statistics measurement of neutral-pion pair production in two-photon collisions. *Physical Review D*, American Physical Society (APS), v. 78, n. 5, sep 2008. Disponível em: <https://doi.org/10.1103/PhysRevD.78.052004>.